UNIVERSITY OF CALIFORNIA
RIVERSIDE

Pore-Space Optimization of Multi-Functional Crystalline Porous Materials

A Dissertation submitted in partial satisfaction
of the requirements for the degree of

Doctor of Philosophy

in

Chemistry

by

Anh Hong

June 2022

Dissertation Committee:
Dr. Pingyun Feng, Chairperson
Dr. Matthew P. Conley
Dr. Boniface P.T. Fokwa

The Dissertation of Anh Hong is approved:

_____

_____

_____

Committee Chairperson

University of California, Riverside

Acknowledgement

I would like to dedicate my most sincere gratitude to all those who have provided me with assistance, guidance, and encouragement, and without whom, this Ph.D coaster ride would not have successfully reached finish line.

Foremost, I would like to extend my warmest thanks to my advisor, Prof. Pingyun Feng, who made this work possible. Thank you for giving me unrestricted freedom to explore the research arena to my heart content and giving me just the right nudge to propel through the hills and accelerate through each stage. Thank you for always believing in me, even in times where I could not. I aspire to one day, attain the strengths, wisdom and vision that you embody.

I am grateful to Prof. Xianhui Bu at CSULB who had introduced me to the amazing world of crystalline porous materials. I appreciate his creative insights and strong attention to details. I truly enjoyed the enlightening discussions we shared and the seemingly endless but very fruitful cycles of manuscript editing that we endured. His unique perspectives on the different topics brought many colors and excitements to our collaborations.

I am very thankful to be surrounded by so many brilliant and delightful lab mates whom I have shared many fond memories with. I want to thank our postdoctoral researchers, Dr. Xiang Zhao and Dr. Huajun Yang, who have continuously provided me with support and guidance since day one at UCR. I appreciate Dr. Yanxiang Wang for always keeping the atmosphere of our lab fun and cozy. I want to extend many thanks to our undergraduate minions, Emily Kusumoputro and Angel Zhou, who have invested long hours towards many of my projects. I also want to thank the visiting scholars who have shared their knowledges and experiences, particularly: Dr. Xiaoxia Jia, Dr. Yong Wang, Dr. Songsong Li, Dr. Dandan Hu, Dr. Kun Lan, Dr. Xiaowu Lei, Dr. Yanli Gai, Dr. Fengming Zheng. It has been a great

experience working with many past and current members of Feng group: Dr. Xitong Chen, Yuchen Xiao, Yichong Chen, and Pooja Ajayan.

I am also thankful to my committee members Prof. Matthew Conley and Prof. Boniface P.T. Fokwa for their valuable comments on my dissertation.

I really appreciate our collaborators: Prof. Boniface P.T. Fokwa group for magnetic studies, Prof. Jing Shi group for electron transport measurements, Prof. Alex Greaney group for computational modeling, and Prof. Yongtao Cui group for atomic force microscopy measurements.

I also like to thank the wonderful staff in our chemistry department, who were always ready to lend a hand every time I sought their assistance.

Finally, I would like to thank my family and friends who have motivated me to overcome all the hurdles during my Ph.D study.

Several chapters of this dissertation, in part or in full, are reprinted from materials in the following publications:

Chapter 2: Hong, A. N.; Yang, H.; Li, T.; Wang, Y.; Wang, Y. X.; Jia, X.; Zhou, A.; Kusumoputro, E.; Li, J.; Bu, X.; Feng, P., Pore-Space Partition and Optimization for Propane-Selective High-Performance Propane/Propylene Separation. *ACS Appl Mater Interfaces.*, **2021**, 13, 52160-52166.

Chapter 3: Hong, A. N.; Kusumoputro, E.; Wang, Y.; Yang, H.; Chen, Y.; Bu, X.; Feng, P., Simultaneous Control of Pore-Space Partition and Charge Distribution in Multi-Modular Metal-Organic Frameworks. *Angew. Chem. Int. Ed.,* **2022**, 134, e202116064.

Chapter 6: Hong, A. N.; Yang, H.; Bu, X.; Feng, P., Roles of Alkali Metals and Ionic Networks in Directing the Formation of Anionic Metal-Organic Frameworks. *Cryst. Growth Des.,* **2020**, 20, 6668-6676.

Dedication

To my family

ABSTRACT OF THE DISSERTATION

Pore-Space Optimization of Multi-Functional Crystalline Porous Materials

by

Anh Hong

Doctor of Philosophy, Graduate Program in Chemistry
University of California, Riverside, June 2022
Dr. Pingyun Feng, Chairperson

The unique characteristics of metal-organic frameworks (MOFs) have sparked interests from scientists and engineers of diverse backgrounds, ushering in rapid development of MOF materials into a large multi-interdisciplinary field. Among different families of materials, the highly robust and modular partitioned-acs (*pacs*) platform is uniquely suited for the exploration of energy related applications.

In the first section, upper and lower limits of pore metrics were mathematically derived and validated with new material synthesis. Many constructed structures also exhibit shapes and sizes that were previously thought of, as impossible to attain. A new strategy was then introduced to construct robust and versatile anionic MOFs. The effects of pore geometry and counter anions were systematically investigated on cationic *pacs* materials. Finally, sulfonation of *pacs* frameworks were carried out to harness the power

associated with this interesting group. The enrichment of *pacs* platform with novel framework design methodologies, result in the construction of optimized materials with impressive properties in a range of gas storage and separation applications.

The vast synthetic space of MOFs encompasses huge numbers of synthetic parameters and variations, giving us plenty of room to investigate new structural features and their related applications. In the second section, we explored novel material design and synthesis strategies to assemble molecular units into novel frameworks with desired functionalities. In particular, we examined ways to build effective ion-transport and magnetic coupling pathways in our new design strategies.

Table of Contents

Chapter 1 Introduction 1

1.1 Metal-organic Framework 1

1.2 Crystal Engineering of Metal-organic Framework 2

1.2.1 Pore Chemistry of Inorganic Unit 3

1.2.2 Pore Space and Function through Organic Linkers 9

1.2.3 Modulating Framework Charge 11

1.3 Metal-organic Frameworks in Energy-related Applications 12

1.3.1 Metal-organic Frameworks in Gas Capture and Storage 12

1.3.2 Metal-organic Frameworks in Separations 16

1.3.3 Metal-organic Frameworks in Ionic Conduction 22

1.3.4 Metal-organic Frameworks Magnetic Studies 23

1.4 Establishment of the Partitioned-*acs* Platform 24

1.5 Scope of this work 27

1.6 Reference 29

Chapter 2 Uncovering Limits of Partitioned-acs Frameworks 47

2.1 Introduction 47

2.2 Experimental Section 49

2.2.1 Chemicals and Materials 49

2.2.2 Synthesis of Organic Linkers 49

2.2.3 Synthesis of Partitioned-acs Frameworks 50

2.2.4 Property Characterization 56

2.3 Results and Discussion 60

2.3.1 Finding limits to the "Swelling" of acs-net 60

2.3.2 Correlating Theoretical Model to *pacs* Structures 68

2.3.3 Volume Maximization for C_3H_6/C_2H_4 Separation 70

2.3.4 Pore Expansion/Compression for C_3H_6/C_3H_6 Separation 73

2.4 Conclusion 82

2.5 Reference 83

Chapter 3 The Robust and Versatile Anionic Partitioned-*acs* Frameworks 86

3.1 Introduction 86

3.2 Experimental Section 89

3.2.1 Chemicals and Materials 89

3.2.2 Synthesis of Acid and Base Forms of Pore-Partitioning Agent 90

3.2.3 Synthesis of tph-based *pacs* 91

3.2.4 Synthesis of Co_2V-tph based *pacs* with Different Organic Salts 94

3.2.5 Property Characterization 96

3.3 Results and Discussion 98

3.3.1 Structure Characterization 98

3.3.2 Hydrolytic Stability 101

3.3.3 Gas Adsorption Studies 104

3.3.4 Vapor Adsorption Studies 111

3.4 Conclusion 112

3.5 Reference 114

Chapter 4 Cationic Partitioned-acs Frameworks and C_2H_2/CO_2 Separation 121

4.1 Introduction 121

4.2 Experimental Section 126

4.2.1 Chemicals and Materials 126

4.2.2 Synthesis of Cationic *pacs* Materials 126

4.2.3 Property Characterization 128

4.3 Results and Discussion 131

4.4 Conclusion 144

4.5 Reference 145

Chapter 5 Sulfonated Partitioned acs Frameworks 149

5.1 Introduction 149

5.2 Experimental Section 151

5.2.1 Chemicals and Materials 151

5.2.2 Synthesis of Organic Precursors....152
5.2.3 Synthesis of Crystalline Porous Materials....153
5.2.4 Property Characterization....155
5.3 Results and Discussion....157
5.3.1 Design and Synthesis of Sulfonated *pacs*....157
5.3.2 Structural Optimization of Sulfonated *pacs*....160
5.3.4 Ionic Conductivity....163
5.4 Conclusion....164
5.5 Reference....164
Chapter 6 The Roles of Alkali Metals and Ionic Network in Directing the Formation of Conductive Metal-Organic Frameworks....167
6.1 Introduction....167
6.2 Experimental Section....171
6.2.1 Chemicals and Materials....171
6.2.2 Construction of M2dsoba (M = Na, K, Cs)....171
6.2.3 Synthesis of sulfonated MOFs....171
6.2.4 Property Characterization....173
6.3 Results and Discussion....177
6.3.1 Crystal Structure....178

6.3.2 Thermal Gravimetric Analysis 189

6.3.3 Ionic Conductivity 190

6.3.4 Gas Adsorption 192

6.4 Conclusion 192

6.5 Reference 194

Chapter 7 Rod-packing Metal-Organic Frameworks for Magnetic Studies 201

7.1 Introduction 200

7.2 Experimental Section 204

7.2.1 Material Synthesis 204

7.2.2 Property Characterization 205

7.3 Results and Discussion 207

7.4 Conclusion 215

7.5 Reference 216

Chapter 8 Conclusion and Outlook 220

List of Figures

Figure 1.1 Illustration of MIL-47/MIL-53 frameworks. (a) Large pore and narrow pore in breathing MIL-53 isostructures. (b) Neutralization of framework through different bridging units 4

Figure 1.2 Heterometal combinations in CPM-200 6

Figure 1.3 Illustration of pillared-layer framework. Metal ion coordinating to ditopic and tetratopic pyridyl-based linkers into 2D sql layers. Inorganic ions pillar layers into 3D pillared-layer frameworks. M^{5+} includes Nb, M^{4+} includes Ti, Si, Ge, Sn, M^{3+} includes Al, Fe 8

Figure 1.4 Illustration of partitioned-acs frameworks (*pacs*) 26

Figure 2.1 Capturing two different degrees of opening of bpdc-based *pacs* through employment of different sized L2 linkers. Enlargement of a-axis results in compression of c-axis (orange pocket) 48

Figure 2.2 Triangular pyramid of the *pacs* platform, where a and c are a- and c-axes, respectively, θ represents degree of opening between L1 linker and height of pyramid, and Z represents the O---O length between two trimers connected by L1 linker.....60

Figure 2.3 Ligand expansion through the "core" component versus "extender" component.....61

Figure 2.4 Potential L2 linkers identified from core expansion and extender strategies.62

Figure 2.5 Single-crystal structures of pore-changing *pacs* platform through substitution of prototype *pacs* (26ndc-tpt) with short L1 (bdc-tpt), longer L1 (bpdc-tpt), shorter L2 (26ndc-tpa), longer L2 (26ndc-tpbtc), shorter L1 and L2 (bdc-tpa), longer L1 and L2 (bpdc-tpbtc).
.....63

Figure 2.6 PXRD patterns of as synthesized and after gas sorption of *pacs* samples. 65

Figure 2.7 EDS analysis of *pacs* materials. 66

Figure 2.8 Thermal stability and porosity of *pacs* materials. (a,c,e) TGA pattern spectra, (b,d,f) N_2 isotherms at 77 K.....67

Figure 2.9 Simulated and experimental crystal volumes at different framework opening degree.....70

Figure 2.10 C_3H_6/C_2H_4 separation performances of *pacs*. (a) C_3H_6 and C_2H_4 isotherms and (b) 50/50 IAST selectivity of CoV-L1-tpbtc *pacs* at 298 K. (c) C_3H_6 and C_2H_4 isotherms and (b) 50/50 IAST selectivity of CoV-bpdc-L2 *pacs* at 298 K 72

Figure 2.11 C_3H_6 and C_3H_8 isotherms of L1 or L2 substituted Co_2V-26ndc-tpt at 298 K 74

Figure 2.12 C_3H_8 and C_3H_6 heat of adsorption for *pacs* in this study. (a) Q_{st} curve from 0 to 5 mmol/g, (b) bar chart comparison of Q_{st} at 1 mmol/g 75

Figure 2.13 (a) C_3H_8 and C_3H_6 isotherm comparison of Co_2V-26ndc-tpt and Co_2V-adc-tpt (< 0.35 bar, 298 K). (b) C_3H_8 and C_3H_6 isotherm comparison of Co_2V-26ndc-tpt and Co_2V-26ndc-tpbtc (< 0.35 bar, 298 K). (c) The calculated C_3H_8/C_3H_6 (50:50) IAST selectivity of *pacs* materials at 298 K. (d) the potential C_3H_6 recovered as a function C_3H_8/C_3H_6 (50:50) IAST selectivity of all reported C_3H_8-selective MOF adsorbents at 298 K, 1 bar.....77

Figure 2.14 Breakthrough curves obtained for C_3H_8/C_3H_6 mixtures (a) 1:1, v/v and (b) 1:15, v/v with CPM-734c at 298 K.....80

Figure 3.1 Comparison between first and second generation designs of anionic *pacs* materials.....88

Figure 3.2 Design of tph-based anionic *pacs* frameworks with different modules 99

Figure 3.3 Simulated as as-synthesized PXRD patterns of tph-based *pacs* materials with different metals, ditopic linker and guest ions 100

Figure 3.4 Simulated as as-synthesized PXRD patterns of tph-based pacs materials with different metals, ditopic linker and guest ions 101

Figure 3.5 Chemical stability of different tph-based *pacs* 102

Figure 3.6 C_2H_2 isotherms of CPM-600-based *pacs*. (a) C_2H_2 uptakes of CPM-600b with anionic metal (Mg) versus neutral metal (CoV) trimers at 273 K and 298 K, (b) C_2H_2 isotherms of CPM-600x-CoV series at 273 K.....105

Figure 3.7 (a) TGA and (b) N_2 analyses of CPM-600x-CoV *pacs* materials 106

Figure 3.8 C_3H_6/C_3H_8 adsorption performances of CPM-600d-based *pacs* at 298 K. (a) Comparison of C3 isotherms between CPM-600d-CoV prototype and CPM-600d-CoV-Ph_4P, (b) Comparison of C3 isotherms between CPM-600d-CoV prototype and CPM-

600d-CoV-dhdmN and (c) Comparison of potential C_3H_8 recovered through employment of different adsorbents in C_3H_8/C_3H_6 (50/50 v/v) separation 109

Figure 3.9 Cyclohexane/Benzene (50/50 v/v) vapor selectivity of CPM-600-CoV prototype and different guest ions.....112

Figure 4.1 Classification of gas separation performance by a combination of individual gas uptake and selectivity 122

Figure 4.2 A tandem modulation approach to combat uptake and selectivity tradeoff .123

Figure 4.3 Volume-max calculation and core-expansion approach employed to optimize pore volume of cationic cpt-based framework. Through core-expansion approach, L2 of varied lengths are inserted into cpt-based MIL-88 framework, resulting in systematic widening of theta angle, and enlargement of crystallographic volume 124

Figure 4.4 C_2H_2 and CO_2 uptake performance of *pacs* materials in this study. (a) C_2H_2 and CO_2 Isotherms at 298 K and (b) 50/50 IAST selectivity comparisons between Co_2-cpt-based *pacs* with different L2, (c) C_2H_2 and CO_2 Isotherms at 298 K and (b) 50/50 IAST selectivity comparisons between cpt-tph-based *pacs* with different transition metal and balancing anions. (e) Effects of tuning different *pacs* modules on the uptake difference between C_2H_2 and CO_2 at 298 K, 1 bar 132

Figure 4.5 PXRD analyses of (a) CPM-124a, (b) CPM-124b, (c) CPM-124c-Co. Left column represents as-synthesized material, whereas column confirms its hydrolytic stability.....133

Figure 4.6 Experimental and simulated PXRD patterns for (a) M_3-cpt-tph and (b) Co-cpt-tph-x *pacs* materials. Simulated PXRD obtained from single crystal XRD data of Co_3-cpt-tph (c) hydrolytic stability of CPM-600c-Ni-Cl.....136

Figure 4.7 TGA CPM-124-based *pacs* materials.....137

Figure 4.8 Selective gas sorption of CPM-124-x-Co-Cl *pacs* materials. (a) N_2 sorption isotherms at 77 K, (b) C_2H_2 and CO_2 isotherms at 273 K and 298 K, (c) Isosteric heat of adsorption obtained from 273 K and 298 K isotherms (d) 50/50 C_2H_2/CO_2 IAST selectivity 138

Figure 4.9 Selective gas sorption of CPM-124c-Co-x *pacs* materials. (a) N_2 sorption isotherms at 77 K, (b) C_2H_2 and CO_2 isotherms at 273 K and 298 K, (c) Isosteric heat of adsorption obtained from 273 K and 298 K isotherms (d) 50/50 C_2H_2/CO_2 IAST selectivity 140

Figure 4.10 Selective gas sorption of CPM-124c-Co-x *pacs* materials. (a) N_2 sorption isotherms at 77 K, (b) C_2H_2 and CO_2 isotherms at 273 K and 298 K, (c) Isosteric heat of adsorption obtained from 273 K and 298 K isotherms (d) 50/50 C_2H_2/CO_2 IAST selectivity 142

Figure 4.11 C_2H_2/CO_2 gas separation performance of CPM-124c-Co-Cl. (a) 50/50 C_2H_2/CO_2 gas separation performance at 2 mL flow rate, 298 K, 1 bar, (b) at different flow rates (c) reusability of material through multiple cycling of breakthrough separation (d) comparison of breakthrough time versus C_2H_2 uptake among top performing porous materials at 50/50 C_2H_2/CO_2 gas separation, 2 mL flow rate 143

Figure 5.1 Overcoming geometry limitations for construction sulfonate *pacs*.....151

Figure 5.2 Phase purity and water stability experiments of (a) CoFe-sndc-tph and (b) CoFe-dsndc-tph.....156

Figure 5.3 Desired mode of coordination for each functional group in sulfonate-*pacs* system 157

Figure 5.4 Estimated closest distance between sulfonate groups in potential In-dsndc-tpt structure.....158

Figure 5.5 CO_2 isotherm comparison between CoIn-sndc-based *pacs* synthesized from tph and tpbtc partitioning agent 159

Figure 5.6 Crystal structures of CoIn-sndc-tpbtc and CoIn-dsndc-tpbtc 161

Figure 5.7 Carbon dioxide isotherms at 273 K for (a) sndc-tph-based *pacs* with CoIn and CoFe metals, (b) CoFe-tph-based *pacs* with different concentration of sulfonate groups 162

Figure 5.8 Nyquist plot of CoFe-dsndc-tph 163

Figure 6.1 Synthetic design for constructing CPM-s1 to CPM-s6 169

Figure 6.2 Dimension of ionic bonding alkali ions in relation to the overall dimension of coordinating framework. (Top left to right) cluster environments of Na^+, 1D chain and 2D sheet of K^+, 3D network of Cs^+. Na (tan), K (purple), Cs (dark purple), O (red) S (yellow). (Bottom right to left) two 1D chains and three 3D network. Zn coordination polyhedron (dark orange), organic linker (orange).....170

Figure 6.3 PXRD of CPM-s1 to CPM-s6 174

Figure 6.4 Thermal gravimetric analysis curve comparisons of materials in this study: (a) materials made from Na_2dsoba ligand, (b) materials made from K_2dsoba ligand, (c) materials from uro-amide solvent system, (d) materials from the aqueous-amide solvent system 175

Figure 6.5 PXRD of simulated, as-synthesized and after conduction measurements of CPM-s2 176

Figure 6.6 PXRD of simulated, as-synthesized and after conduction measurements of CPM-s3 176

Figure 6.7 PXRD of CPM-s3 after gas sorption 177

Figure 6.8 Illustration of CPM-s1. (a) Zn_4O SBU, (b) local coordination environment, (c) 3D anionic framework 179

Figure 6.9 Illustration of CPM-s2. (a) Zn_4O SBU, (b) local coordination environment, (c) 3D anionic framework 180

Figure 6.10 Two anionic MOF-5 type structures viewed from the apex of $Zn_4O(COO)_6$ in (a) CPM-s1, and (c) CPM-s2. DMF molecule is drawn as oxygen for clarity. Transformation from CPM-s1 (b) to two-fold interpenetration CPM-s2 (d).....180

Figure 6.11 Illustration of CPM-s3. (a) Top-down and aerial views of SBU, (b) local coordination environment with two ligands coordinating to same two SBUS highlighted in blue, (c) View of the 3D framework through c-axis, (d) topological net of the framework 182

Figure 6.12 Illustration of CPM-s4. (a) monomeric and paddlewheel SBUs of the framework, (b) binding mode of K^+ along the SO_3^- channel, (c) 3D representation of framework 184

Figure 6.13 Illustration of CPM-s5. (a) metal coordination, (b) 1D metal chain, (c) 3D representation of framework 185

Figure 6.14 Illustration of CPM-s6 186

Figure 6.15 Dimension of ionic bonding alkali ions (top) in relation to the overall dimension of the coordinating frameworks (bottom). Zn (cyan), C (grey), O (red), Na (aquamarine), K (pink), Cs (purple) 187

Figure 6.16 Coordination modes of CPM-s1 to CPM-s6. (a-d) 3D framework of CPM-s1 to CPM-s4. (e-f) 1D coordinating chain of CPM-s5 and CPM-s6 188

Figure 6.17 Nyquist diagram of the powder sample of CPM-s1 at 22 °C, 99 RH 190

Figure 6.18 Gas sorption data of CPM-s3, after ethanol exchanged, and degassed 193

Figure 7.1 Transformation of 3D CPM-s7 to 2D CPM-s8 through in-situ formation of SO_4^{2-} capping agent.....203

Figure 7.2 Experimental and simulated PXRD patterns of CPM-s8 206

Figure 7.3 TGA graph of CPM-s8 206

Figure 7.4 Graphic representations of CPM-s7. a) octahedrally coordinated Mn^{2+} chain and monomeric Mn^{2+} building unit, b) Expansion of Mn(1) and Mn(2) into 2D square layer, c-f) layers connected by Mn(3) and Mn(4) and sulfonate groups into 3D framework with 1D channel. In c-d) pendant groups and Mn(4) are removed for clarity. All non-bonding water molecules are also removed from drawings.....208

Figure 7.5 View of 2D sheets of CPM-s7 along ab-plane. Green circles represent positions which $Mn(HCOO)_2$ connects two adjacent trimers and sulfonate connects nearby trimer.....209

Figure 7.6 Graphic representations of CPM-s8. (a) octahedrally coordinated cobalt pentamer, with Co(1) residing on symmetry equivalent site, (b) 1D cobalt chain with bridging hydroxide, sulfate, and formate linkers, (c) 2D sheet in ac-plane, (d) View of parallelly stacked 2D layers in bc-plane 210

Figure 7.7 Coordination sphere of each unique cobalt in CPM-s8.....212

Figure 7.8 (a) Temperature dependent ZFC and FC molar susceptibility curve of CPM-s8 recorded at 100 Oe. Inset shows the FC inverse molar susceptibility curve (at 1000 Oe) and the Curie-weisss straight line (red). (b) DFT predicted ground state spin density distribution in a 2x1x1 supercell of CPM-s8 213

List of Tables

Table 1.1 Select examples of MOFs with high C_2H_2 storage at 1 bar 15

Table 1.2 Properties of select gases 16

Table 1.3 Selected examples of MOFs for hydrocarbon separation 17

Table 1.4 Select examples of MOFs with high C_2H_2/CO_2 separation performance at 298K 18

Table 2.1 Summary of unitcells of CoV-based *pacs* materials 64

Table 2.2 Summary of MOFs with C_3H_8 uptake 77

Table 3.1 Summary of H-tph to organic cation ratio during synthesis versus NMR.....95

Table 3.2 Crystal data summary of CPM-600(a-d).....97

Table 3.3 Hydrolytic stability of benchmark anionic MOFs. 103

Table 3.4 Summary of gas sorption isotherms and heat of adsorption 107

Table 3.5 Summary of benchmark ionic MOFs for C_2H_2 uptake 109

Table 4.1 Crystal Data summary of CPM-154 *pacs* materials 129

Table 4.2 Elemental analysis of *pacs* in this study by EDS and proposed formula 130

Table 4.3 Summary of gas sorption performances and simulation of materials in this study.....141

Table 4.4 Summary of benchmark ionic MOFs for C_2H_2 uptake.....142

Table 5.1 Range of tunable charge in each of the three *pacs* module 150

Table 6.1 Summary of crystal data and structure refinements for CPM-s1 to CPM-s6 178

Table 6.2 Conductivities of MOFs containing alkali-metals under humid conditions ..191

Chapter 1: Introduction

1.1 Introduction to Metal-organic Frameworks

Over the past several decades, the field of crystalline porous materials (CPM) has evolved from all-inorganic zeolites to include chalcogenides, covalent-organic frameworks (COFs), and hydrogen-bonded organic frameworks (HOFs).[1-5] Among these, MOFs, due to its nature as inorganic-organic hybrids with practically infinite permutations of metal nodes with organic linkers, have resulted in a diverse array of frameworks with intrinsically unique pore characteristics. Depending upon the underlying topological net, the periodic void space of MOFs has features ranging from 0D pore[6] to 1D channel[7] and higher dimensional channels,[8] from regular geometrical shapes (e.g., rectangular,[9] spherical,[10] tubular[11]) to highly irregular conformations (e.g., gourd-like pockets,[12] bottlenecked pore,[13] tri-oval microchannels[14]). MOFs have uniform pore windows ranging from angstroms to nanometers (largest known at 9.8 nm)[15] and internal surface area up to around 7800 m^2/g.[16] Certain structures undergo phase change in response to external stimuli such as guest molecules incorporation, pressure, temperature, light, and electric field.[17] The inherent properties embedded in both inorganic and organic units also allow the assembled MOFs to have rich pore functionalities suitable for different industrial applications such as gas separation,[18] proton conduction,[19] catalysis,[20] etc. MOFs have thus far brought forth many exciting properties unparalleled by other types of porous solids, and fascinating structural features are still expected to be uncovered in advent of new MOF construction.

1.2 Crystal Engineering of Metal-organic Framework

While the search for new MOF structure type continues unabated, the availability of a large library of known MOF structure types presents an increasingly enticing opportunity, not only for application scientists, but also for materials-design specialists traditionally focused on new platform development. With each new MOF structure type developed, the ability to systematically regulate compositional and structural features of a given MOF prototype is gaining greater importance. The degree of tunability differs greatly for different platforms, depending on metal-ligand coordination chemistry and geometry, cluster types, and the number of replaceable components or modules. In-depth understanding of metal chemistry and the synthetic conditions which establish a particular metal cluster or secondary building unit (SBU) creates the possibility of targeting MOFs with predetermined nets. For crosslinking units (e.g., organic ligands), it should be kept in mind that in addition to scaling, functional groups (e.g., triazolates and carboxylates) that appear quite different can be isoreticularly exchangeable for some coordination modes (e.g., trigonalplanar M_3OH trimer). The predictability in crystal engineering allows for more rational design and adjustments to MOFs, leading to incorporation and enhancement of desired properties.

Strategic tailoring of MOFs could be performed at the pre-synthetic design as well as post-synthetic modification (PSM) stage.[21-22] In pre-synthesis design, judicious choices of SBUs, organic linkers, extra-framework guest ions when applicable, and solvents/additives are made to embed the final framework with more desirable pore size and functionalities. The practice of regulating and diversifying frameworks through heterogenizing one or

more framework modules further enables the harnessing of favorable synergistic effects. It is noteworthy though, to mention that complexity of the multicomponent system leads to high diversity in self-assembly stage, which could result in desired crystalline products, unexpected materials, previously reported crystals, or amorphous phases. The built-in component complementarity, e.g., the use of charge-complementary M^{2+}/M^{3+} metal ions to regulate the framework charge and the host-guest charge matching, or the use of charge- or geometry-complementary ligands, has been shown to be an effective strategy to drive the multi-component assemblies. Framework regulation could also occur through post-synthetic ion or ligand exchange, covalent or coordinative functionalization. Post-synthetic methods utilizing covalent or coordinative functionalization generally rely on the stability of the materials, with limitations placed upon organic reaction condition and accessible coordination sites, respectively.

1.2.1 Pore Chemistry of Inorganic Unit

Unlike traditional porous materials such as zeolites and chalcogenides in which only a small subset of metal ions and crosslinking anions (e.g., tetrahedrally coordinated ions in zeolites or supertetrahedral metal chalcogenide clusters) can be used, MOFs can accommodate metal ions from every part of the periodic table. The nuclearity, geometry, and connectivity of inorganic units give rise to MOFs with exceptional architectural diversity.

Additionally, for MOFs with predetermined topologies, the intrinsic properties inherent to individual metal ions result in different coordination chemistry that could have

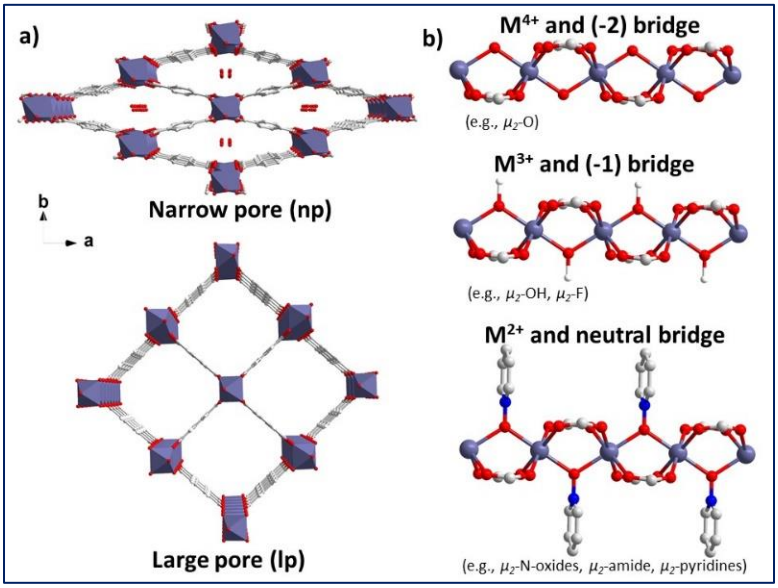

Figure 1.1 Illustration of MIL-47/MIL-53 frameworks. (a) Large pore and narrow pore in breathing MIL-53 isostructures. (b) Neutralization of framework through different bridging units.

vastly different impact on the physical and chemical properties of the final framework. For instance, infinite corner-sharing $(V^{4+})O_6$ octahedra and terephthalate groups are combined to form "non-breathing" MIL-47(V) *sra*-network.[23] When V^{4+} is substituted with Al^{3+}, Sc^{3+}, Cr^{3+}, Fe^{3+}, Ga^{3+}, In^{3+} in the MIL-53 analogs,[24-29] the corner-sharing octahedra have two μ_2-OH groups ($M^{3+}O_4(OH)_2$), which governs the large "breathing" of the framework between large pore (lp) and narrow pore (np) upon guest adsorption (Figure 1.1).[30-31] Special measures taken to prevent oxidation of V^{3+} allows MIL-47 framework to exhibit large lp-np transformation.[32] Further substitution of MIL-53 with divalent metals requires switching of μ_2-OH (or μ_2-F)[33] groups with neutral bridging linkers (e.g., amides,[11, 34] pyridones,[3935] pyridine-N-oxide and derivatives,[36] which in turns could help regulate pore geometry of MOF materials.

Enhancing metal diversity through heterometal doping is another great strategy to harness properties that could not be achieved with only one type of metal ions. Metals with similar attributes such as coordination geometry, oxidation state, ionic radius, rate of reaction tend to share symmetry equivalent sites more easily (e.g., mixing tetrahedrally coordinated Zn^{2+} and Co^{2+} into the same sodalite structure[37] or 12-connected Hf^{4+} and Zr^{4+} in UiO-66).[38] The rod-shaped SBUs of MOF-74 could accommodate as many as 10 different divalent metals in 1 phase.[39] In the case of mixing of metal ions with identical oxidation state (e.g., Zn^{2+}/Co^{2+}, or different Ln^{3+} ions), the entropic factor is a key driving force in crystallization. Sometimes, it is preferable to use metal ions with complementary oxidation states whose ratio (e.g., M^{2+}/M^{3+} ratio) can be responsive to the inclusion of either neutral or charged guest species. Through control of solvent ratio, dissociation/solvation of metal salts, amount of additives, mixing of highly dissimilar metals could also be realized. In CPM-200, the cooperative heterometallic mixing between highly dissimilar metals resulted in 8 combinations of M^{2+}/M^{3+} trimers (Mg/Sc, Mg/V, Mg/Fe, Mg/Ga, Mg/In, Mn/In, Co/In, and Ni/In), four of which, prior to this work, are unknown to crystalline porous materials.[40] CPM-200 is a representative example that demonstrates the charge complementarity resulting from the use of metal ions with different oxidation states can be a driving force in the formation of MOFs with unusual chemical compositions.

The introduction of more than one topologically distinct SBU into the design and synthesis of MOFs also provides opportunities to explore unique structure types and chemical functionalities that are not accessible in the simpler one-SBU system. The

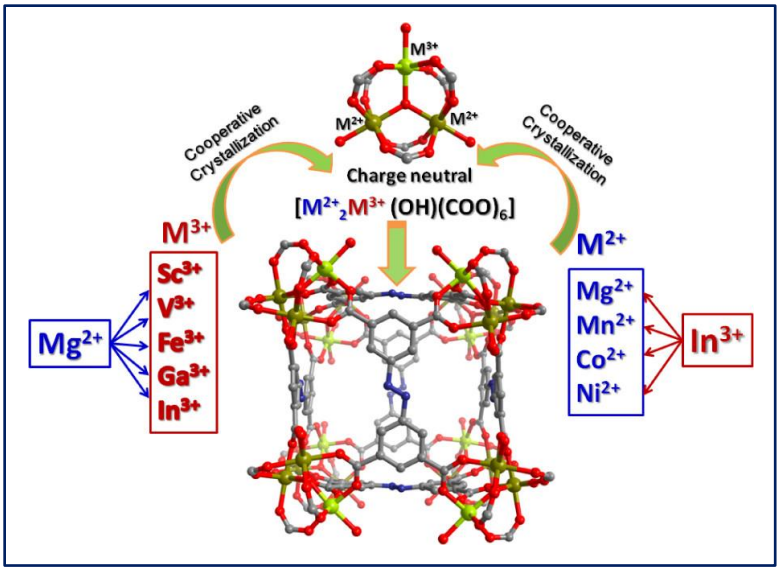

Figure 1.2. Heterometal combinations in CPM-200.

increase of structural complexity challenges us to better predict the chemistry that governs different SBU formations, and precisely control reaction conditions to obtained desired MOF structure. For instance, a novel double-walled cage of $Zn_{36}@Zn_{104}$ (HHU-8) is created recently from five different Zn^{2+} clusters (paddlewheel, O^{2-} connected bi-paddlewheels, COO^{-} connected bi-paddlewheels, trimer and tetramer), which yet again pushes the upper limits of topologically distinct SBU components in a single framework.[41]

Some heterometallic compositions have unique ability to form multi-SBU MOFs when heterometals are not randomized in the same SBU (e.g., M_3O/OH). One prominent system is based on In-MOFs. In addition to the octahedral geometry similar to 3d metal ions, In^{3+} can also adopt 8-coordinated and 4-connected monomeric configuration. When the latter configuration, which is impossible for 3d metal ions, occurs together with 3d ions, very interesting multi-SBU MOFs have been obtained. One such example is CPM-16 where two metals with distinct coordination modes are employed to form zeolite-like

frameworks. Two carboxylate groups of 1,3,5-benzenetricaboxylic acid (H_3btc) coordinate with 4-connected In^{3+} monomer into a $AlPO_4$-5 like framework while a third carboxylate group immobilize V-shaped cobalt dimer (Co_2OH) and Co paddlewheels (Co_2) into the cylindrical walls of the framework.[42]

In addition to metal node regulation, inorganic bridging unit also plays important roles in tuning final framework properties. Inorganic linkers are especially effective for making small-pore MOFs. They can bond to a particular metal site using a single donor site similar to pyridyl groups, and yet carries a charge similar top carboxylate group. The pillared-layer coordination polymer presents an interesting platform with both tunable primary building unit (PBU) and inorganic crosslinker.[43-44] Metal nodes are linked by pyridyl-based ditopic and tetratopic linkers into 2D **sql** sheets that are further connected by inorganic pillars into 3D **pcu** or **fsc** network, respectively (Figure 1.3). The octahedrally coordinating PBUs are composed of late transition metals (i.e., Fe^{2+}, Co^{2+}, Ni^{2+}, Cu^{2+}, Zn^{2+}),[45-47] while the fluorinated inorganic pillars are constructed from metals and metalloids with oxidation states between +3 to +5 (i.e., Al^{3+}, Fe^{3+}, Si^{4+}, Ti^{4+}, Ge^{4+}, Sn^{4+}, Nb^{5+}).[48-51] For the anionic pillars to have an overall -2 charge, M^{3+} metals must contain one neutral coordinating H_2O molecule (e.g., $Al(H_2O)F_5^{2-}$), tetravalent ions are charged balanced by hexafluoro groups (e.g., SiF_6^{2-}), and M^{5+} metals have one oxo^{2-} group (e.g., $NbOF_5^{2-}$). Compared to SiF_6^{2-} pillar in SIFSIX-3-Ni, the bulkier $NbOF_5^{2-}$ pillar in NbOFFIVE-1-Ni results in smaller channel distances. In comparison, the $Al(H_2O)F_5^{2}$ pillar AlFFIVE-1-Ni has weakly coordinated water molecule distributed among the 4 equatorial positions. AlFFIVE-1-Ni has strong affinity towards water uptake, creating

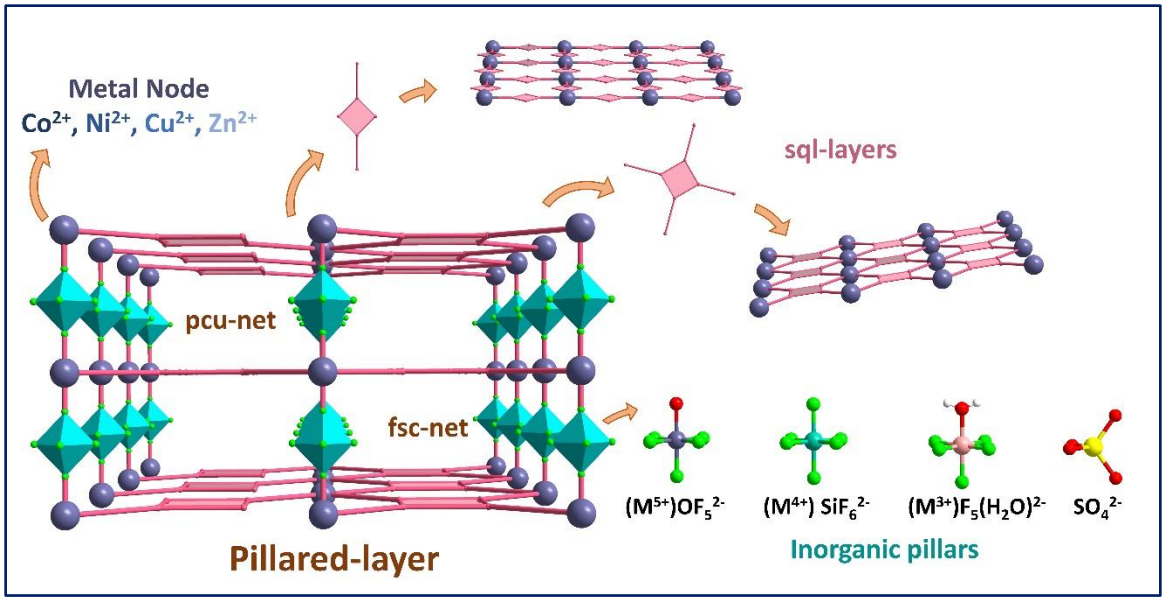

Figure 1.3. Illustration of pillared-layer framework. Metal ion coordinating to ditopic and tetratopic pyridyl-based linkers into 2D sql layers. Inorganic ions pillar layers into 3D pillared-layer frameworks. M^{5+} includes Nb, M^{4+} includes Ti, Si, Ge, Sn, M^{3+} includes Al, Fe.

hydrogen bonding networks. Interestingly, desorption of water molecules is also facile, requiring low regeneration temperature for dehydration of water in channel and coordinating water, leading to trigonal bipyramidal AlF_5^{2-} pillar. For materials with same organic components, simply substituting different metal of the same oxidation state can still lead to changes in pore metrics. For instance, in SIFSIX-1-Cu, substituting Si^{4+} with Ti^{4+} and Sn^{4+} results in increase of M—pillar—M distance from 8.11 to 8.40, and 8.63 Å, respectively. In SIFSIX-3-M, the choice of divalent metal affect M—N distance, leading to **sql** layers of slightly different sizes, and consequently, influenced the adjacent F---F distances. Recent studies reveal the possibility of substituting fluorinated-based pillars with the bent SO_4^{2-}.[52] Other inorganic ions such as PO_4^{3-}, CrO_4^{2-}, MoO_4^{2-}, WO_4^{2-} have also been employed in constructing organic-inorganic hybrids.[53-56]

1.2.2 Pore Space and Function through Organic Linkers

Of no less importance to the design of inorganic unit(s) during MOF synthesis is the strategic control over organic building unit. Such control is not limited to finding or synthesizing ligands not previously used in MOFs, but also include well-established MOF ligands such as bdc^{2-} (1,4-benzenedicarboxylate) and btc^{3-} (1,3,5-benzenetricarboxylate) in new coordination modes or in combination with new inorganic nodes or other organic ligands. Over the years, principles of organic synthesis have continuously aided the construction of novel organic linkers that are highly diverse in geometric shape, size, and functionalities. Inherent properties of these organic linkers directly translate into outstanding pore features, allowing for advancements of MOF materials in various applications.

In general, size of pore aperture and volume directly correspond to the length of organic linkers. For instance, when IRMOF-74 series (Mg-MOF-74 isoreticular structures) expanded the original phenylene unit of 2,5-dihydroxy-1,4-benzenedicarboxylic acid (H_4-p-dobdc) linker to 2, 3, 4, 5, 6, 7, 9, and 11 phenylene units, leading to tunable pore apertures from 14 to 98 Å; with 98 Å being the largest pore aperture reported on crystalline materials.[15] In materials with one linker degree of tunability has generally been restricted by the physical length of the modified portion of organic linker, which are generally > 4 Å for phenyl group addition, or 1-2 Å addition for a 2-atom extension. Such limit could be overcome through homogeneous incorporation of different linkers of varied ratios in MOF.[57-58] In 2020, Yuan et al. employed 7 dicarboxylate linkers of lengths between 4.9 Å (coded LA) and 15.7 Å (LG) to construct 15 isostructural face-centered cubic Zr-MOFs, 8

of which are mixed linkers-based Zr- with lattice metrics in-between parent MOFs.[59]

Pore-functionalization is another essential feature that enriches MOFs with chemical properties, allowing for precise tailoring of functional MOFs in ways that has so far, been unparalleled in other porous materials. Introductions of one or more functional moieties ranges from simple to elaborate design of linker's backbone. In the simplest case, linkers with pre-attached functional moieties are employed in direct MOF synthesis. For instance, Deng et al. have reported as many as 8 different substituents were homogenously combined into one MOF-5 structure.[60] Ionic and covalent functionalization further diversify the type of functional species that could incorporated into scaffold MOF materials. For instance, highly acidic sulfo-based MOFs could form acid-base adduct with alkylamine,[61] amino-functionalized MOFs could form amide linkage with acetic anhydride[62] or thiourea linkage with isocyanate/thiocyanate,[63] aldehyde-containing MOFs could undergo C—C and C—N coupling or C=O reduction reaction[64] and azide containing MOF could proceed through "click" chemistry with alkyne groups.[65] More remarkably, certain MOFs have the robustness to undergo tandem organic reactions. For instance, 7 tandem reactions were carried out upon MTV-IRMOF-74III to achieve enzyme-like pore complexity.[66] Covalent cleavage is another method to control heterogeneity in MOFs. After construction of ZIF-8, solvent-assisted ligand exchange (SALE) technique was carried out to introduce new groups with labile functionalities, followed by bond cleavage to expose functional group to pore surface.[67] Coordination functionalization is another attractive strategy to boost host-guest interaction. Polyalkylamines and alcohol amines are post-synthetically grafted to OMS of MOFs while leaving the remaining flexible "arms"

available to attract guest molecules.[68-69] Through different pore functionalization methods, polarity, hydrophobicity, chirality, etc., characteristics of functionalized linkers could effectively advance MOFs materials in different applications.

1.2.3 Modulating Framework Charge

Ionic MOFs are of great interest owing to unique functionalities of the extra-framework ions. In addition to maintaining overall charge neutrality, the intrinsic shape, size, and functionalities of these ions could effectively enhance performances of materials in an array of applications such as gas separation, ionic conduction, and ion-exchange. Extra-framework ions could also introduce new characteristics that are unknown to parent MOFs (e.g., introducing chiral ion into an achiral host).[70] Over the years, strategic control of synthetic environment, presence of mineralizing/structure-directing agents, ratios of precursors have proven successful in constructing ionic frameworks. Post-synthetic "anion-stripping" or "cation-grafting" techniques could be applied to chemically inert, neutral frameworks, transforming them into respective cationic and anionic frameworks.[71-72] However, deliberate construction of ionic MOFs is most often done through mismatching charge ratio between metal cluster and organic unit. For instance, substitution of the classic zinc tetramer, $[Zn_4(O)(COO)_6]$, with a highly positive rare-earth (RE) tetramer, $[RE_4(\mu_4\text{-}OH)_4(COOH)_6]^{2+}$, transforms the neutral MOF-5 framework into a cationic isostructure.[73] Similarly, substitution of dicarboxylate with a more negatively charged tetracarboxylate linker modified the charge-neutral UiO-66 framework into a anionic isostructure.[74]

1.3 Metal-organic Frameworks in Energy-related Applications

1.3.1 Metal-organic Frameworks in Gas Capture and Storage

Carbon dioxide (CO_2) capture is an important application of MOF research. With CO_2 being the most important contributor to global warming, effective carbon dioxide capturing technologies are in high demand. Porous materials present a promising solution for selective CO_2 capture as they require much less regeneration energy than the widely adopted absorption through aqueous amine solutions.

SIFSIX-series presents a noteworthy example of tuning adsorption properties through pore size approach. In 2013, Nugent et al. reported three pillared-layer structures SIFSIX-2-Cu, interpenetrated SIFSIX-2-Cu-i and SIFSIX-3-Zn with pore size varying from nanoporous to ultra-microporous.[75] The employment of long dpa linkers resulted in $[Cu(dpa)_2(SiF_6)]$ (dpa = 4,4'-dipyridylacetylene, SIFSIX-2-Cu) with pore diagonal of 13.05 Å. When synthetic conditions are tuned to obtain a doubly interpenetrated polymorph, SIFSIX-2-Cu-i exhibits pore diagonal of 5.15 Å. In substituting dpa with a shorter pyz linker, an isostructure $[Zn(pyz)_2(SiF_6)]$ (SIFSIX-3-Zn) with pore diagonal of 3.84 Å is obtained. While interpenetrated SIFSIX-2-Cu-i exhibits the highest CO_2 uptake at 5.41 mmol/g, SIFSIX-3-Zn provides much stronger host-guest interactions, as observed with high CO_2 uptake at 0.1 bar and high Q_{st} of 45 kJ/mol.

Uncoordinated metal site with partial positive charge attracts CO_2 through strong electrostatic interactions. MOF-74 series presents an excellent case study for CO_2 adsorption and separation.[76-78] Neutron diffractions upon different metal types revealed efficient binding of CO_2 to OMS through an end-on manner, among which Mg-MOF-74

presents benchmark CO_2 capacity of 35.2 w.t.% (298 K, 1 bar) with high Q_{st} of 47 kJ/mol.[79] The much stronger affinity of CO_2 towards Mg-MOF-74 compared to other transition metals, originates from the stronger ionic character of Mg—O bond, resulting in increase of charge-quadrupole interaction between Mg and CO_2. Subsequent breakthrough studies reveal Mg-MOF-74 is excellent at capturing CO_2 from flue gas only under dry conditions. After exposing M-MOF-74 (M = Mg, Zn, Ni, Co) to 70% relative humidity, the percent of initial CO_2 capacity retained from CO_2/N_2 separation follows Mg (16%) < Zn (22%) < Ni (61%) < Co (85%).[80] Thus Co-MOF-74 presents the most ideal material in this series for flue gas separation.

MOFs bearing inorganic and organic Lewis basic sites have also shown to enhance CO_2 uptake alkyl amines and alkyl alcohols have also been grafted onto OMS of MOFs.[68, 81-82] In 2011, Mcdonald et al. implemented the first alkylamine grafting on a sodalite-type triazolate-bridged framework CuBTTri (H_3BTTri = 1,3,5-tris(1H-1,2,3-triazol-5-yl)benzene) for CO_2 sorption.[83] With ethylenediamine (en) grafted onto the exposed Cu site, en@CuBTTri exhibits much stronger CO_2 loading at low pressure region, resulting in high Q_{st}^0 (-78 kJ/mol) but moderate regeneration temperature (60 °C). Subsequently, variants of MOF-74-type structures such as Mg_2(p-dobdc), Mg_2(dondc), and Mg_2(dobpdc) were appended with di- and tetra- alkyl amines/alcohols at varied lengths, and substituents.[68-69, 84-89] In these materials, CO_2 is inserted between Mg—N bond, forming carbamate species that is charged-balanced by neighboring ammonium group. Branched and linear alkylamine molecules have also been attached to framework through acid-base

ion-pairing. In Cr-MIL-101-SO_3H, the acidic sulfonyl group forms ionic interaction with one basic amine group, leaving remaining group(s) available for CO_2 capture.[61]

The safe handling and storage of different gas commodities (e.g., H_2, CH_4, C_2H_2) is of great importance. Our group is particularly interested in finding suitable adsorbent to capture acetylene (C_2H_2). Acetylene is highly explosive in nature, which forces it to be compressed below 0.2 MPa, or stored in presence of stabilizers. As a result, storage of C_2H_2 suffers from high cost and compromised purity. Owing to their large pore with functional features, MOFs have shown great potential in gas storage.

MOFs present a great platform to search for ideal C_2H_2 adsorbents (Table 1.1). Several strategic designs have resulted in high C_2H_2 storage adsorbents. The employment of open-metal sites could boost acetylene storage through metal-π interactions. Among different MOFs, MOF-74 has by far the highest OMS density, with 7.5 mmol M^{2+} per cm^3. In 2010, Chen et al. studied acetylene storage with M-MOF-74 (M = Mg^{2+}, Mn^{2+}, Co^{2+}, Zn^{2+}).[90] It was shown that Co-MOF-74, with highest polarizing ability, exhibits highest volumetric uptake of 230 cm^3/cm^3 (197 cm^3g^{-1}) at 1 bar, 298 K.

In addition to high-density OMS, the nanopore space/size also makes important contribution towards deciding suitable adsorbents. Compared to Co-MOF-74, the copper paddlewheel in HKUST-1 constitutes 4.4 mmol Cu^{2+} per cm^3. Thus, a more significant contribution towards the volumetric uptake comes from the spatial arrangement of the **tbo** net of HKUST-1.[91]

Table 1.1 Select examples of MOFs with high C_2H_2 storage at 1 bar.

Adsorbents	SA BET m^2/g)	C_2H_2 uptake at 298K		C_2H_2 uptake at 273K		Qst (kJ/mol)	Ref
		cm^3/g	cm^3/cm^3	cm^3/g	cm^3/cm^3		
ZJU-12	2316	239	191	299	239	29	[92]
dps-VCo-BDC	1883	234	204	330	288	25.7	[93]
MFM-188	2568	232	193	297	247	32.5	[94]
FJI-H8	2025	224	196	277	242	32	[95]
NJU-BAI-17	2423	222	176	296	233	38	[96]
ZJNU-54	2134	211	161	259	197	35.4	[97]
HKUST-1	1502	201	177	249	219	30.4	[91]
Co-MOF-74	1056	197	230	227	264	50.1	[90]
CPM-232	1089	195	178	273	249	24.2	[98]
CPM-233	1320	194	165	267	227	23.2	[98]
MgMOF-74	1495	184	167	209	190	34	[90]
CPM-231	1140	178	163	255	233	24	[98]
Cu-TDPAT	1938	178	139	248	194	42.5	[99]
CoV-bdt-tph	1945	184	--	259	--	23.1	[100]
CPM-733-tpt	1328	176	157	251	223	22.9	[101]
ZJU-5	2823	193	--	290	--	25.4	[102]
ZJU-40/ZJNU-47a	2858	216	--	286	--	27.5	[103]

1.3.2 Metal-organic Frameworks in Separations

Many important chemical feedstocks such as acetylene (C_2H_2), ethylene (C_2H_4), and propylene (C_3H_6) are generally produced through cracking of larger hydrocarbons, which result in mixtures of products. Some mixtures (e.g., C_2H_2/CO_2, C_2H_4/C_2H_6, C_3H_6/C_3H_8) have components with highly similar in physical properties, posing significant purification challenges (Table 1.2). To this date, the most effective method for these separations remains cryogenic distillation, which operates at low temperature and high pressure. Hence it is highly desirable to develop a low-cost and energy-efficient separation method. MOF adsorbents have shown promises in selectively removing unwanted impurities from gas mixtures.

Table 1.2 Properties of select gases.

	Molecular Size ($Å^3$)	**Boiling Point (K)**	**Kinetic Diameter (Å)**	**Polarizability ($x\ 10^{25}\ cm^3$)**	**Quadruple Moment ($x10^{26}$ esu cm^2)**	**Dipole Moment (esu cm)**
CO_2	3.18 x 3.33 x 5.36	194.7	3.3	29.11	4.30	0
C_2H_2	3.32 x 3.34 x 5.70	189.3	3.3	33.3-39.3	3.0	0
C_2H_4	3.28 x 4.18 x 4.84	169.4	4.16	42.52	5.00	0
C_2H_6	3.81 x 4.08 x 4.82	184.5	4.44	44.7	2.17	0
C_3H_6	4.16 x 4.65 x 6.44	225.4	4.68	62.6	0	1.22
C_3H_8	4.02 x 4.52 x 6.61	231.1	5.1	62.9	0	0.28

Table 1.3 Selected examples of MOFs for hydrocarbon separation.

Separation	MOF	Adsorbed Amount* (mmol/g)		Temp (K)	IAST Selectivity+	Ref
Olefin-Paraffin Separation						
C_2H_4/C_2H_6	Fe-MOF-74	6.24	5.19	318	13.6	[104]
	Fe_2(m-dobdc)	6.9	5.9	298	25	[105]
	Ag^I@MIL-101(Cr)-SO_3	4.32	2.9	298	32	[106]
	NOTT-300	4.28	0.85	293	48.7	[107]
	Co-gallate	3.37	0.3	298	52	[108]
	UTSA-280	2.5	0.098	298	52	[109]
	Cu^I@UiO-66$(COOH)_2$	1.86	0.9	298	81	[110]
C_3H_6/C_3H_8	Fe_2(m-dobdc)	7.4	6.08	298	38	[105]
	Co-MOF-74	7.29	5.24	298	46	[111]
	HIAM-301	3.16	<.3	298	>150	[112]
	JNU-3a	2.6	2.1	298	513	[12]
	KAUST-7	1.4	0.04	298	mol. sieve.	[48]
	MAF-23ox	1.3	0.9	298	15	[113]
Paraffin-Olefin Separation						
C_2H_6/C_2H_4	CPM-733	7.13	6.38	298	1.75	[101]
	PCN-250	5.21	4.22	298	1.9	[114]
	$Fe_2(O_2)$(dobdc)	3.32	2.54	298	4.4	[115]
	NIIC-20-Bu	2.5	1.4	298	15.4	[116]
	$Cu(Qc)_2$	1.85	0.78	298	3.4	[117]
	ZIF-7	1.83	1.80	298	1.5	[118]
	MAF-49	1.7	1.6	316	2.7	[119]
C_3H_8/C_3H_6	CPM-734c	8.73	9.31	298	1.44	[120]
	WOFOUR-1-Ni	0.71	0.88	298	1.6	[56]
	ZIF-8	3.30	4.1	298	1.3	[121]
	BUT-10	6.25	6.45	298	1.40	[122]
	Num-7a	2.98	3.09	298	1.77	[123]
	$Ni(ADC)(TED)_{0.5}$	2.32	2.11	298	6.4	[124]

*values obtained at 1 bar

Table 1.4 Select examples of MOFs with high C_2H_2/CO_2 separation performance at 298K.

MOFs	S_A BET (m^2/g)	C_2H_2 Uptake mmol/g 1 bar	CO_2 Uptake mmol/g 1 bar	IAST (1 bar)	C_2H_2/CO_2 Breakthrough Time (min/g)*	Ref
FJI-H8-Me	2044	10.2	4.73	5.3	87	125
MIL-160	1138	8.53	4.01	10	71	126
SIFSIX-Cu-TPA	1330	8.25	4.78	5.3	68	127
SNNU-27-Fe	1570	8.13	2.92	2.0	91	128
FJU-90	1572	8.04	4.60	4.3	22	129
SNNU-45	1007	6.0	4.35	8.5	79	130
ZJNU-13	1352	5.29	3.92	5.64	58	131
JXNU-12(F)	2154	5.16	1.50	4.1	70	132
Cu-ATC	600	5.01	4.02	53.6	127	133
UTSA-74a	830	4.78	3.17	20-9	20	134
NCU-100	358	4.57	~0	1787	53	135
FeNiM'MOF	383	4.29	2.72	24	16	136
CAU-10-H	627	4.00	2.68	4.0	45	137
ZJU-196a	N/A	3.73	0.38	--	7.5	138
ZJUT-2a	350	3.39	2.24	8	15	139
UTSA-300a	311	3.08	0.15	743	12	140
MOF-OH	120	3.04	1.20	25	28	141
JNU-1	818	2.81	2.28	6.6	26	142
JXNU-5	406	2.50	1.55	4.9	56	143
Cu(I)@UiO-66	302	2.30	0.7	185	46	144
NTU-66-Cu	1700	4.98	2.0	33	28	145

*breakthrough experiment at 2 mL/min flow rate.

The employment of OMS to coordinate with π-electron cloud of C_2H_2 presents a promising C_2H_2/CO_2 separation mechanism. In 2016, the 3D framework of UTSA-74 with 1D hexagonal channels containing unsaturated Zn^{2+}dimers adsorbs 4.8 mmol/g C_2H_2 and 3.1 mmol/g at 298 K, 1 bar.[134] Density functional theory (DFT) calculation reveals each Zn^{2+} OMS directly binds to C≡C of C_2H_2. In comparison, two Zn^{2+} sites are needed to

interact with CO_2, thus leading to lower CO_2 uptake and high C_2H_2/CO_2 50/50 Ideal Adsorbed Solution Theory (IAST) selectivity of 9.

Additional metal binding sites could also be introduced to framework in the form of counter-balancing ion. Immobilized Ag(I) in sulfonated (Cr)-MIL-101 resulted in additional π-complexation sites to enhance ethylene interactions, as evidenced in dramatic boost of Q_{st}^0 from 35 kJ/mmol to 120 kJ/mol and much improved C_2H_4/C_2H_6 IAST selectivity from 1.15 to 16.[106] Recently Zhang et al. reported Cu(I)@UiO-66-$(COOH)_2$ with optimal pore window and abundant π-complexation sites for effective C_2H_4 separation.[110] Compared to parent UiO-66-$(COOH)_2$ with pore aperture of 4.8 Å, chelation of Cu(I) onto UiO-66-$(COOH)_2$ effectively reduced pore size to 4.1 Å, which falls in the range of kinetic diameters of C_2H_4 (4.1 Å) and C_2H_6 (4.6 Å). This effectively reduced C_2H_6 uptake by 50% at ambient condition. The simultaneously enhanced C_2H_4 uptake through strong π-complexation and reduced C_2H_6 uptake through pore-contraction effectively resulted in exceptionally high C_2H_4/C_2H_6 IAST selectivity of 80 at 1 bar.

The introduction of Lewis basic sites such as N, O, and F into MOFs is another direction to enhance C_2H_2/CO_2 selectivity. UTSA-300 ([$Zn(dps)_2(SiF_6)$]) presents an excellent example of utilizing functional groups to selectively bind C_2H_2 (H-bonding interaction) over CO_2 (electrostatic repulsion).[140] The microporous material belongs to the SIFSIX-MOF family, where the **sql** layers of Zn-dps are pillared by SiF_6^{2-} group to form 3D framework channels of 3.3 Å. UTSA-300a adsorbs 3.41 mmol/g C_2H_2 at 298 K, 1 bar, but negligible CO_2. High-resolution neutron powder diffraction studies and molecular modeling reveals that fluoride atom exhibits F···H interaction with C_2H_2, allowing these

molecules to enter framework through "head-on" orientation. In comparison, F···C electrostatic interaction and F···O repulsion forces CO_2 to orient "side-on" which prevented their entrance.

Kinetic separation presents a promising mechanism that separates C3 molecules according to their rate of diffusion. [146-148] The first reported kinetic studies on C_3H_6/C_3H_8 separation two were performed with sodalite structures $Zn(2\text{-mim})_2$ (ZIF-8) and $Zn(2\text{-cim})_2$, (2-mim = 2-methylimdazole, 2-cim = 2-chloroimidazole).[149] In substituting the chloro- group with methyl- group, the critical pore-opening aperture is effectively reduced from 3.37 Å to 3.26 Å, and kinetic selectivity is enhanced by a factor of two. Recently, Wang et al. reported a post-synthetic modification of MAF-23 to enhance kinetic separation of C_3 olefin-paraffin pair.[113] The original MAF-23, constructed from Zn^{2+} and btm^{2-} (H_2btm = bis (5-methyl-1*H*-1,2,4-triazol-3-yl)methane)) shows no noticeable discrimination towards propylene and propane. The oxidation of 50% btm^{2-} in framework to btk^{2-} (H_2btk = bis(5-methyl-1,2,4-triazol-3-yl)methanone) resulted in 100-fold C_3H_6/C_3H_8 selectivity enhancement.

Molecular sieving is often viewed as the extreme case of kinetic separation, and several notable works have been reported. In 2016, Cadiau et al. reported a fluorinated pillared-layer KAUST-7 (NbOFFIVE-Ni) as the first adsorbent to separate C_3H_6 from the slightly larger C_3H_8 with the molecular sieving mechanism.[48] Compared to traditional SiF_6^{2-} pillar, employment of $NbOF_5^{2-}$ pillar resulted in tilting of pyrazine molecules through F---H interaction (2.483 Å) and contracting pore aperture to 3.0471 Å (4.965 Å in SIFSIX-3-Ni). KAUST-7 adsorbs 1.4 mmol/g C_3H_6 at 298 K, 1 bar while completely excluding

C_3H_8 molecules. Compared to adsorbents with molecular sieving window laid in tandem along the channel, adsorbents with orthogonally aligned sieving window would allow for faster diffusion of gas molecules, and thus higher energy efficiency. JNU-3a is 3D framework with gourd-shaped pockets (3.7 Å) embedded orthogonally within the 1D channel.[12] Compared to KAUST-7 with tandem pore aperture, C_3H_6 rate constant in JNU-3a is four times greater. Furthermore, clean desorption of C_3H_8 and C_3H_6 during breakthrough experiment allows for collection of 33.2 L/kg C_3H_6 during a single adsorption-desorption cycle.

In olefin-paraffin separation, olefin-selective adsorbents generally require additional adsorption/desorption cycles to attain polymer grade ethylene. In comparison, selective adsorption of the unwanted ethane byproduct would allow for direct purification of C_2H_4 in the separation cycle, allowing for further reduction of energy consumption. An early study of ethane-selective adsorbent was ZIF-7, a zinc imidazolate framework of **sod** topology.[118] The benzene ring of the benzimidazole ligand acts as window guard and allows the symmetry matching ethane molecule to preferentially enter at a lower pressure region than ethylene molecule.

In 2018, Li et al. reported the introduction of peroxo sites into MOFs as new strategy to achieve effective paraffin/olefin separation.[115] By oxidizing Fe-MOF-74 developed by same group in 2012, the resulting $Fe_2(O_2)$dobdc shows preferential C_2H_6 uptake at 3.3 mmol/g over C_2H_4 uptake at 2.6 mmol/g and reversed C_2H_6/C_2H_4 selectivity of 4.4 at 298 K, 1 bar. Neutron powder diffraction experiments of C_2D_6-loaded and C_2D_4-loaded $Fe_2(O_2)$dobdc, reveal much shorter C—D---O interactions between C_2D_6 and Fe-

peroxo sites than C_2D_4 counterpart, likely to better matching between nonplanar ethane molecule uneven pore surface of framework.

1.3.3 Metal-organic Frameworks in Ionic Conduction

Effectiveness of solid-state ionic conductors is critical to the advancement of electrochemical devices.[19] Requisites for a good electrolyte include high conductivity, high thermal and chemical stability during cell operating conditions. The MOF platform has several advantages to aid the synthesis and optimization of new ion-conducting materials. It has well-defined channels that are highly tunable, allowing us to better understand ion-transport pathway and mechanism, facilitating better material optimization designs. Various ions (e.g., H^+, OH^-, Li^+, Na^+, Mg^{2+}) have been transported in the MOF platform. Different conductivity environments, ranging from anhydrous to 100% relative humidity, ambient to 250 °C, have been mimicked in investigating conductive MOFs.

A number of strategies have been proposed to achieve excellent conductivity values. For instance, the introduction of -COOH, $-SO_3H$, $-PO_3H_2$ acidic group could facilitate faster dissociation of certain ions. For instance, the substitution of the aromatic -H with $-NH_2$, -OH, $-(COOH)_2$ to MIL-53(Al) resulted in a conductivity trend following acidity of substituents $-NH_2$ (2.3 E-9 S cm^-) < -H (2.3 E-8 S cm^-) < -OH (4.2 E-7 S cm^-) < COOH (2.0 E-6 S cm^-) at 298 K, 95 % relative humidity (RH).[150] Enhancement of conductivity could be facilitated through tuning of counter ions of ionic MOF materials. For a 2D honeycomb-type $[FeCr(ox)_3]^-$ framework, substitution of different quaternary ammonium cations with different hydrophilicity resulted in a wide range of conductivity

values.[151] A direct comparison between sample with inorganic counterion and organic ammonium ion showed the importance of ammonium in generating hydrogen bonding network to facilitate faster ion-transport. Bulkiness of ammonium group also affect water sorption capacity, which in turns changes conductivity of the framework. Introduction of proton carriers (e.g., H_2SO_4, imidazole, carboxylic acids) into MOFs is an effective way to shorten ion-hopping distance and subsequently, boost conductivity of selected material. For instance, in β-PCMOF2 (a MOF with 1D channel lined with sulfonate group), conductivity dropped from 5.0 E-6 S cm$^-$ at room temp, to < 1 E-8 S cm$^-$ at 70 °C, due to dehydration.[152] By reintroducing a new proton carrier, 1H-1,2,4-triazole, into the pores of β-PCMOF-2, conductivity could reach up to 5 E-4 S cm$^-$ at 150 °C, anhydrous H_2.

1.3.4 Metal-organic Frameworks in Magnetic Studies

Permanent magnets have been integrated to many modern technologies such as power generators, spintronics in magnetic random access memory, magnet induced separations.[153] The highly tunable inorganic and organic components of MOF allows for rational design of new materials with unique magnetic behaviors. Coupling of functional properties such as long-range magnetic ordering and electrical conductivity, or magnetic coupling and porosity.

Several strategic designs have resulted in MOFs with fascinating magnetic properties. One method to construction of magnetic MOFs is through the employment of rod-shaped secondary building units for strong magnetic coupling. For instance, MIL-47(as) with hydroxo-bridged VO_6 octahedra exhibits antiferromagnetic ordering with T_N =

95 K (highest reported to-date from MOFs with diamagnetic linkers).[23] Employing short organic linkers such as oxalic acid could promote both σ- and π-electronic pathways for magnetic superexchange through two connected O–C–O bridge. To this end, the 2D 6-connected metal-oxalate honeycomb family has been extensively investigated. It was found that different metal/heterometal choices, templating agent, counter ions all contribute to different degrees of magnetic enhancement. For instance, the anionic $[(Mn^{3+})(Cr^{3+})ox_3]$ structures show ferromagnetic order with T_c at 5.6-5.9 K.[154] More interestingly, these frameworks also exhibit high proton conduction when counter cation exhibits carboxylic acid group (e.g., $Et_3(CH_2COOH)N^+$), which provides rare examples of compounds that exhibit both ferromagnetism and proton conduction. Employment of radical organic linkers in magnetic MOF construction is another promising direction. These organic linkers will promote stronger interaction through exchange coupling between metal and radical spin. For instance, reaction between tetracyanoethylene (TCEE) with $(Mn^{3+})I_2(THF)_3$ salt resulted in 3D $Mn^{II}(TCNE^{-\bullet})_{1.5}(I_3)_{0.5}\cdot 0.5THF$.[155] The antiferromagnetic coupling between Mn^{3+} center and $TCNE^{-\bullet}$ radical was revealed to exist up to T_c = 171 K, which is the current record for all MOF magnets.

1.4 Establishment of the Partitioned-*acs* Platform

While many applications of porous materials such as immobilization of homogeneous catalysts (especially biomolecules) benefit from high surface area, large pore size, and high pore volume, there are also applications for which small-pore materials could be advantageous. One of such application is the efficient capture and separation of small

gas molecules such as carbon dioxide, methane, and C2- or C3-hydrocarbon gas molecules under ambient conditions. Toward this goal, our group proposed a concept called the pore space partition (PSP), and have subsequently achieved a great experimental success in turning this concept into a large family of porous materials with impressive properties for a range of gas storage and separation applications.[156]

By dividing large pore space into smaller segments and pockets, pore space partition increases the number of host-guest binding sites dramatically (often more than doubling). Even though pore space partition has been shown on other platforms (e.g., CPM-5, MOF-14),[157-158] the *pacs* platform has been shown to be the most versatile so far. The *pacs* platform is a very recent addition to the major MOF platforms and as such it has created many new opportunities in the materials design and property engineering. Among different MOF families that undergo isoreticular design synthesis, the partitioned-acs (*pacs*) platform is exceptionally tunable.[159] The *pacs* prototype has a formula unit of $[M_3(\mu_3\text{-O/OH})(L1)_3(L2)](G1)_x$ ($x \geq 0$) where metal trimers are linked by ditopic L1 ligand to create a 3D *acs*-type framework with 1D hexagonal channels. The pore partitioning L2 ligand coordinates to coplanar trimer sites, segmenting these channels into smaller pockets (Figure 1.4). While many members of the *pacs* family have a neutral framework, it is also common to have a charge mismatch between organic and inorganic units, leading to either cationic or anionic frameworks and counter ions (G1). The most prominent feature of *pacs* system is the capability to substitute every module individually or in combination to yield desired pore metrics and guest recognitions.

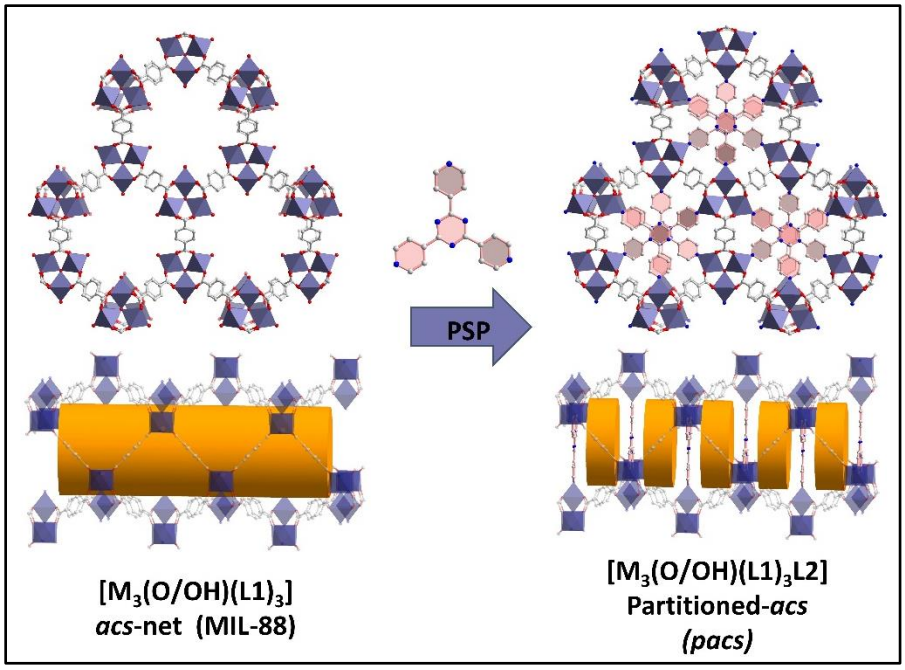

Figure 1.4. Illustration of partitioned-acs frameworks (*pacs*).

The unique opportunities offered by the *pacs* platform can be appreciated by comparison with other major MOF platforms. Most well-known MOF platforms such as HKUST-1 (**tbo**),[2] MOF-5 (**pcu**),[8] UiO-66 (**fcu**),[6] MOF-74 (**msf**)[11] have only two modules (one inorganic node and one organic node) and are intrinsically less tunable compared to the multi-module *pacs* platform. Furthermore, metal trimers of the *pacs* platform can accommodate far more metal ion types compared to paddlewheel dimer in HKUST-1,[160] $[Zn_4O]$-type tetramer in MOF-5,[161] and Zr_6-hexamer in UiO-66.[162] MOF-74 is also limited in both metal type and ligand type compared to the *pacs* platform. Similar to the *pacs* platform, PCN-250/CPM-200 (the soc platform) are based on metal trimers.[40, 163] However, the soc platform is very limited in the ligand choice (a planar tetracarboxylate) and its 6-connected framework is also less stable compared to the *pacs* platform. As an intrinsically multi-modular system, pillared-layer MOFs are compositionally diverse in terms of the

ligand choice (e.g., dicarboxylate, SiF_6^{2-}, and bipyridyl ligands).[164] Pillared-layer is a general concept and is not limited to one particular structure type. While the design concept based on the pillaring of layers is highly versatile, the disadvantages of pillared-layer structures include low framework stability from low connectedness of metal nodes (e.g., 6-connected monomeric metal or dimeric paddlewheel cluster) and ligands (often 2-connected). In addition, pillared-layer structures have the propensity to form interpenetrated structures that can greatly reduce the porosity.[165]

1.5 Scope of this work

The unique characteristics of MOFs have sparked interests from scientists and engineers of diverse backgrounds, ushering in rapid development of MOF materials into a large multi-interdisciplinary field. MOF research in our group is rooted in the fundamental synthetic and structural science whose advance has the potential to reshape other aspects of MOF studies and applications. We are as interested in examining different structure-property relationships to formulate superior framework regulation methodologies as we are with screening different synthetic parameters to target brand new material design. The scope of this dissertation thus embodies both reticular design for material optimization (Chapters 2-5) as well as deliberate synthetic exploration for new material discovery (Chapters 6-7).

In Chapter 2, we set new boundary conditions and limits to our pioneered *pacs* platform. We then utilize these knowledges to successfully identify record setting

isoreticular frameworks in important industrial gas sorption and separations, namely C_3H_6/C_2H_4, and C_3H_6/C_3H_8.

In Chapter 3, we establish a new design strategy on the *pacs* platform to construct versatile anionic MOFs with great robustness and tunability. Compared to the traditionally unstable and less variant anionic *pacs*, our new design results in construction of anionic *pacs* materials with highly controllable counter cations, hydrolytic stability over a wide pH range, and C_2H_2 storage capacity higher than current benchmark ionic material. Additionally, we examined the influence of counter cations upon the selective adsorption of C_3H_8/C_3H_6 and C_6H_6/C_6H_{12} separations.

In chapter 4, we apply the boundary conditions and limits of chapter 2 toward the exploration of effective cationic *pacs* materials for the C_2H_2/CO_2 separation. Specifically, we examine the effects of volume and counter ions in breaking the capacity-selectivity tradeoff in these molecules, through isotherm measurements, theoretical calculations and breakthrough validation.

In chapter 5, we integrate bulky sulfonic acid functional group into our *pacs* platform for the first time and explore their potential applications.

In chapter 6, we design a two-step synthesis strategy to study the influence of different inorganic ions, in constructing novel ionic materials with different conductive pathways. We then investigate potentials of these materials as ionic conductors.

In chapter 7, we target construction of lower dimensional magnetic materials with 1D inorganic chains through *in situ* synthesis of capping agent.

1.6 Reference

1. Li, H.; Laine, A.; O'Keeffe, M.; Yaghi, O. M., *Science* **1999,** *283*, 1145.

2. Chui Stephen, S. Y.; Lo Samuel, M. F.; Charmant Jonathan, P. H.; Orpen, A. G.; Williams Ian, D., A Chemically Functionalizable Nanoporous Material [Cu3(Tma)2(H2o)3]N. *Science* **1999,** *283*, 1148-1150.

3. Subramanian, S.; Zaworotko, M. J., Porous Solids by Design: [Zn(4,4′-Bpy)2(Sif6)]N·Xdmf, a Single Framework Octahedral Coordination Polymer with Large Square Channels. *Angewandte Chemie International Edition in English* **1995,** *34*, 2127-2129.

4. Freund, R.; Canossa, S.; Cohen, S. M.; Yan, W.; Deng, H.; Guillerm, V.; Eddaoudi, M.; Madden, D. G.; Fairen-Jimenez, D.; Lyu, H.; Macreadie, L. K.; Ji, Z.; Zhang, Y.; Wang, B.; Haase, F.; Wöll, C.; Zaremba, O.; Andreo, J.; Wuttke, S.; Diercks, C. S., 25 Years of Reticular Chemistry. *Angew. Chem. Int. Ed.* **2021,** *60*, 23946-23974.

5. Furukawa, H.; Cordova, K. E.; O'Keeffe, M.; Yaghi, O. M., The Chemistry and Applications of Metal-Organic Frameworks. *Science* **2013,** *341*, 1230444.

6. Cavka, J. H.; Jakobsen, S.; Olsbye, U.; Guillou, N.; Lamberti, C.; Bordiga, S.; Lillerud, K. P., A New Zirconium Inorganic Building Brick Forming Metal Organic Frameworks with Exceptional Stability. *J. Am. Chem. Soc.* **2008,** *130*, 13850-13851.

7. Herm Zoey, R.; Wiers Brian, M.; Mason Jarad, A.; van Baten Jasper, M.; Hudson Matthew, R.; Zajdel, P.; Brown Craig, M.; Masciocchi, N.; Krishna, R.; Long Jeffrey, R., Separation of Hexane Isomers in a Metal-Organic Framework with Triangular Channels. *Science* **2013,** *340*, 960-964.

8. Li, H.; Eddaoudi, M.; O'Keeffe, M.; Yaghi, O. M., Design and Synthesis of an Exceptionally Stable and Highly Porous Metal-Organic Framework. *Nature* **1999,** *402*, 276-279.

9. Song, B. Q.; Yang, Q. Y.; Wang, S. Q.; Vandichel, M.; Kumar, A.; Crowley, C.; Kumar, N.; Deng, C. H.; GasconPerez, V.; Lusi, M.; Wu, H.; Zhou, W.; Zaworotko, M. J., Reversible Switching between Nonporous and Porous Phases of a New Sifsix Coordination Network Induced by a Flexible Linker Ligand. *J. Am. Chem. Soc.* **2020,** *142*, 6896-6901.

10. Férey, G.; Mellot-Draznieks, C.; Serre, C.; Millange, F.; Dutour, J.; Surblé, S.; Margiolaki, I., A Chromium Terephthalate-Based Solid with Unusually Large Pore Volumes and Surface Area. *Science* **2005,** *309*, 2040-2042.

11. Rosi, N. L.; Kim, J.; Eddaoudi, M.; Chen, B.; O'Keeffe, M.; Yaghi, O. M., Rod Packings and Metal−Organic Frameworks Constructed from Rod-Shaped Secondary Building Units. *J. Am. Chem. Soc.* **2005,** *127*, 1504-1518.

12. Zeng, H.; Xie, M.; Wang, T.; Wei, R. J.; Xie, X. J.; Zhao, Y.; Lu, W.; Li, D., Orthogonal-Array Dynamic Molecular Sieving of Propylene/Propane Mixtures. *Nature* **2021,** *595*, 542-548.

13. Ye, C.-R.; Wang, W.-J.; Chen, W.; Xiao, Y.; Zhang, H.-F.; Dai, B.-L.; Chen, S.-H.; Wu, X.-D.; Li, M.; Huang, X.-C., Harnessing Shape Complementarity for Upgraded Cyclohexane Purification through Adaptive Bottlenecked Pores in an Imidazole-Containing Mof. *Angew. Chem. Int. Ed.* **2021,** *60*, 23590-23595.

14. Duan, J.; Zhang, Q.; Wang, S.; Zhou, B.; Sun, J.; Jin, W., Controlled Flexibility of Porous Coordination Polymers by Shifting the Position of the –Ch3 Group around Coordination Sites and Their Highly Efficient Gas Separation. *Inorganic Chemistry Frontiers* **2018,** *5*, 1780-1786.

15. Deng, H.; Grunder, S.; Cordova Kyle, E.; Valente, C.; Furukawa, H.; Hmadeh, M.; Gándara, F.; Whalley Adam, C.; Liu, Z.; Asahina, S.; Kazumori, H.; O'Keeffe, M.; Terasaki, O.; Stoddart, J. F.; Yaghi Omar, M., Large-Pore Apertures in a Series of Metal-Organic Frameworks. *Science* **2012,** *336*, 1018-1023.

16. Honicke, I. M.; Senkovska, I.; Bon, V.; Baburin, I. A.; Bonisch, N.; Raschke, S.; Evans, J. D.; Kaskel, S., Balancing Mechanical Stability and Ultrahigh Porosity in Crystalline Framework Materials. *Angew. Chem. Int. Ed. Engl.* **2018,** *57*, 13780-13783.

17. Behera, N.; Duan, J.; Jin, W.; Kitagawa, S., The Chemistry and Applications of Flexible Porous Coordination Polymers. *EnergyChem* **2021,** *3*, 100067.

18. Zhao, X.; Wang, Y.; Li, D.-S.; Bu, X.; Feng, P., Metal–Organic Frameworks for Separation. *Adv. Mater.* **2018,** *30*, 1705189.

19. Lim, D.-W.; Sadakiyo, M.; Kitagawa, H., Proton Transfer in Hydrogen-Bonded Degenerate Systems of Water and Ammonia in Metal–Organic Frameworks. *Chem. Sci.* **2019,** *10*, 16-33.

20. Li, S.; Wang, L.; Su, H.; Hong, A. N.; Wang, Y.; Yang, H.; Ge, L.; Song, W.; Liu, J.; Ma, T.; Bu, X.; Feng, P., Electron Redistributed S-Doped Nickel Iron

Phosphides Derived from One-Step Phosphatization of Mofs for Significantly Boosting Electrochemical Water Splitting. *Adv. Funct. Mater.* **2022,** *n/a*, 2200733.

21. Kalaj, M.; Cohen, S. M., Postsynthetic Modification: An Enabling Technology for the Advancement of Metal-Organic Frameworks. *ACS Cent Sci* **2020,** *6*, 1046-1057.

22. Jiang, H.; Alezi, D.; Eddaoudi, M., A Reticular Chemistry Guide for the Design of Periodic Solids. *Nature Reviews Materials* **2021,** *6*, 466-487.

23. Barthelet, K.; Marrot, J.; Riou, D.; Férey, G., A Breathing Hybrid Organic–Inorganic Solid with Very Large Pores and High Magnetic Characteristics. *Angew. Chem. Int. Ed.* **2002,** *41*, 281-284.

24. Anokhina, E. V.; Vougo-Zanda, M.; Wang, X.; Jacobson, A. J., In(Oh)Bdc·0.75bdch2 (Bdc = Benzenedicarboxylate), a Hybrid Inorganic−Organic Vernier Structure. *J. Am. Chem. Soc.* **2005,** *127*, 15000-15001.

25. Loiseau, T.; Serre, C.; Huguenard, C.; Fink, G.; Taulelle, F.; Henry, M.; Bataille, T.; Férey, G., A Rationale for the Large Breathing of the Porous Aluminum Terephthalate (Mil-53) Upon Hydration. *Chem. Eur. J.* **2004,** *10*, 1373-1382.

26. Mowat, J. P. S.; Miller, S. R.; Slawin, A. M. Z.; Seymour, V. R.; Ashbrook, S. E.; Wright, P. A., Synthesis, Characterisation and Adsorption Properties of Microporous Scandium Carboxylates with Rigid and Flexible Frameworks. *Microporous Mesoporous Mater.* **2011,** *142*, 322-333.

27. Millange, F.; Guillou, N.; Walton, R. I.; Grenèche, J.-M.; Margiolaki, I.; Férey, G., Effect of the Nature of the Metal on the Breathing Steps in Mofs with Dynamic Frameworks. *Chem. Commun.* **2008**, 4732-4734.

28. Volkringer, C.; Loiseau, T.; Guillou, N.; Férey, G.; Elkaïm, E.; Vimont, A., Xrd and Ir Structural Investigations of a Particular Breathing Effect in the Mof-Type Gallium Terephthalate Mil-53(Ga). *Dalton Trans.* **2009**, 2241-2249.

29. Serre, C.; Millange, F.; Thouvenot, C.; Noguès, M.; Marsolier, G.; Louër, D.; Férey, G., Very Large Breathing Effect in the First Nanoporous Chromium(Iii)-Based Solids: Mil-53 or Criii(Oh)·{O2c−C6h4−Co2}·{Ho2c−C6h4−Co2h}X·H2oy. *J. Am. Chem. Soc.* **2002,** *124*, 13519-13526.

30. Bourrelly, S.; Llewellyn, P. L.; Serre, C.; Millange, F.; Loiseau, T.; Férey, G., Different Adsorption Behaviors of Methane and Carbon Dioxide in the Isotypic

Nanoporous Metal Terephthalates Mil-53 and Mil-47. *J. Am. Chem. Soc.* **2005,** *127*, 13519-13521.

31. Bourrelly, S.; Moulin, B.; Rivera, A.; Maurin, G.; Devautour-Vinot, S.; Serre, C.; Devic, T.; Horcajada, P.; Vimont, A.; Clet, G.; Daturi, M.; Lavalley, J.-C.; Loera-Serna, S.; Denoyel, R.; Llewellyn, P. L.; Férey, G., Explanation of the Adsorption of Polar Vapors in the Highly Flexible Metal Organic Framework Mil-53(Cr). *J. Am. Chem. Soc.* **2010,** *132*, 9488-9498.

32. Leclerc, H.; Devic, T.; Devautour-Vinot, S.; Bazin, P.; Audebrand, N.; Férey, G.; Daturi, M.; Vimont, A.; Clet, G., Influence of the Oxidation State of the Metal Center on the Flexibility and Adsorption Properties of a Porous Metal Organic Framework: Mil-47(V). *J. Phys. Chem. C* **2011,** *115*, 19828-19840.

33. Liu, L.; Wang, X.; Jacobson, A. J., Alf·1,4-Benzenedicarboxylate: Synthesis and Absorption Properties. *Dalton Trans.* **2010,** *39*, 1722-1725.

34. Whitfield, T. R.; Wang, X.; Liu, L.; Jacobson, A. J., Metal-Organic Frameworks Based on Iron Oxide Octahedral Chains Connected by Benzenedicarboxylate Dianions. *Solid State Sciences* **2005,** *7*, 1096-1103.

35. Shalini, S.; Dhavale, V. M.; Eldho, K. M.; Kurungot, S.; Ajithkumar, T. G.; Vaidhyanathan, R., 1000-Fold Enhancement in Proton Conductivity of a Mof Using Post-Synthetically Anchored Proton Transporters. *Sci. Rep.* **2016,** *6*, 32489.

36. Xu, G.; Zhang, X.; Guo, P.; Pan, C.; Zhang, H.; Wang, C., Mnii-Based Mil-53 Analogues: Synthesis Using Neutral Bridging M2-Ligands and Application in Liquid-Phase Adsorption and Separation of C6−C8 Aromatics. *J. Am. Chem. Soc.* **2010,** *132*, 3656-3657.

37. Hou, Q.; Zhou, S.; Wei, Y.; Caro, J.; Wang, H., Balancing the Grain Boundary Structure and the Framework Flexibility through Bimetallic Metal-Organic Framework (Mof) Membranes for Gas Separation. *J. Am. Chem. Soc.* **2020,** *142*, 9582-9586.

38. Ye, G.; Wang, H.; Zeng, X.; Wang, L.; Wang, J., Defect-Rich Bimetallic Uio-66(Hf-Zr): Solvent-Free Rapid Synthesis and Robust Ambient-Temperature Oxidative Desulfurization Performance. *Applied Catalysis B: Environmental* **2021,** *299*, 120659.

39. Wang, L. J.; Deng, H.; Furukawa, H.; Gandara, F.; Cordova, K. E.; Peri, D.; Yaghi, O. M., Synthesis and Characterization of Metal-Organic Framework-74 Containing 2, 4, 6, 8, and 10 Different Metals. *Inorg. Chem.* **2014,** *53*, 5881-3.

40. Zhai, Q.-G.; Bu, X.; Mao, C.; Zhao, X.; Feng, P., Systematic and Dramatic Tuning on Gas Sorption Performance in Heterometallic Metal–Organic Frameworks. *J. Am. Chem. Soc.* **2016,** *138*, 2524-2527.

41. Lu, Z.; Du, L.; Guo, R.; Zhang, G.; Duan, J.; Zhang, J.; Han, L.; Bai, J.; Hupp, J. T., Double-Walled Zn36@Zn104 Multicomponent Senary Metal-Organic Polyhedral Framework and Its Isoreticular Evolution. *J. Am. Chem. Soc.* **2021,** *143*, 17942-17946.

42. Zheng, S. T.; Mao, C.; Wu, T.; Lee, S.; Feng, P.; Bu, X., Generalized Synthesis of Zeolite-Type Metal-Organic Frameworks Encapsulating Immobilized Transition-Metal Clusters. *J. Am. Chem. Soc.* **2012,** *134*, 11936-9.

43. Qian, Q.-L.; Gu, X.-W.; Pei, J.; Wen, H.-M.; Wu, H.; Zhou, W.; Li, B.; Qian, G., A Novel Anion-Pillared Metal–Organic Framework for Highly Efficient Separation of Acetylene from Ethylene and Carbon Dioxide. *J. Mater. Chem. A* **2021,** *9*, 9248-9255.

44. Lin, Q.; Mao, C.; Kong, A.; Bu, X.; Zhao, X.; Feng, P., Porphyrinic Coordination Lattices with Fluoropillars. *J. Mater. Chem. A* **2017,** *5*, 21189-21195.

45. Elsaidi, S. K.; Mohamed, M. H.; Simon, C. M.; Braun, E.; Pham, T.; Forrest, K. A.; Xu, W.; Banerjee, D.; Space, B.; Zaworotko, M. J.; Thallapally, P. K., Effect of Ring Rotation Upon Gas Adsorption in Sifsix-3-M (M = Fe, Ni) Pillared Square Grid Networks. *Chem. Sci.* **2017,** *8*, 2373-2380.

46. Elsaidi, S. K.; Mohamed, M. H.; Schaef, H. T.; Kumar, A.; Lusi, M.; Pham, T.; Forrest, K. A.; Space, B.; Xu, W.; Halder, G. J.; Liu, J.; Zaworotko, M. J.; Thallapally, P. K., Hydrophobic Pillared Square Grids for Selective Removal of Co2 from Simulated Flue Gas. *Chem. Commun.* **2015,** *51*, 15530-15533.

47. Shekhah, O.; Belmabkhout, Y.; Chen, Z.; Guillerm, V.; Cairns, A.; Adil, K.; Eddaoudi, M., Made-to-Order Metal-Organic Frameworks for Trace Carbon Dioxide Removal and Air Capture. *Nat. Commun* **2014,** *5*, 4228.

48. Cadiau, A.; Adil, K.; Bhatt, P. M.; Belmabkhout, Y.; Eddaoudi, M., A Metal-Organic Framework–Based Splitter for Separating Propylene from Propane. *Science* **2016,** *353*, 137-140.

49. Nugent, P.; Rhodus, V.; Pham, T.; Tudor, B.; Forrest, K.; Wojtas, L.; Space, B.; Zaworotko, M., Enhancement of Co2 Selectivity in a Pillared Pcu Mom Platform through Pillar Substitution. *Chem. Commun.* **2013,** *49*, 1606-1608.

50. Cadiau, A.; Belmabkhout, Y.; Adil, K.; Bhatt Prashant, M.; Pillai Renjith, S.; Shkurenko, A.; Martineau-Corcos, C.; Maurin, G.; Eddaoudi, M., Hydrolytically Stable Fluorinated Metal-Organic Frameworks for Energy-Efficient Dehydration. *Science* **2017,** *356*, 731-735.

51. Yang, L.; Cui, X.; Zhang, Y.; Yang, Q.; Xing, H., A Highly Sensitive Flexible Metal–Organic Framework Sets a New Benchmark for Separating Propyne from Propylene. *J. Mater. Chem. A* **2018,** *6*, 24452-24458.

52. Sensharma, D.; O'Hearn, D. J.; Koochaki, A.; Bezrukov, A. A.; Kumar, N.; Wilson, B. H.; Vandichel, M.; Zaworotko, M. J., The First Sulfate-Pillared Hybrid Ultramicroporous Material, Sofour-1-Zn, and Its Acetylene Capture Properties. *Angew. Chem. Int. Ed.* **2022,** *61*, e202116145.

53. Mohamed, M. H.; Elsaidi, S. K.; Pham, T.; Forrest, K. A.; Schaef, H. T.; Hogan, A.; Wojtas, L.; Xu, W.; Space, B.; Zaworotko, M. J.; Thallapally, P. K., Hybrid Ultra-Microporous Materials for Selective Xenon Adsorption and Separation. *Angew. Chem. Int. Ed.* **2016,** *55*, 8285-8289.

54. Mohamed, M. H.; Elsaidi, S. K.; Wojtas, L.; Pham, T.; Forrest, K. A.; Tudor, B.; Space, B.; Zaworotko, M. J., Highly Selective Co2 Uptake in Uninodal 6-Connected "Mmo" Nets Based Upon Mo42– (M = Cr, Mo) Pillars. *J. Am. Chem. Soc.* **2012,** *134*, 19556-19559.

55. Ding, Q.; Zhang, Z.; Yu, C.; Zhang, P.; Wang, J.; Cui, X.; He, C.-H.; Deng, S.; Xing, H., Exploiting Equilibrium-Kinetic Synergetic Effect for Separation of Ethylene and Ethane in a Microporous Metal-Organic Framework. *Sci. Adv.* **2020,** *6*, eaaz4322.

56. Yang, L.; Cui, X.; Ding, Q.; Wang, Q.; Jin, A.; Ge, L.; Xing, H., Polycatenated Molecular Cage-Based Propane Trap for Propylene Purification with Recorded Selectivity. *ACS Appl. Mater. Interfaces* **2019,** *12*, 2525–2530.

57. Koh, K.; Van Oosterhout, J. D.; Roy, S.; Wong-Foy, A. G.; Matzger, A. J., Exceptional Surface Area from Coordination Copolymers Derived from Two Linear Linkers of Differing Lengths. *Chem. Sci.* **2012,** *3*, 2429.

58. Kim, H.; Kim, D.; Moon, D.; Choi, Y. N.; Baek, S. B.; Lah, M. S., Symmetry-Guided Syntheses of Mixed-Linker Zr Metal–Organic Frameworks with Precise Linker Locations. *Chem. Sci.* **2019,** *10*, 5801-5806.

59. Yuan, S.; Huang, L.; Huang, Z.; Sun, D.; Qin, J. S.; Feng, L.; Li, J.; Zou, X.; Cagin, T.; Zhou, H. C., Continuous Variation of Lattice Dimensions and Pore Sizes in Metal-Organic Frameworks. *J. Am. Chem. Soc.* **2020,** *142*, 4732-4738.

60. Deng, H.; Doonan Christian, J.; Furukawa, H.; Ferreira Ricardo, B.; Towne, J.; Knobler Carolyn, B.; Wang, B.; Yaghi Omar, M., Multiple Functional Groups of Varying Ratios in Metal-Organic Frameworks. *Science* **2010,** *327*, 846-850.

61. Li, H.; Wang, K.; Feng, D.; Chen, Y.-P.; Verdegaal, W.; Zhou, H.-C., Incorporation of Alkylamine into Metal–Organic Frameworks through a Brønsted Acid–Base Reaction for Co2 Capture. *ChemSusChem* **2016,** *9*, 2832-2840.

62. Wang, Z.; Cohen, S. M., Postsynthetic Covalent Modification of a Neutral Metal−Organic Framework. *J. Am. Chem. Soc.* **2007,** *129*, 12368-12369.

63. Kalaj, M.; Cohen, S. M., Spray-Coating of Catalytically Active Mof–Polythiourea through Postsynthetic Polymerization. *Angew. Chem. Int. Ed.* **2020,** *59*, 13984-13989.

64. Morris, W.; Doonan, C. J.; Furukawa, H.; Banerjee, R.; Yaghi, O. M., Crystals as Molecules: Postsynthesis Covalent Functionalization of Zeolitic Imidazolate Frameworks. *J. Am. Chem. Soc.* **2008,** *130*, 12626-12627.

65. Liu, C.; Li, T.; Rosi, N. L., Strain-Promoted "Click" Modification of a Mesoporous Metal-Organic Framework. *J. Am. Chem. Soc.* **2012,** *134*, 18886-8.

66. Fracaroli, A. M.; Siman, P.; Nagib, D. A.; Suzuki, M.; Furukawa, H.; Toste, F. D.; Yaghi, O. M., Seven Post-Synthetic Covalent Reactions in Tandem Leading to Enzyme-Like Complexity within Metal–Organic Framework Crystals. *J. Am. Chem. Soc.* **2016,** *138*, 8352-8355.

67. Feng, L.; Wang, K. Y.; Lv, X. L.; Powell, J. A.; Yan, T. H.; Willman, J.; Zhou, H. C., Imprinted Apportionment of Functional Groups in Multivariate Metal-Organic Frameworks. *J. Am. Chem. Soc.* **2019,** *141*, 14524-14529.

68. Mao, V. Y.; Milner, P. J.; Lee, J.-H.; Forse, A. C.; Kim, E. J.; Siegelman, R. L.; McGuirk, C. M.; Porter-Zasada, L. B.; Neaton, J. B.; Reimer, J. A.; Long, J. R., Cooperative Carbon Dioxide Adsorption in Alcoholamine- and Alkoxyalkylamine-Functionalized Metal–Organic Frameworks. *Angew. Chem. Int. Ed.* **2019,** *n/a*.

69. Kim, E. J.; Siegelman, R. L.; Jiang, H. Z. H.; Forse, A. C.; Lee, J.-H.; Martell, J. D.; Milner, P. J.; Falkowski, J. M.; Neaton, J. B.; Reimer, J. A.; Weston, S. C.; Long, J. R., Cooperative Carbon Capture and Steam Regeneration with Tetraamine-Appended Metal–Organic Frameworks. *Science* **2020,** *369*, 392.

70. Han, Z.; Wang, K.; Guo, Y.; Chen, W.; Zhang, J.; Zhang, X.; Siligardi, G.; Yang, S.; Zhou, Z.; Sun, P.; Shi, W.; Cheng, P., Cation-Induced Chirality in a Bifunctional

Metal-Organic Framework for Quantitative Enantioselective Recognition. *Nat Commun* **2019,** *10*, 5117.

71. Mao, C.; Kudla, R. A.; Zuo, F.; Zhao, X.; Mueller, L. J.; Bu, X.; Feng, P., Anion Stripping as a General Method to Create Cationic Porous Framework with Mobile Anions. *J. Am. Chem. Soc.* **2014,** *136*, 7579-82.

72. Ameloot, R.; Aubrey, M.; Wiers, B. M.; Gomora-Figueroa, A. P.; Patel, S. N.; Balsara, N. P.; Long, J. R., Ionic Conductivity in the Metal-Organic Framework Uio-66 by Dehydration and Insertion of Lithium Tert-Butoxide. *Chemistry* **2013,** *19*, 5533-6.

73. Luo, T. Y.; Liu, C.; Eliseeva, S. V.; Muldoon, P. F.; Petoud, S.; Rosi, N. L., Rare Earth Pcu Metal-Organic Framework Platform Based on Re4(Mu3-Oh)4(Coo)6(2+) Clusters: Rational Design, Directed Synthesis, and Deliberate Tuning of Excitation Wavelengths. *J. Am. Chem. Soc.* **2017,** *139*, 9333-9340.

74. Yang, Q.; Vaesen, S.; Ragon, F.; Wiersum, A. D.; Wu, D.; Lago, A.; Devic, T.; Martineau, C.; Taulelle, F.; Llewellyn, P. L.; Jobic, H.; Zhong, C.; Serre, C.; De Weireld, G.; Maurin, G., A Water Stable Metal–Organic Framework with Optimal Features for Co2 Capture. *Angew. Chem. Int. Ed.* **2013,** *52*, 10316-10320.

75. Nugent, P.; Belmabkhout, Y.; Burd, S. D.; Cairns, A. J.; Luebke, R.; Forrest, K.; Pham, T.; Ma, S.; Space, B.; Wojtas, L.; Eddaoudi, M.; Zaworotko, M. J., Porous Materials with Optimal Adsorption Thermodynamics and Kinetics for Co2 Separation. *Nature* **2013,** *495*, 80-4.

76. Queen, W. L.; Hudson, M. R.; Bloch, E. D.; Mason, J. A.; Gonzalez, M. I.; Lee, J. S.; Gygi, D.; Howe, J. D.; Lee, K.; Darwish, T. A.; James, M.; Peterson, V. K.; Teat, S. J.; Smit, B.; Neaton, J. B.; Long, J. R.; Brown, C. M., Comprehensive Study of Carbon Dioxide Adsorption in the Metal–Organic Frameworks M2(Dobdc) (M = Mg, Mn, Fe, Co, Ni, Cu, Zn). *Chem. Sci.* **2014,** *5*, 4569-4581.

77. Britt, D.; Furukawa, H.; Wang, B.; Glover, T. G.; Yaghi, O. M., Highly Efficient Separation of Carbon Dioxide by a Metal-Organic Framework Replete with Open Metal Sites. *Proceedings of the National Academy of Sciences of the United States of America* **2009,** *106*, 20637-40.

78. Wu, H.; Simmons, J. M.; Srinivas, G.; Zhou, W.; Yildirim, T., Adsorption Sites and Binding Nature of Co2 in Prototypical Metal−Organic Frameworks: A Combined Neutron Diffraction and First-Principles Study. *J. Phys. Chem. Lett.* **2010,** *1*, 1946-1951.

79. Caskey, S. R.; Wong-Foy, A. G.; Matzger, A. J., Dramatic Tuning of Carbon Dioxide Uptake Via Metal Substitution in a Coordination Polymer with Cylindrical Pores. *J. Am. Chem. Soc.* **2008,** *130*, 10870-10871.

80. Kizzie, A. C.; Wong-Foy, A. G.; Matzger, A. J., Effect of Humidity on the Performance of Microporous Coordination Polymers as Adsorbents for Co2 Capture. *Langmuir : the ACS journal of surfaces and colloids* **2011,** *27*, 6368-73.

81. Deria, P.; Mondloch, J. E.; Tylianakis, E.; Ghosh, P.; Bury, W.; Snurr, R. Q.; Hupp, J. T.; Farha, O. K., Perfluoroalkane Functionalization of Nu-1000 Via Solvent-Assisted Ligand Incorporation: Synthesis and Co2 Adsorption Studies. *J. Am. Chem. Soc.* **2013,** *135*, 16801-4.

82. Choe, J. H.; Kim, H.; Hong, C. S., Mof-74 Type Variants for Co2 Capture. *Materials Chemistry Frontiers* **2021,** *5*, 5172-5185.

83. McDonald, T. M.; D'Alessandro, D. M.; Krishna, R.; Long, J. R., Enhanced Carbon Dioxide Capture Upon Incorporation of N,N′-Dimethylethylenediamine in the Metal–Organic Framework Cubttri. *Chem. Sci.* **2011,** *2*, 2022.

84. Lee, W. R.; Jo, H.; Yang, L.-M.; Lee, H.; Ryu, D. W.; Lim, K. S.; Song, J. H.; Min, D. Y.; Han, S. S.; Seo, J. G.; Park, Y. K.; Moon, D.; Hong, C. S., Exceptional Co2 Working Capacity in a Heterodiamine-Grafted Metal–Organic Framework. *Chem. Sci.* **2015,** *6*, 3697-3705.

85. Choi, S.; Watanabe, T.; Bae, T. H.; Sholl, D. S.; Jones, C. W., Modification of the Mg/Dobdc Mof with Amines to Enhance Co2 Adsorption from Ultradilute Gases. *J Phys Chem Lett* **2012,** *3*, 1136-41.

86. Yeon, J. S.; Lee, W. R.; Kim, N. W.; Jo, H.; Lee, H.; Song, J. H.; Lim, K. S.; Kang, D. W.; Seo, J. G.; Moon, D.; Wiers, B.; Hong, C. S., Homodiamine-Functionalized Metal–Organic Frameworks with a Mof-74-Type Extended Structure for Superior Selectivity of Co2 over N2. *J. Mater. Chem. A* **2015,** *3*, 19177-19185.

87. Jo, H.; Lee, W. R.; Kim, N. W.; Jung, H.; Lim, K. S.; Kim, J. E.; Kang, D. W.; Lee, H.; Hiremath, V.; Seo, J. G.; Jin, H.; Moon, D.; Han, S. S.; Hong, C. S., Fine-Tuning of the Carbon Dioxide Capture Capability of Diamine-Grafted Metal-Organic Framework Adsorbents through Amine Functionalization. *ChemSusChem* **2017,** *10*, 541-550.

88. Milner, P. J.; Siegelman, R. L.; Forse, A. C.; Gonzalez, M. I.; Runčevski, T.; Martell, J. D.; Reimer, J. A.; Long, J. R., A Diaminopropane-Appended Metal–Organic Framework Enabling Efficient Co2 Capture from Coal Flue Gas Via a Mixed Adsorption Mechanism. *J. Am. Chem. Soc.* **2017,** *139*, 13541-13553.

89. Forse, A. C.; Milner, P. J.; Lee, J.-H.; Redfearn, H. N.; Oktawiec, J.; Siegelman, R. L.; Martell, J. D.; Dinakar, B.; Zasada, L. B.; Gonzalez, M. I.; Neaton, J. B.; Long, J. R.; Reimer, J. A., Elucidating Co2 Chemisorption in Diamine-Appended Metal–Organic Frameworks. *J. Am. Chem. Soc.* **2018,** *140*, 18016-18031.

90. Xiang, S.; Zhou, W.; Zhang, Z.; Green, M. A.; Liu, Y.; Chen, B., Open Metal Sites within Isostructural Metal–Organic Frameworks for Differential Recognition of Acetylene and Extraordinarily High Acetylene Storage Capacity at Room Temperature. *Angew. Chem. Int. Ed.* **2010,** *49*, 4615-4618.

91. Xiang, S.; Zhou, W.; Gallegos, J. M.; Liu, Y.; Chen, B., Exceptionally High Acetylene Uptake in a Microporous Metal−Organic Framework with Open Metal Sites. *J. Am. Chem. Soc.* **2009,** *131*, 12415-12419.

92. Duan, X.; Cui, Y.; Yang, Y.; Qian, G., A Novel Methoxy-Decorated Metal–Organic Framework Exhibiting High Acetylene and Carbon Dioxide Storage Capacities. *CrystEngComm* **2017,** *19*, 1464-1469.

93. Wang, Y.; Jia, X.; Yang, H.; Wang, Y.; Chen, X.; Hong, A. N.; Li, J.; Bu, X.; Feng, P., A Strategy for Constructing Pore-Space-Partitioned Mofs with High Uptake Capacity for C2 Hydrocarbons and Co2. *Angew. Chem. Int. Ed.* **2020,** *59*, 19027-19030.

94. Moreau, F.; da Silva, I.; Al Smail, N. H.; Easun, T. L.; Savage, M.; Godfrey, H. G. W.; Parker, S. F.; Manuel, P.; Yang, S.; Schröder, M., Unravelling Exceptional Acetylene and Carbon Dioxide Adsorption within a Tetra-Amide Functionalized Metal-Organic Framework. *Nat. Commun* **2017,** *8*, 14085.

95. Pang, J.; Jiang, F.; Wu, M.; Liu, C.; Su, K.; Lu, W.; Yuan, D.; Hong, M., A Porous Metal-Organic Framework with Ultrahigh Acetylene Uptake Capacity under Ambient Conditions. *Nat. Commun* **2015,** *6*, 7575.

96. Zhang, M.; Li, B.; Li, Y.; Wang, Q.; Zhang, W.; Chen, B.; Li, S.; Pan, Y.; You, X.; Bai, J., Finely Tuning Mofs Towards High Performance in C2h2 Storage: Synthesis and Properties of a New Mof-505 Analogue with an Inserted Amide Functional Group. *Chem. Commun.* **2016,** *52*, 7241-7244.

97. Jiao, J.; Dou, L.; Liu, H.; Chen, F.; Bai, D.; Feng, Y.; Xiong, S.; Chen, D.-L.; He, Y., An Aminopyrimidine-Functionalized Cage-Based Metal–Organic Framework Exhibiting Highly Selective Adsorption of C2h2 and Co2 over Ch4. *Dalton Trans.* **2016,** *45*, 13373-13382.

98. Zhai, Q.-G.; Bu, X.; Mao, C.; Zhao, X.; Daemen, L.; Cheng, Y.; Ramirez-Cuesta, A. J.; Feng, P., An Ultra-Tunable Platform for Molecular Engineering of High-Performance Crystalline Porous Materials. *Nat. Commun* **2016,** *7*, 13645.

99. Liu, K.; Ma, D.; Li, B.; Li, Y.; Yao, K.; Zhang, Z.; Han, Y.; Shi, Z., High Storage Capacity and Separation Selectivity for C2 Hydrocarbons over Methane in the Metal–Organic Framework Cu–Tdpat. *J. Mater. Chem. A* **2014,** *2*, 15823-15828.

100. Hong, A. N.; Kusumoputro, E.; Wang, Y.; Yang, H.; Chen, Y.; Bu, X.; Feng, P., Simultaneous Control of Pore-Space Partition and Charge Distribution in Multi-Modular Metal–Organic Frameworks. *Angew. Chem. Int. Ed.* **2022,** *61*, e202116064.

101. Yang, H.; Wang, Y.; Krishna, R.; Jia, X.; Wang, Y.; Hong, A. N.; Dang, C.; Castillo, H. E.; Bu, X.; Feng, P., Pore-Space-Partition-Enabled Exceptional Ethane Uptake and Ethane-Selective Ethane–Ethylene Separation. *J. Am. Chem. Soc.* **2020,** *142*, 2222-2227.

102. Rao, X.; Cai, J.; Yu, J.; He, Y.; Wu, C.; Zhou, W.; Yildirim, T.; Chen, B.; Qian, G., A Microporous Metal-Organic Framework with Both Open Metal and Lewis Basic Pyridyl Sites for High C2h2 and Ch4 Storage at Room Temperature. *Chem Commun (Camb)* **2013,** *49*, 6719-21.

103. Wen, H.-M.; Wang, H.; Li, B.; Cui, Y.; Wang, H.; Qian, G.; Chen, B., A Microporous Metal–Organic Framework with Lewis Basic Nitrogen Sites for High C2h2 Storage and Significantly Enhanced C2h2/Co2 Separation at Ambient Conditions. *Inorg. Chem.* **2016,** *55*, 7214-7218.

104. Bloch, E. D.; Queen, W. L.; Krishna, R.; Zadrozny, J. M.; Brown, C. M.; Long, J. R., Hydrocarbon Separations in a Metal-Organic Framework with Open Iron(Ii) Coordination Sites. *Science* **2012,** *335*, 1606-1610.

105. Bachman, J. E.; Kapelewski, M. T.; Reed, D. A.; Gonzalez, M. I.; Long, J. R., M2(M-Dobdc) (M = Mn, Fe, Co, Ni) Metal–Organic Frameworks as Highly Selective, High-Capacity Adsorbents for Olefin/Paraffin Separations. *J. Am. Chem. Soc.* **2017,** *139*, 15363-15370.

106. Chang, G.; Huang, M.; Su, Y.; Xing, H.; Su, B.; Zhang, Z.; Yang, Q.; Yang, Y.; Ren, Q.; Bao, Z.; Chen, B., Immobilization of Ag(I) into a Metal-Organic Framework with -So3h Sites for Highly Selective Olefin-Paraffin Separation at Room Temperature. *Chem. Commun.* **2015,** *51*, 2859-2862.

107. Yang, S.; Ramirez-Cuesta, A. J.; Newby, R.; Garcia-Sakai, V.; Manuel, P.; Callear, S. K.; Campbell, S. I.; Tang, C. C.; Schroder, M., Supramolecular Binding and

Separation of Hydrocarbons within a Functionalized Porous Metal-Organic Framework. *Nat Chem* **2014,** *7*, 121-9.

108. Bao, Z.; Wang, J.; Zhang, Z.; Xing, H.; Yang, Q.; Yang, Y.; Wu, H.; Krishna, R.; Zhou, W.; Chen, B.; Ren, Q., Molecular Sieving of Ethane from Ethylene through the Molecular Cross-Section Size Differentiation in Gallate-Based Metal-Organic Frameworks. *Angew. Chem. Int. Ed. Engl.* **2018,** *57*, 16020-16025.

109. Lin, R.-B.; Li, L.; Zhou, H.-L.; Wu, H.; He, C.; Li, S.; Krishna, R.; Li, J.; Zhou, W.; Chen, B., Molecular Sieving of Ethylene from Ethane Using a Rigid Metal–Organic Framework. *Nature Materials* **2018,** *17*, 1128-1133.

110. Zhang, L.; Li, L.; Hu, E.; Yang, L.; Shao, K.; Yao, L.; Jiang, K.; Cui, Y.; Yang, Y.; Li, B.; Chen, B.; Qian, G., Boosting Ethylene/Ethane Separation within Copper(I)-Chelated Metal-Organic Frameworks through Tailor-Made Aperture and Specific Pi-Complexation. *Advanced science* **2020,** *7*, 1901918.

111. Geier, S. J.; Mason, J. A.; Bloch, E. D.; Queen, W. L.; Hudson, M. R.; Brown, C. M.; Long, J. R., Selective Adsorption of Ethylene over Ethane and Propylene over Propane in the Metal–Organic Frameworks M2(Dobdc) (M = Mg, Mn, Fe, Co, Ni, Zn). *Chem. Sci.* **2013,** *4*, 2054-2061.

112. Yu, L.; Han, X.; Wang, H.; Ullah, S.; Xia, Q.; Li, W.; Li, J.; da Silva, I.; Manuel, P.; Rudic, S.; Cheng, Y.; Yang, S.; Thonhauser, T.; Li, J., Pore Distortion in a Metal-Organic Framework for Regulated Separation of Propane and Propylene. *J. Am. Chem. Soc.* **2021,** *143*, 19300-19305.

113. Wang, Y.; Huang, N. Y.; Zhang, X. W.; He, H.; Huang, R. K.; Ye, Z. M.; Li, Y.; Zhou, D. D.; Liao, P. Q.; Chen, X. M.; Zhang, J. P., Selective Aerobic Oxidation of a Metal-Organic Framework Boosts Thermodynamic and Kinetic Propylene/Propane Selectivity. *Angew. Chem. Int. Ed. Engl.* **2019,** *58*, 7692-7696.

114. Chen, Y.; Qiao, Z.; Wu, H.; Lv, D.; Shi, R.; Xia, Q.; Zhou, J.; Li, Z., An Ethane-Trapping Mof Pcn-250 for Highly Selective Adsorption of Ethane over Ethylene. *Chem. Eng. Sci.* **2018,** *175*, 110-117.

115. Li, L.; Lin, R.-B.; Krishna, R.; Li, H.; Xiang, S.; Wu, H.; Li, J.; Zhou, W.; Chen, B., Ethane/Ethylene Separation in a Metal-Organic Framework with Iron-Peroxo Sites. *Science* **2018,** *362*, 443-446.

116. Lysova, A. A.; Samsonenko, D. G.; Kovalenko, K. A.; Nizovtsev, A. S.; Dybtsev, D. N.; Fedin, V. P., A Series of Mesoporous Metal-Organic Frameworks with Tunable Windows Sizes and Exceptionally High Ethane over Ethylene Adsorption Selectivity. *Angew. Chem. Int. Ed.* **2020,** *59*, 20561-20567.

117. Lin, R.-B.; Wu, H.; Li, L.; Tang, X.-L.; Li, Z.; Gao, J.; Cui, H.; Zhou, W.; Chen, B., Boosting Ethane/Ethylene Separation within Isoreticular Ultramicroporous Metal-Organic Frameworks. *J. Am. Chem. Soc.* **2018,** *140*, 12940-12946.

118. Gücüyener, C.; van den Bergh, J.; Gascon, J.; Kapteijn, F., Ethane/Ethene Separation Turned on Its Head: Selective Ethane Adsorption on the Metal−Organic Framework Zif-7 through a Gate-Opening Mechanism. *J. Am. Chem. Soc.* **2010,** *132*, 17704-17706.

119. Liao, P.-Q.; Zhang, W.-X.; Zhang, J.-P.; Chen, X.-M., Efficient Purification of Ethene by an Ethane-Trapping Metal-Organic Framework. *Nat. Commun* **2015,** *6*, 8697.

120. Hong, A. N.; Yang, H.; Li, T.; Wang, Y.; Wang, Y.; Jia, X.; Zhou, A.; Kusumoputro, E.; Li, J.; Bu, X.; Feng, P., Pore-Space Partition and Optimization for Propane-Selective High-Performance Propane/Propylene Separation. *ACS Appl. Mater. Interfaces* **2021,** *13*, 52160-52166.

121. Andres-Garcia, E.; López-Cabrelles, J.; Oar-Arteta, L.; Roldan-Martinez, B.; Cano-Padilla, M.; Gascon, J.; Mínguez Espallargas, G.; Kapteijn, F., Cation Influence in Adsorptive Propane/Propylene Separation in Zif-8 (Sod) Topology. *Chem. Eng. J.* **2019,** *371*, 848-856.

122. He, C.; Wang, Y.; Chen, Y.; Wang, X.; Yang, J.; Li, L.; Li, J., Modification of the Pore Environment in Uio-Type Metal-Organic Framework toward Boosting the Separation of Propane/Propylene. *Chem. Eng. J.* **2021,** *403*, 126428.

123. Yang, S. Q.; Sun, F. Z.; Krishna, R.; Zhang, Q.; Zhou, L.; Zhang, Y. H.; Hu, T. L., Propane-Trapping Ultramicroporous Metal-Organic Framework in the Low-Pressure Area toward the Purification of Propylene. *ACS Appl Mater Interfaces* **2021,** *13*, 35990-35996.

124. Chang, M.; Ren, J.; Wei, Y.; Wang, J.-X.; Yang, Q.; Liu, D.; Chen, J.-F., A Robust Metal-Organic Framework with Guest Molecules Induced Splint-Like Pore Confinement to Construct Propane-Trap for Propylene Purification. *Sep. Purif. Technol.* **2021,** *279*, 119656.

125. Di, Z.; Liu, C.; Pang, J.; Chen, C.; Hu, F.; Yuan, D.; Wu, M.; Hong, M., Cage-Like Porous Materials with Simultaneous High C2 H2 Storage and Excellent C2 H2 /Co2 Separation Performance. *Angew. Chem. Int. Ed. Engl.* **2021**.

126. Ye, Y.; Xian, S.; Cui, H.; Tan, K.; Gong, L.; Liang, B.; Pham, T.; Pandey, H.; Krishna, R.; Lan, P. C.; Forrest, K. A.; Space, B.; Thonhauser, T.; Li, J.; Ma, S.,

Metal–Organic Framework Based Hydrogen-Bonding Nanotrap for Efficient Acetylene Storage and Separation. *J. Am. Chem. Soc.* **2021**.

127. Li, H.; Liu, C.; Chen, C.; Di, Z.; Yuan, D.; Pang, J.; Wei, W.; Wu, M.; Hong, M., An Unprecedented Pillar-Cage Fluorinated Hybrid Porous Framework with Highly Efficient Acetylene Storage and Separation. *Angew. Chem. Int. Ed.* **2021,** *60*, 7547-7552.

128. Xue, Y. Y.; Bai, X. Y.; Zhang, J.; Wang, Y.; Li, S. N.; Jiang, Y. C.; Hu, M. C.; Zhai, Q. G., Precise Pore Space Partitions Combined with High-Density Hydrogen-Bonding Acceptors within Metal-Organic Frameworks for Highly Efficient Acetylene Storage and Separation. *Angew. Chem. Int. Ed. Engl.* **2021,** *60*, 10122-10128.

129. Ye, Y.; Ma, Z.; Lin, R. B.; Krishna, R.; Zhou, W.; Lin, Q.; Zhang, Z.; Xiang, S.; Chen, B., Pore Space Partition within a Metal-Organic Framework for Highly Efficient C2h2/Co2 Separation. *J. Am. Chem. Soc.* **2019,** *141*, 4130-4136.

130. Li, Y.-P.; Wang, Y.; Xue, Y.-Y.; Li, H.-P.; Zhai, Q.-G.; Li, S.-N.; Jiang, Y.-C.; Hu, M.-C.; Bu, X., Ultramicroporous Building Units as a Path to Bi-Microporous Metal–Organic Frameworks with High Acetylene Storage and Separation Performance. *Angew. Chem. Int. Ed.* **2019,** *58*, 13590-13595.

131. Xu, T.; Jiang, Z.; Liu, P.; Chen, H.; Lan, X.; Chen, D.; Li, L.; He, Y., Immobilization of Oxygen Atoms in the Pores of Microporous Metal–Organic Frameworks for C2h2 Separation and Purification. *ACS Applied Nano Materials* **2020,** *3*, 2911-2919.

132. Fu, X.-P.; Wang, Y.-L.; Zhang, X.-F.; Krishna, R.; He, C.-T.; Liu, Q.-Y.; Chen, B., Collaborative Pore Partition and Pore Surface Fluorination within a Metal–Organic Framework for High-Performance C2h2/Co2 Separation. *Chem. Eng. J.* **2022,** *432*, 134433.

133. Niu, Z.; Cui, X.; Pham, T.; Verma, G.; Lan, P. C.; Shan, C.; Xing, H.; Forrest, K. A.; Suepaul, S.; Space, B.; Nafady, A.; Al-Enizi, A. M.; Ma, S., A Mof-Based Ultra-Strong Acetylene Nano-Trap for Highly Efficient C2h2/Co2 Separation. *Angew. Chem. Int. Ed.* **2021,** *60*, 5283-5288.

134. Luo, F.; Yan, C.; Dang, L.; Krishna, R.; Zhou, W.; Wu, H.; Dong, X.; Han, Y.; Hu, T. L.; O'Keeffe, M.; Wang, L.; Luo, M.; Lin, R. B.; Chen, B., Utsa-74: A Mof-74 Isomer with Two Accessible Binding Sites Per Metal Center for Highly Selective Gas Separation. *J. Am. Chem. Soc.* **2016,** *138*, 5678-84.

135. Wang, J.; Zhang, Y.; Su, Y.; Liu, X.; Zhang, P.; Lin, R.-B.; Chen, S.; Deng, Q.; Zeng, Z.; Deng, S.; Chen, B., Fine Pore Engineering in a Series of Isoreticular Metal-Organic Frameworks for Efficient C2h2/Co2 Separation. *Nat. Commun* **2022,** *13*, 200.

136. Gao, J.; Qian, X.; Lin, R.-B.; Krishna, R.; Wu, H.; Zhou, W.; Chen, B., Mixed Metal-Organic Framework with Multiple Binding Sites for Efficient C2h2/Co2 Separation. *Angew. Chem., Int. Ed.* **2020,** *59*, 4396-4400.

137. Pei, J.; Wen, H.-M.; Gu, X.-W.; Qian, Q.-L.; Yang, Y.; Cui, Y.; Li, B.; Chen, B.; Qian, G., Dense Packing of Acetylene in a Stable and Low-Cost Metal–Organic Framework for Efficient C2h2/Co2 Separation. *Angew. Chem. Int. Ed.* **2021,** *60*, 25068-25074.

138. Zhang, L.; Jiang, K.; Li, L.; Xia, Y.-P.; Hu, T.-L.; Yang, Y.; Cui, Y.; Li, B.; Chen, B.; Qian, G., Efficient Separation of C2h2 from C2h2/Co2 Mixtures in an Acid–Base Resistant Metal–Organic Framework. *Chem. Commun.* **2018,** *54*, 4846-4849.

139. Wen, H.-M.; Liao, C.; Li, L.; Yang, L.; Wang, J.; Huang, L.; Li, B.; Chen, B.; Hu, J., Reversing C2h2–Co2 Adsorption Selectivity in an Ultramicroporous Metal–Organic Framework Platform. *Chem. Commun.* **2019,** *55*, 11354-11357.

140. Lin, R. B.; Li, L.; Wu, H.; Arman, H.; Li, B.; Lin, R. G.; Zhou, W.; Chen, B., Optimized Separation of Acetylene from Carbon Dioxide and Ethylene in a Microporous Material. *J. Am. Chem. Soc.* **2017,** *139*, 8022-8028.

141. Gong, W.; Cui, H.; Xie, Y.; Li, Y.; Tang, X.; Liu, Y.; Cui, Y.; Chen, B., Efficient C2h2/Co2 Separation in Ultramicroporous Metal–Organic Frameworks with Record C2h2 Storage Density. *J. Am. Chem. Soc.* **2021**.

142. Zeng, H.; Xie, M.; Huang, Y. L.; Zhao, Y.; Xie, X. J.; Bai, J. P.; Wan, M. Y.; Krishna, R.; Lu, W.; Li, D., Induced Fit of C2 H2 in a Flexible Mof through Cooperative Action of Open Metal Sites. *Angew. Chem. Int. Ed. Engl.* **2019,** *58*, 8515-8519.

143. Liu, R.; Liu, Q.-Y.; Krishna, R.; Wang, W.; He, C.-T.; Wang, Y.-L., Water-Stable Europium 1,3,6,8-Tetrakis(4-Carboxylphenyl)Pyrene Framework for Efficient C2h2/Co2 Separation. *Inorg. Chem.* **2019,** *58*, 5089-5095.

144. Zhang, L.; Jiang, K.; Yang, L.; Li, L.; Hu, E.; Yang, L.; Shao, K.; Xing, H.; Cui, Y.; Yang, Y.; Li, B.; Chen, B.; Qian, G., Benchmark C2h2/Co2 Separation in an Ultra-Microporous Metal-Organic Framework Via Copper(I)-Alkynyl Chemistry. *Angew. Chem., Int. Ed.* **2021,** *60*, 15995-16002.

145. Chen, S.; Behera, N.; Yang, C.; Dong, Q.; Zheng, B.; Li, Y.; Tang, Q.; Wang, Z.; Wang, Y.; Duan, J., A Chemically Stable Nanoporous Coordination Polymer with Fixed and Free Cu2+ Ions for Boosted C2h2/Co2 Separation. *Nano Research* **2021,** *14*, 546-553.

146. Li, L.; Lin, R.-B.; Wang, X.; Zhou, W.; Jia, L.; Li, J.; Chen, B., Kinetic Separation of Propylene over Propane in a Microporous Metal-Organic Framework. *Chem. Eng. J.* **2018,** *354*, 977-982.

147. Peng, J.; Wang, H.; Olson, D. H.; Li, Z.; Li, J., Efficient Kinetic Separation of Propene and Propane Using Two Microporous Metal Organic Frameworks. *Chem. Commun.* **2017,** *53*, 9332-9335.

148. Lee, C. Y.; Bae, Y.-S.; Jeong, N. C.; Farha, O. K.; Sarjeant, A. A.; Stern, C. L.; Nickias, P.; Snurr, R. Q.; Hupp, J. T.; Nguyen, S. T., Kinetic Separation of Propene and Propane in Metal−Organic Frameworks: Controlling Diffusion Rates in Plate-Shaped Crystals Via Tuning of Pore Apertures and Crystallite Aspect Ratios. *J. Am. Chem. Soc.* **2011,** *133*, 5228-5231.

149. Li, K.; Olson, D. H.; Seidel, J.; Emge, T. J.; Gong, H.; Zeng, H.; Li, J., Zeolitic Imidazolate Frameworks for Kinetic Separation of Propane and Propene. *J. Am. Chem. Soc.* **2009,** *131*, 10368-10369.

150. Shigematsu, A.; Yamada, T.; Kitagawa, H., Wide Control of Proton Conductivity in Porous Coordination Polymers. *J. Am. Chem. Soc.* **2011,** *133*, 2034-2036.

151. Sadakiyo, M.; Ōkawa, H.; Shigematsu, A.; Ohba, M.; Yamada, T.; Kitagawa, H., Promotion of Low-Humidity Proton Conduction by Controlling Hydrophilicity in Layered Metal–Organic Frameworks. *J. Am. Chem. Soc.* **2012,** *134*, 5472-5475.

152. Taylor, J. M.; Dawson, K. W.; Shimizu, G. K. H., A Water-Stable Metal–Organic Framework with Highly Acidic Pores for Proton-Conducting Applications. *J. Am. Chem. Soc.* **2013,** *135*, 1193-1196.

153. Thorarinsdottir, A. E.; Harris, T. D., Metal–Organic Framework Magnets. *Chem. Rev.* **2020,** *120*, 8716-8789.

154. Ōkawa, H.; Sadakiyo, M.; Yamada, T.; Maesato, M.; Ohba, M.; Kitagawa, H., Proton-Conductive Magnetic Metal–Organic Frameworks, {Nr3(Ch2cooh)}[Maiimbiii(Ox)3]: Effect of Carboxyl Residue Upon Proton Conduction. *J. Am. Chem. Soc.* **2013,** *135*, 2256-2262.

155. Stone, K. H.; Stephens, P. W.; McConnell, A. C.; Shurdha, E.; Pokhodnya, K. I.; Miller, J. S., Mnii(Tcne)3/2(I3)1/2–a 3d Network-Structured Organic-Based Magnet and Comparison to a 2d Analog. *Adv. Mater.* **2010,** *22*, 2514-2519.

156. Zhai, Q.-G.; Bu, X.; Zhao, X.; Li, D.-S.; Feng, P., Pore Space Partition in Metal–Organic Frameworks. *Acc. Chem. Res.* **2017,** *50*, 407-417.

157. Zheng, S.-T.; Bu, J. T.; Li, Y.; Wu, T.; Zuo, F.; Feng, P.; Bu, X., Pore Space Partition and Charge Separation in Cage-within-Cage Indium−Organic Frameworks with High Co2 Uptake. *J. Am. Chem. Soc.* **2010,** *132*, 17062-17064.

158. Wu, Y.-P.; Tian, J.-W.; Liu, S.; Li, B.; Zhao, J.; Ma, L.-F.; Li, D.-S.; Lan, Y.-Q.; Bu, X., Bi-Microporous Metal–Organic Frameworks with Cubane [M4(Oh)4] (M=Ni, Co) Clusters and Pore-Space Partition for Electrocatalytic Methanol Oxidation Reaction. *Angew. Chem. Int. Ed.* **2019,** *58*, 12185-12189.

159. Zheng, S.-T.; Zhao, X.; Lau, S.; Fuhr, A.; Feng, P.; Bu, X., Entrapment of Metal Clusters in Metal–Organic Framework Channels by Extended Hooks Anchored at Open Metal Sites. *J. Am. Chem. Soc.* **2013,** *135*, 10270-10273.

160. Lorzing, G. R.; Balto, K. P.; Antonio, A. M.; Trump, B. A.; Brown, C. M.; Bloch, E. D., Elucidating the Structure of the Metal–Organic Framework Ru-Hkust-1. *Chem. Mater.* **2020,** *32*, 7710-7715.

161. Trousselet, F.; Archereau, A.; Boutin, A.; Coudert, F.-X., Heterometallic Metal–Organic Frameworks of Mof-5 and Uio-66 Families: Insight from Computational Chemistry. *J. Phys. Chem. C* **2016,** *120*, 24885-24894.

162. Bakuru, V. R.; Churipard, S. R.; Maradur, S. P.; Kalidindi, S. B., Exploring the Brønsted Acidity of Uio-66 (Zr, Ce, Hf) Metal–Organic Frameworks for Efficient Solketal Synthesis from Glycerol Acetalization. *Dalton Trans.* **2019,** *48*, 843-847.

163. Feng, D.; Wang, K.; Wei, Z.; Chen, Y.-P.; Simon, C. M.; Arvapally, R. K.; Martin, R. L.; Bosch, M.; Liu, T.-F.; Fordham, S.; Yuan, D.; Omary, M. A.; Haranczyk, M.; Smit, B.; Zhou, H.-C., Kinetically Tuned Dimensional Augmentation as a Versatile Synthetic Route Towards Robust Metal–Organic Frameworks. *Nat. Commun* **2014,** *5*, 5723.

164. ZareKarizi, F.; Joharian, M.; Morsali, A., Pillar-Layered Mofs: Functionality, Interpenetration, Flexibility and Applications. *J. Mater. Chem. A* **2018,** *6*, 19288-19329.

165. Bureekaew, S.; Sato, H.; Matsuda, R.; Kubota, Y.; Hirose, R.; Kim, J.; Kato, K.; Takata, M.; Kitagawa, S., Control of Interpenetration for Tuning Structural

Flexibility Influences Sorption Properties. *Angew. Chem. Int. Ed.* **2010,** *49*, 7660-7664.

Chapter 2: Uncovering Limits of Partitioned-*acs* Frameworks

2.1 Introduction

Since the early 2000's, pioneers in the field have demonstrated remarkable tunability of MOF structures through length of linker design and since then, the family of synthesizable linkers continues to expand, pushing the limits of pore diameter, surface area and pore volume of crystalline materials to ultrahigh records.[1-2] At the same time, development of new reticular design methods continues to fine-tune pore-structures, allowing for precise adjustments of metrics at sub-Angstrom scale.

Among different MOF families that undergo isoreticular design synthesis, the *pacs* platform has a clear advantage. The platform is built upon the anisotropic hexagonal symmetry group, with a- and c-axes directly represented by L2 and L1 linkers, respectively. The a and c axial lengths can be mix-and-match at-will, allowing for precise control over framework size, shape and volume. The high tolerance towards mismatched linkers of different sizes is ascribed the role segregation of different modules in our platform. The coordination between trimer and L1 forms the intrinsically flexible underlying **acs** topological net where the degree "swelling" is dependent upon the length of stationed L2 linker. A larger L2 would allow for more "swelling" through enlargement of channel base (a-axis) and contraction of channel height (c-axis) (Figure 2.1). Thus far, we have enjoyed

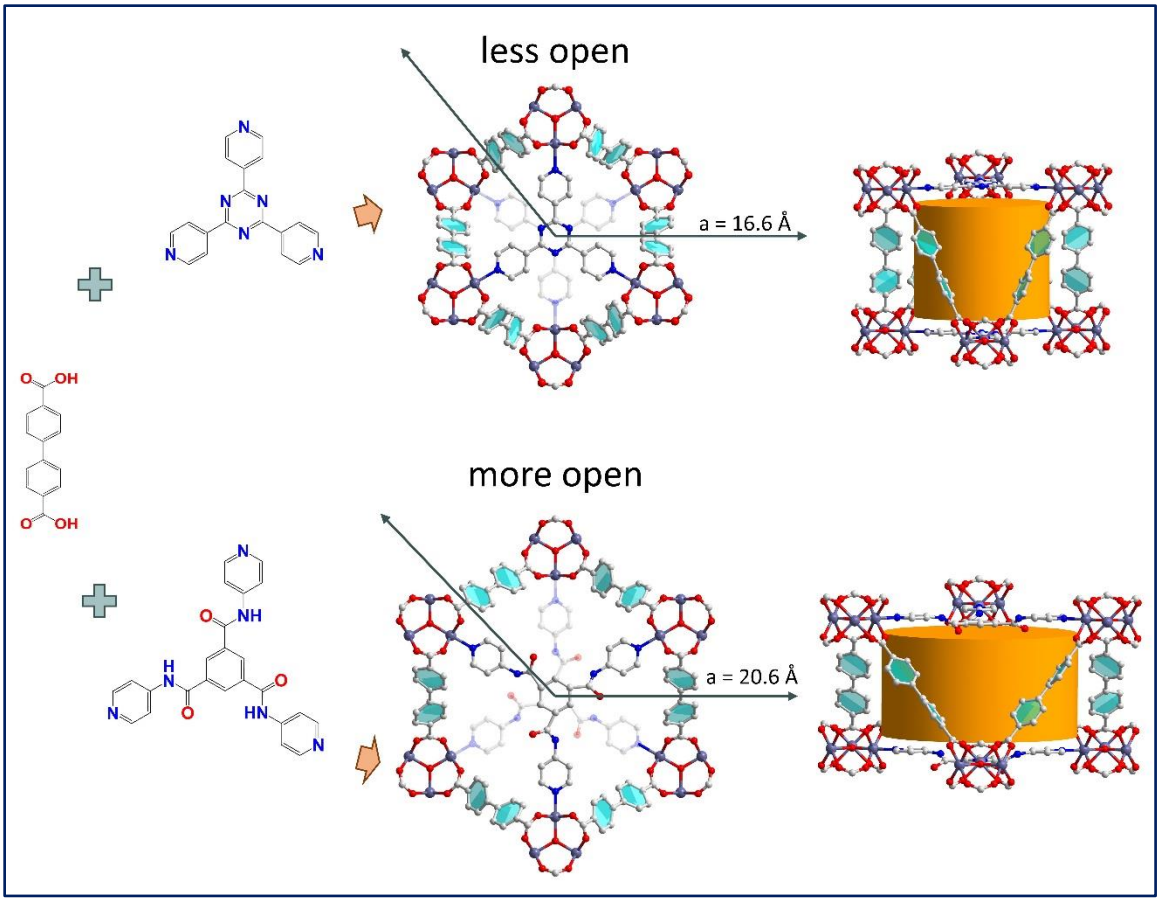

Figure 2.1 Capturing two different degrees of opening of bpdc-based *pacs* through employment of different sized L2 linkers. Enlargement of a-axis results in compression of c-axis (orange pocket).

great successes in the *pacs* platform through exploratory experimental approach. With better insights from the platform, we hope to deploy more practical geometric boundaries and requisites to serve as guidelines for reticular design of *pacs* platform.

Herein, we mathematically derive the upper and lower limits of framework dimensions, translate these parameters to the physical limits of L1 and L2 scaling ratios, and index a new library of *pacs* of varied sizes to validate our theoretical model. We then identify potential *pacs* materials to use as adsorbents to separate important industrial gas mixtures.

2.2 Experimental Section

2.2.1 Chemicals and Materials

Vanadium (III) chloride (VCl_3) was purchased from ACROS Organics. Cobalt (II) nitrate hexahydrate ($Co(NO_3)_2 \cdot 6H_2O$), Cobalt (II) chloride hexahydrate ($CoCl_2 \cdot 6H_2O$), acetone, methanol (MeOH), ethanol (EtOH), N,N-dimethylacetamide (DMA), N,N-dimethylformamide (DMF), dichloromethane (CH_2Cl_2), 1,1,1,5,5,5-hexafluoro-2,4-pentanedione (HFP), trifluoroacetic acid (TFA), fluoroboric acid 48 w.t. % (HBF_4) and hydrochloric acid 38 w.t. % (HCl) were purchased from Fischer Scientific Co., N-methylformamide (NMF), 4-pyridylamidine hydrochloride, sodium tricyanomethanide ($Na(C(CN)_3)$), 1,4-benzenedicarboxylic acid (H_2bdc), 2,6-naphthalenedicarboxylic acid (2,6-H_2ndc), 4,4'-biphenyldicarboxylic acid (H_2bpdc), 4,4'-azobenzenedicarboxylic acid (H_2adc), 2,4,6-Tri(4-pyridyl)-1,3,5-triazine (tpt), 1,3-Dimethyl-2-imidazolidinone (DMI), 1,3-dimethyl 3,4,5,6-tetrahydro-2(1H)-pyrimidinone (DMPU) were obtained from TCI-America. All reagents were used as received without further purification. 4-(1H-tetrazol-5-yl)benzoic acid (H_2tba), tris(4-pyridyl)amine (tpa), 1,3,5-Tris(4-pyridylethynyl)benzene (tpab), tris[4-(4-pyridyl)phenyl]amine (tppa), and 1,3,5-Tris(4-pyridylphenyl)benzene (tppb) were purchased from Yanshen Technology Co., Ltd.

2.2.2 Synthesis of Organic Linkers

Synthesis of N,N',N''-tri(4-pyridinyl)-1,3,5-benzenetri-carboxamide (tpbtc): The amide condensation reaction was carried out according to ref.[3] A solution containing 60 g of DMA and 8 g of 1,3,5-benzenetricarbonyl trichloride was added dropwise to a stirring

solution containing 9.6 g 4-aminopyridine, 0.9 g 4-dimethylaminopyridine and 240 g of DMA. The resulting pale-yellow solution was stirred at room temperature for 5 days. The suspension was then filtered and dried in vacuum oven at 60 °C overnight to obtain off-white crystalline product. NMR (*d*6-DMSO) ^{1}H: 9.06 (3H, s), 8.81 (6H, d). 8.48 (6H, d).

2,5,8-tri-(4-pyridyl)-1,3,4,6,7,9-hexaazaphenalene (H-tph): The hexaazaphenalene condensation reaction was carried out according to ref [4] with modification. $NaC(CN)_3$ (0.750 g, 6.6 mmol) and pyridine-4-amidine hydrochloride (4.50 g, 28 mmol) were briefly mixed in a teflon-lined stainless steel autoclave before being heated to 200 °C overnight. After allowing vessel to cool to ambient temperature, 10 w.t. % HCl solution was added to dissolve the crude product. After filtering undissolved particulates, the solution was neutralized with acetone, and isolated. The dissolution in HCl and neutralization in acetone were repeated a second time. The product was isolated and dried overnight under vacuum at 60 °C to obtain the final light tan powder (50 %). ^{1}H NMR d_6-DMSO: 8.69 (d), 9.01 (d).

2.2.3 Synthesis of Partitioned-acs Frameworks

CPM-731a (CoV-bdc-tpa): In a 20 mL glass vial, $Co(NO_3)_2 \cdot 6H_2O$ (58 mg, ~0.2 mmol), VCl_3 (16 mg, ~0.1 mmol), H_2bdc (51 mg, ~0.3 mmol), and tpa (25 mg, ~0.1 mmol) were dissolved in 6 g DMA 6 g MeOH and 0.6 g HBF_4. After stirring for 2 hours, the vial was placed in a 120 °C oven for 4 days. Brown hexagonal plates were obtained after solution is cooled to ambient temperature.

CPM-731b (CoV-bdc-tpt): In a 20 mL glass vial, $Co(NO_3)_2 \cdot 6H_2O$ (58 mg, ~0.2 mmol), VCl_3 (16 mg, ~0.1 mmol), H_2bdc (51 mg, ~0.3 mmol), and tpa (25 mg, ~0.1 mmol) were dissolved in 6 g NMF and 0.03 g HCl. After stirring for 2 hours, the vial was placed in a 120 ℃ oven for 4 days. Dark-red hexagonal plates were obtained after solution is cooled to ambient temperature.

CPM-701c (Co-bdc-tph): In a 20 mL glass vial, $Co(ClO_4)_2 \cdot 6H_2O$ (37 mg, ~0.1 mmol), VCl_3 (8 mg, ~0.05 mmol), bdc (28 mg, ~0.2 mmol), and H-tph (25 mg, ~0.05 mmol) were dissolved in 6 g NMF, 1 g DMPU, and 0.03 g HFP. After stirring for 2 hours, the vial was placed in a 120 ℃ oven for 5 days. Red microcrystalline materials were obtained after solution is cooled to ambient temperature.

CPM-800c (Ni-bdc-tph) In a 20 mL glass vial, $Ni(NO_3)_2 \cdot 6H_2O$ (90 mg, ~0.3 mmol), bdc (51 mg, ~0.3 mmol), H-tph (42 mg, ~0.1 mmol), and were dissolved in 6 g DMA,0.6 g H_2O and 0.6 g TFA. After stirring for 2 hours, the vial was placed in a 140 ℃ oven for 16 hours. Large green hexagonal crystals were obtained after solution is cooled to ambient temperature.

CPM-702a (Co-tba-tpa): In a 20 mL glass vial, $CoCl_2 \cdot 6H_2O$ (24 mg, ~0.1 mmol), tba (19 mg, ~0.1 mmol), and tpa (08 mg, ~0.03 mmol) were dissolved in 3 g DMA, 03 HBF_4. After stirring for 2 hours, the vial was placed in a 90 ℃ oven for 3 days. Pink hexagonal plates were obtained after solution is cooled to ambient temperature.

CPM-702d (Co-tba-tph): In a 20 mL glass vial, $CoCl_2 \cdot 6H_2O$ (24 mg, ~0.1 mmol), tba (19 mg, ~0.1 mmol), and H-tph (15 mg, ~0.03 mmol) were dissolved in 3 g DMA, 0.3 g

HBF_4. After stirring for 2 hours, the vial was placed in a 90 ℃ oven for 3 days. Pink hexagonal plates were obtained after solution is cooled to ambient temperature.

CPM-702d (Co-tba-tpbtc): In a 20 mL glass vial, $CoCl_2 \cdot 6H_2O$ (24 mg, ~0.1 mmol), tba (19 mg, ~0.1 mmol), and tpbtc (15 mg, ~0.03 mmol) were dissolved in 2 g DMF, 1 g DMPU, and 0.03 g HFP. After stirring for 2 hours, the vial was placed in a 120 ℃ oven for 3 days. Pink hexagonal plates were obtained after solution is cooled to ambient temperature.

CPM-733a (CoV-26ndc-tpa): In a 20 mL glass vial, $Co(NO_3)_2 \cdot 6H_2O$ (58 mg, 0.20 mmol), VCl_3 (16 mg, 0.10 mmol), 2,6-H_2ndc (65 mg, 0.30 mmol, and tpt (31 mg, 0.10 mmol) were dissolved in 4.0 g NMF and 0.04 g of HCl (38 w.t. %). After stirring for 2 hours, the vial was placed in a 120 ℃ oven for 5 days. Dark-red hexagonal prisms-were isolated by sonication and filtration.

CPM-733b (CoV-26ndc-tpt): In a 20 mL glass vial, $Co(NO_3)_2 \cdot 6H_2O$ (58 mg, 0.20 mmol), VCl_3 (16 mg, 0.10 mmol), 2,6-H_2ndc (65 mg, 0.30 mmol, and tpt (31 mg, 0.10 mmol) were dissolved in 4.0 g NMF and 0.04 g of HCl (38 w.t. %). After stirring for 2 hours, the vial was placed in a 120 ℃ oven for 5 days. Dark-red spindle-shaped crystals were isolated by sonication and filtration.

CPM-733d (CoV-26ndc-tpbtc): In a 20 mL glass vial, $Co(NO_3)_2 \cdot 6H_2O$ (58 mg, 0.20 mmol), VCl_3 (16 mg, 0.10 mmol), 2,6-H_2ndc (65 mg, 0.30 mmol), and tpbtc (45 mg, 0.10 mmol) were dissolved in 6.0 g NMF. After stirring for 2 hours, the vial was placed in a 120 ℃ oven for 5 days. Orange-brown hexagonal plates were isolated by sonication and filtration.

CPM-703e (Co-26ndc-tpab):. In a 20 mL glass vial, $CoCl_2 \cdot 6H_2O$ (24 mg, ~0.1 mmol), 26-H_2ndc (21 mg, ~0.1 mmol), and tpab (13 mg, ~0.03 mmol) were dissolved in 2 g DMF, 1 g DMPU, and 0.03 g HFP. After stirring for 2 hours, the vial was placed in a 120 ℃ oven for 3 days. Red hexagonal prisms were obtained after solution is cooled to ambient temperature.

CPM-733e (CoV-26ndc-tpab): In a 20 mL glass vial, $Co(NO_3)_2 \cdot 6H_2O$ (29 mg, ~0.1 mmol), VCl_3 (8 mg, ~0.05 mmol), 26-H_2ndc (21 mg, ~0.1 mmol), and tpab (13 mg, ~0.03 mmol) were dissolved in 3 g NMF. After stirring for 2 hours, the vial was placed in a 120 ℃ oven for 2 days. Dark-red hexagonal prisms were obtained after solution is cooled to ambient temperature.

CPM-704a (Co3-bpdc-tpa): In a 20 mL glass vial, $Co(NO_3)_2 \cdot 6H_2O$ (58 mg, ~0.2 mmol), VCl_3 (16 mg, ~0.1 mmol), bpdc (74 mg, ~0.3 mmol), and tpa (25 mg, ~0.1 mmol) were dissolved in 6 g NMF and 0.03 g HCl. After stirring for 2 hours, the vial was placed in a 120 ℃ oven for 4 days. microcrystalline plates were obtained after solution is cooled to ambient temperature.

CPM-734a (CoV-bpdc-tpa): In a 20 mL glass vial, $CoCl_2 \cdot 6H_2O$ (25 mg, ~0.1 mmol), VCl_3 (10 mg, ~0.05 mmol), bpdc (36 mg, ~0.15 mmol), and tpa (17 mg, ~0.1 mmol) were dissolved in 6 g DMA and 6 g EtOH, 0.5 g HBF_4 (48 w.t. %). After stirring for 2 hours, the vial was placed in a 100 ℃ oven for 4 days. Large hexagonal plates were obtained after solution is cooled to ambient temperature.

CPM-734b (CoV-bpdc-tpt) In a 20 mL glass vial, $Co(NO_3)_2 \cdot 6H_2O$ (58 mg, ~0.2 mmol), VCl_3 (16 mg, ~0.1 mmol), bpdc (74 mg, ~0.3 mmol), and tpt (31 mg, ~0.1 mmol) were

dissolved in 4 g DMF and 0.1 g HF. After stirring for 2 hours, the vial was placed in a 120 ℃ oven for 7 days. Orange-brown hexagonal plates were obtained after solution was cooled to ambient temperature. Microcrystalline material with impurities is obtained in absent of HF.

CPM-734d (CoV-bpdc-tpbtc): In a 20 mL glass vial, $Co(NO_3)_2 \cdot 6H_2O$ (58 mg, ~0.2 mmol), VCl_3 (16 mg, ~0.1 mmol), bpdc (74 mg, ~0.3 mmol), and tpbtc (45 mg, ~0.1 mmol) were dissolved in 6 g NMF. After stirring for 2 hours, the vial was placed in a 120 ℃ oven for 5 days. Orange-brown hexagonal plates are obtained after solution is cooled to ambient temperature.

CPM-234d (MgV-bpdc-tpbtc): In a 20 mL glass vial, $Mg(NO_3)_2 \cdot 6H_2O$ (50 mg, ~0.2 mmol), VCl_3 (16 mg, ~0.1 mmol), bpdc (74 mg, ~0.3 mmol), and tpbtc (45 mg, ~0.1 mmol) were dissolved in 6 g DMF. After stirring for 2 hours, the vial was placed in a 120 ℃ oven for 5 days. Light pink hexagonal plates were obtained after solution was cooled to ambient temperature.

CPM-834d (NiV-bpdc-tpbtc): In a 20 mL glass vial, $Ni(NO_3)_2 \cdot 6H_2O$ (60 mg, ~0.2 mmol), VCl_3 (16 mg, ~0.1 mmol), bpdc (74 mg, ~0.3 mmol), and tpbtc (45 mg, ~0.1 mmol) were dissolved in 6 g DMA. After stirring for 2 hours, the vial was placed in a 120 ℃ oven for 7 days. light-brown hexagonal plates were obtained after solution was cooled to ambient temperature.

CPM-734f (CoV-bpdc-tppa): In a 20 mL glass vial, $Co(NO_3)_2 \cdot 6H_2O$ (58 mg, ~0.2 mmol), VCl_3 (16 mg, ~0.1 mmol), bpdc (74 mg, ~0.3 mmol), and tppa (48 mg, ~0.1 mmol) were dissolved in 6 g NMF and 0.03 g HCl. After stirring for 2 hours, the vial was placed

in a 120 ℃ oven for 7 days. Hexagonal prisms were obtained after solution is cooled to ambient temperature.

CPM-734g (CoV-bpdc-tppb): In a 20 mL glass vial, $Co(NO_3)_2 \cdot 6H_2O$ (58 mg, ~0.2 mmol), VCl_3 (16 mg, ~0.1 mmol), bpdc (74 mg, ~0.3 mmol), and tppb (53 mg, ~0.1 mmol) were dissolved in 6 g DMA and 0.6 g HBF_4. After stirring for 2 hours, the vial was placed in a 120 ℃ oven for 3 days. Large hexagonal plates were obtained after solution is cooled to ambient temperature. Gas sorption was performed from material synthesized from NMF-DMPU-HFP solution (4:2:0.03 g).

CPM-735a (CoV-adc-tpa): In a 20 mL glass vial, $Co(NO_3)_2 \cdot 6H_2O$ (58 mg, ~0.2 mmol), VCl_3 (16 mg, ~0.1 mmol), adc (81 mg, ~0.3 mmol), and tpa (25 mg, ~0.1 mmol) were dissolved in 6 g DMA, 6 g EtOH and 0.6 g HBF_4. After stirring for 2 hours, the vial was placed in a 120 ℃ oven for 4 days. Red crystals were obtained after solution is cooled to ambient temperature.

CPM-735b (CoV-adc-tpt): In a 20 mL glass vial, $Co(NO_3)_2 \cdot 6H_2O$ (58 mg, 0.20 mmol), VCl_3 (16 mg, 0.10 mmol), H_2adc (81 mg, 0.30 mmol), and tpt (31 mg, 0.10 mmol) were dissolved in 6.0 g NMF and 0.06 g HCl (38 w.t. %). After stirring for 2 hours, the vial was placed in a 120 ℃ oven for 7 days. Dark-red hexagonal plates were isolated by sonication and filtration (yield: 40 % based on Co).

CPM-735d (CoV-adc-tpbtc): In a 20 mL glass vial, $Co(NO_3)_2 \cdot 6H_2O$ (58 mg, ~0.2 mmol), VCl_3 (16 mg, ~0.1 mmol), adc (81 mg, ~0.3 mmol), and tpbtc (45 mg, ~0.1 mmol) were dissolved in 6 g NMF. After stirring for 2 hours, the vial was placed in a 120 ℃ oven for

7 days. Red hexagonal plates were obtained after solution is cooled to ambient temperature.

CPM-735f (CoV-adc-tppa): In a 20 mL glass vial, $Co(NO_3)_2 \cdot 6H_2O$ (58 mg, ~0.2 mmol), VCl_3 (16 mg, ~0.1 mmol), adc (81 mg, ~0.3 mmol), and tppa (48 mg, ~0.1 mmol) were dissolved in 6 g NMF and 0.03 g HCl. After stirring for 2 hours, the vial was placed in a 120 ℃ oven for 3 days. Hexagonal prisms were obtained after solution is cooled to ambient temperature.

CPM-705g (Co-adc-tppb): In a 20 mL glass vial, $CoCl_2 \cdot 6H_2O$ (24 mg, ~0.1 mmol), adc (27 mg, ~0.1 mmol), and tppb (18 mg, ~0.03 mmol) were dissolved in 2 g DMA and 0.2 g HBF_4. After stirring for 2 hours, the vial was placed in a 120 ℃ oven for 3 days. Large hexagonal plates were obtained after solution is cooled to ambient temperature.

2.2.4 Property Characterization

Single-Crystal X-ray Diffraction (SCXRD). Characterization. The single-crystal X-ray diffraction measurements were performed on a Bruker diffractometer using graphite-monochromated MoKα (λ= 0.71073 Å) radiation at room temperature. Diffraction data were integrated and scaled by 'multi-scan' method with the Bruker APEX software. The structure was solved by direct methods and refined using SHELXTL.[5] SQUEEZE routine in PLATON software package was employed to fix solvents in lattice pores.[6] Crystal data, as well as details of data collection and refinements, are summarized in Table 2.1.

Powder X-ray Diffraction (PXRD). Powder X-ray diffraction experiments were performed on a PANalytical Empyrean Series 2 with CuKα radiation (40 kV, 40 mA, λ =

1.5418 Å). The data collection was performed at room temperature in the range from 5° to 40° with a step size of ~0.013°. Mercury 4.3.0 is used to simulate powder pattern from single crystal data.

Thermogravimetric (TG) Measurement. A TA Instruments TGA Q500 thermal analyzer was used to measure the TG curve by heating the sample from 30 ℃ to 800 ℃ with heating rate of 5℃/min under nitrogen flow. The flow rate of the nitrogen gas was controlled at about 60 milliliters per minute.

Energy dispersive spectroscopy (EDS). The semi-quantitative elemental analyses of different MOF samples were performed by using a FEI NNS450 field emission scanning electron microscope equipped with 50 mm^2 X-Max50 SDD energy dispersive spectroscopy (EDS) detector. Data acquisition was performed with an accelerating voltage of 15kV~20 kV and 60 s accumulation time.

Gas Sorption Measurement. Gas sorption measurements were carried out on a Micromeritics ASAP 2020 and ASAP 2020 Plus physisorption analyzers. Most as-synthesized samples were immersed in CH_2Cl_2 and refreshed daily for five consecutive times. The samples were then transferred to the gas sorption tube and the dried under open flow of N_2 gas for 15 minutes. The degas process was carried out at 60 ^oC for 12 hours. For CPM-736d (Co_2V-adc-tpbtc), material was immersed in 200 proof EtOH for 2 consecutive days, and refereshed every 8 hours. Afterward, sample was transferred to teflon cup, and underwent critical CO_2(l) exchange, with 30 minute purging, and 30 minute heating at 40 °C. Upon cooling, sample was immediately transferred to gas sorption tube and activated at 40 °C for another 6 hours.

Isosteric Heat of Adsorption (Q_{st}). The isosteric heats of adsorption for all the gases were calculated using the isotherms at 273 K and 298 K, following the Clausius-Clapeyron equation. It was done with the calculation program embedded in the software of ASAP 2020 plus. High accuracy of the Q_{st} was found in all the calculations as evidenced by the linearity in the isosteres.

Selectivity by IAST. To evaluate the C_3H_8/C_3H_6 separation performance, the selectivity was calculated by ideal adsorbed solution theory (IAST). Dual-site Langmuir Freundlich (DSLF) model was employed to fit the gas adsorption isotherms over the entire pressure range. DSLF model can be written as:

$$N = \frac{N_{sat,a} b_a p^{1/n_a}}{1+b_a p^{1/n_a}} + \frac{N_{sat,b} b_b p^{1/n_b}}{1+b_b p^{1/n_b}} \quad (1)$$

where N (mmol/g) is the amount adsorbed, p (mmol/g) is the pressure of bulk gas at equilibrium, N_{sat} (mmol/g) is the saturation loading, b (bar^{-1}) is the Langmuir affinity parameter and 1/n (dimensionless) is the index of heterogeneity. The "*a*" and "*b*" subscripts correspond to two different site identities. The R factors for all the fitting are higher than 99.9%. The detailed methodology for calculating the amount of A and B adsorption from a mixture by IAST is described elsewhere.[7] The adsorption selectivity is finally defined as:

$$S = \frac{q_A/q_B}{P_A/P_B} \quad (2)$$

where S is the IAST selectivity, q_i (i = A or B) is the mole fraction in the adsorbed phase and p_i is the mole fraction in the gas phase.

Separation Potential.[8] The separation potential (ΔQ) is a combined metric, which considers both uptake capacity and selectivity. It is defined to quantify mixture separations in fixed bed adsorbers. Based on IAST selectivity results, the gravimetric separation potential is calculated:

$$\Delta Q = q_{C3H8}\,\frac{b}{a} - q_{C3H6} \tag{3}$$

where a and b are v/v ratio in C_3H_8/C_3H_6 mixture and q_{C3H8} and q_{C3H6} are C_3H_8 and C_3H_6 uptakes in the IAST calculated mixture, respectively. For 50/50 mixture, the formula (3) can be simplified to:

$$\Delta Q = q_{C3H8} - q_{C3H6} \tag{4}$$

ΔQ is that it represents the maximum amount of pure C_3H_6 that can be recovered during the adsorption phase of fixed bed separation.

Breakthrough Experiment. Breakthrough experiments for the C_3H_8/C_3H_6 mixtures were performed in a homemade apparatus. Approximately 0.7346 g of the CH_2Cl_2-exchanged sample was placed in a stainless-steel adsorption column (inner dimensions 4×125 mm). The sample in the adsorption column was purged with heated argon gas (333 K) for 12 h at a flow rate of 100 mL/min to completely remove the solvent. After the activation was complete, the adsorption column was cooled to 298 K under an argon purge, followed by the introduction of a propane/propylene mixture (1:1 or 1:15, v/v). The raw mixed gas flow rate was maintained at constant 2 mL/min controlled by a mass flow controller. The purity of the eluted gas was monitored by gas chromatography with a thermal conductivity detector (GC-2014; Shimadzu).

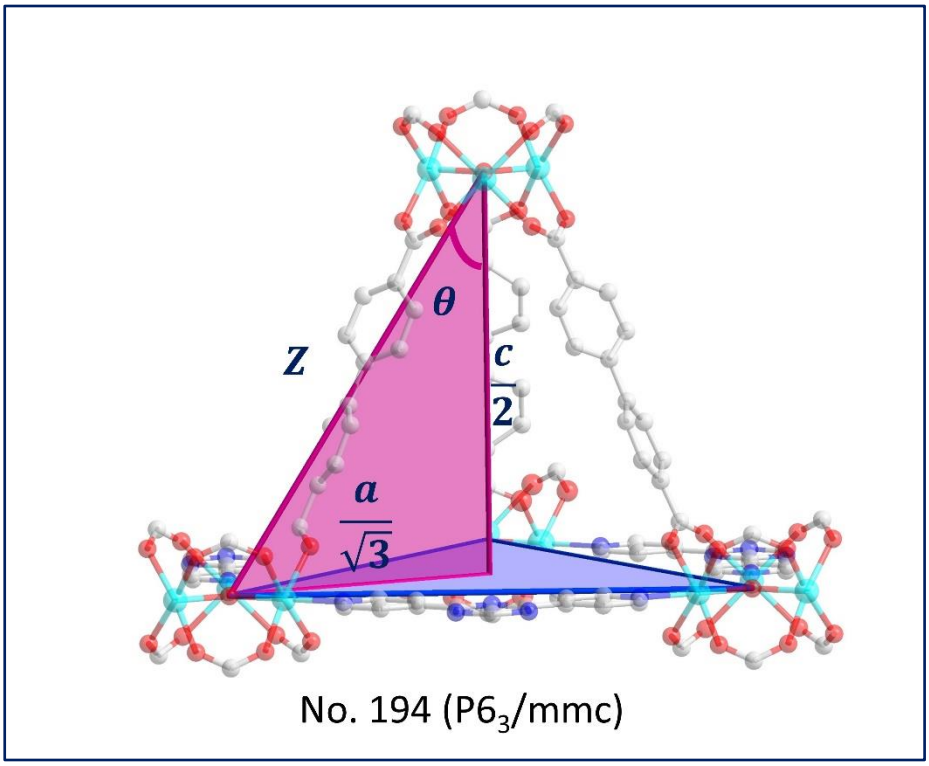

Figure 2.2 Triangular pyramid of the *pacs* platform, where a and c are a- and c-axes, respectively, θ represents degree of opening between L1 linker and height of pyramid, and Z represents the O---O length between two trimers connected by L1 linker.

2.3 Results and Discussions

2.3.1 Finding Limits to the "Swelling" of acs-net

The "swelling" for the underlying **acs**-net can be expressed by the angle (θ) of a right triangle that formed between L1 (hypothenuse, labeled Z) and pyramid's height (adjacent, $\frac{c-axis}{2}$). We can write a volume expression based on this θ to monitor the change of volume as a result of change in "swelling" degree. The volume expression:

$$V(\theta) = 3\sqrt{3Z^3(\sin(\theta))^2\cos(\theta)}\,; \qquad \theta > \arctan\left(\frac{360a}{c\pi\sqrt{3}}\right) \tag{5}$$

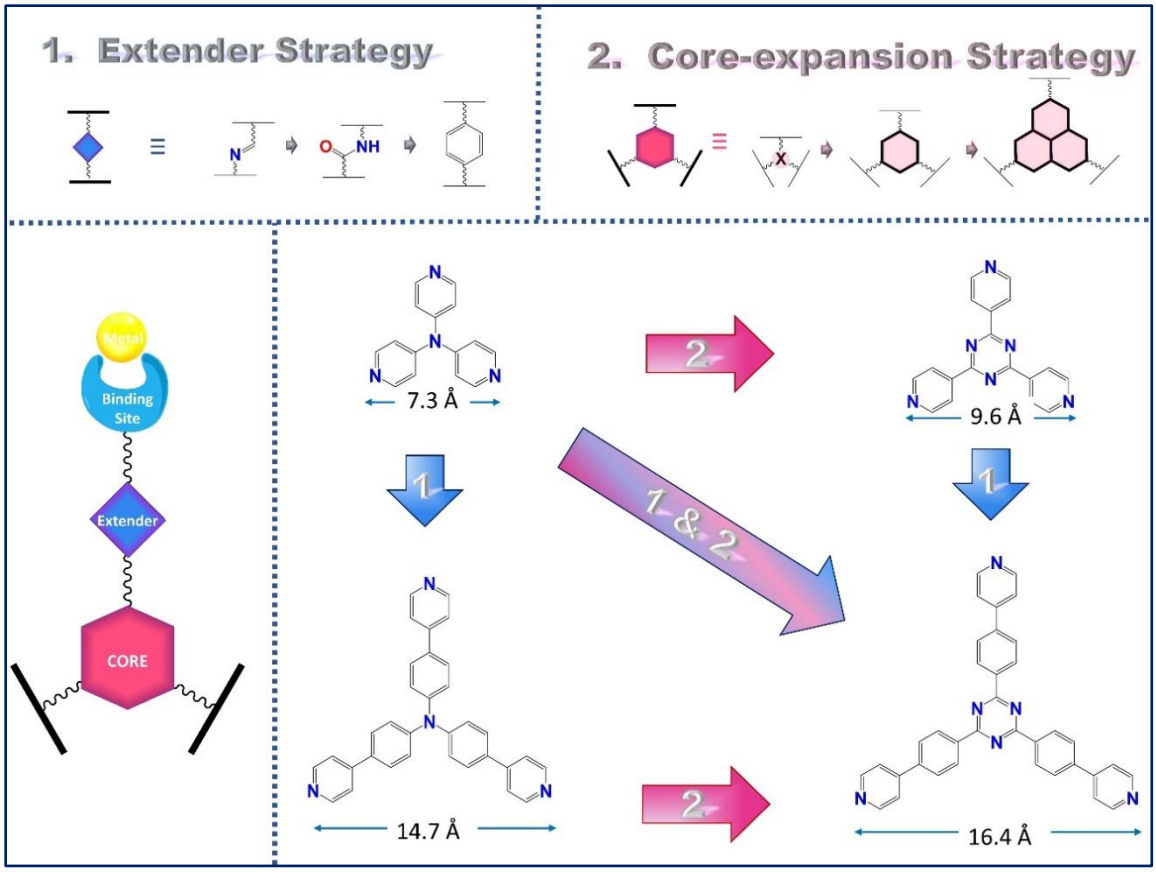

Figure 2.3 Ligand expansion through the "core" component versus "extender" component.

where "Z" could be calculated based on length of L1 or obtained directly from crystal-data. The minimum θ or minimum volume of the framework occurs when framework is closed, (i.e., dried framework without any solvent, pendent linkers or pore-partitioning agent). Such value could be approximated from unitcell of dried sample. Based upon this equation, the θ at which volume is the maximum is 54.5°, which corresponds to a c/a ratio = 0.817 and L2/L1 = $\sqrt{2}$. Finally, we are also interested in identifying the maximum θ, or the maximum allowable channel opening of the **acs**-net.

Figure 2.4 Potential L2 linkers identified from core expansion and extender strategies.

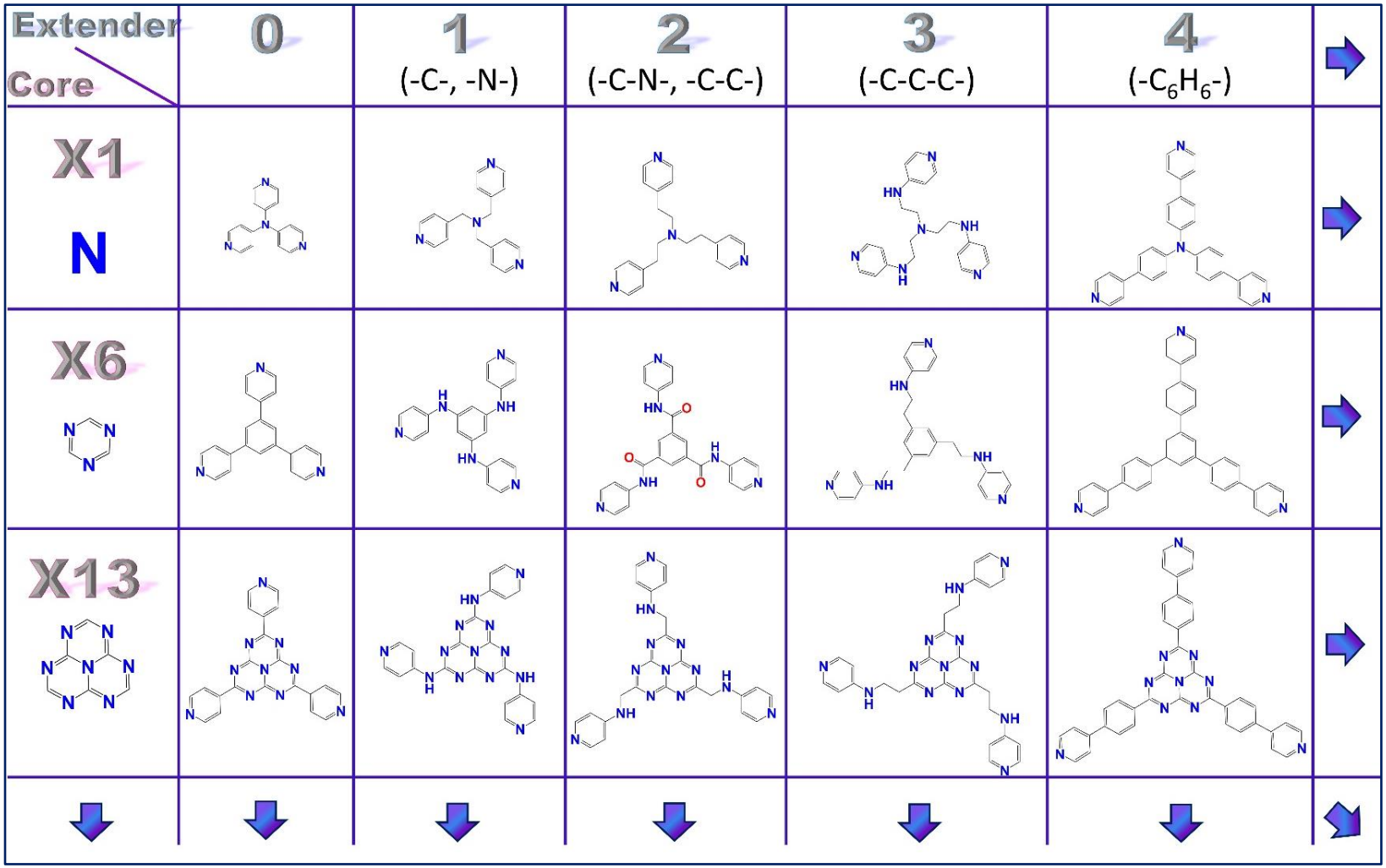

Figure 2.5 Single-crystal structures of pore-changing *pacs* platform through substitution of prototype *pacs* (26ndc-tpt) with short L1 (bdc-tpt), longer L1 (bpdc-tpt), shorter L2 (26ndc-tpa), longer L2 (26ndc-tpbtc), shorter L1 and L2 (bdc-tpa), longer L1 and L2 (bpdc-tpbtc).

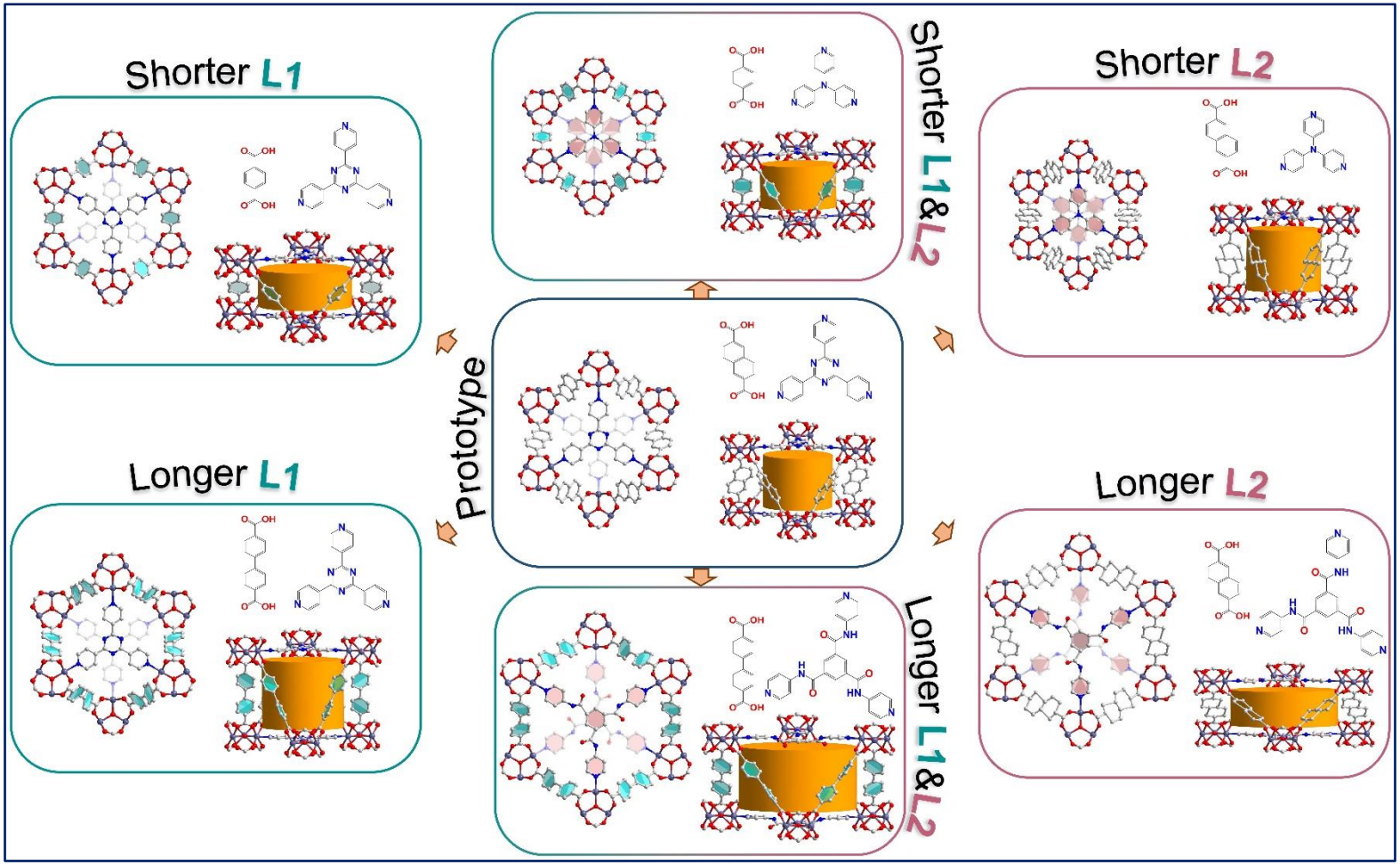

Table 2.1 Summary of unitcells of CoV-based *pacs* materials.

Co_xV_{3-x}	bdc (6.9 Å)	tba (8.4 Å)	26ndc (9.1 Å)	bpdc (11.2 Å)	adc (13.0 Å)
tpa (7.3 Å)	a: 14.50 Å c: 17.54 Å c/a: 1.21		a: 14.42 Å c: 16.8 Å c/a: 1.55		
tpt (9.6 Å)	a: 16.89 Å c: 14.94 Å c/a: 0.88	a: 16.78 Å c: 18.92 Å c/a: 1.12	a:16.80 Å c: 20.70Å c/a: 1.23	a: 16.81Å c: 25.69Å c/a: 1.53	a: 16.89 Å c: 30.15 Å c/a: 1.78
H-tph (11.9 Å)	a: 19.12 Å c: 11.19Å c/a: 0.59	a: 19.12Å c: 16.19Å c/a: 0.85	a: 19.14 Å c: 18.50 Å c/a: 0.97	a: 19.12Å c: 24.01Å c/a: 1.26	a: 19.4 Å c: 28.9 Å c/a: 1.5
tpbtc (13.7 Å)	MIL-88	a: 21.09 Å c: 13.37 Å c/a: 0.63	a: 20.92 Å c: 16.08 Å c/a: 0.77	a: 20.64 Å c: 22.05 Å c/a: 1.07	a: 20.83 Å c: 27.26 Å c/a: 1.31
tpab (14.0 Å)	N/A	MIL-88	a: 21.34 Å c: 15.37 Å c/a: 0.72		
tppa (14.7 Å)	N/A	N/A	Powder	a: 22.14 Å c: 21.45 Å c/a: 0.97	a: 22.4 Å c: 26.9 Å c/a: 1.2
tppb (16.4 Å)	N/A	N/A	N/A	a: 24.64 Å c: 17.96 Å c/a: 0.73	a: 24.45 Å c: 23.91 Å c/a: 0.98

*N/A: did not attempt to synthesize *pacs*.

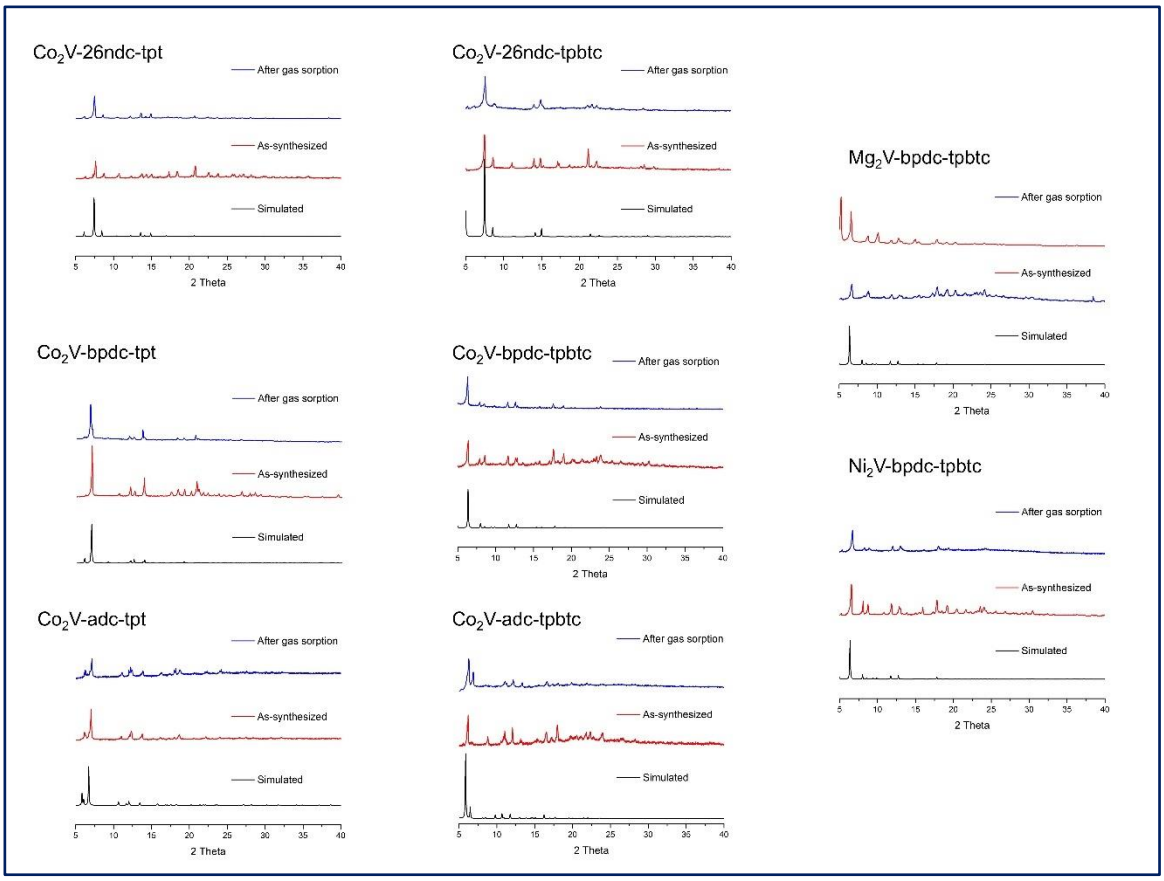

Figure 2.6 PXRD patterns of as synthesized and after gas sorption of *pacs* samples.

Figure 2.7 EDS analysis of *pacs* materials.

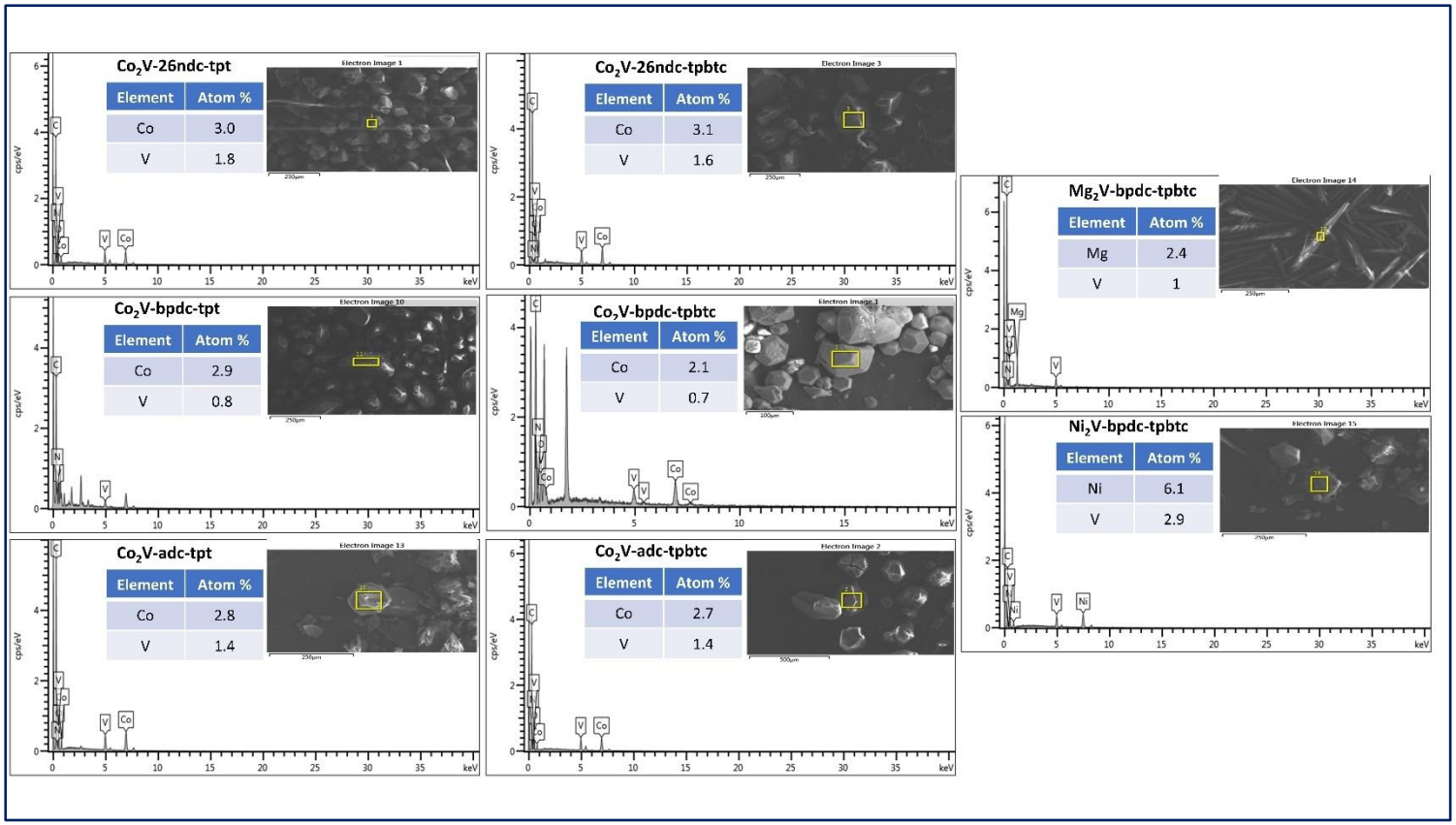

Figure 2.8 Thermal stability and porosity of *pacs* materials. (a,c,e) TGA pattern spectra, (b,d,f) N_2 isotherms at 77 K.

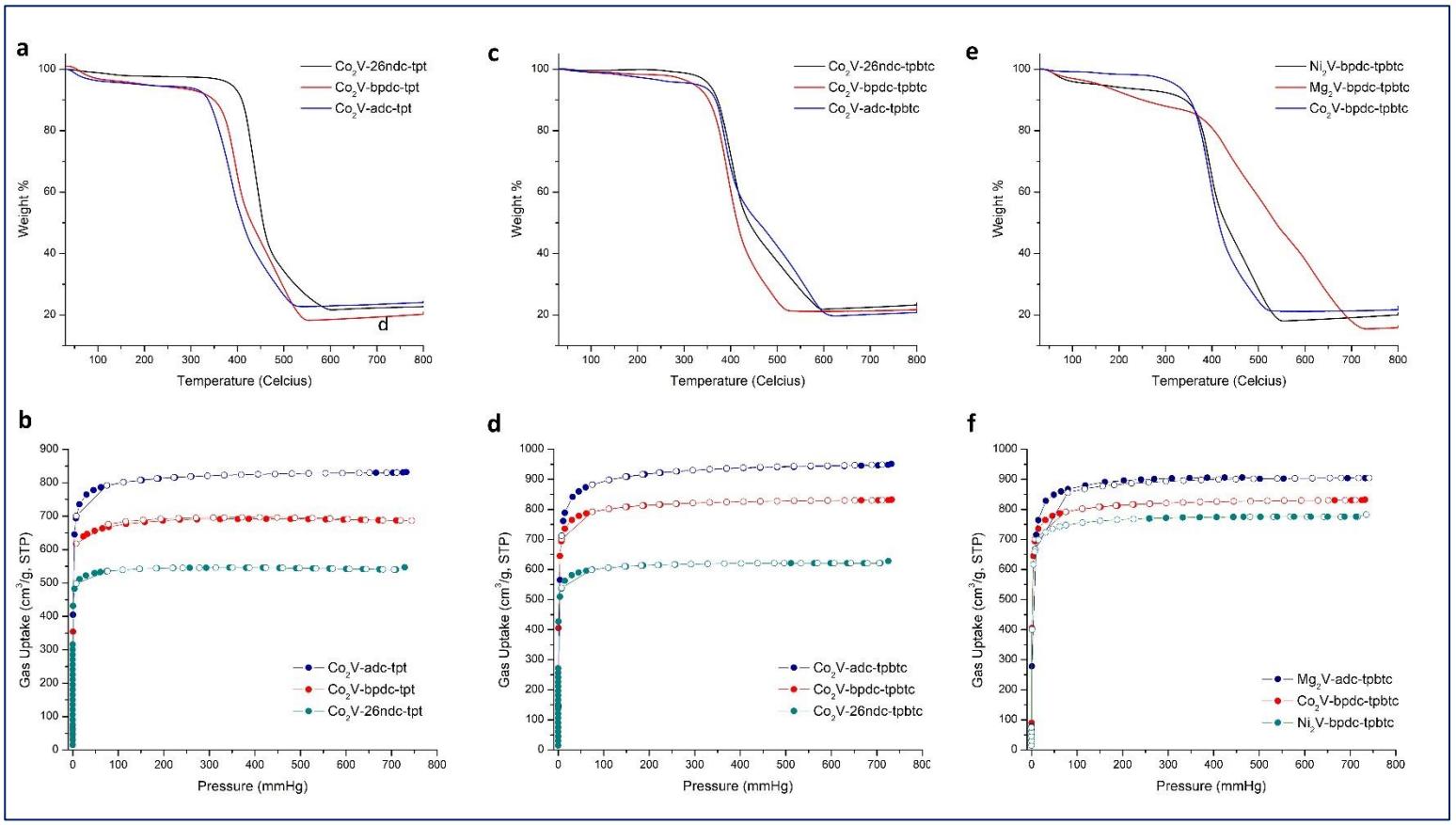

2.3.2 Correlating Theoretical Model to *pacs* Structures

Prior to *pacs* synthesis and unicell examination, we must acquire precursors of different lengths. In order to identify new potential linkers, we deconstruct prototype ligand into three parts: core, extender and peripheral. The extender connects the core to the peripheral binding site. In the case of lengthening linker only through core-expansion (e.g., amine to triazine) or extender strategy (e.g., amide to benzene), the tunable length would be very limited. In comparison, permutations of both compartments allow for much wider range of linkers of varied sizes (Figure 2.3). As shown in Figure 2.4, we indexed potential L2 precursors based upon permutations of both core-expansion strategy and extender strategy. With 3 different core and 5 extenders, 15 different L2 linkers of varied sizes could be constructed. Identification of new core and extender would further multiple the number of available L2 linkers.

With a new library of available linkers, the number of permutable pore shape and size of our *pacs* platform dramatically increase. For instance, the M_3-26ndc-tpt prototype could accommodate substitution of shorter L1 (M_3-14bdc-tpt), longer L1 (M_3-bpdc-tpt), shorter L2 (M_3-14bdc-tpa), longer L2 (M_3-26ndc-tpbtc), shorter L1 and L2 (M_3-14bdc-tpa), longer L1 and L2 (M_3-bpdc-tpbtc). Many combinations that were previously thought of, as impossible to achieve, are successfully synthesized herein.

In fact, we sought to outline the critical parameters in the design of *pacs* materials: the upper and lower limits of c/a ratio as well as c/a at which crystallographic volume is maximized. It is important to note that metals with very different ionic radii and bonding character could change c/a ratio by as much as 0.06 (c/a of M_3-bdc-tpt = 0.86 (Mn) and

0.92 (In)). We attempt to minimize the effect of c/a ratio by keeping metal source to CoV phase (Although in some cases, only pure Co_3 crystals could result in suitable crystal sizes).

In the first case, upper limit of c/a ratio is governed by length of L1 linker. The smallest observable a-axis is ~10 Å (closed form). Elongation of L1 linker would lengthen c-axis, resulting in enlargement of c/a ratio. For instance, both MIL-88b(Fe) and MIL-88d(Fe) have a-axis values at ~10 Å.[9] However, the shorter bdc^{2-} (6.9 Å) in MIL-88b(Fe) resulted in c-axis ~19.1 Å and c/a ratio ~1.98 while the longer $bpdc^{2-}$ (12.1 Å) in MIL-88d(Fe) resulted in c-axis of 27.6, and c/a ratio ~2.7. With maximum c/a ratio accredited to the "closed" **acs**-net, incorporation of any pore-partition agent would cause pore to open, and thus lower c/a ratio. As a result, accessing the upper limit of c/a ratio by *pacs* is not as important as finding the lower limit of c/a ratio.

The lower limit to c/a ratio is attributed to the largest allowable installation of L2 linker. Prior to the work, the lowest c/a ratio attained is 0.86 (Mn_3-bdc-tpt). Herein, we took the first leap and constructed CoV-26ndc-tpbtc with c/a = 0.77. Following this success, we gradually pushed the c/a limits to 0.72 with CoV-26ndc-tpab, and 0.63 with Co_3-tba-tpbtc. Successful crystallization and characterization of these materials prompted us to take another bold leap to 0.59 with Co_3-bdc-tph. At this extraordinarily low c/a ratio limit, both bdc^{2-} and H-tph linkers are highly disordered, with several carbon atoms being entirely out-of-plane. We also attempted to construct *pacs* from tba and tpab linkers (est. c/a ~ 0.58) without any success. Powder X-ray diffraction pattern of the phase constructed from tba-tpab combination show characteristic pattern of the **acs**-net. However, the

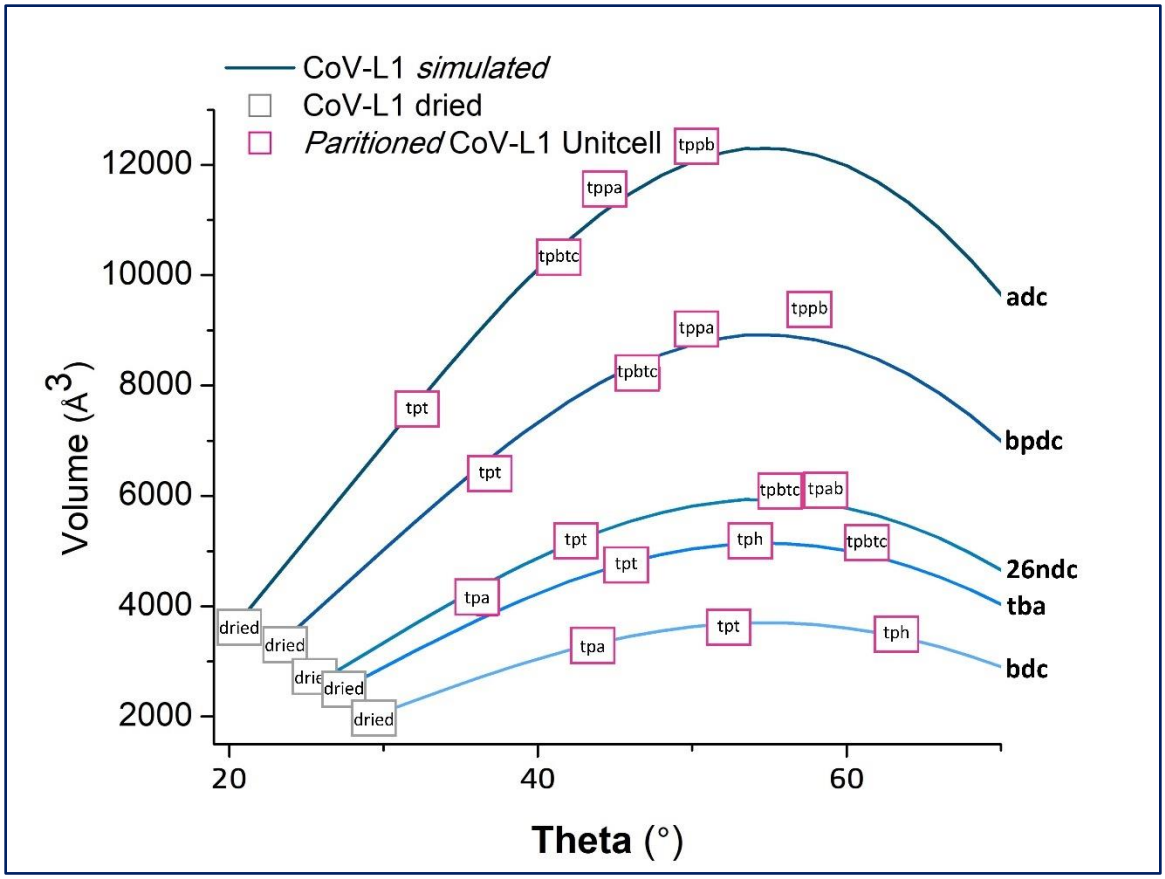

Figure 2.9 Simulated and experimental crystal volumes at different framework opening degree.

dramatic shifting of [101] peak to higher 2θ angle is indicative of smaller pore-opening as a result from absence of tpab pore-partitioning agent. Similar phenomenon were observed with bdc-tpbtc, and 26ndc-tppb combinations. We could conclude from crystal data that the maximum opening of **acs**-net for each L1 linker must be greater than c/a ratio of 0.59. For L1-L2 combinations that lead to ratio beyond this limit, only non-partitioned crystalline product could be constructed at best.

Finally, we were interested in determining the maximum volume for each L1 linker. As shown in Table 2.1 and Figure 2.5, for each L1 linker, substituting L2 of different sizes resulted in changes to crystallographic volume that are identical to our predictions. For

each framework constructed from the same L1, the maximum crystallographic volume belongs to *pacs* with c/a ratio closest to predicted 0.816, thus validating our mathematical calculations.

2.3.3 Volume Maximization for C_3H_6/C_2H_4 Separation

Knowledge of critical values in *pacs* design has proven to be highly useful in guiding us through reticular synthesis. The search for *pacs* with ideal pore size for C_3H_6/C_2H_4 separation is one prominent example exemplifying this power. Initial C_3H_6 sorption isotherms for Co_2V-26ndc-tpbtc, Co_2V-bpdc-tpbtc and Co_2V-adc-tpbtc at 298 K reveal uptake increases with increasing framework surface area and volume. Co_2V-26ndc-tpbtc with smallest BET surface area (1944 m^2/g) and pore volume (0.905 cm^3/g) also exhibits the lowest C_3H_6 uptake at 229.8 cm^3/g at 298 K, 1 bar. In comparison, Co_2V-adc-tpbtc, with largest BET surface area (2914 m^2/g) and pore volume (1.30 cm^3/g), has the highest C_3H_6 uptake at 311.1 cm^3/g at 298 K, 1 bar. C_2H_4 isotherms on the other hand, decreases with increasing surface area and volume: 26ndc (113.6 cm^3/g) > bpdc (59.1 cm^3/g) > adc (36.7 cm^3/g) at 298 K, 1 bar.

The increase of surface area and volume allows for better packing of the larger C_3H_6 molecule, but worse host-guest interaction with the smaller C_2H_4. Thus CoV-adc-tpbtc was expected to have the highest selectivity among the three adsorbents. However, 50/50 Ideal Adsorption Solution Theory (IAST) calculation shows Co_2V-adc-tpbtc with the lowest selectivity among the three adsorbents. A closer look at the isotherms shows that while all C_2H_4 isotherms exhibit similar linear graphs, C_3H_6 isotherms have very

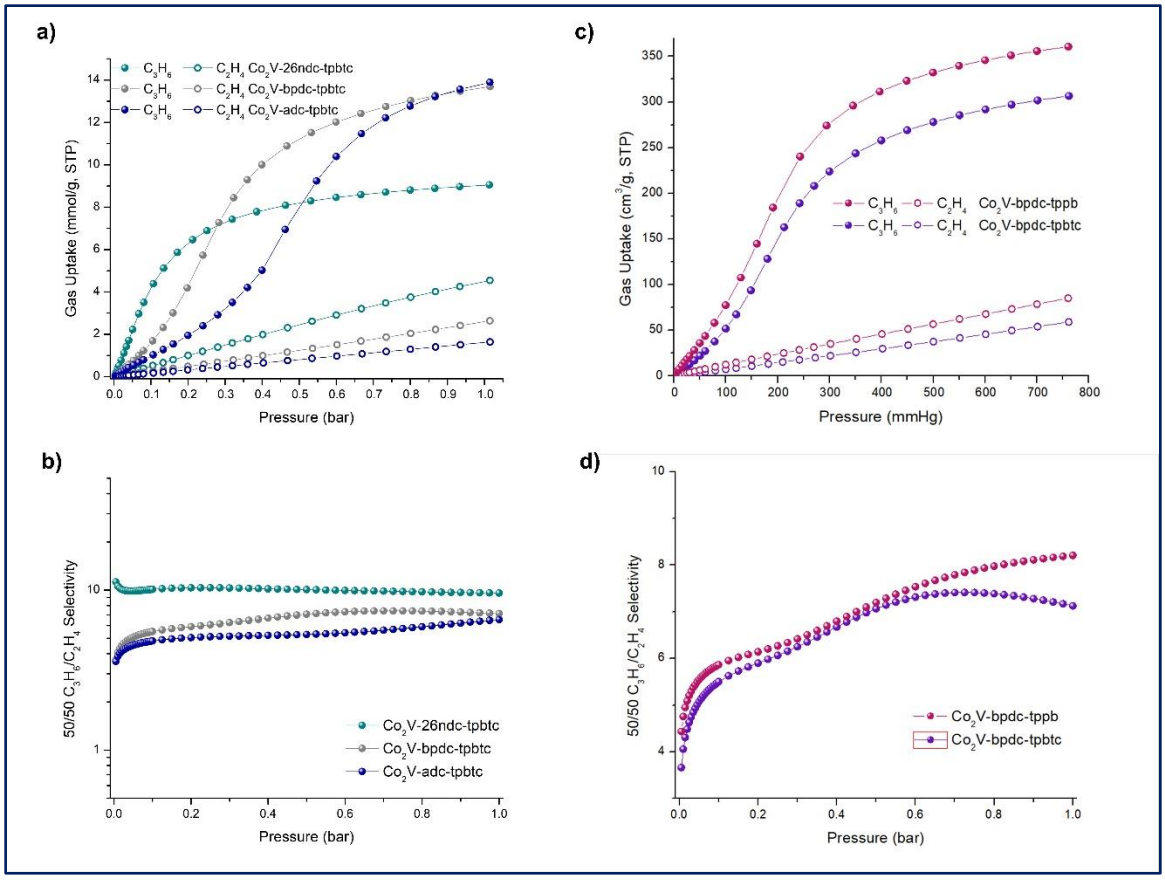

Figure 2.10 C_3H_6/C_2H_4 separation performances of *pacs*. (a) C_3H_6 and C_2H_4 isotherms and (b) 50/50 IAST selectivity of CoV-L1-tpbtc *pacs* at 298 K. (c) C_3H_6 and C_2H_4 isotherms and (b) 50/50 IAST selectivity of CoV-bpdc-L2 *pacs* at 298 K.

different shapes. As L1 linkers are elongated to result in larger pore area and volume, isotherm curves transformed from the typical type I graph to a sigmoidal shape. The sigmoidal curve represents low initial host-guest interaction until certain gate-opening pressure that allows for more sorption from both host-guest and guest-guest interactions. Sigmoidal curve with higher gate-opening pressure will have lower selectivity because the pressure range in which gas molecules cannot be discriminated will be much larger. Thus, Co_2V-26ndc-tpbtc, with the ability to discriminate C_3H_6 from C_2H_4 from very low-pressure region, had the highest selectivity. The potential to separate a gas mixture is dependent

upon both the uptake capacity and selectivity of the material. As such, Co_2V-bpdc-tpbtc is the best adsorbent for when measuring with separation potential.

To further enhance this performance, we turned our attention towards L2 optimization. The c/a ratio of Co_2V-bpdc-tpbtc is 1.06, or approximately 0.263 away from maximum volume. To enhance pore volume of bpdc-based framework, we chose Co_2V-bpdc-tppb (c/a = 0.73), the isostructure with c/a ratio closest to c/a at V_{max} ($\Delta_{c/a}$ = 0.087). True to our prediction, Co_2V-bpdc-tppb has BET surface area and volume greater than that of Co_2V-bpdc-tpbtc, allowing for higher C_3H_6 uptake of 360.6 cm^3/g at 298 K, 1 bar. Unlike substitution of L1 linkers, framework enlargement with L2 substitution does not change overall shape of C_3H_6 isotherm. As a result, IAST of Co_2V-bpdc-tppb does not decrease, allowing for overall separation potential to be the highest among *pacs* materials. It is worth noting that the separation potential of Co_2V-bpdc-tppb at 10.97 mmol/g is also higher than the previous record at 7.3 mmol/g from iso-MOF-4.[10]

2.3.4 Pore Expansion/Compression for C_3H_6/C_3H_6 Separation

From single-crystal X-ray diffraction, the framework in these *pacs* materials could be visualized as segmented hexagonal-shaped channels with isosceles triangular pore windows. To increase the height of each segment (along the c-axis) and triangular pore window, we substituted 2,6-ndc^{2-} with adc^{2-} linker. To enlarge the width of each segment and triangular pore window, we substituted tpt linker with tpbtc. An added benefit of this type of substitution strategy is that both adc^{2-} and tpbtc come with additional electronegative atoms (N and O) to potentially enhance hydrogen-bonding interactions.

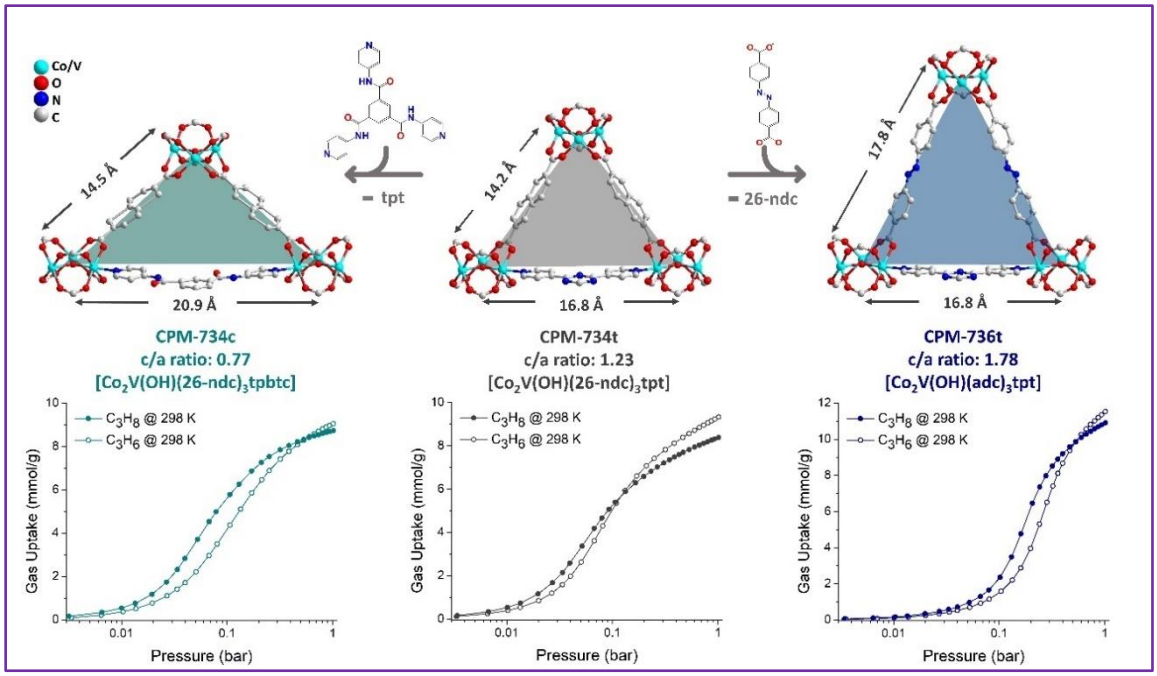

Figure 2.11 C_3H_6 and C_3H_8 isotherms of L1 or L2 substituted Co_2V-26ndc-tpt at 298 K. With C_3H_8 having more hydrogens than C_3H_6, a greater number of hydrogen-bonding becomes possible to increase the overall host-guest interaction.

Consistent with the ratio of the metal precursors in the starting synthesis mixtures, the Co^{2+} to V^{3+} heterometallic compositions in these *pacs* materials are approximately 2:1 ratio, as confirmed by EDS and single-crystal X-ray diffraction analyses. These materials are also highly stable. The Co_2V-adc-tpt is thermally stable up to 350 °C, while Co_2V-26ndc-tpt and Co_2V-26ndc-tpbtc are stable up to 400 °C. Structural integrities of these materials are maintained after repeated gas adsorption-desorption experiments. In particular, Co_2V-26ndc-tpt retains high crystallinity after a 24-hour immersion in water.

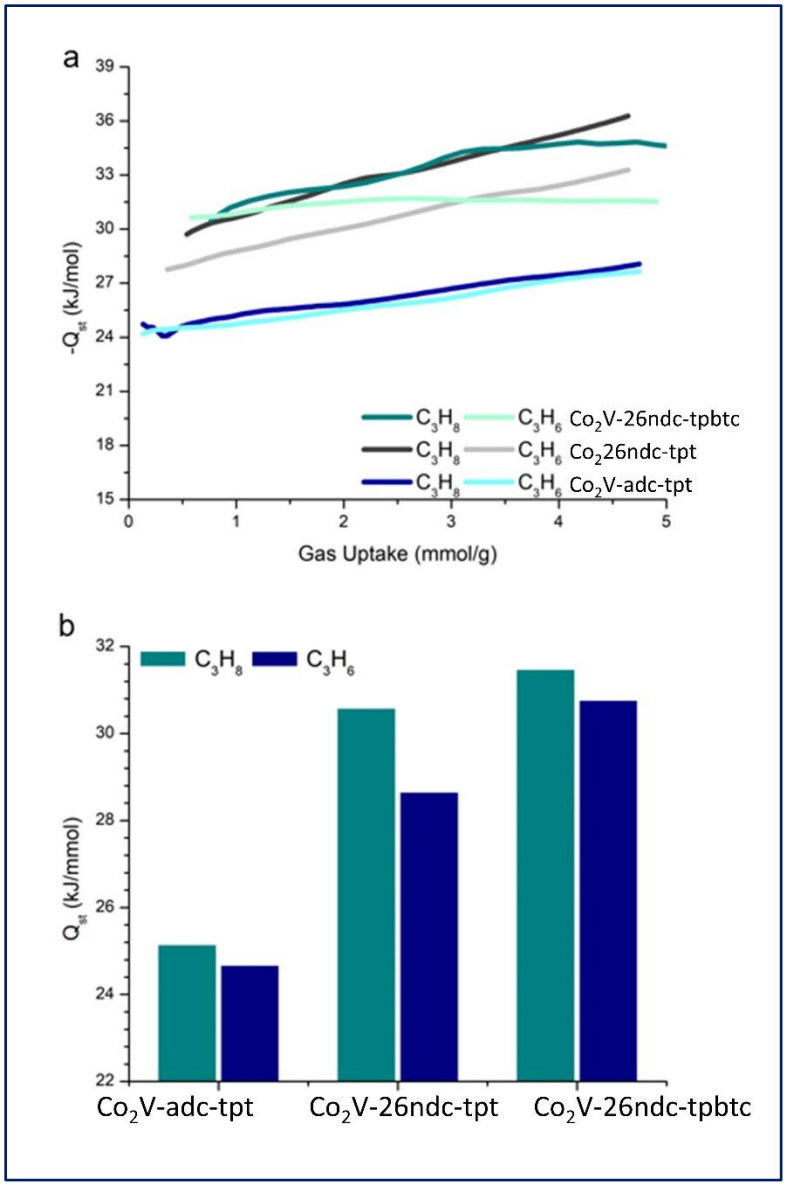

Figure 2.12 C_3H_8 and C_3H_6 heat of adsorption for *pacs* in this study. (a) Q_{st} curve from 0 to 5 mmol/g, (b) bar chart comparison of Q_{st} at 1 mmol/g.

Table 2.2 Summary of MOFs with C_3H_8 uptake.

MOFs	S_A BET (m^2/g)	Active Site	C_3H_8 uptake 298 K 1 bar (mmol/g)	C_3H_8 uptake 273K 1 bar (mmol/g)	Qst (kJ/mol)	Working Capacity (0.1 – 1bar)	Ref.
FJI-H23	3740	OMS	14.54	16.15	--	10.3	[11]
Co_2V-adc-tpt	**2087**	**PSP**	**10.9**	**12.7**	**25.2[c]**	**8.6**	**This work**
Iso-MOF-4	2925	OMS, π---H	10.75	11.99	30.9	7.4	[10]
UiO-67	1775	π---H	9.28	10.3	36	6.3	[12]
Zr-bipy	1605	π---H	8.21	9.77	31	5.4	[12]
HKUST	1650	OMS	7.72[a]	--	35	1.9	[13]
MgMOF-74	1668	OMS	7.24[b]	--	34.5	1.44	[14]
BUT-11	1233	π---H, SO_2	6.25	6.7	27	1.1	[12]
MOF-74(Fe)	1536	OMS	6.12	--	33	0.52	[15]
Zr-NDC	1178	π---H	5.35	6.07	32	2.45	[12]
CoMOF-74	1448	OMS	5.22	--	47	1.0	[14]
UiO-66	1014	π---H	3.94	5.04	33	1.48	[12]
Co_2(m-dobdc)	--	OMS	6.1[b]	--	49	1.25	[16]
MIL-101-SO3H	1856	OMS	3.8	--	30	2.95	[17]
MIL-101-SO3-Ag	1253	OMS	3.0	--	60	2.38	[17]
UPC-33	934	π---H	4.18	4.99	18.39	3.34	[18]
Cd2(AzDC)2(TPT)2](DMF)3	392	π system	2.71	2.92	40.77	1.2	[19]
$[Co_4(TC_4A)Cl](L)_2[(CH_3CH_2)_4N]\}n$	657	OMS, $(C_2H_5)_4N^+$	2.88	3.799	21.8	0.88	[20]
UPC-21	1725	OMS	4.60	5.19	--	1.2	[21]
MIL-100(Fe)	2266	OMS	4.04	--	--	3.40	[22]
Cu(0.6)@MIL-100(Fe)	1490	OMS, Cu^+	2.22	--	--	1.95	[22]
FJI-C1	1726	Et_4N^+	6.33	7.18	26.8	3.63	[23]
NKU-FlexMOF-1a	952	Electrostatic interaction	2.71	2.90	52.5	.187	[24]

[a] measured at 303 K, [b] measured at 296 K
[c] Q_{st} at 1 mmol, calculated from 298 and 273 K isotherms.

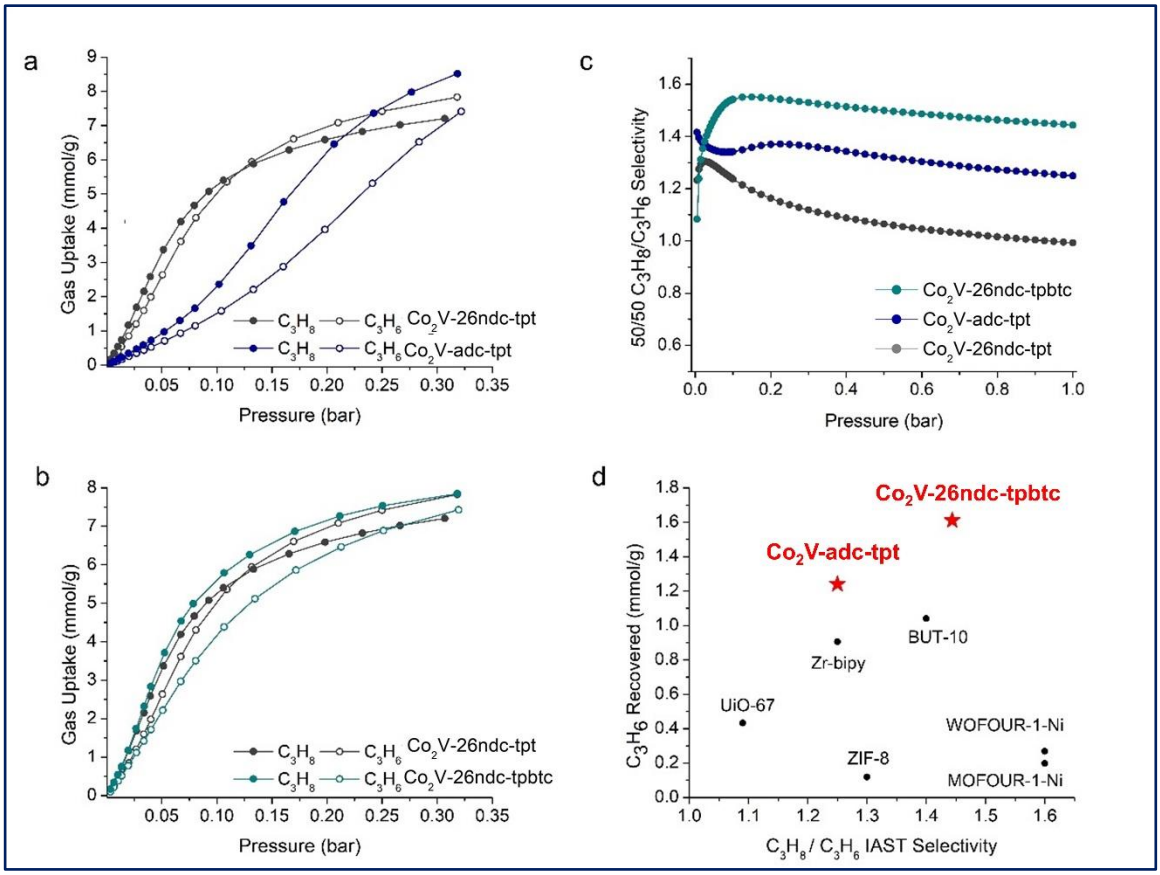

Figure 2.13 (a) C_3H_8 and C_3H_6 isotherm comparison of Co_2V-26ndc-tpt and Co_2V-adc-tpt (< 0.35 bar, 298 K). (b) C_3H_8 and C_3H_6 isotherm comparison of Co_2V-26ndc-tpt and Co_2V-26ndc-tpbtc (< 0.35 bar, 298 K). (c) The calculated C_3H_8/C_3H_6 (50:50) IAST selectivity of *pacs* materials at 298 K. (d) the potential C_3H_6 recovered as a function C_3H_8/C_3H_6 (50:50) IAST selectivity of all reported C_3H_8-selective MOF adsorbents at 298 K, 1 bar.

The permanent porosities of *pacs* materials are probed by N_2 gas sorption experiments at 77 K. All materials show type I N_2 adsorption isotherms. The Brunauer-Emmett-Teller (BET) surface area increases from 1727 m^2/g to 1944 m^2/g when tpt is replaced with tpbtc in Co_2V-2,6-ndc-based *pacs* and to 2087 m^2/g when 2,6-ndc^{2-} is replaced with adc^{2-} in Co_2V-tpt-based *pacs*. The corresponding pore volumes are 0.82, 0.91, and 1.07 cm^3/g for Co_2V-26ndc-tpt, Co_2V-26ndc-tpbtc and Co_2V-adc-tpt

respectively. In addition, NLDFT modeling gives pore size distribution primarily at 8.6 Å for Co_2V-26ndc-tpt, 9.3 Å for Co_2V-26ndc-tpbtc and 10.9 Å for Co_2V-adc-tpt. These pore apertures correspond closely to cavity sizes determined from crystal structures. It is worth noting that the substitution of a ditopic linker here results in much larger increase in the crystallographic unit cell volume (44.3% increase from 5060 $Å^3$ to 7302 $Å^3$) than the substitution of a tritopic linker (20.4% increase from 5060 $Å^3$ to 6093 $Å^3$). As a result, the surface area, pore volume, and pore aperture of Co_2V-adc-tpt are larger than Co_2V-26ndc-tpbtc.

Considering the permanent porosity and large cages in these crystalline porous materials, isotherms of C_3H_6 and C_3H_8 gases are then obtained at 273 K and 298 K. All three adsorbents exhibit excellent C_3H_8 adsorptions, with increase of capacity corresponding to enlargement of surface area and pore volume. As a result, Co_2V-26ndc-tpt, with the largest surface area and volume, shows the highest adsorption capacity of 10.9 mmol/g at 1 bar, 298 K among three materials reported here. To our knowledge, this is also the highest so far among MOFs reported to be C_3H_8-selective. Even if compared to all reported MOFs, the C_3H_8 uptake capacity of Co_2V-adc-tpt is outstanding. For comparison, the C_3H_8 adsorption capacity of well-known benchmark MOFs at 298 K, 1 bar are: iso-MOF-4 (10.7 mmol/g),[10] UiO-67 (9.3 mmol/g),[12] HKUST-1 (7.7 mmol/g),[13] and MgMOF-74 (7.2 mmol/g),[14] and FJI-H23 (14.5 mmol/g).[11]

All three adsorbents show higher C_3H_6 uptakes at 1 bar, likely due to more efficient packing of smaller C_3H_6 than C_3H_8 gas molecules, In the lower pressure region, the stronger host-guest interaction with larger gas molecule allows for higher C_3H_8 uptakes. The exact

position of crossover points and the difference between C_3H_8 and C_3H_6 uptake quantities are dependent on size and functionality of ditopic and tritopic ligands.

As shown in Figure 2.13, the isotherms of Co_2V-26ndc-tpt show higher C_3H_8 than C_3H_6 uptakes in pressure region below 0.1 bar, and no discrimination at 0.1 bar. In comparison, the adc substituted Co_2V-adc-tpt, with larger surface area and pore volume, shows delay in both C_3H_8 and C_3H_6 uptakes. The enlarged Co_2V-adc-tpt framework also exhibits C_3H_8 preference over a wider pressure region (up to 0.5 bar), and larger discrimination between C_3H_8 and C_3H_6, (uptake difference of 0.77 mmol/g at 0.1 bar, 298 K).

Whereas the gas uptake thresholds for both C_3H_6 and C_3H_8 curves in the adc substituted Co_2V-adc-tpt are shifted to higher pressure region than Co_2V-26ndc-tpt, only C_3H_6 gas threshold of the tpbtc substituted Co_2V-26ndc-tpbtc is shifted to higher pressure region than that of Co_2V-26ndc-tpt. The C_3H_8 isotherm of Co_2V-26ndc-tpbtc in low pressure region is steeper than that of Co_2V-26ndc-tpt. We speculate that the amide functional group in tpbtc may play a role in interacting with C_3H_8. Similar to Co_2V-adc-tpt, Co_2V-26ndc-tpbtc also exhibits selective C_3H_8 preference up to 0.5 bar, with C_3H_8 and C_3H_6 uptake difference of 1.4 mmol/g at 0.1 bar, 298 K.

The isosteric heat of adsorption (Q_{st}) is employed to confirm C_3H_8 binding preference. The C_3H_8 Q_{st} value at 1 mmol/g is highest for Co_2V-26ndc-tpbtc (31.5 kJ/mol), followed by Co_2V-26ndc-tpt (30.6 kJ/mol) and Co_2V-adc-tpt (25.19 kJ/mol). In comparison, the C_3H_6 Q_{st} value at 1 mmol/g is lower for Co_2V-26ndc-tpbtc (30.8 kJ/mol),

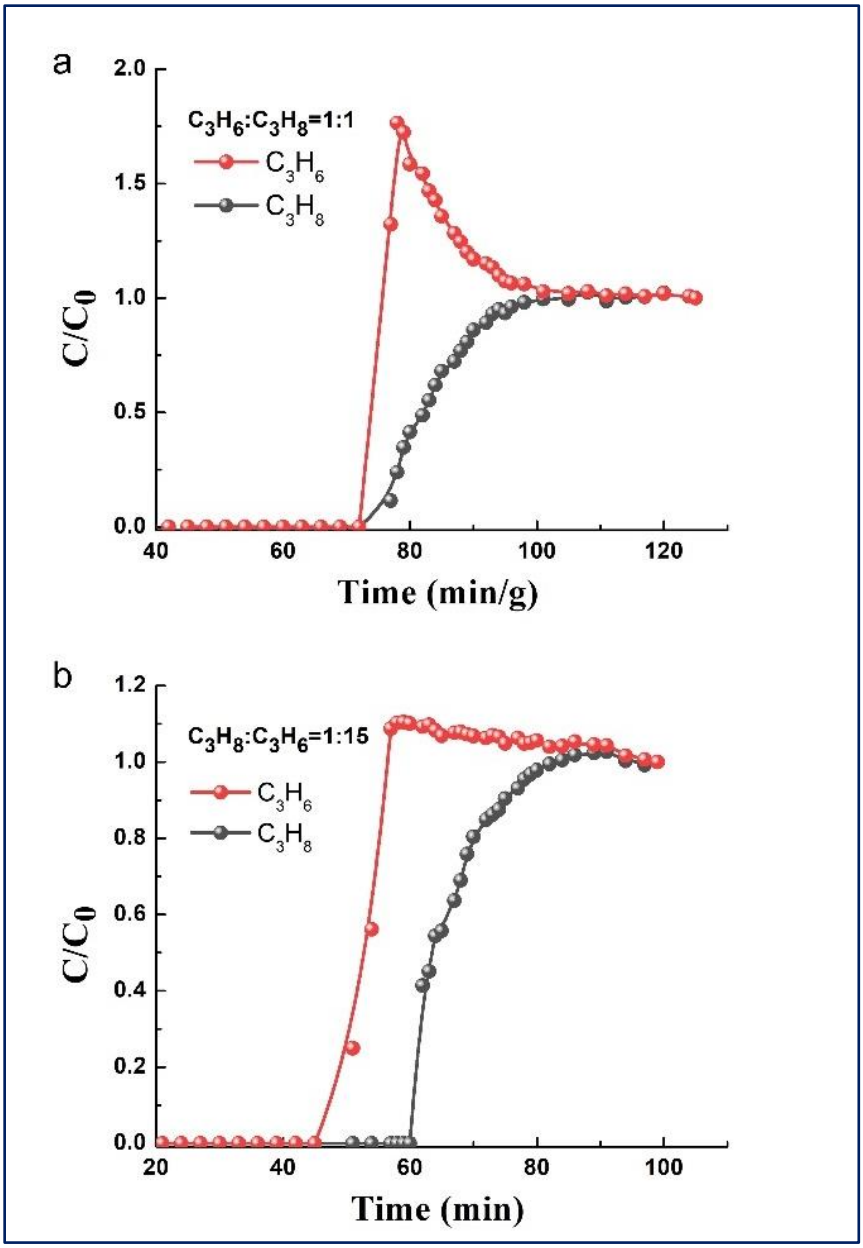

Figure 2.14 Breakthrough curves obtained for C_3H_8/C_3H_6 mixtures (a) 1:1, v/v and (b) 1:15, v/v with Co_2V-26ndc-tpbtc at 298 K.

Co_2V-26ndc-tpt (28.7 kJ/mol) and Co_2V-adc-tpt (24.7 kJ/mol). These results indicate that proper pore size optimization and addition of suitable functional groups could effectively enhance C_3H_8 adsorption capacity, thus potentially boosting separation performance.

We further explored the adsorption selectivity of the *pacs* adsorbents through dual-site Langmuir-Freundlich fitting of isotherms followed by IAST selectivity prediction. For 50:50 (v/v) C_3H_8/C_3H_6 gas mixture at 0.1 bar, 298 K, the calculated selectivity is 1.24 for Co_2V-26ndc-tpt. The C_3H_8/C_3H_6 selectivity decreases to below 1 (C_3H_6 selective) at 1 bar. In comparison, both Co_2V-26ndc-tpbtc and Co_2V-adc-tpt IAST selectivity are maintained between 1.54-1.44 and 1.34-1.24 for pressure between 0.1 and 1 bar, respectively. While these selectivity values are comparable to benchmarks WOFOUR-1-Ni (2.5-1.6),[25] ZIF-8 (1.4-1.3)[26] and BUT-10 (1.52-1.4),[27] the superior uptake capacity of Co_2V-26ndc-tpbtc and Co_2V-adc-tpt gives them an advantage in the overall separation performance.

As is well known that IAST selectivity alone cannot evaluate the separation performance. Thus, we employ the separation potential, a metric that is influenced by both adsorption capacity and selectivity, to estimate the maximum amount of pure C_3H_6 potentially recovered from the mixture. Although Co_2V-26ndc-tpbtc does not have the highest reported IAST selectivity, its highest C_3H_8 gas uptake among C_3H_8-selective materials allows it to have the highest potential C_3H_8 recovered from C_3H_8/C_3H_6 (50:50 v/v) mixture (Figure 2.13). The separation potentials of these adsorbents on the industrially relevant C_3H_8/C_3H_6 (1:15 v/v) mixture are also evaluated.

The C_3H_8 selectivity performance of Co_2V-26ndc-tpbtc has been experimentally evaluated through C_3H_8/C_3H_6 breakthrough experiments. For both 1:1 and 1:15 (v/v) C_3H_8/C_3H_6 mixed with inert argon gas eluted through the column packed with Co_2V-26ndc-tpbtc powder, the C_3H_6 is first detected while C_3H_8 is trapped in the adsorbent. The polymer-grade C_3H_6 (>99.99%) could be collected from C_3H_8/C_3H_6 (1:15 v/v) mixture

after several minutes of separation process. Multiple breakthrough cycles were also performed on Co_2V-26ndc-tpbtc. The maintenance of separation performance after several cycles confirms the reusability of this adsorbent.

2.4 Conclusion

In summary, we defined new limits to the *pacs* platform and sought to confirm these models with experimentally constructed frameworks. Many L1 and L2 combinations obtained here were previously thought of as impossible to form *pacs*. Pore size optimization of *pacs* materials also afforded excellent uptake capacity and selectivity for C_3H_6/C_2H_4 and C_3H_8/C_3H_6 separations. Overall, this work offers exciting results and new guidance on *pacs* platform to advance adsorbents for industrially relevant separations.

2.5 Reference

1. Eddaoudi, M.; Kim, J.; Rosi, N.; Vodak, D.; Wachter, J.; Keeffe, M.; Yaghi, O. M., Systematic Design of Pore Size and Functionality in Isoreticular Mofs and Their Application in Methane Storage. *Science* **2002,** *295*, 469-472.

2. Li, P.; Vermeulen Nicolaas, A.; Malliakas Christos, D.; Gómez-Gualdrón Diego, A.; Howarth Ashlee, J.; Mehdi, B. L.; Dohnalkova, A.; Browning Nigel, D.; O'Keeffe, M.; Farha Omar, K., Bottom-up Construction of a Superstructure in a Porous Uranium-Organic Crystal. *Science* **2017,** *356*, 624-627.

3. Zhao, X.; Bu, X.; Zhai, Q.-G.; Tran, H.; Feng, P., Pore Space Partition by Symmetry-Matching Regulated Ligand Insertion and Dramatic Tuning on Carbon Dioxide Uptake. *J. Am. Chem. Soc.* **2015,** *137*, 1396-1399.

4. Yakiyama, Y.; Ueda, A.; Morita, Y.; Kawano, M., Crystal Surface Mediated Structure Transformation of a Kinetic Framework Composed of Multi-Interactive Ligand Tphap and Co(Ii). *Chem. Commun.* **2012,** *48*, 10651-10653.

5. Sheldrick, G., A Short History of Shelx. *Acta Crystallogr. A* **2008,** *64*, 112-122.

6. Spek, A., Single-Crystal Structure Validation with the Program Platon. *J. Appl. Crystallogr.* **2003,** *36*, 7-13.

7. Myers, A. L.; Prausnitz, J. M., Thermodynamics of Mixed-Gas Adsorption. *AlChE J.* **1965,** *11*, 121-127.

8. Krishna, R., Screening Metal–Organic Frameworks for Mixture Separations in Fixed-Bed Adsorbers Using a Combined Selectivity/Capacity Metric. *RSC Adv.* **2017,** *7*, 35724-35737.

9. Horcajada, P.; Salles, F.; Wuttke, S.; Devic, T.; Heurtaux, D.; Maurin, G.; Vimont, A.; Daturi, M.; David, O.; Magnier, E.; Stock, N.; Filinchuk, Y.; Popov, D.; Riekel, C.; Férey, G.; Serre, C., How Linker's Modification Controls Swelling Properties of Highly Flexible Iron(Iii) Dicarboxylates Mil-88. *J. Am. Chem. Soc.* **2011,** *133*, 17839-17847.

10. Fan, W.; Wang, X.; Zhang, X.; Liu, X.; Wang, Y.; Kang, Z.; Dai, F.; Xu, B.; Wang, R.; Sun, D., Fine-Tuning the Pore Environment of the Microporous Cu-Mof for High Propylene Storage and Efficient Separation of Light Hydrocarbons. *ACS Cent. Sci.* **2019,** *5*, 1261-1268.

11. Huang, P.; Chen, C.; Hong, Z.; Pang, J.; Wu, M.; Jiang, F.; Hong, M., Azobenzene Decorated Nbo-Type Metal–Organic Framework for High-Capacity Storage of Energy Gases. *Inorg. Chem.* **2019,** *58*, 11983-11987.

12. Wang, X.; Li, L.; Wang, Y.; Li, J.-R.; Li, J., Exploiting the Pore Size and Functionalization Effects in Uio Topology Structures for the Separation of Light Hydrocarbons. *CrystEngComm* **2017,** *19*, 1729-1737.

13. Jiwoong Yoon; Intae Jang, L.; Kwan-Young; Youngkyu Hwang; Jang, J., Adsorptive Separation of Propylene and Propane on a Porous Metal-Organic Framework, Copper Trimesate. *Bull. Korean Chem. Soc.* **2010,** *31*, 220-223.

14. He, Y.; Krishna, R.; Chen, B., Metal–Organic Frameworks with Potential for Energy-Efficient Adsorptive Separation of Light Hydrocarbons. *Energy Environ. Sci.* **2012,** *5*, 9107-9120.

15. Bloch, E. D.; Queen, W. L.; Krishna, R.; Zadrozny, J. M.; Brown, C. M.; Long, J. R., Hydrocarbon Separations in a Metal-Organic Framework with Open Iron(Ii) Coordination Sites. *Science* **2012,** *335*, 1606-1610.

16. Bachman, J. E.; Kapelewski, M. T.; Reed, D. A.; Gonzalez, M. I.; Long, J. R., M2(M-Dobdc) (M = Mn, Fe, Co, Ni) Metal–Organic Frameworks as Highly Selective, High-Capacity Adsorbents for Olefin/Paraffin Separations. *J. Am. Chem. Soc.* **2017,** *139*, 15363-15370.

17. Chang, G.; Huang, M.; Su, Y.; Xing, H.; Su, B.; Zhang, Z.; Yang, Q.; Yang, Y.; Ren, Q.; Bao, Z.; Chen, B., Immobilization of Ag(I) into a Metal-Organic Framework with -So3h Sites for Highly Selective Olefin-Paraffin Separation at Room Temperature. *Chem. Commun.* **2015,** *51*, 2859-2862.

18. Fan, W.; Wang, Y.; Zhang, Q.; Kirchon, A.; Xiao, Z.; Zhang, L.; Dai, F.; Wang, R.; Sun, D., An Amino-Functionalized Metal-Organic Framework, Based on a Rare Ba12(Coo)18(No3)2 Cluster, for Efficient C3/C2/C1 Separation and Preferential Catalytic Performance. *Chem. Eur. J.* **2018,** *24*, 2137-2143.

19. Zhang, Y.; Meng, X.-Q.; Ding, H.-J.; Wang, X.; Yu, M.-H.; Zhang, S.-M.; Chang, Z.; Bu, X.-H., Rational Construction of Breathing Metal–Organic Frameworks through Synergy of a Stretchy Ligand and Highly Variable Π–Π Interaction. *ACS Appl. Mater. Interfaces* **2019,** *11*, 20995-21003.

20. Geng, D.; Zhang, M.; Hang, X.; Xie, W.; Qin, Y.; Li, Q.; Bi, Y.; Zheng, Z., A 2d Metal–Thiacalix[4]Arene Porous Coordination Polymer with 1d Channels: Gas Absorption/Separation and Frequency Response. *Dalton Trans.* **2018,** *47*, 9008-9013.

21. Zhang, M.; Xin, X.; Xiao, Z.; Wang, R.; Zhang, L.; Sun, D., A Multi-Aromatic Hydrocarbon Unit Induced Hydrophobic Metal–Organic Framework for Efficient C2/C1 Hydrocarbon and Oil/Water Separation. *J. Mater. Chem. A* **2017,** *5*, 1168-1175.

22. Kim, A.-R.; Yoon, T.-U.; Kim, E.-J.; Yoon, J. W.; Kim, S.-Y.; Yoon, J. W.; Hwang, Y. K.; Chang, J.-S.; Bae, Y.-S., Facile Loading of Cu(I) in Mil-100(Fe) through Redox-Active Fe(Ii) Sites and Remarkable Propylene/Propane Separation Performance. *Chem. Eng. J.* **2018,** *331*, 777-784.

23. Huang, Y.; Lin, Z.; Fu, H.; Wang, F.; Shen, M.; Wang, X.; Cao, R., Porous Anionic Indium–Organic Framework with Enhanced Gas and Vapor Adsorption and Separation Ability. *ChemSusChem* **2014,** *7*, 2647-2653.

24. Yu, M.-H.; Space, B.; Franz, D.; Zhou, W.; He, C.; Li, L.; Krishna, R.; Chang, Z.; Li, W.; Hu, T.-L.; Bu, X.-H., Enhanced Gas Uptake in a Microporous Metal–Organic Framework Via a Sorbate Induced-Fit Mechanism. *J. Am. Chem. Soc.* **2019,** *141*, 17703-17712.

25. Yang, L.; Cui, X.; Ding, Q.; Wang, Q.; Jin, A.; Ge, L.; Xing, H., Polycatenated Molecular Cage-Based Propane Trap for Propylene Purification with Recorded Selectivity. *ACS Appl. Mater. Interfaces* **2019,** *12*, 2525–2530.

26. Böhme, U.; Barth, B.; Paula, C.; Kuhnt, A.; Schwieger, W.; Mundstock, A.; Caro, J.; Hartmann, M., Ethene/Ethane and Propene/Propane Separation Via the Olefin and Paraffin Selective Metal–Organic Framework Adsorbents Cpo-27 and Zif-8. *Langmuir : the ACS journal of surfaces and colloids* **2013,** *29*, 8592-8600.

27. He, C.; Wang, Y.; Chen, Y.; Wang, X.; Yang, J.; Li, L.; Li, J., Modification of the Pore Environment in Uio-Type Metal-Organic Framework toward Boosting the Separation of Propane/Propylene. *Chem. Eng. J.* **2021,** *403*, 126428.

Chapter 3: The Robust and Versatile Anionic Partitioned-*acs* Frameworks

3.1 Introduction

Anionic metal-organic frameworks (MOFs), similar to zeolites with negative frameworks, represent only a minute fraction of MOFs that are typically neutral.[1] The availability of stable and tunable anionic MOFs can enable new applications in sorption,[2-4] ion exchange,[5-6] etc.[7-14]. Currently, few systematical strategies are available to construct and tune anionic MOFs.[15-17] Even in systems that can accommodate host-guest modification, the degree of tunability is limited, and the reduction in porosity and stability is often taken as a necessary tradeoff.[18-22] Hence, the development of methods to systematically construct stable anionic MOFs with a wide degree of tunability poses a significant challenge.

The neutral 9-connected *pacs* system has proven be an ultra-tunable platform, capable of setting performance records in many applications. The different combinations of these modules allows *pacs* materials to be incredibly versatile, and hence, capable of setting performance records in applications.[23-29] It has been shown that anionic *pacs* materials can be made from all-M^{2+} ions to give negative trimer $[(M^{2+})_3(\mu_3\text{-OH})(COO^-)_6]$, whereas the inclusion of M^{3+} could turn the framework neutral or cationic.[25, 30-31] Given the possibility for 3d-metals to adopt both M^{2+} and M^{3+}, only some metal types (e.g., Mg^{2+},

Zn^{2+}) could guarantee anionic trimer, which poses two major problems: stability and versatility. First, ligand-field stabilization energy plays no roles in stabilizing M—O or M—N bonds (M=Mg/Zn). Consequently, these trimers are more prone to ligand exchange (water degradation in particular). Additionally, the synthesis using all-M^{2+} trimers eliminates many benefits from other metal types or heterometal chemistry (e.g., Co-V). Thus, the metal-node-based strategy to develop anionic *pacs* dramatically limits the true potential of the *pacs* platform.

By taking advantage of highly modular features of the *pacs* platform where the charge property of each module can be independently engineered and allocated, we envision a method for creating anionic MOFs by shifting negative charges from hydrolysis-prone metal nodes to chemically resistant core of pore partition ligands. This method permits much more freedom in metal choices and also makes it possible to increase the metal-ligand bond strength by harnessing desirable properties of diverse metal types beyond d^0 and d^{10} M^{2+} ions.

This work marks the introduction of the first negatively charged organic pore partition ligand, 2,5,8-tri-(4-pyridyl)-1,3,4,6,7,9-hexaazaphenalene (H-tph). The tripyridyl

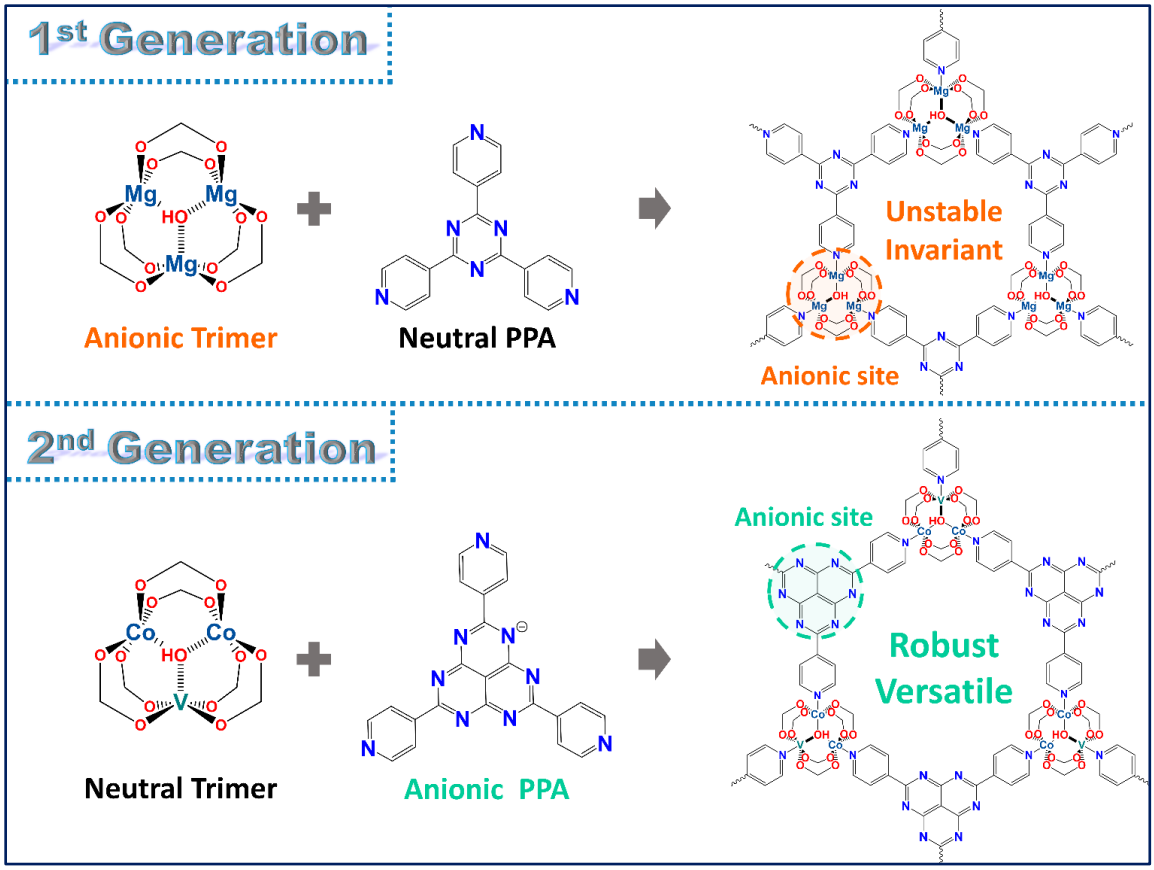

Figure 3.1 Comparison between first and second generation designs of anionic *pacs* materials.

linker has an acidic N-rich hexaazaphenalene (hap) core that readily resonance-stabilizes the deprotonated form. By shifting negative charge to hexaazaphenalene core of PPA, the inorganic node could accommodate both anionic and neutral metal variations, leaving much room for property optimization. Versatility of the 2nd generation anionic *pacs* platform was further demonstrated through systematic variations of trimer (anionic and neutral), ditopic linker (dicarboxylates, diazolates, mixed carboxylate-azolate) and counter balancing cations (quaternary ammonium or phosphonium ion with alkyl, hydroxyl and/or aromatic groups). The high compatibility of H-tph with various *pacs* modules (M_3-L1-G1)

results in a large library of robust anionic materials of varied size, shape and functionality. These examples show great potential to develop robust and versatile anionic MOFs with optimized host-guest recognition for selective gas and vapor sorption.

3.2 Experimental Section

3.2.1 Chemicals and Materials.

All reagents were used as received without further purification. Vanadium (III) chloride (VCl_3) was purchased from ACROS Organics. Iron (III) chloride hexahydrate ($FeCl_3 \cdot 6H_2O$), Magnesium nitrate hexahydrate ($Mg(NO_3)_2 \cdot 6H_2O$), Cobalt (II) chloride tetrahydrate ($CoCl_2 \cdot 4H_2O$), Cobalt (II) nitrate hexahydrate ($Co(NO_3)_2 \cdot 6H_2O$), Nickel (II) nitrate hexahydrate ($Ni(NO_3)_2 \cdot 6H_2O$), Nickel (II) chloride tetrahydrate ($NiCl_2 \cdot 4H_2O$), Zinc nitrate hexahydrate ($Zn(NO_3)_2 \cdot 6H_2O$), acetone, methanol (MeOH), ethanol (EtOH), benzene (Bn), cyclohexane (Ch), N,N-dimethylacetamide (DMA), N,N-dimethylformamide (DMF), dichloromethane (CH_2Cl_2), 1,1,1,5,5,5-hexafluoro-2,4-pentanedione (HFP), trifluoroacetic acid (TFA), fluoroboric acid 48 w.t. % (HBF_4) and hydrochloric acid 38 w.t. % (HCl) were purchased from Fischer Scientific Co., N-methylformamide (NMF), 4-pyridylamidine hydrochloride, sodium tricyanomethanide ($Na(C(CN)_3)$), 2,6-naphthalenedicarboxylic acid (2,6-H_2ndc), 4,4'-biphenyldicarboxylic acid (H_2bpdc), 1,3-dimethyl 3,4,5,6-tetrahydro-2(1H)-pyrimidinone (DMPU) were obtained from TCI-America while 4-(1H-tetrazol-5-yl)benzoic acid (H_2tba) and 1,4-benzeneditetrazole (H_2bdt) were purchased from Yanshen Technology Co., Ltd. All deuterated solvents were obtained from Cambridge Isotope Laboratories, Inc. and Sigma

Aldrich American Co. All ammonium and phosphonium salts (tetraethylammonium chloride (Et_4NCl), tetrapropylammonium chloride (Pr_4NCl), tetrabutylammonium chloride (Bu_4NCl), tetrapentylammonium chloride (Pen_4NCl), tetrahexylammonium chloride (Hex_4NCl), (2-hydroxyethyl)trimethylammonium chloride (htmNCl), bis(2-hydroxyethyl)dimethylammonium chloride (dhdmNCl), tetraphenylphosphonium bromide (Ph_4PBr) were obtained from Aldrich American Co.

3.2.2 Synthesis of Acid and Base Forms of Pore-Partitioning Agent.

2,5,8-tri-(4-pyridyl)-1,3,4,6,7,9-hexaazaphenalene (H-tph): The hexaazaphenalene condensation reaction was carried out according to ref [32] with modification. $NaC(CN)_3$ (0.750 g, 6.6 mmol) and pyridine-4-amidine hydrochloride (4.50 g, 28 mmol) were briefly mixed in a teflon-lined stainless steel autoclave before being heated to 200 °C overnight. After allowing vessel to cool to ambient temperature, 10 w.t. % HCl solution was added to dissolve the crude product. After filtering undissolved particulates, the solution was neutralized with acetone, and isolated. The dissolution in HCl and neutralization in acetone were repeated a second time. The product was isolated and dried overnight under vacuum at 60 °C to obtain the final light tan powder (50 %). ^{1}H NMR d_6-DMSO: 8.69 (d), 9.01 (d).

Sodium 2,5,8-tri-(4-pyridyl)-1,3,4,6,7,9-hexaazaphenalenate (Na-tph): Synthesis process was similar to H-tph, except 6M NaOH aqueous solution employed instead of acetone. ^{1}H NMR d_6-DMSO: 8.40 (d), 8.80 (d).

3.2.3 Synthesis of tph-based *pacs.*

CPM-600a-CoV (CoV-tba-tph): In a 20 mL glass vial, $CoCl_2 \cdot 6H_2O$ (76 mg, 0.3 mmol), VCl_3 (16 mg, 0.1 mmol), H_2tba (57 mg, 0.3 mmol), and H-tph (42 mg, ~0.1 mmol) were dissolved in 6.0 g NMF. After stirring for 2 hours, the vial was placed in a 120 ℃ oven for 5 days. Red-orange hexagonal shaped crystals were obtained after solution was cooled to ambient temperature.

CPM-600b-Mg (Mg_3-26ndc-tph): In a 20 mL glass vial, $Mg(NO_3)_2 \cdot 6H_2O$ (75 mg, 0.3 mmol), 26-H_2ndc (65 mg, 0.3 mmol), and H-tph (42 mg, ~0.1 mmol) were dissolved in 4.0 g DMA, 2.0 g DMPU and 0.06 g HFP. After stirring for 2 hours, the vial was placed in a 130 ℃ oven for 5 days. Large, clear hexagonal prisms were obtained after solution was cooled to ambient temperature.

CPM-600b-Co (Co_3-26ndc-tph): In a 20 mL glass vial, $CoCl_2 \cdot 6H_2O$ (76 mg, 0.3 mmol), 26-H_2ndc (65 mg, 0.3 mmol), and H-tph (42 mg, ~0.1 mmol) were dissolved in 6.0 g DMA and 1.2 g HBF_4 (48 w.t. %). After stirring for 2 hours, the vial was placed in a 120 ℃ oven for 5 days. Pink hexagonal shaped crystals were obtained after solution was cooled to ambient temperature.

CPM-600b-Zn (Zn_3-26ndc-tph): In a 20 mL glass vial, $Zn(NO_3)_2 \cdot 6H_2O$ (90 mg, 0.3 mmol), 26-H_2ndc (65 mg, 0.3 mmol), and H-tph (42 mg, ~0.1 mmol) were dissolved in 4.0 g DMA, 2.0 g DMPU and 0.06 g HFP. After stirring for 2 hours, the vial was placed in a 130 ℃ oven for 5 days. Large, clear hexagonal prisms were obtained after solution was cooled to ambient temperature.

CPM-600b-CoV (Co_2V-26ndc-tph): In a 20 mL glass vial, $Co(NO_3)_2 \cdot 6H_2O$ (58 mg, 0.2 mmol), VCl_3 (16 mg, 0.1 mmol), 26-H_2ndc (65 mg, 0.3 mmol), and H-tph (42 mg, ~0.1 mmol) were dissolved in 6.0 g DEF and 1 drop HCl (36 w.t.%). After stirring for 2 hours, the vial was placed in a 120 ℃ oven for 5 days. Dark-red hexagonal shaped crystals were obtained after solution was cooled to ambient temperature.

CPM-600b-CoFe (Co_2Fe-26ndc-tph): In a 23 mL teflon cup, $Co(NO_3)_2 \cdot 6H_2O$ (58 mg, 0.2 mmol), $FeCl_3 \cdot 6H_2O$ (27 mg, 0.1 mmol), 26-H_2ndc (65 mg, 0.3 mmol), and H-tph (42 mg, ~0.1 mmol were dissolved in 6.0 g DMA and 0.6 g TFA. After stirring for 2 hours, the teflon cup was sealed in an autoclave and placed in a 150 ℃ oven for 2 days. Brown powder was obtained after solution was cooled to ambient temperature.

CPM-600b-NiFe (Ni_2Fe-26ndc-tph): In a 23 mL teflon cup, $Ni(NO_3)_2 \cdot 6H_2O$ (60 mg, 0.2 mmol), $FeCl_3 \cdot 6H_2O$ (27 mg, 0.1 mmol), 26-H_2ndc (65 mg, 0.3 mmol), and H-tph (42 mg, ~0.1 mmol) were dissolved in 6.0 g DMA and 0.6 g TFA. After stirring for 2 hours, the teflon cup was sealed in an autoclave and 150 ℃ oven for 2 days. Yellow-green powder was obtained after solution was cooled to ambient temperature.

CPM-600c-Co (Co_3-bdt-tph): In a 20 mL glass vial, $CoCl_2 \cdot 6H_2O$ (50 mg, 0.2 mmol), VCl_3 (16 mg, 0.1 mmol), H_2bdt (64 mg, 0.3 mmol), and H-tph (42 mg, ~0.1 mmol) were dissolved in 6.0 g DMA and 1.0 g HBF_4 (48 w.t. %). After stirring for 2 hours, the vial was placed in a 90 ℃ oven for 2 days. Orange hexagonal shaped crystals were obtained after solution was cooled to ambient temperature.

CPM-600c-Ni (Ni_3-bdt-tph): In a 20 mL glass vial, $NiCl_2 \cdot 6H_2O$ (78 mg, 0.3 mmol), H_2bdt (64 mg, 0.3 mmol), and H-tph (42 mg, ~0.1 mmol) were dissolved in 6.0 g DMF and

2.0 g DMPU and 0.06 g HFP. After stirring for 2 hours, the vial was placed in a 140 ℃ oven for 7 days. Green hexagonal shaped crystals were obtained after solution was cooled to ambient temperature.

CPM-600c-CoV (CoV-bdt-tph): In a 20 mL glass vial, $CoCl_2 \cdot 6H_2O$ (50 mg, 0.2 mmol), VCl_3 (16 mg, 0.1 mmol), H_2bdt (64 mg, 0.3 mmol), and H-tph (42 mg, ~0.1 mmol) were dissolved in 6.0 g DMA and 1.0 g HBF_4 (48 w.t. %). After stirring for 2 hours, the vial was placed in a 90 ℃ oven for 2 days. Red-orange hexagonal shaped crystals were obtained after solution was cooled to ambient temperature.

CPM-600d-MgV (Mg_2V-bpdc-tph): In a 20 mL glass vial, $MgCl_2 \cdot 6H_2O$ (40 mg, 0.2 mmol), VCl_3 (16 mg, 0.1 mmol), H_2bpdc (73 mg, 0.3 mmol), and H-tph (42 mg, ~0.1 mmol) were dissolved in 6.0 g DMF. After stirring for 2 hours, the vial was placed in a 120 ℃ oven for 5 days. Light-pink hexagonal-shaped crystals were obtained after solution was cooled to ambient temperature.

CPM-600d-CoV (Co_2V-bpdc-tph): In a 20 mL glass vial, $Co(NO_3)_2 \cdot 6H_2O$ (58 mg, 0.2 mmol), VCl_3 (16 mg, 0.1 mmol), H_2bpdc (73 mg, 0.3 mmol), and H-tph (42 mg, ~0.1 mmol) were dissolved in 6.0 g NMF and 1 drop HCl (36 w.t.%). After stirring for 2 hours, the vial was placed in a 120 ℃ oven for 5 days. Light-brown hexagonal shaped crystals were obtained after solution was cooled to ambient temperature.

CPM-600d-CoFe (Co_2Fe-bpdc-tph): In a 23 mL Teflon cup, $Co(NO_3)_2 \cdot 6H_2O$ (58 mg, 0.2 mmol), $FeCl_3 \cdot 6H_2O$ (27 mg, 0.1 mmol), H_2bpdc (73 mg, 0.3 mmol), and H-tph (42 mg, ~0.1 mmol) were dissolved in 6.0 g DMA and 0.6 g TFA. After stirring for 2 hours, the

teflon cup was sealed in an autoclave and placed in a 150 ℃ oven for 2 days. Brown powder was obtained after solution was cooled to ambient temperature.

CPM-600d-NiFe (Ni_2Fe-bpdc-tph): In a 23 mL Teflon cup, $Ni(NO_3)_2 \cdot 6H_2O$ (58 mg, ~0.2 mmol), $FeCl_3 \cdot 6H_2O$ (27 mg, 0.1 mmol), H_2bpdc (73 mg, ~0.3 mmol), and tph (42 mg, ~0.1 mmol) were dissolved in 6.0 g DMA and 0.6 g TFA. After stirring for 2 hours, the Teflon cup was sealed in an autoclave and placed in a 150 ℃ oven for 2 days. Yellow-green powder was obtained after solution was cooled to ambient temperature.

CPM-600d-CoV (Co_2V-adc-tph): In a 20 mL glass vial, $Co(NO_3)_2 \cdot 6H_2O$ (58 mg, 0.2 mmol), VCl_3 (16 mg, 0.1 mmol), H_2adc (81 mg, 0.3 mmol), and H-tph (42 mg, ~0.1 mmol) were dissolved in 6.0 g NMF and 1 drop HCl (36 w.t.%). After stirring for 2 hours, the vial was placed in a 120 ℃ oven for 5 days. Dark-red hexagonal shaped crystals were obtained after solution was cooled to ambient temperature.

3.2.4 Synthesis of Co_2V-tph based *pacs* with Different Organic Salts

The type and concentration of organic salt in synthesis has direct impact on final product, allowing for precise control over pore environment of *pacs* materials. Two parent materials, CPM-600b-CoV (Co_2V-26ndc-tph) and CPM-600d-CoV (Co_2V-bpdc-tph), are employed here to demonstrate these behaviors.

Co_2V-26ndc-tph-Et_4N (L_2:cat 1:0.4): In a 20 mL glass vial, $Co(NO_3)_2 \cdot 6H_2O$ (58 mg, 0.2 mmol), VCl_3 (16 mg, 0.1 mmol), 26-H_2ndc (65 mg, 0.3 mmol), H-tph (42 mg, ~0.1 mmol) and Et_4NCl (33 mg, 0.2 mmol) were dissolved in 6.0 g NMF. After stirring for 2 hours, the vial was placed in a 120 ℃ oven for 5 days. Dark-red hexagonal shaped crystals were

obtained after solution was cooled to ambient temperature. All precurors and synthetic environment were kept constant when substituting Et_4NCl with other organic salts, as shown in Table 3.1.

Co_2V-bpdc-tph-Ph_4P (L_2:cat 1:0.63): In a 20 mL glass vial, $Co(NO_3)_2 \cdot 6H_2O$ (58 mg, 0.2 mmol), VCl_3 (16 mg, 0.1 mmol), H_2bpdc (73 mg, 0.3 mmol), H-tph (42 mg, ~0.1 mmol) and tpPBr (95 mg, 0.23 mmol) were dissolved in 6.0 g NMF. After stirring for 2 hours, the vial was placed in a 120 ℃ oven for 5 days. Light-brown hexagonal shaped crystals were obtained after solution was cooled to ambient temperature. All precurors and synthetic environment were kept constant when substituting Et_4NCl with other organic salts, as shown in Table 3.1.

Table 3.1 Summary of tph to organic cation ratio during synthesis versus NMR.

Co_2V-based *pacs*	Synthesis		Ratio (tph : cation from salt)	
	H-tph (mg)	organic salt (mg)	molar ratio	NMR ratio
26ndc + Et_4N^+	42	33	1 : 2	1 : 0.36
26ndc + Pr_4N^+	42	57	1 : 2.5	1 : 0.12
26ndc + Bu_4N^+	42	58	1 : 1.85	1 : 0.45
26ndc + Bu_4N^+	42	110	1 : 3.86	1 : 0.63
26ndc + Bu_4N^+	42	276	1 : 9.45	1 : 0.92
26ndc + Bu_4N^+	42	415	1 : 15	1 : 1
26ndc + Pen_4N^+	42	75	1 : 2	1 : 0.55
26ndc + Hex_4N^+	42	84	1 : 2	1 : 0.54
26ndc + $dhdmN^+$	42	85	1 : 5	1 : 0.58
26ndc + $htmN^+$	42	28	1 : 2	1: 0.42
bpdc + Ph_4P^+	42	95	1 : 2.26	1 : 0.63
bpdc + Bu_4N^+	42	65	1 : 2.34	1 : 0.43

3.2.5. Property Characterization

pH Stability Examination: pH of aqueous solutions were prepared through dilutions of HCl (36 w.t.%) or NaOH and confirmed with pH-meter. For each analysis, ~50 mg of isolated sample was rinsed in chosen aqueous solution (20 mL x3). The decanted solid was finally imersed in 10 mL of aqueous solution for ambient temperature testing, or 25 mL distilled water for H_2O refluxing.

Nuclear Magnetic Resonance (NMR): ^1H NMR spectra were recorded on Bruker Avance NEO 400 MHz or Bruker Avance 600 MHz NMR spectrometer. The spectrometers were automatically tuned and matched to the correct operating frequencies, with spectra reported in parts per million (δ) with respect to tetramethylsilane (TMS, δ=0). Spectra were processed using Bruker Topsin 1.3. Deconvolution was employed for peaks with overlapping regions, but only integration of targeted peak is shown in spectra for clarity.

Organic Cation Measurement. To ensure NMR analysis of organic cation excludes any organic salt on the surface of *pacs*, the as-synthesized material was washed multiple times in DMF and immersed in CH_2Cl_2 or EtOH and refreshed three times, once every 12 hours. The sample was dried overnight at 80 °C in vacuum oven. About 3-5 mg dried sample was added to a 1 mL disposable centrifuge-tube, followed by 4 drops of DCl (36 w.t. %), and 0.5 mL d_6-DMSO. The tube was capped, and placed on a vortex mixer for 30 seconds. Any solution with precipitate was diluted further with d_6-DMSO and vortexed until clear homogeneous solution is obtained. The clear blue solution was transferred to a 5 mm NMR tube.

Vapor Sorption Measurement: The as-synthesized sample was immersed in CH_2Cl_2 and refreshed daily for five consecutive times. The sample was then evacuated overnight at 60 ^oC. The sample was placed in a small glass vial, which was placed in a larger glass vial containing benzene:cyclohexane mixture (1:1 v/v). The solid was exposed to vapor for specified time, followed with digestion by 4 drops of DCl (36 w.t. %), and 0.5 mL d_6-DMSO. The solution was vortexed for 30 seconds. Any solution with precipitate was diluted further with d_6-DMSO vortexed until clear homogeneous solution is obtained. The clear blue solution was transferred to a 5 mm NMR tube for characterization.

Gas Sorption Measurement Gas sorption measurements were carried out on a Micromeritics ASAP 2020 and ASAP 2020 Plus physisorption analyzers. The as-synthesized sample was immersed in CH_2Cl_2 and refreshed daily for five consecutive times. The sample was then transferred to the gas sorption tube and the dried under open flow of N_2 gas for 15 minutes. The degas process was carried out at 60 ^oC for 12 hours.

Other Characterization: SCXRD, PXRD, TGA, EDS, gas adsoption measurements and calculations were carried out as mentioned in 2.2.4.

Table 3.2 Crystal Data summary of CPM-600(a-d).

Code	*Space Group*	*a (Å)*	*b (Å)*	*c (Å)*	*α*	*β*	*γ*	Vol $(Å)^3$	R(F)
CPM-600a-Co	*$P6_3/mmc$*	19.118	19.118	16.195	90	90	120	5126	0.045
CPM-600b-CoV	*$P6_3/mmc$*	19.143	19.143	18.504	90	90	120	5872	0.081
CPM-600c-CoV	*$P6_3/mmc$*	18.942	18.942	20.094	90	90	120	6244	0.024
CPM-600d-CoV	*$P6_3/mmc$*	19.15	19.15	24.01	90	90	120	7628	0.131

3.3 Results and Discussion

3.3.1 Structure Characterization

The anionic tph-*pacs* family reported here has the formula $[(M1)_{3-x}(M2)_x(O/OH/)(L1)_3(L2)]G1$ and denoted as CPM-600x-M-G1, where x corresponds to L1 (a = H_2tba, b = $H_2$26ndc, c = H_2bdt, d = H_2bpdc), M corresponds to $[(M1)_{3-x}(M2)_x(O/OH)]$ (Mg_3, Zn_3, Co_3, Ni_3, Mg_xV_y, Co_xV_y, Co_xFe_y, Ni_xFe_y) and G1 corresponds to (Et_4N^+, Pr_4N^+, Bu_4N^+, Pen_4N^+, Hex_4N^+, $htmN^+$, $dhdmN^+$, Ph_4P^+) (Figure 3.2). Single crystal X-ray diffraction patterns of Co_xV_y-tph-based *pacs* were first collected and refined. Table 4.2 summarizes unit cell parameters and refinement factors. PXRD patterns of tph-based *pacs* with different permutations of metals, L1, and counter balancing ions were then collected and compared to those simulated from refined single crystal data (Figure 3.3). Matching of patterns between as-synthesized samples and simulations confirmed phase purity of bulk materials. For heterometallic phases, EDS was employed to estimate ratio of M^{2+} metal to M^{3+} metal. As shown in Figure 3.4, all heterometal phases shows M^{2+} to M^{3+} ratios greater than 1, denoting presence of only neutral or anionic trimer.

Central to optimizing pore environment anionic *pacs* materials is the identity and concentration of the 4th module: guest ions. CPM-600b-CoV and CPM-600d-CoV were employed to demonstrate the correlation between ratio of added organic cation to the formula unit. Through simple addition of different quaternary ammonium or phosphonium salt into the synthetic pot, simultaneous construction of anionic *pacs* and substitution of hexaazaphenalene's counter-balancing ion could occur. ^{1}HNMR was then employed to

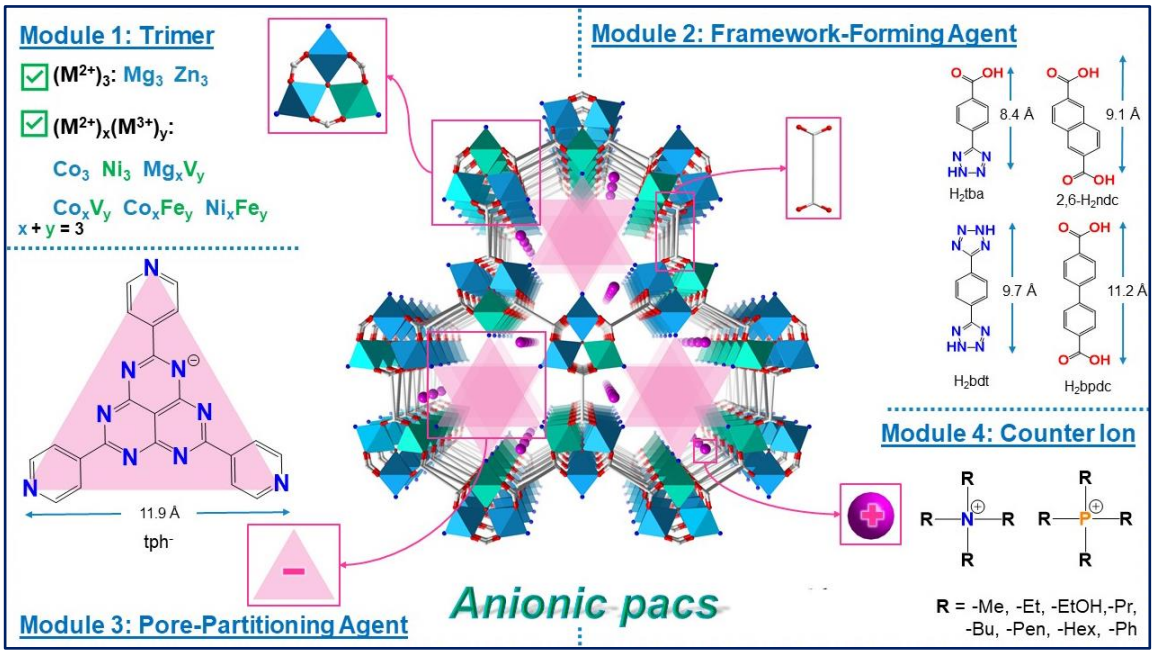

Figure 3.2 Design of tph-based anionic *pacs* frameworks with different modules.

calculate the ratio of the added organic cation to the formula unit (Table 4.1). Ten different CPM-600b-CoV and CPM-600d-CoV are constructed at approximately 2 mmol equivalence. The final cation to tph ratio obtained from NMR varied slightly from initial addition. Furthermore, CPM-600b-CoV was synthesized with 1.85, 3.66, 9.45 and 15 mmol of Bu_4NCl to 1 mmol of H-tph, which resulted in NMR ratios of 0.45, 0.63, 0.92 and 1 cation to 1 tph, respectively. Thus, proving the feasibility of tuning ratio of quaternary ammonium/phosphonium ion in anionic *pacs* synthesis.

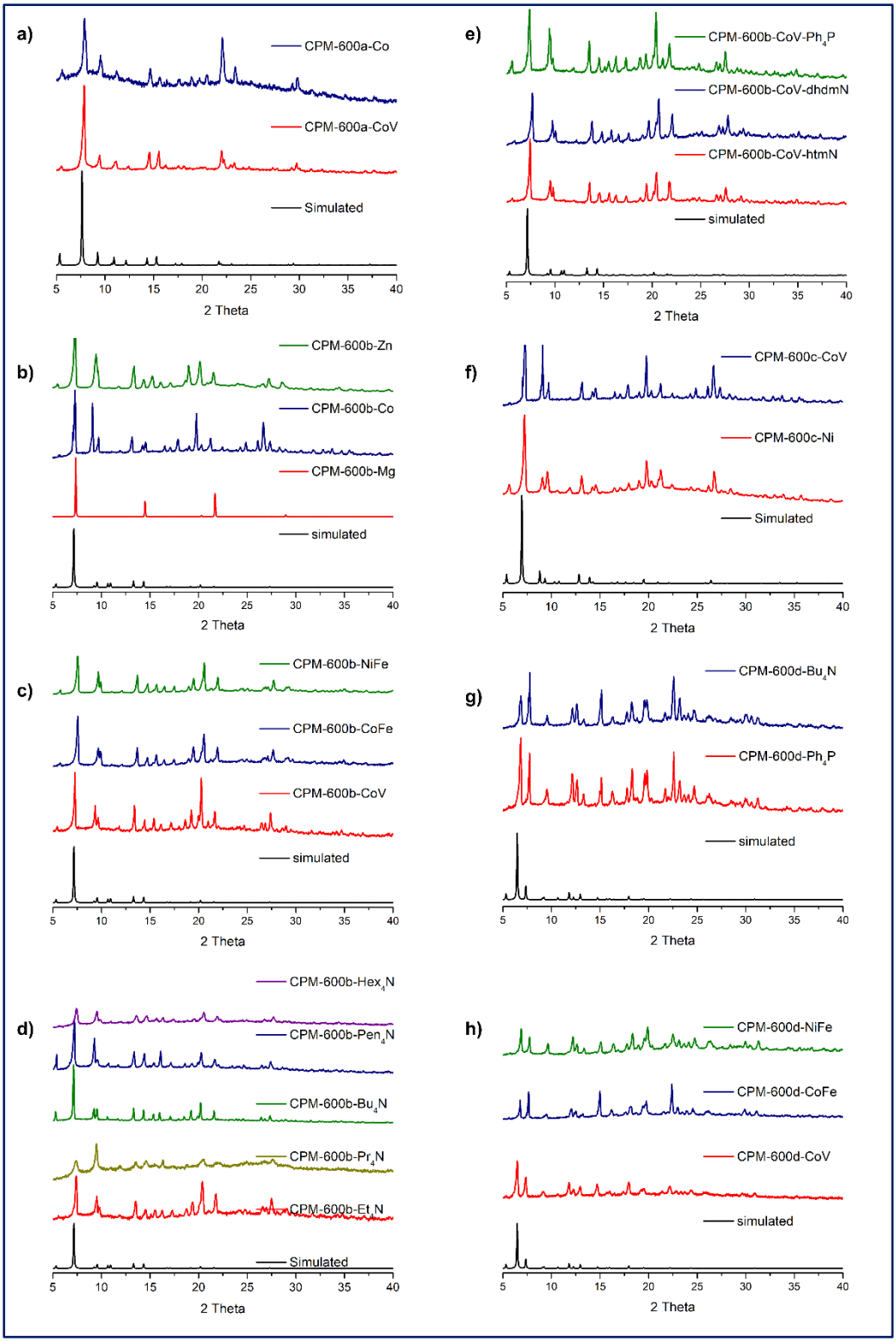

Figure 3.3 Simulated as as-synthesized PXRD patterns of tph-based *pacs* materials with different metals, ditopic linker and guest ions.

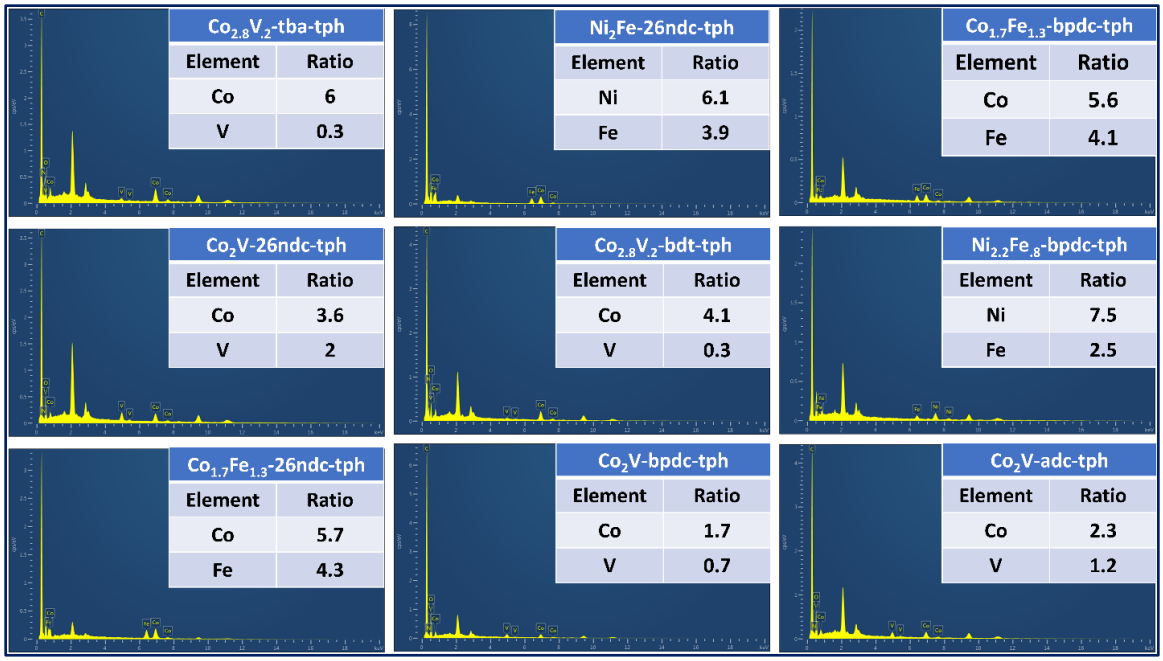

Figure 3.4 Simulated as as-synthesized PXRD patterns of tph-based *pacs* materials with different metals, ditopic linker and guest ions.

3.3.2 Hydrolytic Stability

Hydrolytic stability is an important requisite for many applications, yet the number of water-stable anionic MOFs is limited.[33-34] The charge-reallocation strategy presented here, allows for development of a large family of water-stable anionic materials. With strength of coordination bond mainly responsible for hydrolytic stability, the weak Mg—O/Mg—N coordination of anionic Mg-trimer in CPM-600b-Mg could not maintain water stability for even 5 minutes. In comparison, the neutral Co_2V trimer in CPM-600b-CoV is stable in water for at least 3 days (Figure 3.5a). CPM-600b-CoV also maintains chemical stability within pH range 3-11 for at least 24 hours (Figure 3.5b).

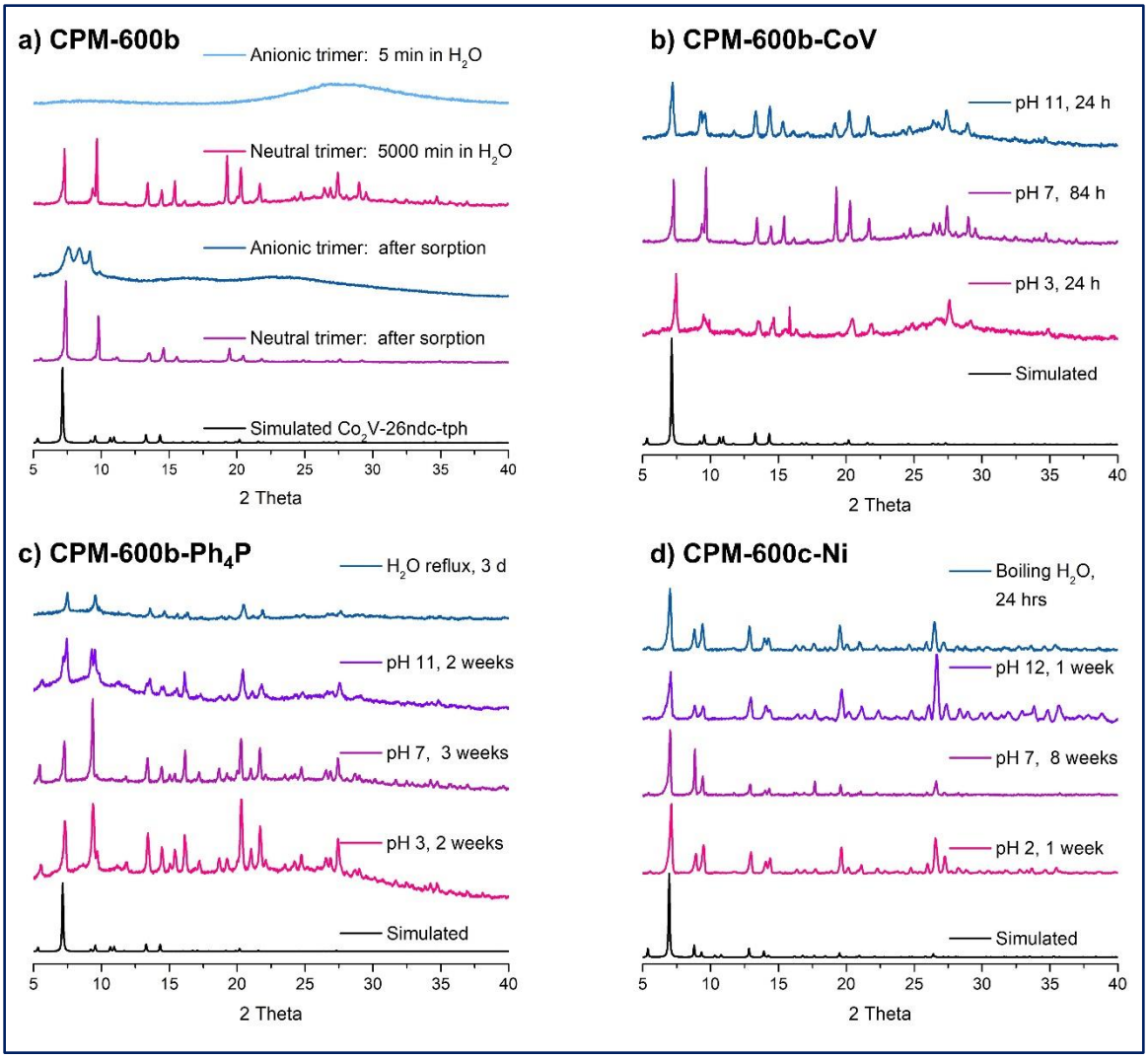

Figure 3.5 Chemical stability of different tph-based *pacs*.

The hydrolytic stability of CPM-600b-CoV could further be enhanced through choice of counter cation. For instance, the *pacs* material prepared from the addition of 10 mmol Ph_4PBr extends stability to at least 21 days, and pH range 3-11 for 14 days (Figure 3.5c). This is likely due to the presence of bulky hydrophobic Ph_4P^+ counterions that impede H_2O attack on metal sites and thus allow the material to maintain chemical stability over a much longer period.

In addition to high chemical stability observed in carboxylate-based *pacs*, we also witnessed remarkable properties with azolate-based *pacs* materials. In particular, CPM-600c-Ni reported here maintains water stability for at least 2 months and stability in pH 2-12 for at least 7 days. The material also shows modest stability of 24 hours in refluxing H_2O (Figure 3.4d). Such high chemical stability achieved with tph ligands is comparable to benchmark anionic materials (Table 3.3).

Table 3.3 Hydrolytic stability of benchmark anionic MOFs.

Name	Ambient H_2O (day)	Boiling H_2O (day)	pH range	Acid (day)	Base (day)	Ref.
LnMOF1	90	--	4-12	0.05	0.05	[35]
Ni_3-bdt-tph	**56**	**1**	**2-12**	**7**	**7**	**This Work**
UiO-66($SO_3H)_2$	30	30	--	--	--	[9]
NTU-66-Cu	30	1	2-12	30	30	[36]
Bio-MOF-1	28	--	7-7.4	--	14	[16]
CPM-600b-Ph_4N	**24**	**--**	**3-11**	**14**	**14**	**This Work**
NOTT-200	10[a]	--	--	--	--	[4]
JXNU-5	10	--	--	--	--	[37]
BUT-8(Cr)	7	--	Conc.-11	7	7	[7]
NU-1300	7	--	1-10	7	7	[5]
CPM-5	7	0.49	--	--	--	[15]
MIL-101-*p*COOH	6	--	--	--	--	[38]
JXNU-4	3	--	4-11	1	1	[39]
AUBM-1	3	--	1-12	3	3	[40]
[Me_2NH_2][Eu(ox)$_2$(H_2O)]	3	1	4-7	0.16	--	[41]

3.3.3 Gas Adsorption Studies

Acetylene, ethylene, and propylene are all important raw organic building blocks whose storage and separation poses great challenges to many industrial sectors. Several benchmark materials with desirable features such as micro-pore, open-metal sites, and functional linkers have shown promising C_2H_2 storage capacity at ambient temperature and pressure.[42-44] The anionic *pacs* reported here presents an additional level of tunability (through counter cation) to further enhance interactions with these small gas molecules.

Previously, the formation the anionic Mn_3-26ndc-tpp (SNNU-28(Mn), tpp = 2,4,6-tri(4-pyridinyl)-1- pyridine) *pacs*, shows negligible C_2H_2 uptake, due to framework instability.[31] Similarly, the anionic CPM-600b-Mg reported here exhibits small uptakes of 2.52 and 1.84 mmol/g at 1 bar, 273 K and 298 K, respectively (Figure 3.6a). PXRD of the material after one gas sorption cycle shows unidentifiable phase change. (Figure 3.5a). In SNNU-28(Mn) where PPA is neutral, the substitution of Mn^{2+} with Mg^{2+} or Zn^{2+} would unlikely improve stability whereas other metals or metal combinations could likely form neutral or cationic frameworks. Here, shifting of the negative charge from metal cluster to tph linker allows us to incorporate a much wider range of metal sources into anionic *pacs*. As a result, the construction of CPM-600b-CoV, results in C_2H_2 uptakes of 9.4 mmol/g and 6.2 mmol/g at 1 bar, 273 K and 298 K, respectively. This is a dramatic boost, from the 1st generation of unstable anionic *pacs* materials. After repeated gas sorption-desorption cycles, PXRD shows CPM-600b-CoV still retains high crystallinity (Figure 3.5a).

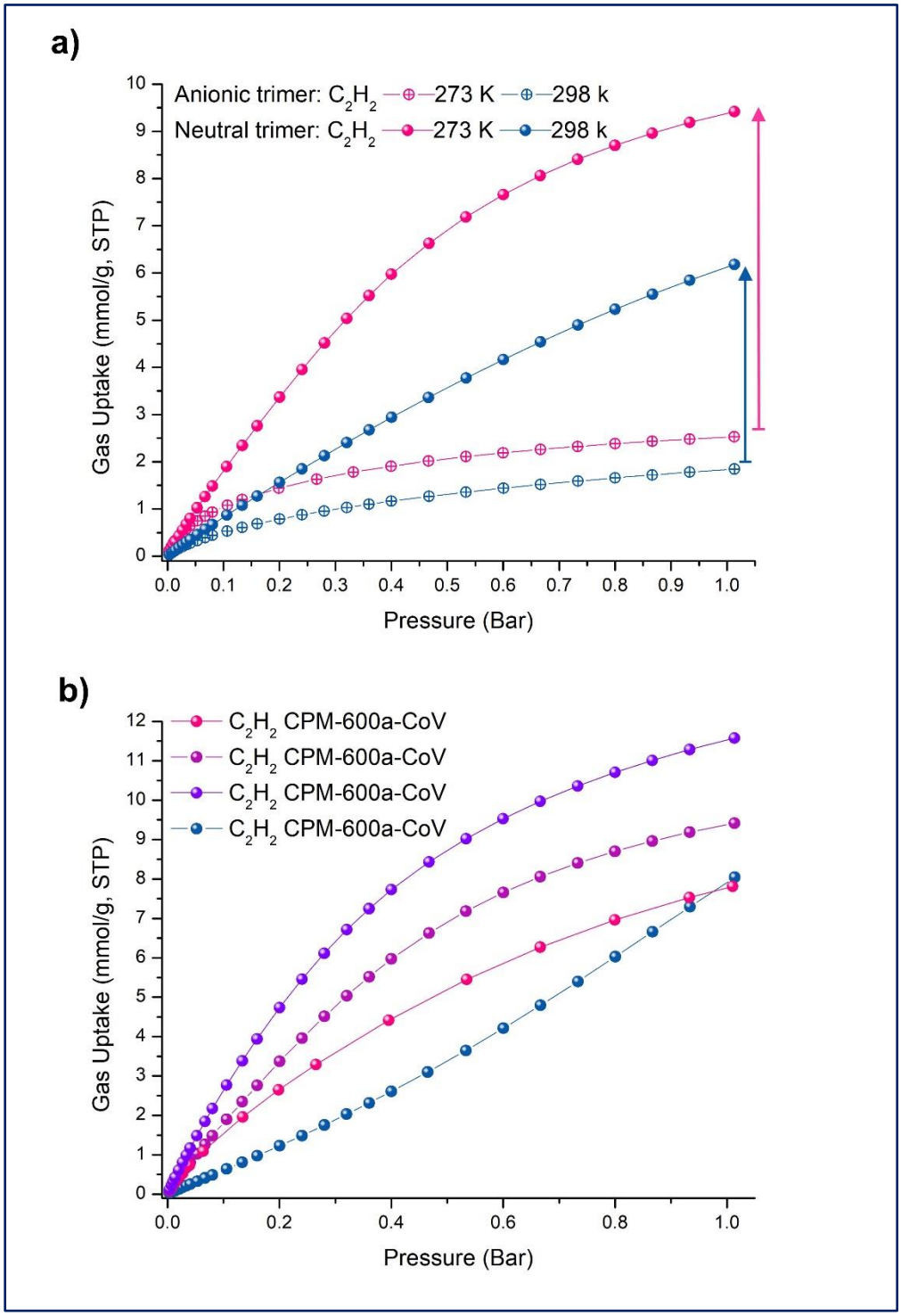

Figure 3.6 C_2H_2 isotherms of CPM-600-based *pacs*. (a) C_2H_2 uptakes of CPM-600b with anionic metal (Mg) versus neutral metal (CoV) trimers at 273 K and 298 K, (b) C_2H_2 isotherms of CPM-600x-CoV series at 273 K.

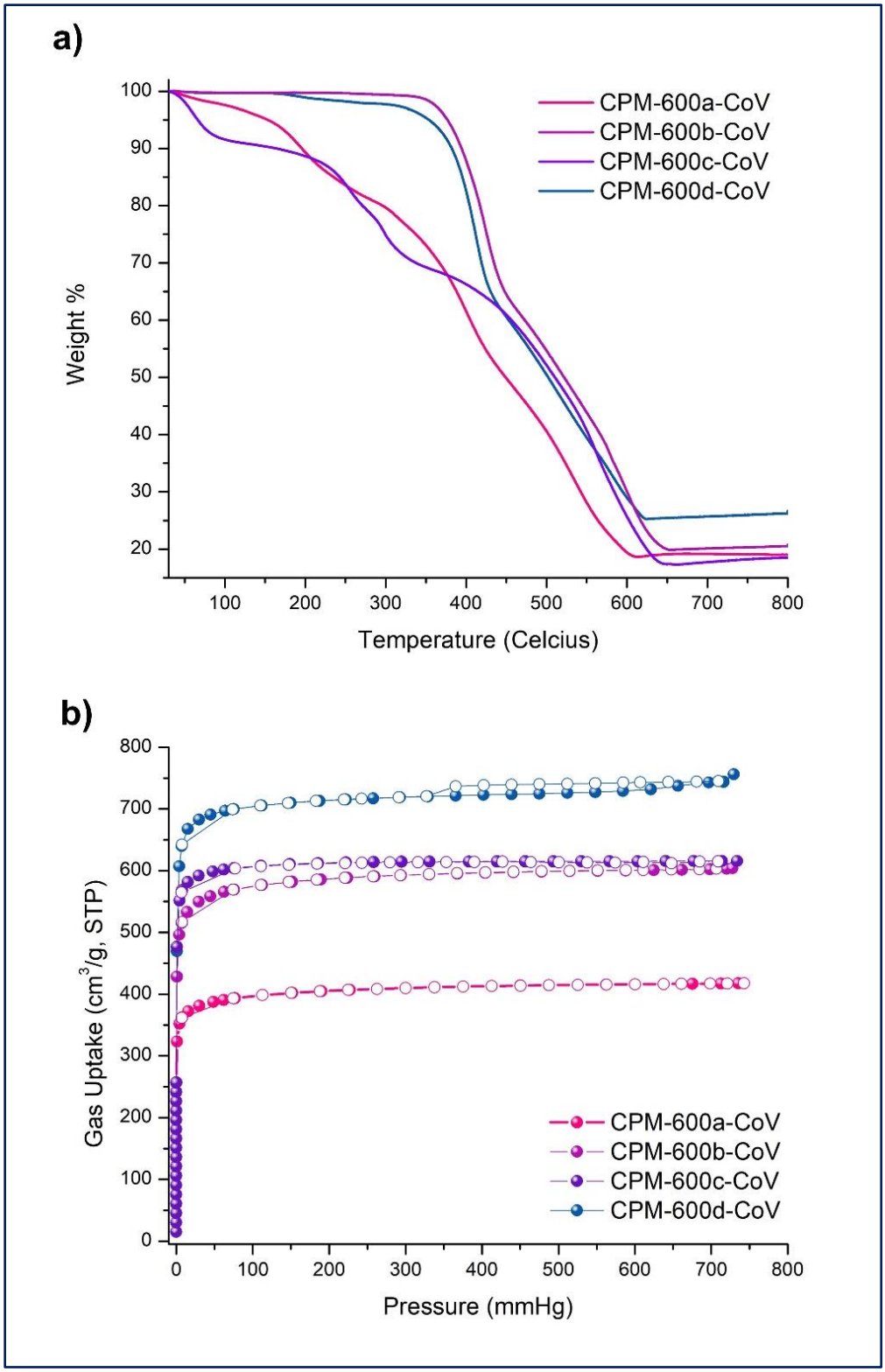

Figure 3.7 (a) TGA and (b) N_2 analyses of CPM-600x-CoV *pacs* materials.

Table 3.4 Summary of gas sorption isotherms and heat of adsorption.

	CPM-600b-CoV	CPM-600c-CoV	CPM-600d-CoV
S_A Langmuir (m^2/g)	2298	2676	3120
S_A BET (m^2/g)	1666	1945	2260
Pore Volume (cm^3/g)	0.815	0.927	1.05
C_3H_8 298 K (mmol/g)	7.86	9.29	10.7
C_3H_8 273 K (mmol/g)	8.43	12.0	11.8
Q_{st}^0 (kJ/mol)	29.5	30.5	24.4
C_3H_6 298 K (mmol/g)	8.41	10.1	11.5
C_3H_6 273 K (mmol/g)	9.16	11.2	12.9
Q_{st}^0 (kJ/mol)	23.1	30.0	23.4
C_2H_6 298 K (mmol/g)	6.33	6.64	4.78
C_2H_6 273 K (mmol/g)	8.42	8.90	9.90
Q_{st}^0 (kJ/mol)	23.8	18.33	17.4
C_2H_4 298 K (mmol/g)	5.17	5.68	3.03
C_2H_4 273 K (mmol/g)	7.88	8.30	6.69
Q_{st}^0 (kJ/mol)	22.7	19.7	19.3
C_2H_2 298 K (mmol/g)	6.17	8.23	3.39
C_2H_2 273 K (mmol/g)	9.42	11.6	8.04
Q_{st}^0 (kJ/mol)	25.3	23.1	20.4
CO_2 298 K (mmol/g)	2.50	3.30	1.63
CO_2 273 K (mmol/g)	5.74	6.60	3.23
Q_{st}^0 (kJ/mol)	19.6	14.6	17.0
*Isotherm values obtained at 1 bar			

Table 3.5 Summary of benchmark ionic MOFs for C_2H_2 uptake.

MOFs	*Charge*	S_A BET (m^2/g)	C_2H_2 298 K 1 bar (mmol/g)	C_2H_2 273K 1 bar (mmol/g)	Qst (kJ/mol)	Ref.
CoV-bdt-tph	**anionic**	**1945**	**8.20**	**11.60**	**23.1**	**This Work**
NBU-8	anionic	1467	8.17	10.47	34.6	[45]
FJU-90a	cationic	1572	8.04	9.64	25.1	[26]
$[Co_6(OH)_2(INA)_6(CPT)_3](NO_3)$	cationic	1158	7.28	10.04	40	[46]
$(CoCl_4)_{0.25}[Co_3(\mu_3\text{-}OH)(CPT)_{4.5}]$	anionic	1927	6.52	9.82	26.3	[47]
SNNU-60	anionic	60.8	5.53	6.94	33.3	[48]
PCP-33	anionic	1248	5.44	--	27.5	[49]
$[Co_3(\mu_3\text{-}OH)(cpt)_3Co_3(\mu_3\text{-}OH)(L)_3(H_2O)_9](NO_3)_4$	cationic	196	5.40	--	34.2	[50]
NTU-66-Cu	anionic	1700	4.98	6.56	32.3	[36]
FJU-6-TATB	anionic	1306	4.91	0.00	29	[51]
$[(CH_3)_2NH_2]_2[Dy_6(\mu_3\text{-}OH)_8(FTZB)_6(H_2O)_6]$	anionic	861	4.87	6.25	26.7	[52]
$[Cu_6(L)_3(H_2O)_4(HCOO)]\cdot Me_2NH_2^+$	anionic	1599	4.80	9.42	35.3	[53]
ZJNU-115	anionic	1291	4.73	6.16[a]	--	[54]
$(NH_2Me_2)[Cd_3(\mu_3\text{-}OH)(tpt)(TZB)_3]$	anionic	1123	4.73	7.50	33.2	[30]
SNNU-150-Al	cationic	--	4.33	6.74	29	[55]
CPM-107	anionic	319	4.33	0.00	37	[56]
$[Co_6(OH)_2(INA)_6(TZB)_3](H_2NMe_2)_2$	anionic	1124	3.88	5.13	28	[46]
JCM-1	cationic	550	3.35	4.24	36.9	[57]
$[Me_2NH_2]\cdot[Zn_3(ALP)(TDC)_{2.5}]$	anionic	410	3.06	4.31	31.1	[58]
SNNU-23	anionic	624	2.79	4.15	62.2	[59]
JXNU-5a	anionic	407	2.50	6.16	32.9	[37]
FJU-36a	anionic	409	2.46	2.97	32.9	[60]
$(Me_2NH_2)[In_{1.5}(FBDC)(BDC)]$	anionic	307	2.37	3.04	37	[61]
Cu^I@UiO-66-$(COOH)_2$	anionic	302	2.31	2.50	74.5	[3]
Gd-MOF	anionic	238	1.44	1.74	--	[62]
$Fe(tpy)_2$@ECUT-300	anionic	370	1.37	--	--	[63]

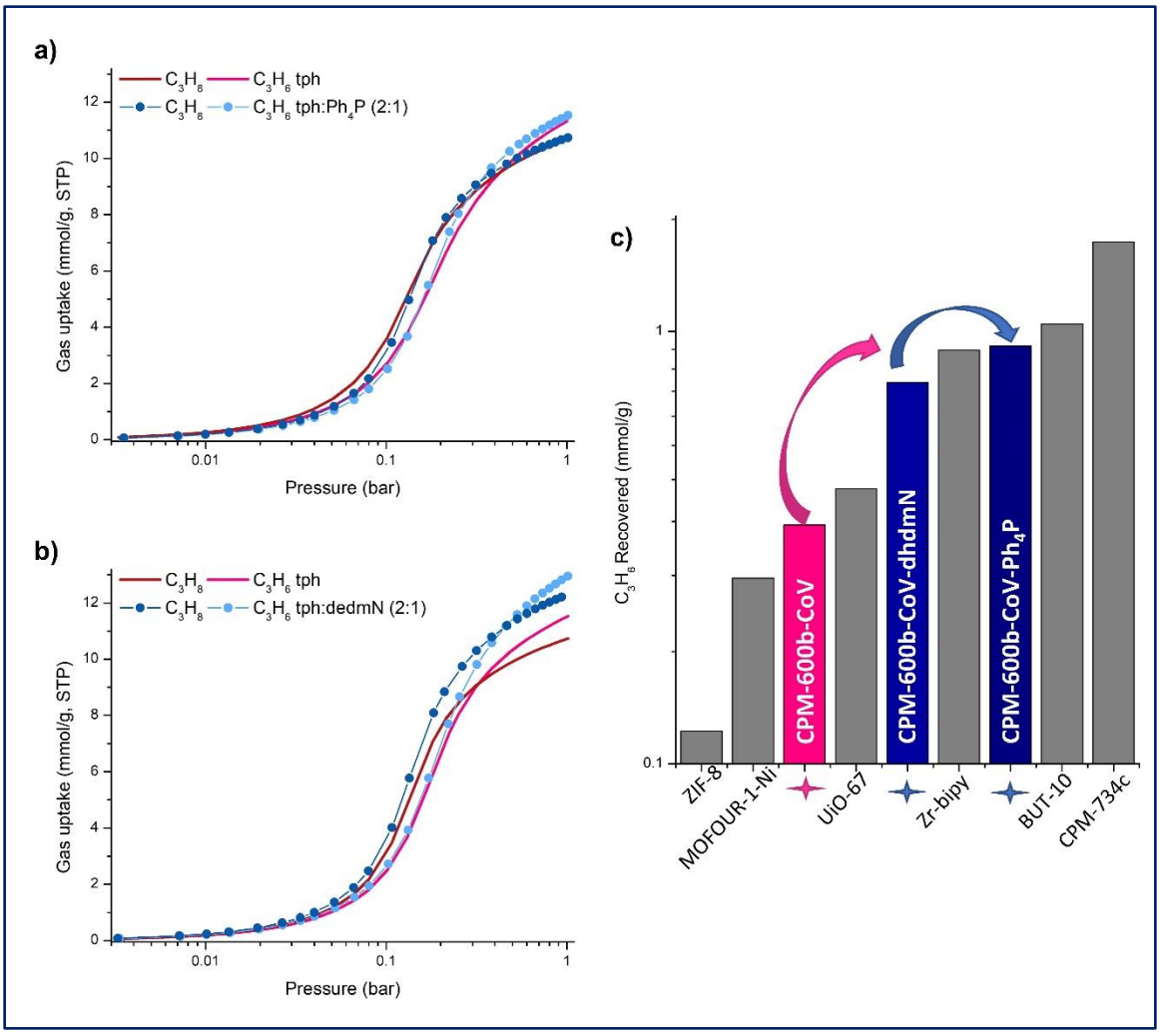

Figure 3.8 C_3H_6/C_3H_8 adsorption performances of CPM-600d-based *pacs* at 298 K. (a) Comparison of C3 isotherms between CPM-600d-CoV prototype and CPM-600d-CoV-Ph_4P, (b) Comparison of C3 isotherms between CPM-600d-CoV prototype and CPM-600d-CoV-dhdmN and (c) Comparison of potential C_3H_8 recovered through employment of different adsorbents in C_3H_8/C_3H_6 (50/50 v/v) separation

With the success of CPM-600b-CoV, we then systematically study the general porosity, C2, C3 uptake trends, to tailor specific anionic tph-*pacs* to the needs of different applications. All materials underwent TGA analyses to confirm complete removal of guest molecules after activation. As shown in Figure 3.7a, only CPM-600c-CoV has a small weight loss before 100 °C, which is a result from H_2O vapor sorption during transfer of

activated material to TGA analyzer. Next N_2 adsorption at 77 K was carried out to probe surface area and porosity. All anionic *pacs* reported here show type-I N_2 adsorption isotherms (Figure 3.7b). The surface areas and pore volumes of these materials are within expected range, based on other reported *pacs*, suggesting that they are well activated. After confirming porosity of anionic *pacs*, we then studied the adsorptions of C_2H_2, C_2H_4, C_2H_6, C_3H_6, C_3H_8 at 273 and 298 K for tph-based *pacs* with different L1 lengths. Table 3.4 summarizes the uptakes at 1 bar, 273 and 298 K, and isosteric heat of adsorption.

Interestingly, the C_2H_2 uptake trend at 273 K follows $bpdc^{2-} < tba^{2-} < 26ndc^{2-} < bdt^{2-}$(Figure 3.6b). Generally, with enlarged framework having extra-large volume, host-guest interaction is dramatically diminished, thus resulting in poor uptake. Since Co_2V-bpdc-tph framework is too large, and thus exhibits poor uptake, CoV-bdt-tph, with the next largest surface area and pore volume, exhibits the highest C_2H_2 uptakes of 11.6 and 8.23 mmol/g at 273 K and 298 K, respectively. In fact, these values are also higher than the best performing ionic MOF materials NBU-8 (10.5, 8.15)[45], FJU-90a (9.64, 8.04)[26], SNNU-60 (6.94, 5.53)[48]. C_2H_4 and C_2H_6 uptakes for CoV-bdt-tph are also the highest among all tph-*pacs* materials. Thus, the bdt-tph *pacs* combination offers the most ideal pore aperture and functionalities for optimal uptakes of small C2 molecules.

With larger C3 molecules, the elongated L1 linkers provides larger pore volume for higher uptake. Co_2V-bpdc-tph exhibits C_3H_6 and C_3H_8 uptakes of 12.9 and 11.8 mmol/g at 273 K, and 11.5 and 10.7 mmol/g at 298 K. While the C3 uptake capacities are among the top-three MOF materials,[64-65] the uptake difference between these two molecules is modest. We sought to introduce additional hydroxyl groups in organic cations to boost O-

--H interactions. Compared to Co_2V-bpdc-tph that could potentially recover 0.357 mmol/g C_3H_6 from C_3H_8/C_3H_6 1:1 mixture at 1 bar, 298 K, the incorporation of 0.5 $dhdmN^+$ per formula unit resulted in 0.925 mmol/g of potentially recoverable C_3H_6 (Figure 3.8). This is higher than ZIF-8 (0.119)[66], MOFOUR-1-Ni (0.269)[67], UiO-67 (0.433)[68], but slightly lower than BUT-10 (1.04)[68] and CPM-734c (1.61)[27].

3.3.4 Vapor Adsorption Studies

Cyclohexane (C_6H_{12}) is a crucial intermediate in the petrochemical industry. However, the C_6H_{12} production results in benzene/cyclohexane mixtures that must undergo energy-intensive purifications. Porous materials provide a promising platform for C_6H_6/C_6H_{12} separation. (Table S12). Herein, we present the first case study on utilizing aliphatic organic cation to enhance C_6H_6/C_6H_{12} selectivity.

With Co_2V-26ndc-tph as the parent framework, we chose to incorporate Et_4N^+, Bu_4N^+ and $dhdmN^+$. Co_2V-26ndc-tph adsorbs 3.6 and 0.9 C_6H_6 and C_6H_{12} molecules per formula unit (mpf), respectively. With the substitution of 0.5 Bu_4N^+ mpf, the uptake of C_6H_6 increases to 4.8, while C_6H_{12} stayed the same. Further increase of Bu_4N^+ to 1 mpf resulted in 5% decrease of C_6H_6 but 20% decrease for C_6H_{12}. We speculate that while alkyl chain enhances π-H with C_6H_6, slight H-H repulsion with C_6H_{12} is observed when pore volume has higher concentration of Bu_4N^+. Interestingly, the shortening of the alkyl length to Et_4N did not increase C_6H_{12} uptake. The addition of 0.4 Et_4N mpf resulted in an increase of C_6H_6 to 5.8 while keeping C_6H_{12} at 0.9 mpf. The addition of two OH groups into $dhdmN^+$, slightly increased the concentration of C_6H_{12} to 1 mpf, likely through electronegative-H

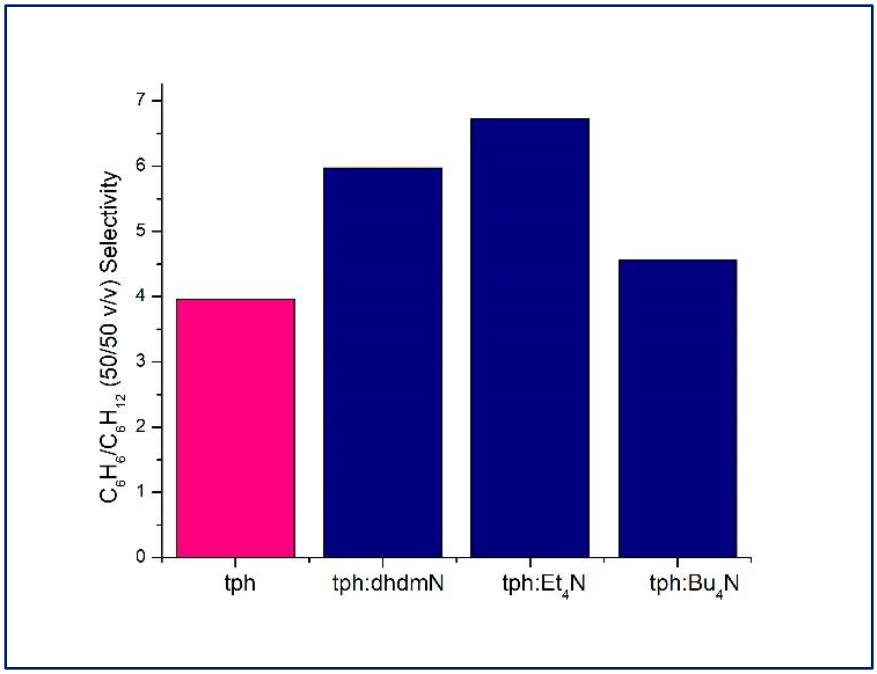

Figure 3.9 Cyclohexane/Benzene (50/50 v/v) vapor selectivity of CPM-600-CoV prototype and different guest ions.

interaction. This shows that length, functionality, and concentration of cations all contribute to enhancing C_6H_6/C_6H_{12} selectivity (Figure 3.9).

3.4 Conclusion

We report here a new synthesis concept that combines pore-space partition strategy with charge reallocation strategy to construct a large isoreticular series of anionic *pacs* type (partitioned-*acs*) porous materials. Over two dozen anionic *pacs* materials have been made to demonstrate their excellent chemical stability and high degree of tunability to tailored applications. Notably, Ni_3-bdt-tph (bdt = 1,4-benzeneditetrazole) exhibits month-long water stability, while CoV-bdt-tph sets new record for C_2H_2 storage capacity under ambient conditions for ionic MOFs. In addition to diverse framework modules, we illustrate the

feasibility to systematically tune the type and concentration of counter cation species and demonstrate how hydroxy, aliphatic and aromatic functional groups would influence both the materials' chemical stability and capability to separate industrial relevant C_3H_8/C_3H_6 and C_6H_6/C_6H_{12} mixtures. We believe that this material design and synthesis strategy will lead to useful anionic MOFs for a large range of applications.

3.5 Reference

1. Zhao, S.-N.; Zhang, Y.; Song, S.-Y.; Zhang, H.-J., Design Strategies and Applications of Charged Metal Organic Frameworks. *Coord. Chem. Rev.* **2019,** *398*, 113007.

2. Chang, G.; Huang, M.; Su, Y.; Xing, H.; Su, B.; Zhang, Z.; Yang, Q.; Yang, Y.; Ren, Q.; Bao, Z.; Chen, B., Immobilization of Ag(I) into a Metal-Organic Framework with -So3h Sites for Highly Selective Olefin-Paraffin Separation at Room Temperature. *Chem. Commun.* **2015,** *51*, 2859-2862.

3. Zhang, L.; Jiang, K.; Yang, L.; Li, L.; Hu, E.; Yang, L.; Shao, K.; Xing, H.; Cui, Y.; Yang, Y.; Li, B.; Chen, B.; Qian, G., Benchmark C2h2/Co2 Separation in an Ultra-Microporous Metal-Organic Framework Via Copper(I)-Alkynyl Chemistry. *Angew. Chem., Int. Ed.* **2021,** *60*, 15995-16002.

4. Yang, S.; Lin, X.; Blake, A. J.; Walker, G. S.; Hubberstey, P.; Champness, N. R.; Schröder, M., Cation-Induced Kinetic Trapping and Enhanced Hydrogen Adsorption in a Modulated Anionic Metal–Organic Framework. *Nat. Chem.* **2009,** *1*, 487-493.

5. Li, P.; Vermeulen, N. A.; Gong, X.; Malliakas, C. D.; Stoddart, J. F.; Hupp, J. T.; Farha, O. K., Design and Synthesis of a Water-Stable Anionic Uranium-Based Metal-Organic Framework (Mof) with Ultra Large Pores. *Angew. Chem. Int. Ed. Engl.* **2016,** *55*, 10358-62.

6. Liu, X.; Xiao, Z.; Xu, J.; Xu, W.; Sang, P.; Zhao, L.; Zhu, H.; Sun, D.; Guo, W., A Nbo-Type Copper Metal–Organic Framework Decorated with Carboxylate Groups Exhibiting Highly Selective Co2adsorption and Separation of Organic Dyes. *J. Mater. Chem. A* **2016,** *4*, 13844-13851.

7. Yang, F.; Xu, G.; Dou, Y.; Wang, B.; Zhang, H.; Wu, H.; Zhou, W.; Li, J.-R.; Chen, B., A Flexible Metal–Organic Framework with a High Density of Sulfonic Acid Sites for Proton Conduction. *Nature Energy* **2017,** *2*, 877-883.

8. Liu, S.-S.; Han, Z.; Yang, J.-S.; Huang, S.-Z.; Dong, X.-Y.; Zang, S.-Q., Sulfonic Groups Lined Along Channels of Metal–Organic Frameworks (Mofs) for Super-Proton Conductor. *Inorg. Chem.* **2020,** *59*, 396-402.

9. Phang, W. J.; Jo, H.; Lee, W. R.; Song, J. H.; Yoo, K.; Kim, B.; Hong, C. S., Superprotonic Conductivity of a Uio-66 Framework Functionalized with Sulfonic Acid Groups by Facile Postsynthetic Oxidation. *Angew. Chem. Int. Ed. Engl.* **2015,** *54*, 5142-6.

10. Sadakiyo, M.; Yamada, T.; Kitagawa, H., Proton Conductivity Control by Ion Substitution in a Highly Proton-Conductive Metal–Organic Framework. *J. Am. Chem. Soc.* **2014,** *136*, 13166-13169.

11. Nagarkar, S. S.; Unni, S. M.; Sharma, A.; Kurungot, S.; Ghosh, S. K., Two-in-One: Inherent Anhydrous and Water-Assisted High Proton Conduction in a 3d Metal–Organic Framework. *Angew. Chem. Int. Ed.* **2014,** *53*, 2638-2642.

12. Taylor, J. M.; Dawson, K. W.; Shimizu, G. K. H., A Water-Stable Metal–Organic Framework with Highly Acidic Pores for Proton-Conducting Applications. *J. Am. Chem. Soc.* **2013,** *135*, 1193-1196.

13. Tian, J.; Saraf, L. V.; Schwenzer, B.; Taylor, S. M.; Brechin, E. K.; Liu, J.; Dalgarno, S. J.; Thallapally, P. K., Selective Metal Cation Capture by Soft Anionic Metal–Organic Frameworks Via Drastic Single-Crystal-to-Single-Crystal Transformations. *J. Am. Chem. Soc.* **2012,** *134*, 9581-9584.

14. Xu, G.-W.; Wu, Y.-P.; Dong, W.-W.; Zhao, J.; Wu, X.-Q.; Li, D.-S.; Zhang, Q., A Multifunctional Tb-Mof for Highly Discriminative Sensing of Eu3+/Dy3+ and as a Catalyst Support of Ag Nanoparticles. *Small* **2017,** *13*, 1602996.

15. Zheng, S.-T.; Bu, J. T.; Li, Y.; Wu, T.; Zuo, F.; Feng, P.; Bu, X., Pore Space Partition and Charge Separation in Cage-within-Cage Indium−Organic Frameworks with High Co2 Uptake. *J. Am. Chem. Soc.* **2010,** *132*, 17062-17064.

16. An, J.; Shade, C. M.; Chengelis-Czegan, D. A.; Petoud, S.; Rosi, N. L., Zinc-Adeninate Metal−Organic Framework for Aqueous Encapsulation and Sensitization of near-Infrared and Visible Emitting Lanthanide Cations. *J. Am. Chem. Soc.* **2011,** *133*, 1220-1223.

17. Liu, Y.; Li, G.; Li, X.; Cui, Y., Cation-Dependent Nonlinear Optical Behavior in an Octupolar 3d Anionic Metal–Organic Open Framework. *Angew. Chem. Int. Ed.* **2007,** *46*, 6301-6304.

18. Xue, D.-X.; Cairns, A. J.; Belmabkhout, Y.; Wojtas, L.; Liu, Y.; Alkordi, M. H.; Eddaoudi, M., Tunable Rare-Earth Fcu-Mofs: A Platform for Systematic Enhancement of Co2 Adsorption Energetics and Uptake. *J. Am. Chem. Soc.* **2013,** *135*, 7660-7667.

19. Chen, S.; Zhang, J.; Wu, T.; Feng, P.; Bu, X., Multiroute Synthesis of Porous Anionic Frameworks and Size-Tunable Extraframework Organic Cation-Controlled Gas Sorption Properties. *J. Am. Chem. Soc.* **2009,** *131*, 16027-16029.

20. Sadakiyo, M.; Ōkawa, H.; Shigematsu, A.; Ohba, M.; Yamada, T.; Kitagawa, H., Promotion of Low-Humidity Proton Conduction by Controlling Hydrophilicity in Layered Metal–Organic Frameworks. *J. Am. Chem. Soc.* **2012,** *134*, 5472-5475.

21. Xue, D.-X.; Belmabkhout, Y.; Shekhah, O.; Jiang, H.; Adil, K.; Cairns, A. J.; Eddaoudi, M., Tunable Rare Earth Fcu-Mof Platform: Access to Adsorption Kinetics Driven Gas/Vapor Separations Via Pore Size Contraction. *J. Am. Chem. Soc.* **2015,** *137*, 5034-5040.

22. Alezi, D.; Peedikakkal, A. M. P.; Weseliński, Ł. J.; Guillerm, V.; Belmabkhout, Y.; Cairns, A. J.; Chen, Z.; Wojtas, Ł.; Eddaoudi, M., Quest for Highly Connected Metal–Organic Framework Platforms: Rare-Earth Polynuclear Clusters Versatility Meets Net Topology Needs. *J. Am. Chem. Soc.* **2015,** *137*, 5421-5430.

23. Yang, H.; Wang, Y.; Krishna, R.; Jia, X.; Wang, Y.; Hong, A. N.; Dang, C.; Castillo, H. E.; Bu, X.; Feng, P., Pore-Space-Partition-Enabled Exceptional Ethane Uptake and Ethane-Selective Ethane–Ethylene Separation. *J. Am. Chem. Soc.* **2020,** *142*, 2222-2227.

24. Wang, Y.; Jia, X.; Yang, H.; Wang, Y.; Chen, X.; Hong, A. N.; Li, J.; Bu, X.; Feng, P., A Strategy for Constructing Pore-Space-Partitioned Mofs with High Uptake Capacity for C2 Hydrocarbons and Co2. *Angew. Chem. Int. Ed.* **2020,** *59*, 19027-19030.

25. Zhao, X.; Bu, X.; Nguyen, E. T.; Zhai, Q.-G.; Mao, C.; Feng, P., Multivariable Modular Design of Pore Space Partition. *J. Am. Chem. Soc.* **2016,** *138*, 15102-15105.

26. Ye, Y.; Ma, Z.; Lin, R. B.; Krishna, R.; Zhou, W.; Lin, Q.; Zhang, Z.; Xiang, S.; Chen, B., Pore Space Partition within a Metal-Organic Framework for Highly Efficient C2h2/Co2 Separation. *J. Am. Chem. Soc.* **2019,** *141*, 4130-4136.

27. Hong, A. N.; Yang, H.; Li, T.; Wang, Y.; Wang, Y.; Jia, X.; Zhou, A.; Kusumoputro, E.; Li, J.; Bu, X.; Feng, P., Pore-Space Partition and Optimization for Propane-Selective High-Performance Propane/Propylene Separation. *ACS Appl. Mater. Interfaces* **2021,** *13*, 52160-52166.

28. Wang, Y.; Zhao, X.; Yang, H.; Bu, X.; Wang, Y.; Jia, X.; Li, J.; Feng, P., A Tale of Two Trimers from Two Different Worlds: A Cof-Inspired Synthetic Strategy for Pore-Space Partitioning of Mofs. *Angew. Chem. Int. Ed.* **2019,** *58*, 6316-6320.

29. Wei, Y.-S.; Zhang, M.; Kitta, M.; Liu, Z.; Horike, S.; Xu, Q., A Single-Crystal Open-Capsule Metal–Organic Framework. *J. Am. Chem. Soc.* **2019,** *141*, 7906-7916.

30. Yang, H.-R.; Chen, W.-Y.; Chen, D.-M.; Zheng, Y.-P.; Fang, S.-M., A Pacs-Type Metal-Organic Framework Based on [Cd3(Oh)] Clusters for Effective C2h2/Co2 Separation and fluorescent Detection of Tnp in Water. *J. Solid State Chem.* **2020,** *291*, 121658.

31. Xue, Y. Y.; Bai, X. Y.; Zhang, J.; Wang, Y.; Li, S. N.; Jiang, Y. C.; Hu, M. C.; Zhai, Q. G., Precise Pore Space Partitions Combined with High-Density Hydrogen-Bonding Acceptors within Metal-Organic Frameworks for Highly Efficient Acetylene Storage and Separation. *Angew. Chem. Int. Ed. Engl.* **2021,** *60*, 10122-10128.

32. Yakiyama, Y.; Ueda, A.; Morita, Y.; Kawano, M., Crystal Surface Mediated Structure Transformation of a Kinetic Framework Composed of Multi-Interactive Ligand Tphap and Co(Ii). *Chem. Commun.* **2012,** *48*, 10651-10653.

33. Ding, M.; Cai, X.; Jiang, H.-L., Improving Mof Stability: Approaches and Applications. *Chem. Sci.* **2019,** *10*, 10209-10230.

34. McHugh, L. N.; McPherson, M. J.; McCormick, L. J.; Morris, S. A.; Wheatley, P. S.; Teat, S. J.; McKay, D.; Dawson, D. M.; Sansome, C. E. F.; Ashbrook, S. E.; Stone, C. A.; Smith, M. W.; Morris, R. E., Hydrolytic Stability in Hemilabile Metal–Organic Frameworks. *Nat. Chem.* **2018,** *10*, 1096-1102.

35. Zhao, J.; He, X.; Zhang, Y.; Zhu, J.; Shen, X.; Zhu, D., Highly Water Stable Lanthanide Metal–Organic Frameworks Constructed from 2,2′-Disulfonyl-4,4′-Biphenyldicarboxylic Acid: Syntheses, Structures, and Properties. *Cryst. Growth Des.* **2017,** *17*, 5524-5532.

36. Chen, S.; Behera, N.; Yang, C.; Dong, Q.; Zheng, B.; Li, Y.; Tang, Q.; Wang, Z.; Wang, Y.; Duan, J., A Chemically Stable Nanoporous Coordination Polymer with Fixed and Free Cu2+ Ions for Boosted C2h2/Co2 Separation. *Nano Research* **2021,** *14*, 546-553.

37. Liu, R.; Liu, Q.-Y.; Krishna, R.; Wang, W.; He, C.-T.; Wang, Y.-L., Water-Stable Europium 1,3,6,8-Tetrakis(4-Carboxylphenyl)Pyrene Framework for Efficient C2h2/Co2 Separation. *Inorg. Chem.* **2019,** *58*, 5089-5095.

38. Ko, N.; Choi, P. G.; Hong, J.; Yeo, M.; Sung, S.; Cordova, K. E.; Park, H. J.; Yang, J. K.; Kim, J., Tailoring the Water Adsorption Properties of Mil-101 Metal–Organic Frameworks by Partial Functionalization. *J. Mater. Chem. A* **2015,** *3*, 2057-2064.

39. Ma, H. F.; Liu, Q. Y.; Wang, Y. L.; Yin, S. G., A Water-Stable Anionic Metal-Organic Framework Constructed from Columnar Zinc-Adeninate Units for Highly

Selective Light Hydrocarbon Separation and Efficient Separation of Organic Dyes. *Inorg. Chem.* **2017,** *56*, 2919-2925.

40. Atallah, H.; M, E. L. M.; Jelle, A.; Lough, A.; Hmadeh, M., A Highly Stable Indium Based Metal Organic Framework for Efficient Arsenic Removal from Water. *Dalton Trans* **2018,** *47*, 799-806.

41. Wang, X.; Qin, T.; Bao, S.-S.; Zhang, Y.-C.; Shen, X.; Zheng, L.-M.; Zhu, D., Facile Synthesis of a Water Stable 3d Eu-Mof Showing High Proton Conductivity and Its Application as a Sensitive Luminescent Sensor for Cu2+ Ions. *J. Mater. Chem. A* **2016,** *4*, 16484-16489.

42. Di, Z.; Liu, C.; Pang, J.; Chen, C.; Hu, F.; Yuan, D.; Wu, M.; Hong, M., Cage-Like Porous Materials with Simultaneous High C2 H2 Storage and Excellent C2 H2 /Co2 Separation Performance. *Angew. Chem. Int. Ed. Engl.* **2021**.

43. Moreau, F.; da Silva, I.; Al Smail, N. H.; Easun, T. L.; Savage, M.; Godfrey, H. G. W.; Parker, S. F.; Manuel, P.; Yang, S.; Schröder, M., Unravelling Exceptional Acetylene and Carbon Dioxide Adsorption within a Tetra-Amide Functionalized Metal-Organic Framework. *Nat. Commun* **2017,** *8*, 14085.

44. Pang, J.; Jiang, F.; Wu, M.; Liu, C.; Su, K.; Lu, W.; Yuan, D.; Hong, M., A Porous Metal-Organic Framework with Ultrahigh Acetylene Uptake Capacity under Ambient Conditions. *Nat. Commun* **2015,** *6*, 7575.

45. Li, Q.; Wu, N.; Li, J.; Wu, D., A Highly Connected Trinuclear Cluster Based Metal-Organic Framework for Efficient Separation of C2h2/C2h4 and C2h2/Co2. *Inorg. Chem.* **2020,** *59*, 13005-13008.

46. Chen, D.-M.; Tian, J.-Y.; Liu, C.-S.; Chen, M.; Du, M., Charge Control in Two Isostructural Anionic/Cationic Coii Coordination Frameworks for Enhanced Acetylene Capture. *Chem. Eur. J.* **2016,** *22*, 15035-15041.

47. Chen, D.-M.; Zhang, N.-N.; Tian, J.-Y.; Liu, C.-S.; Du, M., Quest for the Ncb-Type Metal-Organic Framework Platform: A Bifunctional Ligand Approach Meets Net Topology Needs. *Inorg. Chem.* **2017,** *56*, 7328-7331.

48. Zhang, J.-W.; Hu, M.-C.; Li, S.-N.; Jiang, Y.-C.; Zhai, Q.-G., Ligand Torsion Triggered Two Robust Fe-Tetratopic Carboxylate Frameworks with Enhanced Gas Uptake and Separation Performance. *Chem. Eur. J.* **2017,** *23*, 6693-6700.

49. Duan, J.; Jin, W.; Krishna, R., Natural Gas Purification Using a Porous Coordination Polymer with Water and Chemical Stability. *Inorg. Chem.* **2015,** *54*, 4279-4284.

50. Chen, D.-M.; Sun, C.-X.; Zhang, N.-N.; Si, H.-H.; Liu, C.-S.; Du, M., Tunable Robust Pacs-Mofs: A Platform for Systematic Enhancement of the C2h2 Uptake and C2h2/C2h4 Separation Performance. *Inorg. Chem.* **2018,** *57*, 2883-2889.

51. Liu, L.; Yao, Z.; Ye, Y.; Yang, Y.; Lin, Q.; Zhang, Z.; O'Keeffe, M.; Xiang, S., Integrating the Pillared-Layer Strategy and Pore-Space Partition Method to Construct Multicomponent Mofs for C2h2/Co2 Separation. *J. Am. Chem. Soc.* **2020,** *142*, 9258-9266.

52. Li, Y.-Z.; Wang, H.-H.; Wang, G.-D.; Hou, L.; Wang, Y.-Y.; Zhu, Z., A Dy6-Cluster-Based Fcu-Mof with Efficient Separation of C2h2/C2h4 and Selective Adsorption of Benzene. *Inorganic Chemistry Frontiers* **2021,** *8*, 376-382.

53. Liu, Z.; Lv, L.; He, Y.; Feng, Y., An Anionic Metal–Organic Framework Constructed from a Triazole-Functionalized Diisophthalate Featuring Hierarchical Cages for Selective Adsorptive C2h2/Ch4 and Co2/Ch4 Separation. *CrystEngComm* **2017,** *19*, 2795-2801.

54. Fan, L.; Zhou, P.; Wang, X.; Yue, L.; Li, L.; He, Y., Rational Construction and Performance Regulation of an in(Iii)-Tetraisophthalate Framework for One-Step Adsorption-Phase Purification of C2h4 from C2 Hydrocarbons. *Inorg. Chem.* **2021,** *60*, 10819-10829.

55. Lv, H.-J.; Li, Y.-P.; Xue, Y.-Y.; Jiang, Y.-C.; Li, S.-N.; Hu, M.-C.; Zhai, Q.-G., Systematic Regulation of C2h2/Co2 Separation by 3p-Block Open Metal Sites in a Robust Metal–Organic Framework Platform. *Inorg. Chem.* **2020,** *59*, 4825-4834.

56. Yang, H.; Trieu, T. X.; Zhao, X.; Wang, Y.; Wang, Y.; Feng, P.; Bu, X., Lock-and-Key and Shape-Memory Effects in an Unconventional Synthetic Path to Magnesium Metal–Organic Frameworks. *Angew. Chem. Int. Ed.* **2019,** *58*, 11757-11762.

57. Lee, J.; Chuah, C. Y.; Kim, J.; Kim, Y.; Ko, N.; Seo, Y.; Kim, K.; Bae, T. H.; Lee, E., Separation of Acetylene from Carbon Dioxide and Ethylene by a Water-Stable Microporous Metal–Organic Framework with Aligned Imidazolium Groups inside the Channels. *Angew. Chem. Int. Ed.* **2018,** *57*, 7869-7873.

58. Li, Y.-Z.; Wang, G.-D.; Yang, H.-Y.; Hou, L.; Wang, Y.-Y.; Zhu, Z., New Supercage Metal–Organic Framework Based on Allopurinol Ligands Showing Acetylene Storage and Separation. *Chem. Eur. J.* **2020,** *26*, 16402-16407.

59. Zhang, J.-W.; Hu, M.-C.; Li, S.-N.; Jiang, Y.-C.; Zhai, Q.-G., Microporous Rod Metal–Organic Frameworks with Diverse Zn/Cd–Triazolate Ribbons as Secondary

Building Units for Co2 Uptake and Selective Adsorption of Hydrocarbons. *Dalton Trans.* **2017,** *46*, 836-844.

60. Liu, L.; Yao, Z.; Ye, Y.; Chen, L.; Lin, Q.; Yang, Y.; Zhang, Z.; Xiang, S., Robustness, Selective Gas Separation, and Nitrobenzene Sensing on Two Isomers of Cadmium Metal–Organic Frameworks Containing Various Metal–O–Metal Chains. *Inorg. Chem.* **2018,** *57*, 12961-12968.

61. Chu, Q.; Zhang, B.; Zhou, H.; Liu, B.; Hou, L.; Wang, Y.-Y., Effective C2h2 Separation and Nitrofurazone Detection in a Stable Indium–Organic Framework. *Inorg. Chem.* **2020,** *59*, 2853-2860.

62. Zhan, C.-H.; Huang, D.-P.; Wang, Y.; Mao, W.-T.; Wang, X.-J.; Jiang, Z.-G.; Feng, Y.-L., Four Anionic Ln-Mofs for Remarkable Separation of C2h2–Ch4/Co2–Ch4 and Highly Sensitive Sensing of Nitrobenzene. *CrystEngComm* **2021,** *23*, 2788-2792.

63. Gu, S. F.; Xiong, X. H.; Gong, L. L.; Zhang, H. P.; Xu, Y.; Feng, X. F.; Luo, F., Classified Encapsulation of an Organic Dye and Metal–Organic Complex in Different Molecular Compartments for White-Light Emission and Selective Adsorption of C2h2 over Co2. *Inorg. Chem.* **2021,** *60*, 8211-8217.

64. Huang, P.; Chen, C.; Hong, Z.; Pang, J.; Wu, M.; Jiang, F.; Hong, M., Azobenzene Decorated Nbo-Type Metal–Organic Framework for High-Capacity Storage of Energy Gases. *Inorg. Chem.* **2019,** *58*, 11983-11987.

65. Fan, W.; Wang, X.; Zhang, X.; Liu, X.; Wang, Y.; Kang, Z.; Dai, F.; Xu, B.; Wang, R.; Sun, D., Fine-Tuning the Pore Environment of the Microporous Cu-Mof for High Propylene Storage and Efficient Separation of Light Hydrocarbons. *ACS Cent. Sci.* **2019,** *5*, 1261-1268.

66. Böhme, U.; Barth, B.; Paula, C.; Kuhnt, A.; Schwieger, W.; Mundstock, A.; Caro, J.; Hartmann, M., Ethene/Ethane and Propene/Propane Separation Via the Olefin and Paraffin Selective Metal–Organic Framework Adsorbents Cpo-27 and Zif-8. *Langmuir : the ACS journal of surfaces and colloids* **2013,** *29*, 8592-8600.

67. Yang, L.; Cui, X.; Ding, Q.; Wang, Q.; Jin, A.; Ge, L.; Xing, H., Polycatenated Molecular Cage-Based Propane Trap for Propylene Purification with Recorded Selectivity. *ACS Appl. Mater. Interfaces* **2019,** *12*, 2525–2530.

68. He, C.; Wang, Y.; Chen, Y.; Wang, X.; Yang, J.; Li, L.; Li, J., Modification of the Pore Environment in Uio-Type Metal-Organic Framework toward Boosting the Separation of Propane/Propylene. *Chem. Eng. J.* **2021,** *403*, 126428.

Chapter 4: Cationic Partitioned-*acs* Frameworks and C_2H_2/CO_2 Separation

4.1 Introduction

The capacity for strategic optimization of space and functionality in solid-state materials is a central facet to many applications. One of such is the purification of acetylene (C_2H_2), an important organic building block whose industrial production yields C_2H_2/CO_2 mixtures.[1] Employment of low-cost porous adsorbents for the selective adsorption of C_2H_2 presents a promising purification alternative with lower energy demand and higher sustainability. Among various adsorbents, MOFs have attracted tremendous attention owing to their highly tunable pore size and pore chemistry. Since the first reported C_2H_2-selective adsorbent, $Cu_2(pzdc)_2(pyz)$, in 2005,[2] many excellent adsorbents have been developed to address C_2H_2/CO_2 separation. Nevertheless, a general tradeoff between C_2H_2 uptake capacity and C_2H_2/CO_2 selectivity is often observed, since a boost in pore-space (capacity) presumably leads to poor host-guest interaction (selectivity), and vice versa.

An extra level of difficulty is added to simultaneously maximize uptake and selectivity. Materials with both higher C_2H_2 and CO_2 uptakes may offer higher IAST selectivity. However, optimized selectivity is reached with increase of C_2H_2 and decrease

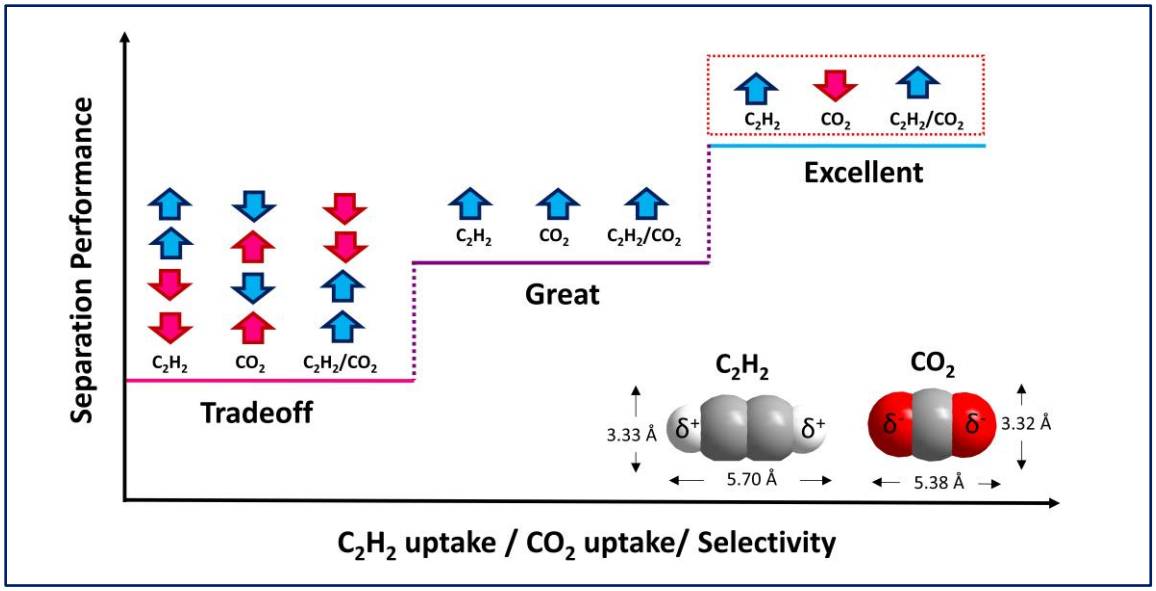

Figure 4.1 Classification of gas separation performance by a combination of individual gas uptake and selectivity.

of CO_2 (Figure 4.1). Our review of literature reveals two possible approaches that could lead to the strategic design of materials with optimized separation performance. One method is microregulating pore-space of ultramicroporous materials to better fit C_2H_2 molecules.[3-4] For instance, the substitution of TiF_6^{2-} with SiF_6^{2-} from TIFSIX-4-Ni to SIFSIX-21-Ni, allows for better fitting of C_2H_2, less favorable fitting of CO_2 and overall higher selectivity.[5] Introduction of functional sites is another promising method to optimize separation performance.[6-9] For instance, substituting 1,3-benzenedicarboxylate with a smaller, oxygen-bearing 2,5-thiophenedicarboxylate from CAU-10H to MIL-160 results in stronger hydrogen bonding interactions, undesirable O-bonding interactions, and overall higher selectivity performance.[10] While these results are promising, continuing effort is needed to promote porous materials to commercialization stage.

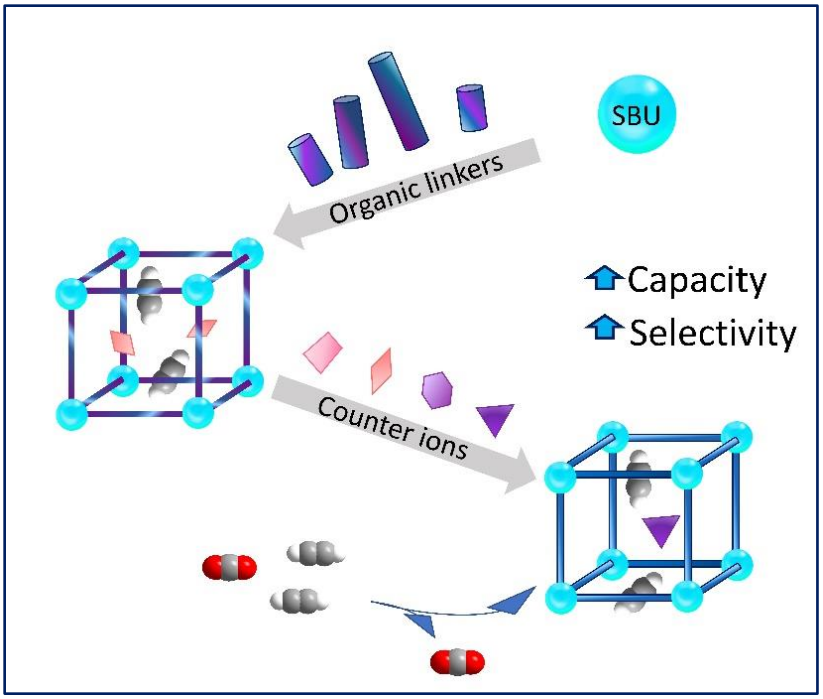

Figure 4.2 A tandem modulation approach to combat uptake and selectivity tradeoff.

Counter-balancing ion is an important, yet often overlooked variable in C_2H_2 sorption studies.[11-12] In addition to balancing framework charge, a counter ion with ideal size, functionality and spatial orientation could in theory, segregate large cavities into tight binding pockets for enhanced uptakes and/or regulate influx of gas through different charge-induced forces. In practice, however, mismatches of inherent properties between parent framework and counter-balancing ion could have unintended sacrifices such as reduced preferential adsorbent-adsorbate interactions, porosity, or stability; and thus, resulting in modest performance.

We believe that such compromises could be avoided through dual modulation of both parent framework and counter balancing ions. As shown in Figure 4.1, a tandem modulation approach is proposed to optimize both parent framework and extra charge

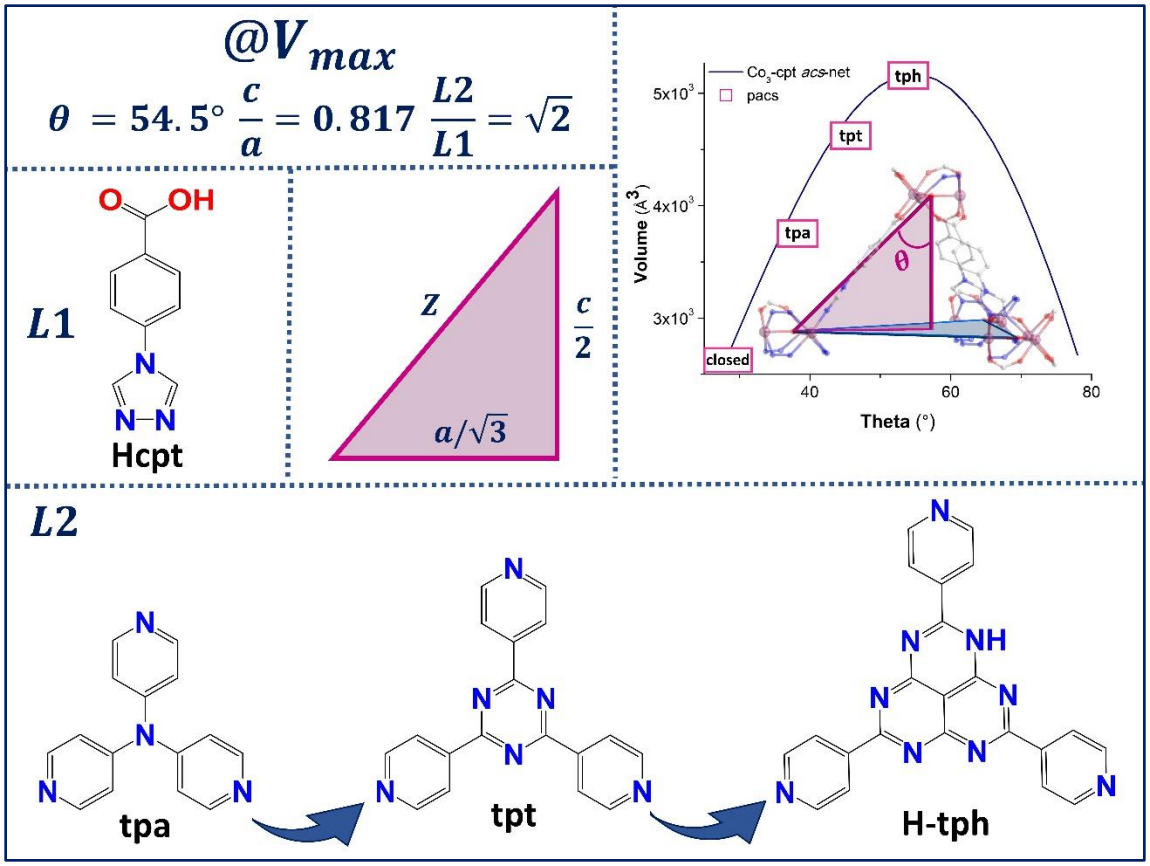

Figure 4.3 Volume-max calculation and core-expansion approach employed to optimize pore volume of cationic cpt-based framework. Through core-expansion approach, L2 of varied lengths are inserted into cpt-based Mil-88 framework, resulting in systematic widening of theta angle, and enlargement of crystallographic volume.

balancing ion. While not mutually exclusive, structural optimization of parent framework mainly boosts uptake capacity, and counter-balancing ion helps discriminate different gas molecules. The synergistic cooperation between parent framework and charge-balancing species will bear geometrically ideal functional pore that allows for maximal C_2H_2 uptake capacity and C_2H_2/CO_2 selectivity, simultaneously.

Herein, we show the effectiveness of this strategy through a family of cationic *pacs* materials. From trigonometric derivation described in Chapter 2, estimated maximum volume of the framework occurs when the length ratio of L2/L1 is approximately $\sqrt{2}$ or

1.41 (Figure 4.3). In accounting for ideal C_2H_2-selective adsorbents to generally have pore size less than 7 Å, we fix L1 linker to the (-1) charged H-cpt (4-(*p*-carboxyphenyl)-1,2,4-triazole). With Hcpt at 8.4 Å, a L2 at ~11.9 Å would allow the cationic *pacs* material to have the largest pore volume. Three L2 linkers of varied lengths are identified through core-expansion strategy: tpa (7.3 Å) tpt (9.6 Å) and H-tph (11.9 Å), with L1/L2 ratios approximately 0.869, 1.14, 1.42, respectively. Insertion of these L2 into $[Co_3(OH)(cpt)_3]^+$ framework results in three novel cationic *pacs* materials for examination of selective C_2H_2 uptake trend. Optimization of pore volume is complemented by micro-regulation of different inorganic charge-balancing ions for best selectivity. In total, 8 isostructural cationic cpt-based *pacs* materials are constructed to demonstrate C_2H_2/CO_2 predicted gas separation trends.

4.2. Experimental Section

4.2.1 Chemicals and Materials

Iron (II) chloride tetrahydrate ($FeCl_2 \cdot 4H_2O$), Cobalt (II) chloride hexa hydrate ($CoCl_2 \cdot 4H_2O$), Cobalt (II) bromide hydrate ($CoBr_2 \cdot xH_2O$), Cobalt (II) perchlorate hexahydrate ($Co(ClO_4)_2 \cdot 6H_2O$), Cobalt (II) tetrafluoroborate hydrate ($Co(BF_4)_2 \cdot xH_2O$) (Nickel (II) chloride hexahydrate ($NiCl_2 \cdot 6H_2O$), acetone, ethanol (EtOH), N,N-dimethylacetamide (DMA), N,N-dimethylformamide (DMF), dichloromethane (CH_2Cl_2), trifluoroacetic acid (TFA), fluoroboric acid 48 w.t. % (HBF_4) and hydrochloric acid 38 w.t. % (HCl) were purchased from Fischer Scientific Co., while N-methylformamide (NMF), 4-pyridylamidine hydrochloride, sodium tricyanomethanide ($Na(C(CN)_3)$), 2,4,6-tri(4-pyridinyl)-1,3,5-triazine (tpt), 1,1,1,5,5,5-hexafluoro-2,4- pentanedione (HFP) were obtained from TCI-America while tri(4-pyridinyl)amine (tpa), 4-(*p*-carboxyphenyl)-1,2,4-triazole (Hcpt) were purchased from ET Co., Ltd. 2,5,8-tri-(4'-pyridyl)-1,3,4,6,7,9-hexaazaphenalene (H-tph) was synthesized according to Chapter 3.2.2**.** All reagents were used as received without further purification.

4.2.2 Synthesis of Cationic *pacs* Materials

(CPM-124a-Co-Cl) Co_3-cpt-tpa-Cl: In a 20 mL glass vial, $CoCl_2 \cdot 6H_2O$ (76 mg, 0.3 mmol), Hcpt (57 mg, 0.3 mmol), and H-tpa (42 mg, 0.1 mmol) were dissolved in 4.0 g NMF, 2.0 g DMPU, and 60 μL HFP. After stirring for 2 hours, the vial was placed in a 140 ℃ oven for 3 days. Red-orange hexagonal shaped crystals were obtained after solution was cooled to ambient temperature.

(CPM-124b-Co-Cl) Co_3-cpt-tpt-Cl: In a 20 mL glass vial, $CoCl_2 \cdot 6H_2O$ (76 mg, 0.3 mmol), Hcpt (57 mg, 0.3 mmol), and H-tphap (42 mg, 0.1 mmol) were dissolved in 6.0 g DMA and 0.6 g HBF_4 (48 w.t. %). After stirring for 2 hours, the vial was placed in a 140 °C oven for 2 days. Red-orange hexagonal shaped crystals were obtained after solution was cooled to ambient temperature.

(CPM-124c-Co-Cl) Co_3-cpt-tph-Cl: In a 20 mL glass vial, $CoCl_2 \cdot 6H_2O$ (76 mg, 0.3 mmol), Hcpt (57 mg, 0.3 mmol), and H-tph (42 mg, 0.1 mmol) were dissolved in 6.0 g DMA and 1.0 g HBF_4 (48 w.t. %). After stirring for 2 hours, the vial was placed in a 90 °C oven for 2 days. Red-orange hexagonal shaped crystals were obtained after solution was cooled to ambient temperature.

(CPM-124c-Co-Br) Co_3-cpt-tph-Br: In a 20 mL glass vial, $CoBr_2 \cdot 4H_2O$ (98 mg, 0.3 mmol), Hcpt (57 mg, 0.3 mmol), and H-tph (42 mg, 0.1 mmol) were dissolved in 4.0 g NMF and 2.0 g DMPU, 0.06 g HFP. After stirring for 2 hours, the vial was placed in a 140 °C oven for 3 days. Red-orange hexagonal shaped crystals were obtained after solution was cooled to ambient temperature.

(CPM-124c-ClO_4) Co_3-cpt-tph-ClO_4: In a 20 mL glass vial, $Co(ClO_4)_2 \cdot 6H_2O$ (105 mg, 0.3 mmol), Hcpt (57 mg, 0.3 mmol), and H-tph (42 mg, 0.1 mmol) were dissolved in 6.0 g DMF 2.0 g DMPU, and 0.06 g HFP. After stirring for 2 hours, the vial was placed in a 120 °C oven for 3 days. Red-orange hexagonal shaped crystals were obtained after solution was cooled to ambient temperature.

(CPM-124c-BF_4) Co_3-cpt-tph-BF_4: In a 20 mL glass vial, $Co(BF_4)_2 \cdot 4H_2O$ (105 mg, 0.3 mmol), Hcpt (57 mg, 0.3 mmol), and H-tph (42 mg, 0.1 mmol) were dissolved in 6.0 g

DMA and 0.6 g HBF_4 (48 w.t. %). After stirring for 2 hours, the vial was placed in a 100 ℃ oven for 3 days. Red-orange hexagonal shaped crystals were obtained after solution was cooled to ambient temperature.

(CPM-124c-Fe-Cl) Fe_3-cpt-tph-Cl: In a 20 mL glass vial, $FeCl_2 \cdot 4H_2O$ (60 mg, 0.3 mmol), Hcpt (57 mg, 0.3 mmol), and H-tph (42 mg, 0.1 mmol) were dissolved in 4.0 g DMF, 2.0 g DMPU, and 60 μL HFP. After stirring for 2 hours, the vial was placed in a 140 ℃ oven for 5 days. Orange-brown microcrystalline were obtained after solution was cooled to ambient temperature.

(CPM-124c-Ni-Cl) Ni_3-cpt-tph-Cl: In a 20 mL glass vial, $NiCl_2 \cdot 6H_2O$ (75 mg, 0.3 mmol), Hcpt (57 mg, 0.3 mmol), and H-tph (42 mg, 0.1 mmol) were dissolved in 4.0 g NMF, 2.0 g DMPU, and 60 μL HFP. After stirring for 2 hours, the vial was placed in a 140 ℃ oven for 5 days. Green microcrystalline were obtained after solution was cooled to ambient temperature.

4.2.3 Property Characterization

Gas Sorption Measurement. Gas sorption measurements were carried out on a Micromeritics ASAP 2020 and ASAP 2020 Plus physisorption analyzers. The as-synthesized sample was immersed in CH_2Cl_2 and refreshed daily for five consecutive times. The sample was then transferred to the gas sorption tube and the dried under open flow of N_2 gas for 15 minutes. The degas process was carried out at 60 ^oC for 12 hours.

Breakthrough Measurement. Breakthrough experiments for the C_2H_2/CO_2 mixtures were performed in a homemade apparatus. Approximately 0.7346 g of the CH_2Cl_2-exchanged and activated sample was pelletized, broken into pieces and passed through

Sample was activated using the method mentioned above. Then, the sample was pelletized (20-25 MPa) and broken into pieces and captured between 60 and 40 standard mesh sieves. The uniform sized powder was then loaded into a U-shaped glass (length: 13 cm, inner diameter: 0.45 cm), stationed by cottons at both ends. A 10 sccm mass flow controller was used to monitor concentration of He, CO_2 and C_2H_2 gas input. Purity of eluted gas was monitored by mass spectrometer residual gas analysis mass spectrometer from Hiden Co. Sample was regenerated under 60 C with 7 ml/min He flow for 2 h.

Other Characterization: SCXRD, PXRD, TGA and EDS, isosteic heat of adsorption, IAST selectivity and separation potential were obtained as mentioned in 2.2.4.

Table 4.1 Crystal Data summary of CPM-124 *pacs* materials.

Code	*Space Group*	a (Å)	b (Å)	c (Å)	α	β	γ	Vol $(Å)^3$	R(F)
CPM-124a-Co-Cl	P63/mmc	14.473	14.473	20.667	90	90	120	3749	0.13
CPM-124b-Co-Cl	P63/mmc	16.765	16.765	18.936	90	90	120	4609	0.10
CPM-124c-Co-Cl	P63/mmc	19.097	19.097	16.361	90	90	120	5164	0.11
CPM-124c-Co-ClO_4	P63/mmc	19.109	19.109	16.285	90	90	120	5150	0.056

Table 4.2 Elemental analysis of *pacs* in this study by EDS and proposed formula.

MOFs	M/X_1	M/X_2	Σ anions/M_3	Proposed Formula
CPM-124a-Co-Cl	X = Cl 0.75	N/A	2.25	$[Co_3(OH)(cpt)_3(tpa)](Cl)_{2.25}$
CPM-124b-Co-Cl	X = Cl 0.140	X = F 2.08	1.99	$[Co_3(OH)(cpt)_3(tpt)](Cl)_{0.43}(BF_4)_{1.56}$
CPM-124b-Co-Cl	X = Cl 0.157	X = F 1.12	1.32	$[Co_3(OH)(cpt)_3(tph)_{0.68}(H\text{-}tph)_{0.32}](Cl)_{0.47}(BF_4)_{0.84}$
CPM-124c-Co-Cl	X = F 1.70	N/A	1.28	$[Co_3(OH)(cpt)_3(tph)_{0.72}(H\text{-}tph)_{0.32}](BF_4)_{1.28}$
CPM-124c-Co-ClO_4	X = Cl 0.353	N/A	1.06	$[Co_3(OH)(cpt)_3(tph)](ClO_4)_{1.06}$
CPM-124c-Co-Br	X = Br 0.342	N/A	1.03	$[Co_3(OH)(cpt)_3(tph)]Br_{1.03}$
CPM-124c-Ni-Cl	X = Cl 0.351	N/A	1.05	$[Ni_3(OH)(cpt)_3(tph)]Cl_{1.05}$
CPM-124-Fe-Cl	X = Cl 0.333	N/A	1.00	$[Fe_3(OH)(cpt)_3(tph)]Cl$

4.3 Results and Discussion

Insertion of partitioning agents of varied lengths into the $[Co_3(OH)(cpt)_3]^{2+}$ cationic framework allows for construction of novel *pacs* of three different dimensions. As shown in Figure 4.4, enlarging pore-partitioning agent results in enlargement of framework along ab-plane and flattening of framework along c-axis. Single crystal X-ray analysis confirms crystallographic volume expansion from 3749 Å (tpa) to 4609 Å (tpt) and 5109 Å (tph). As predicted by Chapter 2, where L2/L1 = $\sqrt{2}$ at Vol_{max}, CPM-124c-Co-Cl with L2/L1 = 1.42, having the highest volumetric volume. Following confirming of phase purity through PXRD analysis (Figure 4.5), and proper activation method through TGA analysis (Figure 4.7a), N_2 isotherms at 77 K were collected (Figure 4.8a) Brunauer-Emmett-Teller (BET) surface area and volume obtained show increase from 1070 m^2/g (tpa) to 1408 m^2/g (tpt) and 2046 m^2/g (H-tph). The corresponding volumes are 0.392 cm^3/g, 0.530 cm^3/g, and 0.759 cm^3/g. Thus, CPM-124c-Co-Cl, with the most optimal crystallographic volume, exhibits the highest surface area and pore volume.

The dramatic 200% boost in both surface area and pore volume from substitution of tpa to H-tph linker is matched with impressive optimization of C_2H_2 uptake capacity. As shown in Figure 4.8b, CPM-124a-Co-Cl shows modest C_2H_2 of 130 cm^3/g at 298 K, 1 bar. The substitution of tpa with tpt and H-tph results in CPM-124b-Co-Cl and CPM-124c-Co-Cl with much more remarkable uptakes at 156 cm^3/g and 200 cm^3/g, respectively. This C_2H_2 uptake capacity is higher than the previous benchmark ionic material, NBU-8, at 180 cm^3/g.[13] In fact, CPM-124c-Co-Cl exhibits higher C_2H_2 uptake than most C_2H_2-selective materials such as UTSA-74 (104 cm^3/g),[14] UPC-200(Al)-F-BIM (144 cm^3/g),[9] FJU-90

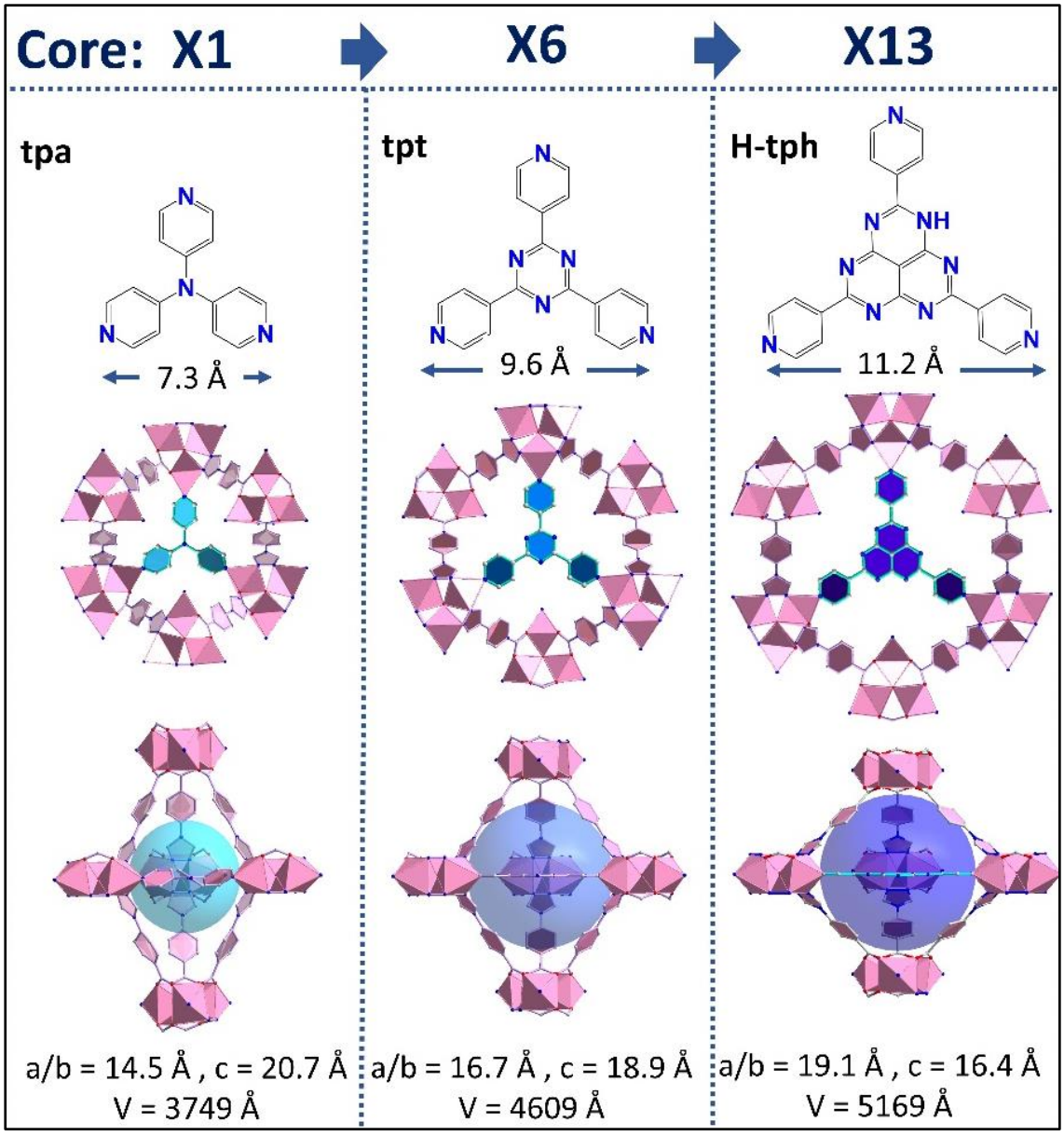

Figure 4.4 C_2H_2 and CO_2 uptake performance of *pacs* materials in this study. (a) C_2H_2 and CO_2 Isotherms at 298 K and (b) 50/50 IAST selectivity comparisons between Co_2-cpt-based *pacs* with different L2, (c) C_2H_2 and CO_2 Isotherms at 298 K and (b) 50/50 IAST selectivity comparisons between cpt-tph-based *pacs* with different transition metal and balancing anions. (e) Effects of tuning different *pacs* modules on the uptake difference between C_2H_2 and CO_2 at 298 K, 1 bar.

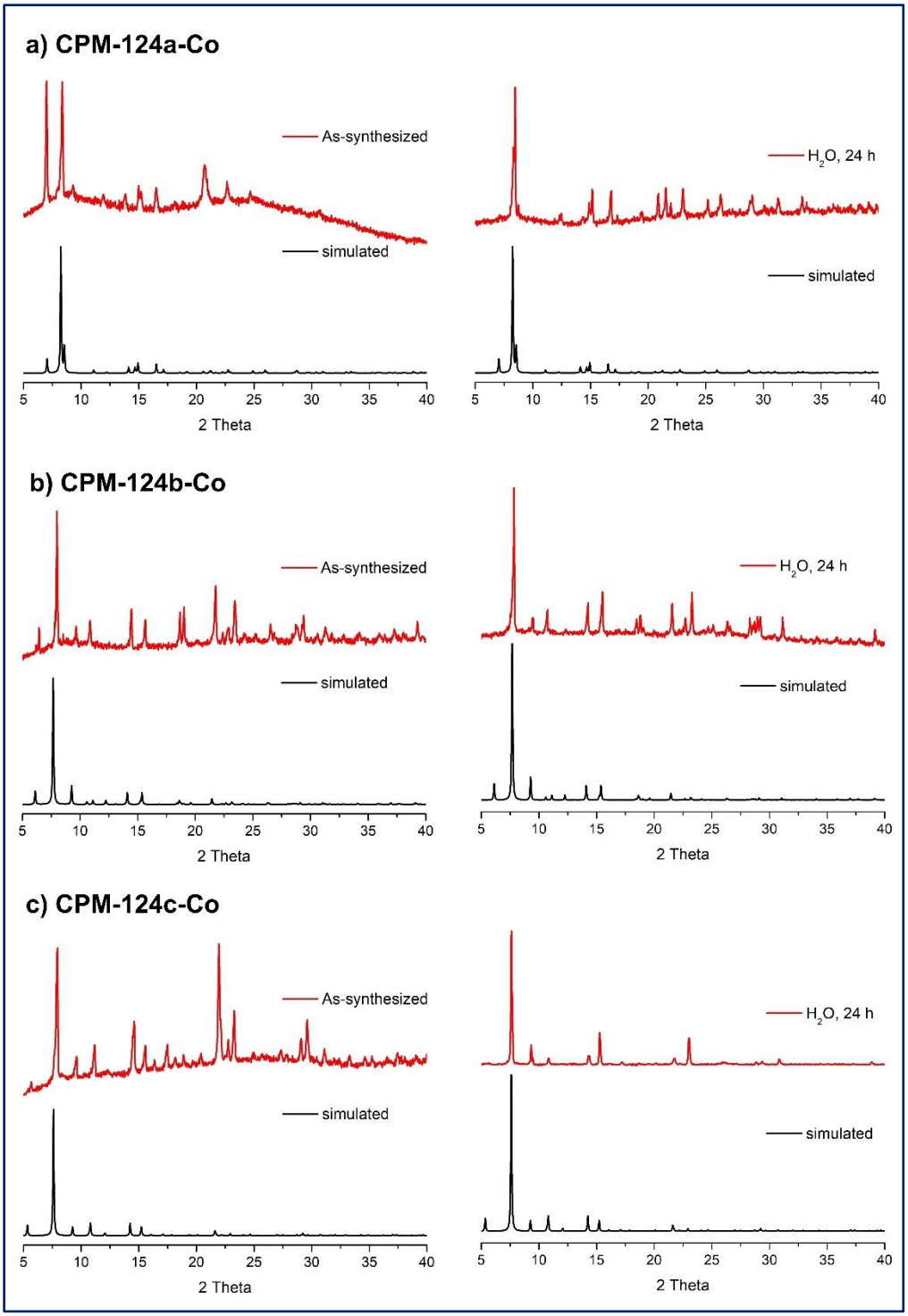

Figure 4.5 PXRD analyses of (a) CPM-124a, (b) CPM-124b, (c) CPM-124c-Co. Left column represents as-synthesized material, whereas column confirms its hydrolytic stability.

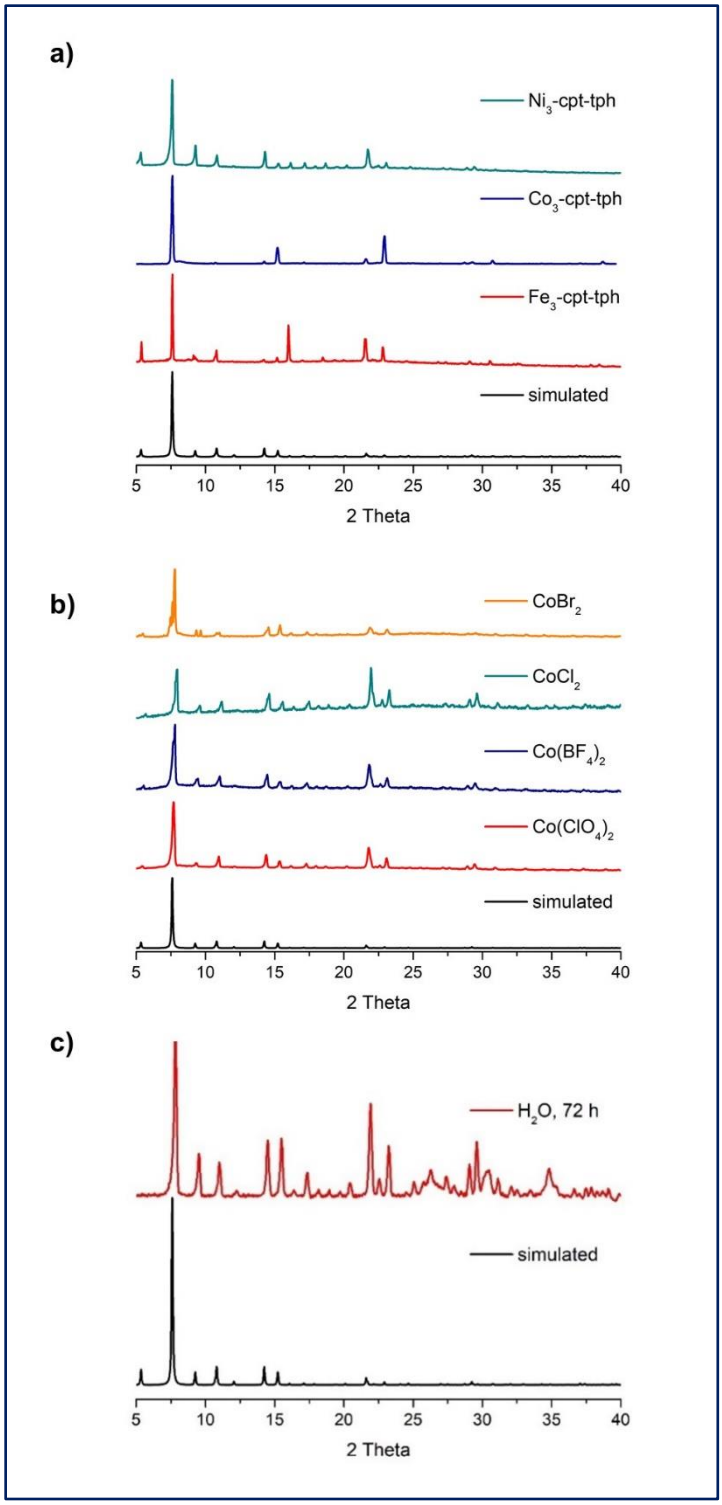

Figure 4.6 Experimental and simulated PXRD patterns for (a) M_3-cpt-tph and (b) Co-cpt-tph-x *pacs* materials. Simulated PXRD obtained from single crystal XRD data of Co_3-cpt-tph (c) hydrolytic stability of CPM-600c-Ni-Cl.

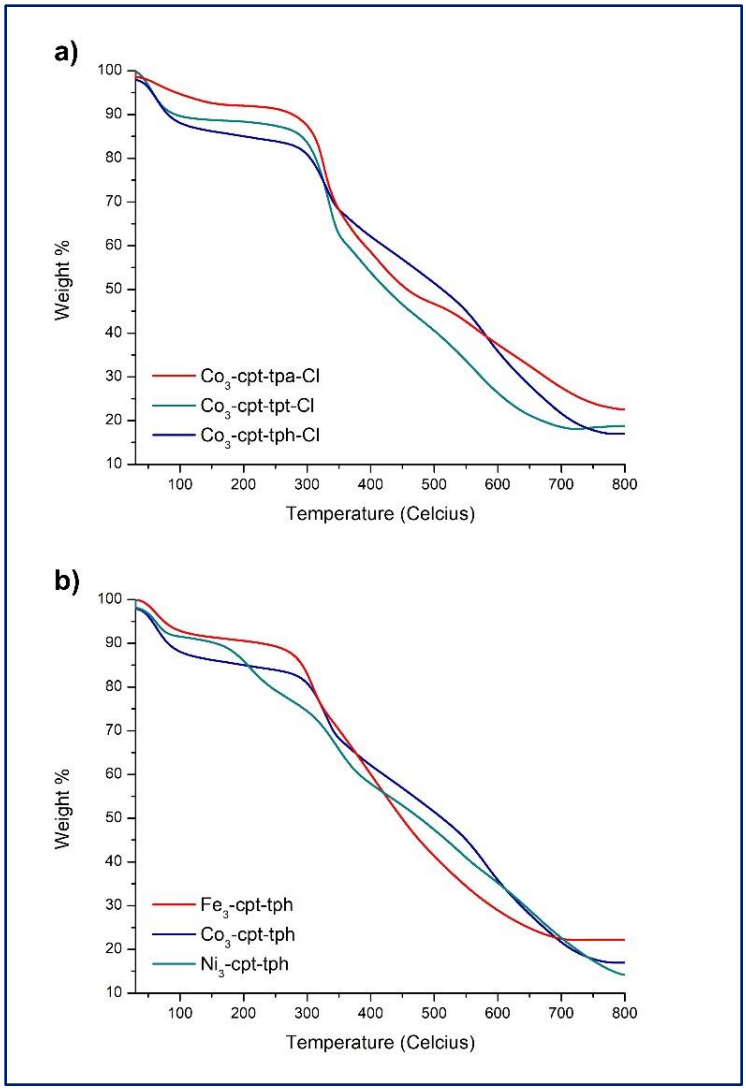

Figure 4.7 TGA figures for CPM-124-based *pacs* materials.

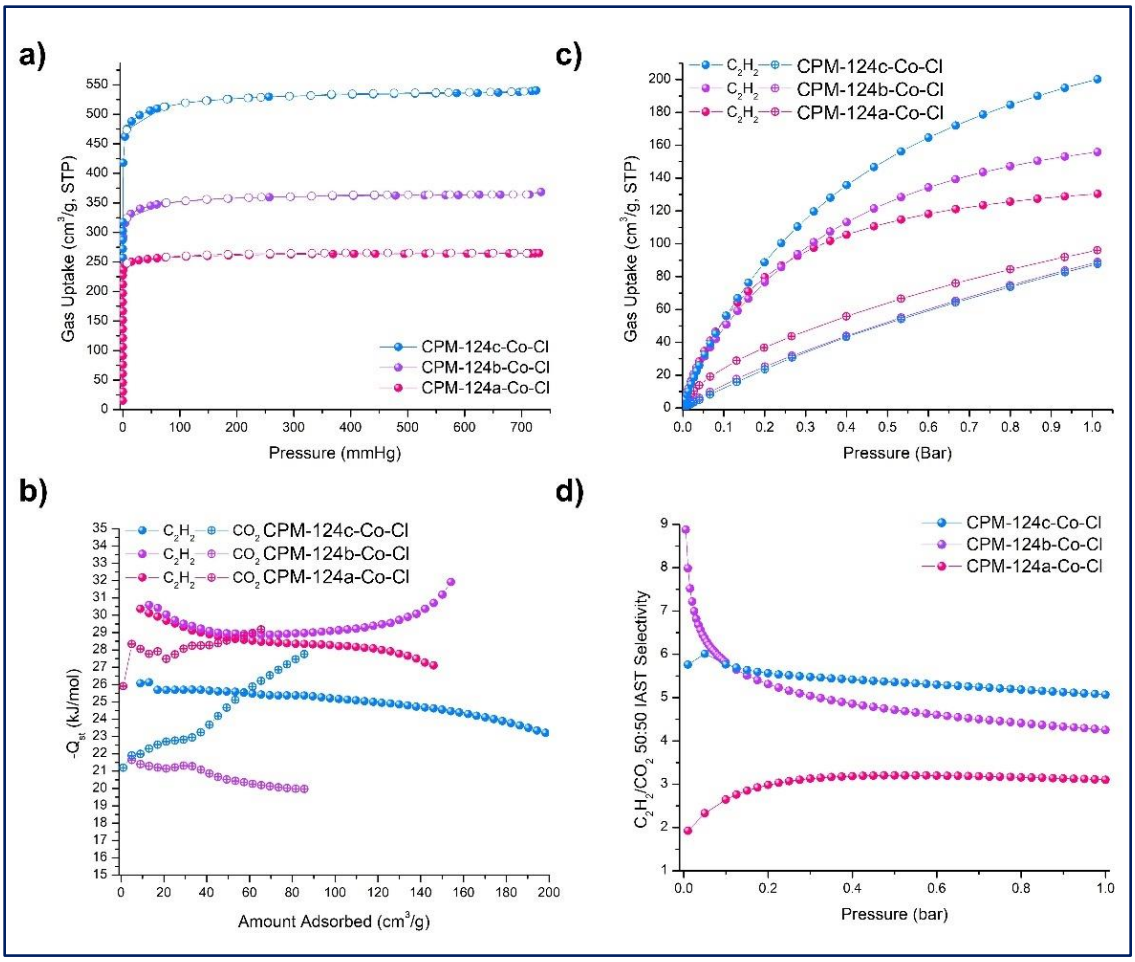

Figure 4.8 Selective gas sorption of CPM-124-x-Co-Cl *pacs* materials. (a) N_2 sorption isotherms at 77 K, (b) C_2H_2 and CO_2 isotherms at 273 K and 298 K, (c) Isosteric heat of adsorption obtained from 273 K and 298 K isotherms (d) 50/50 C_2H_2/CO_2 IAST selectivity.

(180 cm^3/g),[15] SIFSIX-Cu-TPA (185 cm^3/g)[16] and only lower than FJI-H8-Me (229 cm^3/g).[17]

In comparison, the CO_2 uptake trend is in reversed that of the C_2H_2 trend. CPM-124a-Co-Cl, with smallest volume, exhibits the highest CO_2 uptake (96.1 cm^3/g), while, CPM-124c-Co-Cl with largest volume, exhibits lowest CO_2 uptake (87 cm^3/g) at 298 K, 1 bar. The difference between C_2H_2 and CO_2 uptakes is more than tripled, from tpa insertion (34.4 cm^3/g) to tph insertion (113 cm^3/g) at 298 K, 1 bar (Figure 4.10c). In all cases,

isosteric heat of adsorption (Q_{st}^0) calculated based on 273 K and 298 K isotherms are much higher for C_2H_2 (26.1-30.5 kJ/mol), than CO_2 (21.2-25.9 kJ/mol), which is indicative of stronger C_2H_2-*pacs* interactions.

The phenomenal difference in adsorption performance between C_2H_2 and CO_2 prompted us to explore selectivity through ideal adsorbed solution theory (IAST) calculations (Figure 4.7d). Unlike most traditional materials, where increasing uptake capacity generally results in lowering of selectivity, both C_2H_2 uptake and 50/50 C_2H_2/CO_2 IAST selectivity trend in this work follows tpa < tpt < H-tph. Even more remarkable is the fact that CO_2 follow the reversed order of H-tph > tpt > tpa. That is, CPM-124c-Co-Cl, with largest surface area and pore volume, simultaneously exhibits highest C_2H_2 uptake, lowest CO_2 and highest 50/50 C_2H_2/CO_2 IAST selectivity. While materials with higher C_2H_2 and CO_2 uptakes may offer higher IAST selectivity, optimal separation performance is reached when increase of C_2H_2 and selectivity is matched with decrease of CO_2.

We speculate that this unusual high uptake-high selectivity phenomenon lies in the second module of our structure design: the inorganic anion. Crystallographic studies show Cl^- of cationic CPM-124c-Co-Cl is seen near L1 linker of the triangular pore, where it is stabilized by multiple weak Cl···H ion-dipole interactions (2.3-3.5 Å) with triazole and benzene rings (Figure 4.10a). The presence of these chloride anions could further attract C_2H_2 through new Cl···H-C≡C, which manifested in rapid and dramatic C_2H_2 uptakes in low-pressure region. In comparison, CO_2 isotherm remains linear and shallow, representing little gas-adsorbent interaction. While L2 helps optimize pore space for

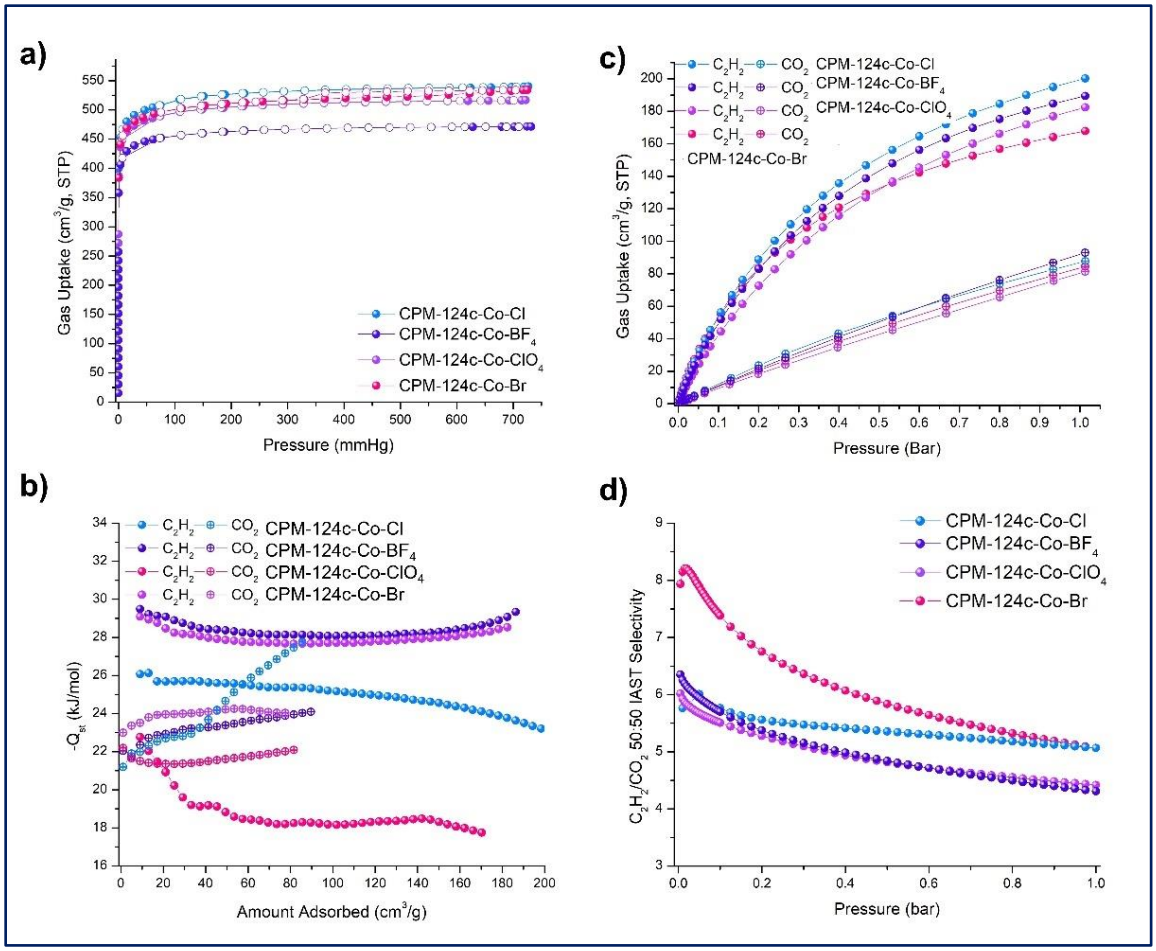

Figure 4.9 Selective gas sorption of CPM-124c-Co-x *pacs* materials. (a) N_2 sorption isotherms at 77 K, (b) C_2H_2 and CO_2 isotherms at 273 K and 298 K, (c) Isosteric heat of adsorption obtained from 273 K and 298 K isotherms (d) 50/50 C_2H_2/CO_2 IAST selectivity.

efficient packing of C_2H_2 molecule, counter anion contributes to strong initial C_2H_2 interaction over CO_2 leading to higher C_2H_2 selectivity.

Further optimization was carried out through introduction of different anions, as inherent chemical properties and geometrical configuration of these anions dictate their spatial arrangement in our *pacs* system. From SCXRD diffraction of CPM-124c-Co-x Cl^- ions show strong dipole interactions near L1 linkers, while ClO_4^- anions reside above or below trimeric clusters and are stabilized by anion-π interactions with surrounding

aromatic rings of L1 (Figure 4.10a-b). In similar framework type, Br^- have been reported to appear in similar positioning to Cl^- whereas BF_4^- appears near ClO_4^- anions. Prior to gas sorption studies, we compared phase purity of CPM-124c-Co-x (x = Cl^-, Br^-, ClO_4^-, BF_4^-) with powder X-ray diffraction (PXRD) (Figure 4.5) and ratio of framework to anion through energy dispersive spectroscopy (EDS) (Table 4.2).

As shown in Figure 4.8a, N_2 sorption isotherms of CPM-124c-Co material with different ions exhibits slightly different N_2 adsorption. The resulting BET surface area and pore volume of CPM-124c-Co-x follows are approximately the same for $Cl^- \approx Br^- \approx ClO_4^-$ and slightly higher for BF_4^- (1827 m^2/g). The C_2H_2 uptake of CPM-124c-Co-x at 0.01 bar, 298 K follows x = $Cl^- > Br^- > ClO_4^- > BF_4^-$, which infers that the spherical anions guarding pore-window show higher attraction towards C_2H_2, than the tetrahedral anions residing inside the cages. At 1 bar, the packing efficiency of C_2H_2 in CPM-124c-Co-x follows $Cl^- > ClO_4^- > BF_4^- > Br^-$. In comparison, CO_2 uptake of different anions in Co_3-cpt-tph are nearly identical at 0.01 bar, but slowly deviate and follow $ClO_4^- > Cl^- > Br^- > BF_4^-$ at 1 bar. More interestingly, Br^- and Cl^- ions resulted in higher 50/50 C_2H_2/CO_2 IAST selectivity at 1 bar than BF_4^- and ClO_4^- ions. As observed from SCXRD, the two different positions may have large contribution towards discrimination of individual gas molecules, leading to different IAST selectivity. Overall, CPM-124c-Co-Cl, exhibits the highest uptake and highest selectivity among different ions, resulting in highest separation potential for breakthrough examination.

Chemical stability of porous materials is an important prerequisite for industrial application. Thus, we investigate impact of different metal ions (Fe^{2+}, Co^{2+}, Ni^{2+}) on

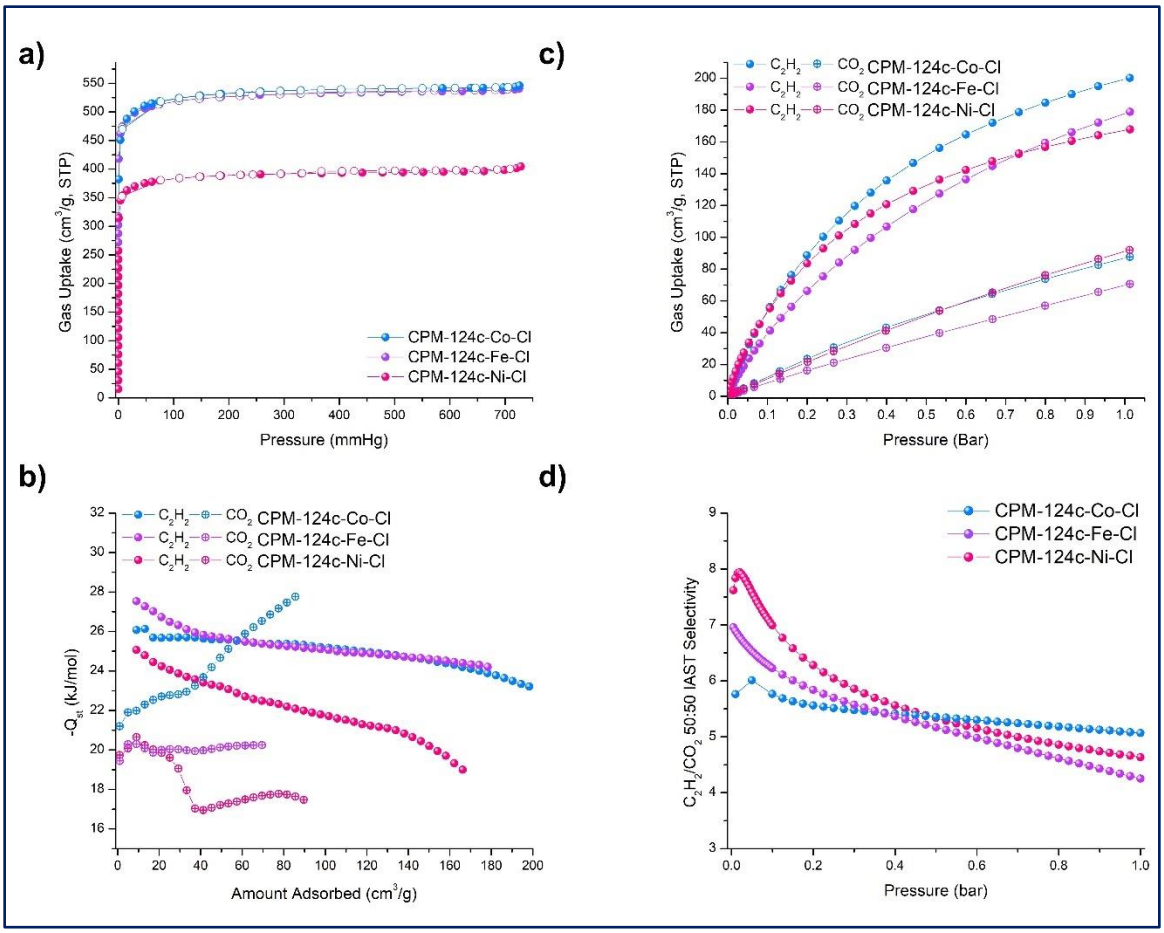

Figure 4.10 Selective gas sorption of CPM-124c-Co-x *pacs* materials. (a) N_2 sorption isotherms at 77 K, (b) C_2H_2 and CO_2 isotherms at 273 K and 298 K, (c) Isosteric heat of adsorption obtained from 273 K and 298 K isotherms (d) 50/50 C_2H_2/CO_2 IAST selectivity.

chemical stability of *pacs* in this study. The order of stability follows $Ni^{2+} > Co^{2+} > Fe^{2+}$. Ni-based exhibits water stability for at least 3 days, Co-based exhibits stability for at least 1 day, whereas Fe-based *pacs* shows phase change after 24 hours. The smaller ionic radius and larger crystal field stabilization energy allows Ni^{2+} to have the strongest coordination bond with organic linkers, resulting in highest chemical stability. The C_2H_2 separation potential of CPM-124c-Ni-Cl (96 cm^3/g) is lower than that of CPM-124c-Co-Cl (113 cm^3/g) (Figure 4.9d). The N_2 isotherm of Ni^{2+} phase is also much lower than those of Fe^{2+}

Table 4.3 Summary of gas sorption performances and simulation of materials in this study.

CPM-124x-M-G1	BET Surface Area (m^2/g)	Pore Volume (cm^3/g)	C_2H_2 1bar 298 K (mmol/g)	$CO_2$1bar 298 K (mmol/g)	C_2H_2 1bar 273 K (mmol/g)	CO_2 1 bar 273 K (mmol/g)	Q_{st}^0 C_2H_2 (kJ/mol)	Q_{st}^0 CO_2 (kJ/mol)	IAST Selectivity C_2H_2/CO_2 50/50 (1 bar)	Separation Potential (mmol/g)
124c-Co-Cl	2046	0.759	8.93	3.91	10.79	8.64	26.1	21.2	5.07	5.02
124c-Co-BF_4	1827	.680	8.14	3.63	10.9	7.39	29.1	23.0	4.42	4.63
124c-Co-ClO_4	1992	0.731	8.46	4.15	11.0	8.32	29.5	22.0	4.30	4.50
124c-Co-Br	2005	0.739	7.72	3.77	9.18	7.13	22.8	22.2	5.07	4.42
124c-Ni-Cl	1550	0.573	7.49	4.02	8.48	6.16	25.1	19.7	4.63	4.28
124c-Fe-Cl	2071	0.778	7.98	3.16	10.8	6.18	27.5	19.4	4.25	4.14
124b-Co-Cl	1408	0.526	6.96	3.97	8.68	6.21	30.5	21.6	4.25	3.88
124a-Co-Cl	1070	0.392	5.82	4.29	7.00	6.69	29.8	25.9	3.10	2.83

Table 4.4 Summary of benchmark ionic MOFs for C_2H_2 uptake.

MOFs	S_A BET (m^2/g)	C_2H_2 Uptake mmol/g 1 bar	CO_2 Uptake mmol/g 1 bar	IAST (1 bar)	C_2H_2/CO_2 Breakthrough Time (min/g)	Ref
FJI-H8-Me	2044	10.2	4.73	5.3	87	[17]
Co_3-cpt-tph-Cl	**2046**	**8.93**	**3.91**	**5.07**	**72**	**This Work**
MIL-160	1138	8.53	4.01	10	71	[10]
SIFSIX-Cu-TPA	1330	8.25	4.78	5.3	68	[16]
SNNU-27-Fe	1570	8.13	2.92	2.0	91	[18]
FJU-90	1572	8.04	4.60	4.3	22	[15]
SNNU-45	1007	6.0	4.35	8.5	79	[19]
ZJNU-13	1352	5.29	3.92	5.64	58	[20]
JXNU-12(F)	2154	5.16	1.50	4.1	70	[7]
Cu-ATC	600	5.01	4.02	53.6	127	[21]
UTSA-74a	830	4.78	3.17	20-9	20	[14]
NCU-100	358	4.57	~0	1787	53	[3]
FeNiM'MOF	383	4.29	2.72	24	16	[22]
CAU-10-H	627	4.00	2.68	4.0	45	[23]
UTSA-300a	311	3.08	0.15	743	12	[24]
MOF-OH	120	3.04	1.20	25	28	[25]
JNU-1	818	2.81	2.28	6.6	26	[26]
JXNU-5	406	2.50	1.55	4.9	56	[27]
Cu(I)@UiO-66	302	2.30	0.7	185	46	[8]
[Cu(BDC-Br)H2O0.5(DMF)2.5	303	1.53	1.08	3.9	34	[28]
SNNU-150-Al	--	4.33	1.98	7.3	27	[11]
NTU-66-Cu	1700	4.98	2.0	33	28	[29]

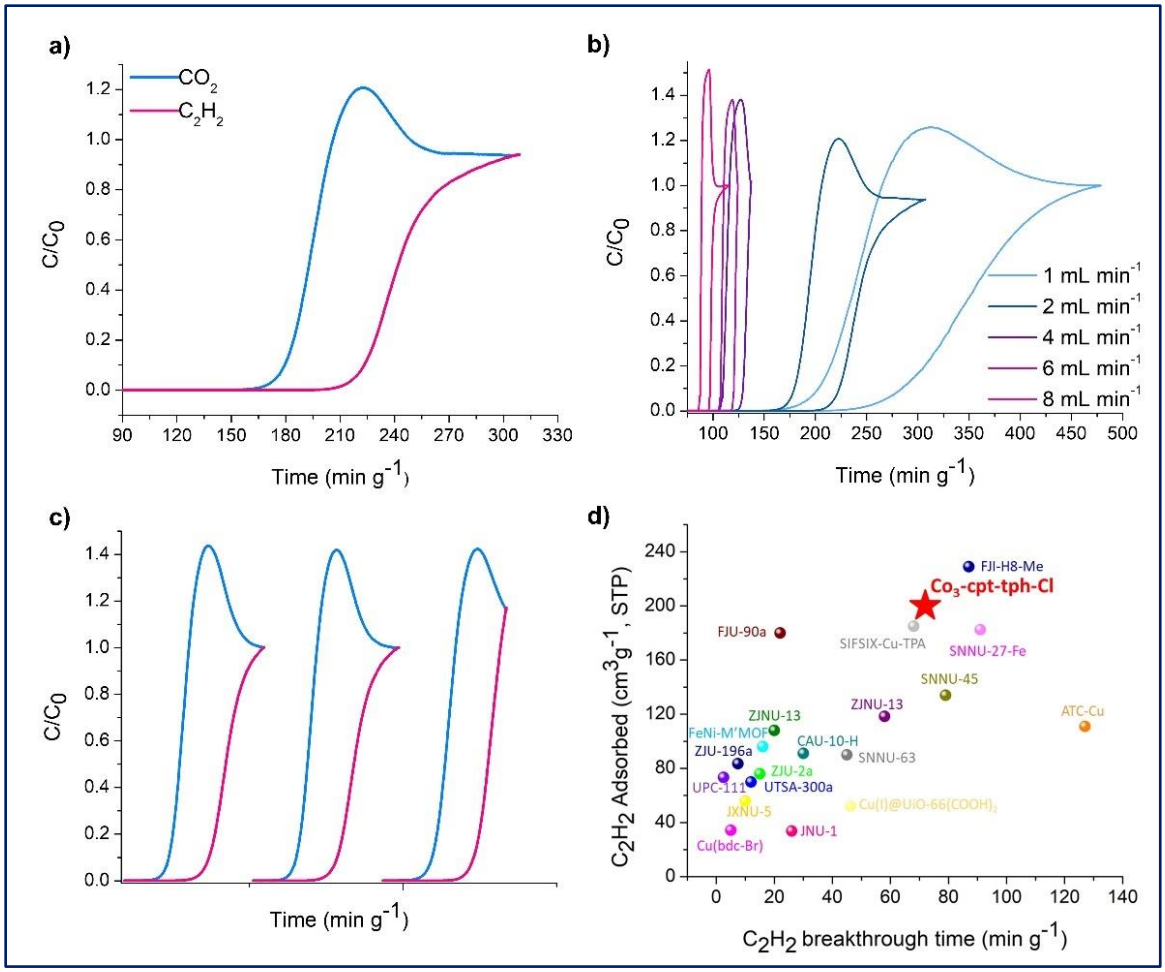

Figure 4.11 C_2H_2/CO_2 gas separation performance of CPM-124c-Co-Cl. (a) 50/50 C_2H_2/CO_2 gas separation performance at 2 mL flow rate, 298 K, 1 bar, (b) at different flow rates (c) reusability of material through multiple cycling of breakthrough separation (d) comparison of breakthrough time versus C_2H_2 uptake among top performing porous materials at 50/50 C_2H_2/CO_2 gas separation, 2 mL flow rate.

and Co^{2+}, suggesting inadequate activation (Figure 4.10a). However, TGA analysis shows that no additional guest molecule could be removed without collapsing final framework (Figure 4.7b). With moderate stability and much higher separation potential, we deemed CPM-124c-Co-Cl as the most promising adsorbent for C_2H_2/CO_2 separation. We further examine C_2H_2 selectivity performance of Co_3-cpt-tph-Cl through fixed-bed breakthrough experiments under ambient conditions. An equimolar mixture of C_2H_2 and CO_2 (50/50,

v/v) was allowed to pass through a column filled with activated CPM-124c-Co-Cl at flow rate of 2 ml min^{-1}. As shown in Figure 4.11a, CO_2 was eluted first while C_2H_2 is maintained in the column for another 72 min g^{-1} before detection. This value surpasses many benchmark MOF materials under similar conditions, such as UTSA-300a (12 min g^{-1}),[24] FeNi-M'MOF (16 min g^{-1}),[22] UTSA-74a (20 min g^{-1}),[14] FJU-90a (22 min g^{-1}),[15] CAU-10-H (45 min g^{-1}),[23] Cu(I)@UiO-66-$(COOH)_2$ (46 min g^{-1}),[8] SIFSIX-Cu-TPA (68 min g^{-1})[16] (Figure 4.10d). To meet practical industrial application, we further examine CPM-124c-Co-Cl at different flow rates (1 mL min^{-1}, 4 mL min^{-1}, 6 mL min^{-1}, and 8 mL min^{-1}) (Figure 4.11b). High C_2H_2/CO_2 separation capability is maintained at different flow rates. The cycling test of CPM-124c-Co-Cl shows all cycles are consistent with one another, demonstrating high stability and reusability of the adsorbent (Figure 4.11c).

4.4 Conclusion

In summary, we successfully optimized the pore-space and functionality of a flexible cationic *acs*-type framework for C_2H_2/CO_2 separation. Through introduction of varied PPA linkers into cationic material, we simultaneously boosted C_2H_2 uptake from 130 cm^3/g to 200 cm^3/g and selectivity from 3.1 to 5.1 at 298 K, 1 bar. We further demonstrated the importance of anions and metal, in microregulating pore space and functionality, and chemical stability. The optimized adsorbent exhibits dynamic breakthrough performance that surpasses most MOFs materials reported to date. Overall, we believe our study presents an important example of how ionic porous frameworks could break the uptake-selectivity tradeoff that has plagued the field of gas separation.

4.5 Reference

1. Fu, X.-P.; Wang, Y.-L.; Liu, Q.-Y., Metal–Organic Frameworks for C2h2/Co2 Separation. *Dalton Trans.* **2020,** *49*, 16598-16607.

2. Matsuda, R.; Kitaura, R.; Kitagawa, S.; Kubota, Y.; Belosludov, R. V.; Kobayashi, T. C.; Sakamoto, H.; Chiba, T.; Takata, M.; Kawazoe, Y.; Mita, Y., Highly Controlled Acetylene Accommodation in a Metal-Organic Microporous Material. *Nature* **2005,** *436*, 238-41.

3. Wang, J.; Zhang, Y.; Su, Y.; Liu, X.; Zhang, P.; Lin, R.-B.; Chen, S.; Deng, Q.; Zeng, Z.; Deng, S.; Chen, B., Fine Pore Engineering in a Series of Isoreticular Metal-Organic Frameworks for Efficient C2h2/Co2 Separation. *Nat. Commun* **2022,** *13*, 200.

4. Peng, Y.-L.; Pham, T.; Li, P.; Wang, T.; Chen, Y.; Chen, K.-J.; Forrest, K. A.; Space, B.; Cheng, P.; Zaworotko, M. J.; Zhang, Z., Robust Ultramicroporous Metal–Organic Frameworks with Benchmark Affinity for Acetylene. *Angew. Chem. Int. Ed.* **2018,** *57*, 10971-10975.

5. Kumar, N.; Mukherjee, S.; Harvey-Reid, N. C.; Bezrukov, A. A.; Tan, K.; Martins, V.; Vandichel, M.; Pham, T.; van Wyk, L. M.; Oyekan, K.; Kumar, A.; Forrest, K. A.; Patil, K. M.; Barbour, L. J.; Space, B.; Huang, Y.; Kruger, P. E.; Zaworotko, M. J., Breaking the Trade-Off between Selectivity and Adsorption Capacity for Gas Separation. *Chem* **2021,** *7*, 3085-3098.

6. Liu, L.; Yao, Z.; Ye, Y.; Yang, Y.; Lin, Q.; Zhang, Z.; O'Keeffe, M.; Xiang, S., Integrating the Pillared-Layer Strategy and Pore-Space Partition Method to Construct Multicomponent Mofs for C2h2/Co2 Separation. *J. Am. Chem. Soc.* **2020,** *142*, 9258-9266.

7. Fu, X.-P.; Wang, Y.-L.; Zhang, X.-F.; Krishna, R.; He, C.-T.; Liu, Q.-Y.; Chen, B., Collaborative Pore Partition and Pore Surface Fluorination within a Metal–Organic Framework for High-Performance C2h2/Co2 Separation. *Chem. Eng. J.* **2022,** *432*, 134433.

8. Zhang, L.; Jiang, K.; Yang, L.; Li, L.; Hu, E.; Yang, L.; Shao, K.; Xing, H.; Cui, Y.; Yang, Y.; Li, B.; Chen, B.; Qian, G., Benchmark C2h2/Co2 Separation in an Ultra-Microporous Metal-Organic Framework Via Copper(I)-Alkynyl Chemistry. *Angew. Chem., Int. Ed.* **2021,** *60*, 15995-16002.

9. Fan, W.; Yuan, S.; Wang, W.; Feng, L.; Liu, X.; Zhang, X.; Wang, X.; Kang, Z.; Dai, F.; Yuan, D.; Sun, D.; Zhou, H. C., Optimizing Multivariate Metal-Organic

Frameworks for Efficient C2h2/Co2 Separation. *J. Am. Chem. Soc.* **2020,** *142*, 8728-8737.

10. Ye, Y.; Xian, S.; Cui, H.; Tan, K.; Gong, L.; Liang, B.; Pham, T.; Pandey, H.; Krishna, R.; Lan, P. C.; Forrest, K. A.; Space, B.; Thonhauser, T.; Li, J.; Ma, S., Metal–Organic Framework Based Hydrogen-Bonding Nanotrap for Efficient Acetylene Storage and Separation. *J. Am. Chem. Soc.* **2021**.

11. Lv, H.-J.; Li, Y.-P.; Xue, Y.-Y.; Jiang, Y.-C.; Li, S.-N.; Hu, M.-C.; Zhai, Q.-G., Systematic Regulation of C2h2/Co2 Separation by 3p-Block Open Metal Sites in a Robust Metal–Organic Framework Platform. *Inorg. Chem.* **2020,** *59*, 4825-4834.

12. Chen, D.-M.; Zhang, N.-N.; Tian, J.-Y.; Liu, C.-S.; Du, M., Quest for the Ncb-Type Metal–Organic Framework Platform: A Bifunctional Ligand Approach Meets Net Topology Needs. *Inorg. Chem.* **2017,** *56*, 7328-7331.

13. Li, Q.; Wu, N.; Li, J.; Wu, D., A Highly Connected Trinuclear Cluster Based Metal-Organic Framework for Efficient Separation of C2h2/C2h4 and C2h2/Co2. *Inorg. Chem.* **2020,** *59*, 13005-13008.

14. Luo, F.; Yan, C.; Dang, L.; Krishna, R.; Zhou, W.; Wu, H.; Dong, X.; Han, Y.; Hu, T. L.; O'Keeffe, M.; Wang, L.; Luo, M.; Lin, R. B.; Chen, B., Utsa-74: A Mof-74 Isomer with Two Accessible Binding Sites Per Metal Center for Highly Selective Gas Separation. *J. Am. Chem. Soc.* **2016,** *138*, 5678-84.

15. Ye, Y.; Ma, Z.; Lin, R. B.; Krishna, R.; Zhou, W.; Lin, Q.; Zhang, Z.; Xiang, S.; Chen, B., Pore Space Partition within a Metal-Organic Framework for Highly Efficient C2h2/Co2 Separation. *J. Am. Chem. Soc.* **2019,** *141*, 4130-4136.

16. Li, H.; Liu, C.; Chen, C.; Di, Z.; Yuan, D.; Pang, J.; Wei, W.; Wu, M.; Hong, M., An Unprecedented Pillar-Cage Fluorinated Hybrid Porous Framework with Highly Efficient Acetylene Storage and Separation. *Angew. Chem. Int. Ed.* **2021,** *60*, 7547-7552.

17. Di, Z.; Liu, C.; Pang, J.; Chen, C.; Hu, F.; Yuan, D.; Wu, M.; Hong, M., Cage-Like Porous Materials with Simultaneous High C2 H2 Storage and Excellent C2 H2 /Co2 Separation Performance. *Angew. Chem. Int. Ed. Engl.* **2021**.

18. Xue, Y. Y.; Bai, X. Y.; Zhang, J.; Wang, Y.; Li, S. N.; Jiang, Y. C.; Hu, M. C.; Zhai, Q. G., Precise Pore Space Partitions Combined with High-Density Hydrogen-Bonding Acceptors within Metal-Organic Frameworks for Highly Efficient Acetylene Storage and Separation. *Angew. Chem. Int. Ed. Engl.* **2021,** *60*, 10122-10128.

19. Li, Y.-P.; Wang, Y.; Xue, Y.-Y.; Li, H.-P.; Zhai, Q.-G.; Li, S.-N.; Jiang, Y.-C.; Hu, M.-C.; Bu, X., Ultramicroporous Building Units as a Path to Bi-Microporous Metal–Organic Frameworks with High Acetylene Storage and Separation Performance. *Angew. Chem. Int. Ed.* **2019,** *58*, 13590-13595.

20. Xu, T.; Jiang, Z.; Liu, P.; Chen, H.; Lan, X.; Chen, D.; Li, L.; He, Y., Immobilization of Oxygen Atoms in the Pores of Microporous Metal–Organic Frameworks for C2h2 Separation and Purification. *ACS Applied Nano Materials* **2020,** *3*, 2911-2919.

21. Niu, Z.; Cui, X.; Pham, T.; Verma, G.; Lan, P. C.; Shan, C.; Xing, H.; Forrest, K. A.; Suepaul, S.; Space, B.; Nafady, A.; Al-Enizi, A. M.; Ma, S., A Mof-Based Ultra-Strong Acetylene Nano-Trap for Highly Efficient C2h2/Co2 Separation. *Angew. Chem. Int. Ed.* **2021,** *60*, 5283-5288.

22. Gao, J.; Qian, X.; Lin, R.-B.; Krishna, R.; Wu, H.; Zhou, W.; Chen, B., Mixed Metal-Organic Framework with Multiple Binding Sites for Efficient C2h2/Co2 Separation. *Angew. Chem., Int. Ed.* **2020,** *59*, 4396-4400.

23. Pei, J.; Wen, H.-M.; Gu, X.-W.; Qian, Q.-L.; Yang, Y.; Cui, Y.; Li, B.; Chen, B.; Qian, G., Dense Packing of Acetylene in a Stable and Low-Cost Metal–Organic Framework for Efficient C2h2/Co2 Separation. *Angew. Chem. Int. Ed.* **2021,** *60*, 25068-25074.

24. Lin, R. B.; Li, L.; Wu, H.; Arman, H.; Li, B.; Lin, R. G.; Zhou, W.; Chen, B., Optimized Separation of Acetylene from Carbon Dioxide and Ethylene in a Microporous Material. *J. Am. Chem. Soc.* **2017,** *139*, 8022-8028.

25. Gong, W.; Cui, H.; Xie, Y.; Li, Y.; Tang, X.; Liu, Y.; Cui, Y.; Chen, B., Efficient C2h2/Co2 Separation in Ultramicroporous Metal–Organic Frameworks with Record C2h2 Storage Density. *J. Am. Chem. Soc.* **2021**.

26. Zeng, H.; Xie, M.; Huang, Y. L.; Zhao, Y.; Xie, X. J.; Bai, J. P.; Wan, M. Y.; Krishna, R.; Lu, W.; Li, D., Induced Fit of C2 H2 in a Flexible Mof through Cooperative Action of Open Metal Sites. *Angew. Chem. Int. Ed. Engl.* **2019,** *58*, 8515-8519.

27. Liu, R.; Liu, Q.-Y.; Krishna, R.; Wang, W.; He, C.-T.; Wang, Y.-L., Water-Stable Europium 1,3,6,8-Tetrakis(4-Carboxylphenyl)Pyrene Framework for Efficient C2h2/Co2 Separation. *Inorg. Chem.* **2019,** *58*, 5089-5095.

28. Cui, H.; Ye, Y.; Arman, H.; Li, Z.; Alsalme, A.; Lin, R.-B.; Chen, B., Microporous Copper Isophthalate Framework of Mot Topology for C2h2/Co2 Separation. *Cryst. Growth Des.* **2019,** *19*, 5829-5835.

29. Chen, S.; Behera, N.; Yang, C.; Dong, Q.; Zheng, B.; Li, Y.; Tang, Q.; Wang, Z.; Wang, Y.; Duan, J., A Chemically Stable Nanoporous Coordination Polymer with Fixed and Free Cu2+ Ions for Boosted C2h2/Co2 Separation. *Nano Research* **2021,** *14*, 546-553.

Chapter 5: Sulfonated Partitioned-*acs* Frameworks

5.1 Introduction

The ability to have tailored appendment of functional groups within the interior pore surface endows metal-organic frameworks with essential chemical properties that are highly sought after in different applications, and thus positioning this class of materials at a greater advantage over more traditional solids. Among different functional groups, the hydrophilic and polar sulfonic acid that readily undergoes proton exchange presents attractive opportunities.[1-6]

Reticular sulfonic acid functionalization has thus far, cluttered in few limited MOF platforms (i.e., MIL-53, MIL-101, UiO-66), working primarily with hard metals (i.e., Al^{3+}, Cr^{3+}, Zr^{4+}).[2, 7-8] This could be attributed to the hygroscopic nature of sulfonate group, which accelerates the decomposition of many MOFs that exhibit kinetic H_2O stability. The flexible functional group with versatile modes of coordination also leads to a much higher degree of structural unpredictability, and consequently, posing a significant challenge towards materialization of isoreticular products.

The high degree of tunability and robustness of the *pacs* platform presents a promising arena to design and customize novel sulfonate-based porous solids and tap into

Table 5.1 Range of tunable charge in each of the three *pacs* module.

Trimer		SO_3-dicarobyxlate		L2		Framework Charge
$(M^{3+})_3(O)$	+7	$(H_2\text{-dsndc}^{2-})_3$ $(H\text{-sndc}^{2-})_3$	-6	L2	0	+1
$(M^{3+})_2(M^{2+})(OH)$	+7	$(H\text{-dsndc}^{3-})_2(dsndc^{4-})$ $(H\text{-sndc}^{2-})_2(sndc^{3-})$	-7			
		$(H\text{-dsndc}^{3-})_2(dsndc^{4-})$ $(H\text{-sndc}^{2-})(sndc^{3-})_2$	-8			
$(M^{3+})(M^{2+})_2(OH)$	+6	$(H\text{-dsndc}^{3-})_3$ $(sndc^{3-})_3$	-9			
$(M^{3+})_2(M^{2+})(O)$	+6	$(H\text{-dsndc}^{3-})_2(dsndc^{4-})$	-10			
		$(H\text{-dsndc}^{3-})(dsndc^{4-})_2$	-11			
$(M^{2+})_3(OH)$	+5	$(dsndc^{4-})_3$	-12	tph^{1-}	-1	-8

unexplored properties. One of such would be the range of tunable charge in final framework. As shown in Table 5.1, the charge of each *pacs* module could independently be tuned, which potentially results in novel MOFs with the widest range to tunable charge.[9]

The pendent sulfonic acid is unlike any other functional groups that have previously been attached to *pacs*.[10-14] Compared to the neutral (i.e., $-CH_3$, -F, $-NO_2$) or weakly acidic/basic (i.e., -OH, $-NH_2$) groups, the highly acidic $-SO_3H$ could easily dissociate and coordinate with metal center, consequently resulting in non-*pacs* products. In absence of metal coordination, sulfonate group would require presence of counter balancing ions, which increases the likelihood of steric hindrance in the system, also leading to non-*pacs* products. Hydrolytic stability must be taken into account in the designing of sulfonate *pacs*, as it is an important requisite for many applications.

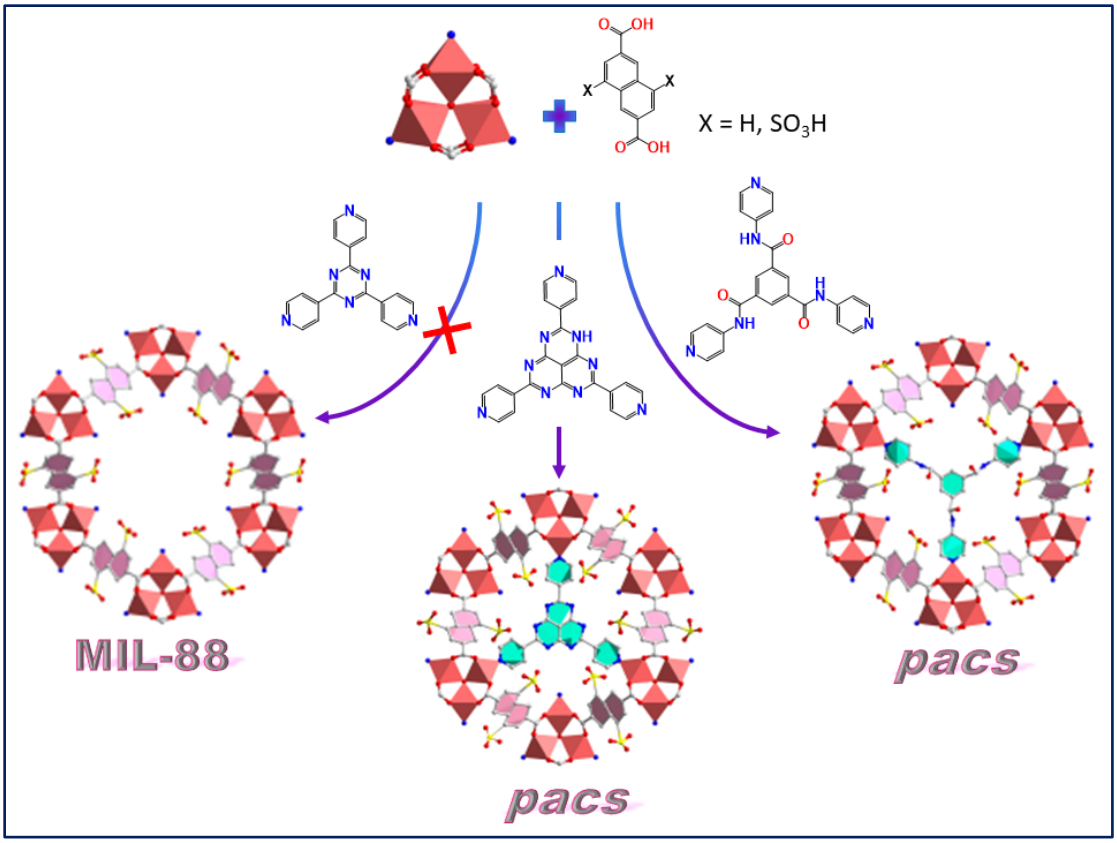

Figure 5.1. Overcoming geometry limitations for construction sulfonate *pacs*.

Herein, we report the successful design, synthesis and optimization of sulfonate *pacs* materials. Pore geometry was first optimized to remove steric effects from sulfonate group. Among different sulfonate *pacs* design and synthesis, the phase constructed from H-tph partitioning agent was identified as having goldilocks-like geometry and stability. With this result, we next performed framework tuning to optimize sulfonate *pacs* for CO_2 capture and proton conduction.

5.2 Experimental Section

5.2.1 Chemicals and Materials

All reagents were used as received without further purification. Iron (III) chloride hexahydrate ($FeCl_3 \cdot 6H_2O$), Cobalt (II) nitrate hexahydrate ($Co(NO_3)_2 \cdot 6H_2O$), acetone, methanol (MeOH), ethanol (EtOH), benzene (Bn), cyclohexane (Ch), N,N-dimethylacetamide (DMA), N-dimethylformamide (NMF), dichloromethane (CH_2Cl_2), trifluoroacetic acid (TFA), and hydrochloric acid 38 w.t. % (HCl) were purchased from Fischer Scientific Co., N-methylformamide (NMF), 4-pyridylamidine hydrochloride, 2,6-naphthalenedicarboxylic acid (2,6-H_2ndc) and N-methylpyrrolidone (NMP) were obtained from TCI-America. Oleum, Indium chloride 98% ($InCl_3$), triflic acid (HoTf) were obtained from Sigma Aldrich.

5.2.2 Synthesis of Organic Precursors

Synthesis of 4-sulfo-napthalene-2,6-dicarboxylic acid (H_3sndc)

Naphthalene-2,6-dicarboxylic acid (4 g) was added to 10 mL of oleum (SO_3, 30 w.t. %) in a 100 mL round-bottom flask equipped with reflux condenser. The reaction mixture was stirred vigorously at 85 °C for 6 hours. Solution mixture was dissolved in distilled water, followed by precipitation in HCl (36 w.t.%) (~140 mL). Isolated product was washed with ice-water to removed trapped HCl and dried in vacuum over at 120 °C overnight. Yield (90%).

Synthesis of 4,8-disulfo-napthalene-2,6-dicarboxylic acid (H_4dsndc)

H_4L was synthesized according to reported literature with slight modification.[15] Naphthalene-2,6-dicarboxylic acid (4 g) was added to 20 mL of oleum (SO_3, 30 w.t. %) in a 100 mL round-bottom flask equipped with reflux condenser. The reaction mixture was stirred vigorously at 150 °C for 6 hours. Solution mixture was dissolved in distilled water, followed by precipitation in HCl (36 w.t.%). Isolated product was washed with ice-water to removed trapped HCl and dried in vacuum over at 120 °C overnight. Yield (85%), ^{1}HNMR (600 MHz, DMSO-d_6 δ, ppm): 8.5 (d), 9.6 (d).

Synthesis 2,5,8-tri-(4-pyridyl)-1,3,4,6,7,9-hexaazaphenalene (H-tph): The hexaazaphenalene condensation reaction was carried out according to Chapter 2.2.2

Synthesis of N,N',N''-tri(4-pyridinyl)-1,3,5-benzenetri-carboxamide (tpbtc): The amide condensation reaction was carried out according to Chapter 2.2.2

5.2.3 Synthesis of Crystalline Porous Materials

Synthesis of In_3-dsndc (CPM-s9-In). In a 23 mL glass vial, $InCl_3$ (34 mg, 0.15 mmol) and H_4dsndc (61 mg, 0.15 mmol) were dissolved in 3.0 g NMF 2.0 g NMP and 0.03 g HOTf. After stirring for 2 hours, the vial was placed in a 120 °C oven for 10 days. Elongated clear hexagonal prisms were obtained after solution was cooled to ambient temperature.

Synthesis of Co_2In-sndc-tph (CPM-s10-CoIn). In a 23 mL glass vial, $Co(NO_3)\cdot 6H_2O$ (60 mg, 0.2 mmol) $InCl_3$ (23 mg, 0.1 mmol), H_3sndc (92 mg, 0.3 mmol) and H-tph (45 mg, 0.1 mmol) were dissolved in 6.0 g NMF. After stirring for 2 hours, the vial was placed in

a 120 ℃ oven for 4 days. Pink hexagonal plates were obtained after solution was cooled to ambient temperature.

Synthesis of Co_2Fe-sndc-tph (CPM-s10-CoFe). In a 23 mL Teflon cup, $Co(NO_3)\cdot 6H_2O$ (60 mg, 0.2 mmol) $FeCl_3$ (27 mg, 0.1 mmol), H_3sndc (96 mg, 0.3 mmol) and H-tph (45 mg, 0.1 mmol) were dissolved in 6.0 g DMA and 0.6 g TFA. After stirring for 2 hours, the cup was sealed and placed in a 150 ℃ oven for 5 days. Tan-colored microcrystalline powder were obtained after solution was cooled to ambient temperature.

Synthesis of Co_2In-dsndc-tph (CPM-s20-CoIn). In a 23 mL glass vial, $Co(NO_3)\cdot 6H_2O$ (60 mg, 0.3 mmol) $InCl_3$ (23 mg, 0.1 mmol), H_4dsndc (112 mg, 0.3 mmol) and H-tph (45 mg, 0.1 mmol) were dissolved in 6.0 g NMF. After stirring for 2 hours, the vial was placed in a 120 ℃ oven for 4 days. Pink hexagonal plates were obtained after solution was cooled to ambient temperature.

Synthesis of Co_2Fe-dsndc-tph (CPM-s20-CoFe). In a 23 mL Teflon cup, $Co(NO_3)\cdot 6H_2O$ (60 mg, 0.2 mmol) $FeCl_3$ (27 mg, 0.1 mmol), H_4dsndc (113 mg, 0.3 mmol) and H-tph (45 mg, 0.1 mmol) were dissolved in 6.0 g DMA and 0.6 g TFA. After stirring for 2 hours, the vial was placed in a 150 ℃ oven for 5 days. Tan-colored microcrystalline powder were obtained after solution was cooled to ambient temperature.

Synthesis of Co_2In-sndc-tpbtc (CPM-s11-CoIn). In a 23 mL glass vial, $Co(NO_3)\cdot 6H_2O$ (60 mg, 0.2 mmol) $InCl_3$ (23 mg, 0.1 mmol), H_3sndc (92 mg, 0.3 mmol) and tpbtc (47 mg, 0.1 mmol) were dissolved in 6.0 g NMF. After stirring for 2 hours, the vial was placed in a 120 ℃ oven for 7 days. Pink hexagonal plates were obtained after solution was cooled to ambient temperature.

Synthesis of In_2Co-dsndc-tpbtc (CPM-s21-InCo). In a 23 mL glass vial, $Co(NO_3)\cdot 6H_2O$ (16 mg, 0.05 mmol) $InCl_3$ (23 mg, 0.1 mmol), H_4dsndc (62 mg, 0.3 mmol) and tpbtc (25 mg, 0.05 mmol) were dissolved in 3.0 g NMF. After stirring for 2 hours, the vial was placed in a 120 ℃ oven for 4 days. Pink hexagonal plates were obtained after solution was cooled to ambient temperature.

5.2.4 Property Characterization

Conductivity Measurements. The compacted powder samples for conductivity measurements were prepared by pressing the single-crystal sample into pellet (13 mm in diameter and around 1 mm in thickness pelletized at 50 MPa). The pellet was sandwiched between two blocking stainless-steel electrodes and fixed with a clamp for measurements. AC impedance spectroscopy measurements were performed using a Solartron 1260 impedance/gain-phase analyzer connected to a Solartron 1287 electrochemistry interface. Zplot 2.6b was used as the control software and ZView 2.6b was used as the analysis software. A typical measurement was made over a frequency range between 5 MHz to 1 Hz and a 100 mV (peak voltage) was applied as AC signals. Variable impedance spectra were collected over different humidity and temperature obtained by saturated salt solutions and the water bath. Ionic conductivity (S cm^{-1}) was calculated using the formula $\sigma = L/AR$, where L is the pellet thickness while A is the pellet area in contact with the stainless-steel electrodes. R is the complex impedance obtained from the Nyquist plot.

Gas Sorption Measurement Gas sorption measurements were carried out on a Micromeritics ASAP 2020 and ASAP 2020 Plus physisorption analyzers. The as-synthesized sample was immersed in CH_2Cl_2 and refreshed daily for five consecutive

times. The sample was then transferred to the gas sorption tube and the dried under open flow of N_2 gas for 15 minutes. The degas process was carried out at 60 ^oC for 12 hours.

Other Characterization: SCXRD, PXRD, TGA, EDS, gas adsoption measurements and calculations were carried out as mentioned in 2.2.4.

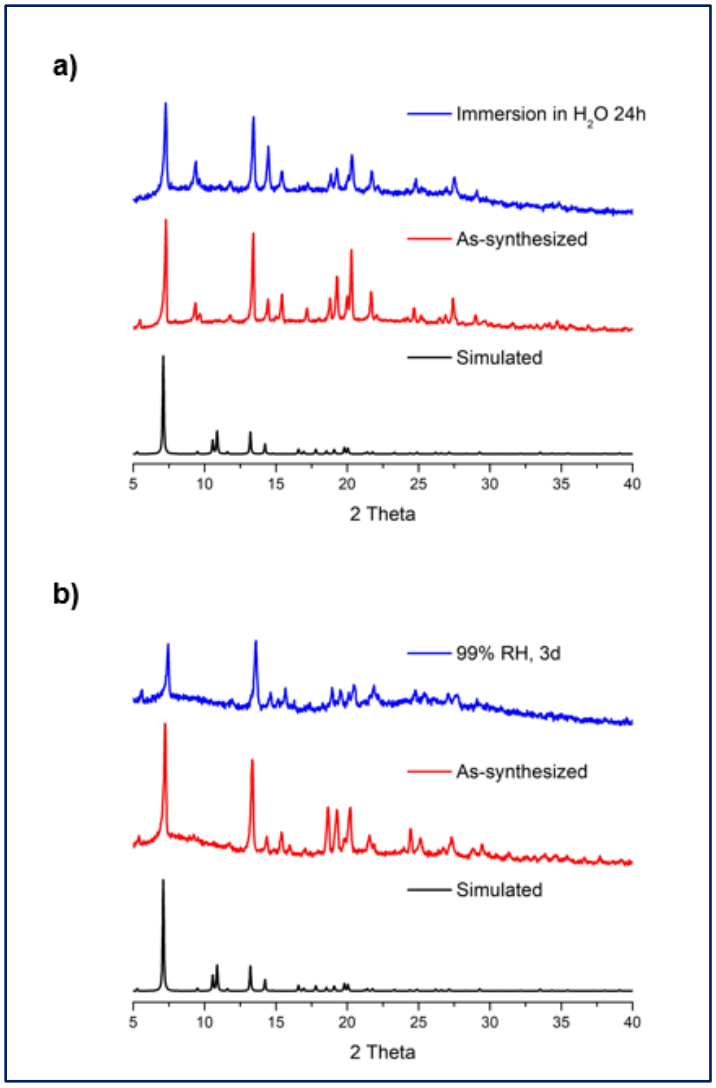

Figure 5.2 Phase purity and water stability experiments of (a) CoFe-sndc-tph and (b) CoFe-dsndc-tph.

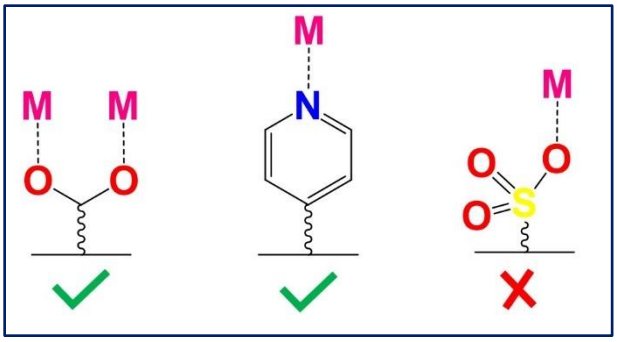

Figure 5.3 Desired mode of coordination for each functional group in sulfonate-*pacs* system.

5.3 Results and Discussion

5.3.1 Design and Synthesis of Sulfonated *pacs*

The success of sulfonate *pacs* synthesis was built upon many detailed planning stages. From the linker design stage, we specifically chose to have sulfonate group being at least one carbon away from carboxylate group. Although sulfonate is known to have weaker metal coordination (with most metals) than carboxylate or pyridine counterparts, having sulfonate group too close another binding site (e.g., carboxylate and sulfonate at ortho from one another) could still lead to strong metal-complexation through sulfonate-carboxylate chelation, and thus preventing formation of trimer SBU for *pacs* synthesis. Hence, 4-sulfo-napthalene-2,6-dicarboxylic acid (H_3sndc) and 4,8-disulfo-napthalene-2,6-dicarboxylic acid (H_4dsndc) were chosen as framework-forming agents.

The length of pore-partitioning agent is another crucial parameter in constructing sulfonate *pacs*. Our initial attempts to combine H_4dsncd with tpt did not yield any *pacs* materials. In the best scenario of reticular synthesis design, only the non-partitioned framework was constructed (In_3-dsndc, CPM-s9). Single-crystal XRD analysis of CPM-

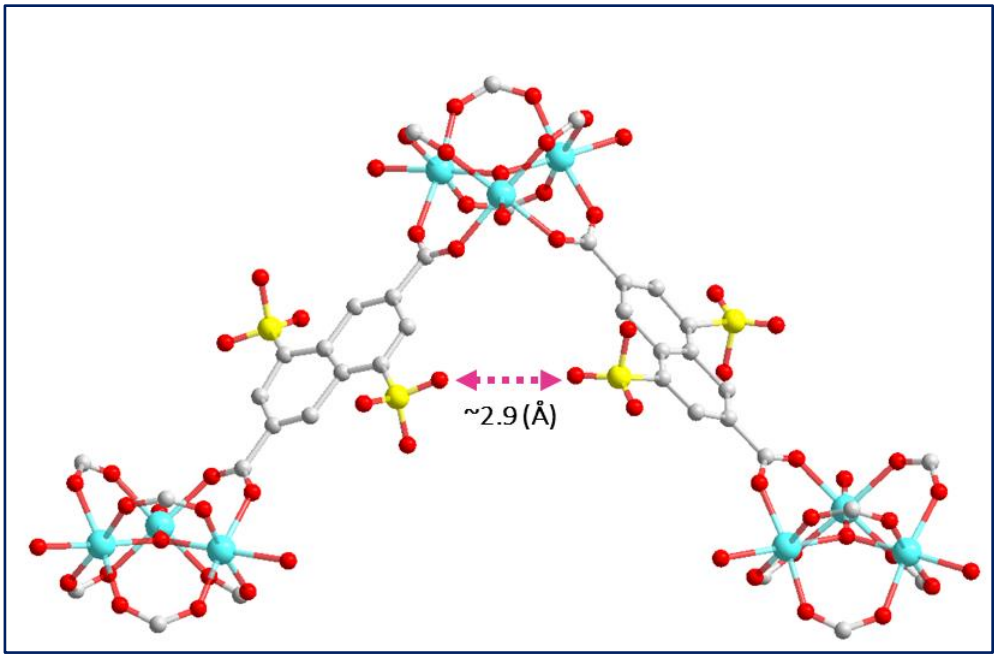

Figure 5.4 Estimated closest distance between sulfonate groups in potential In-dsndc-tpt structure.

s9 revealed unicell a/b axes of 19.11 Å and closest O---O distance between neighboring sulfonate groups of ~3.3 Å. We noted that In_3-26ndc-tpt (CPM-83-In) has a/b axes of 16.97 Å. Thus, construction of In-dsndc-tpt would require reduction of a/b axes in CPM-s9 by 2.13 Å, which corresponds to O---O distance between neighboring sulfonate groups at ~2.9 Å. While this distance is well within a proper distance of a hydrogen bond (2.7-3.3 Å), it could be too small for other counter ions. Considering the likelihood of sulfonic acid dissociating and charged balanced by organic cations during *pacs* synthesis, larger pore-partitioning agents could prove to be more beneficial in construction of sulfonate *pacs*.

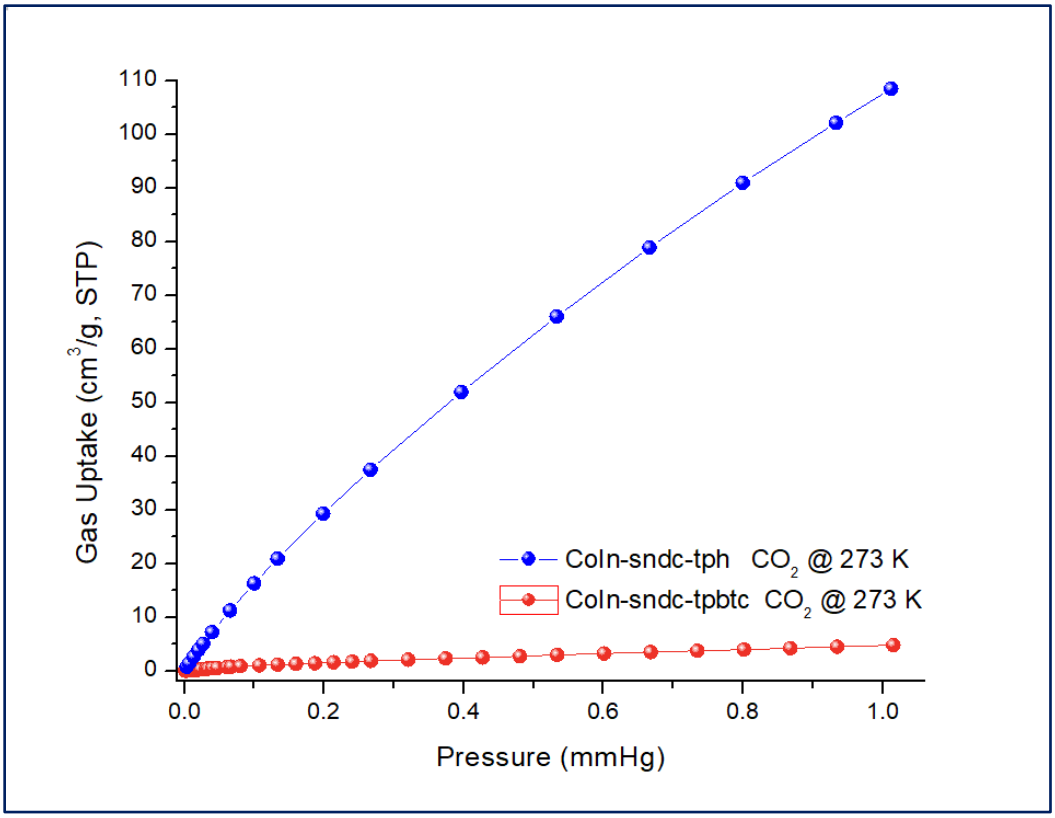

Figure 5.5 CO_2 isotherm comparison between CoIn-sndc-based *pacs* synthesized from tph and tpbtc partitioning agent.

We then identified H-tph and tpbtc, L2 linkers with lengths at 1.2 and 1.4 times that of tpt, as our next pore-partitioning candidates. True to our prediction, the first sulfonated *pacs* materials could now be constructed through these larger pore-partitioning agents. After confirming phase purity of InCo-sndc-tph and InCo-sndc-tpbtc, we performed initial CO_2 isotherm examinations. While InCo-sndc-tph shows promising CO_2 uptake of 110 cm^3/g at 273 K, 1 bar, InCo-sndc-tpbtc phase shows negligible CO_2 uptake (Figure 5.5). We attribute this to the potential acceleration of tpbtc when in presence of sulfonate group.

As shown in Figure 5.6, the employment of H_4dsndc for construction of CoIn-dsndc-tpbtc resulted in the elongation of oxygen of amide group and 90° out-of-plane rotation between core benzene ligand and peripheral pyridyl group. In comparison, substitution of H_4dsndc with H_3sndc did not result in any abnormality to the configuration of tpbtc. The difference between the two crystal structures correspond directly to the increase of sulfonate composition in the framework. Since the hydroscopic nature of sulfonate group could quickly draw H_2O molecules into the channels to facilitate hydrolysis of tpbtc. By doubling the concentration of sulfonic acid, hydrolysis reaction is accelerated, as witnessed by loss of conjugation in tpbtc of the InCo-dsndc-tpbtc phase.

Overall, H-tph serves as the most promising L2 linker in construction of sulfonated *pacs* material. The highly robust tpt was too small to allow potential *pacs* framework to accommodate steric hindrance from different sulfonate and counter ions. In comparison, the ideal size of tpbtc has the ability to construct *pacs* with most optimal crystallographic volume (c/a ratio = 0.806 in InCo-dsndc-tpbtc) but fall short in terms of stability. Thus tph-based sulfonated *pacs* presents the best prototype to explore different potential properties.

5.3.2 Structural Optimization of Sulfonated *pacs*

In this work, we first examined In-based *pacs* because In^{3+} tends form the best single crystals, in terms of size and crystallinity. With adequate acquisition of crystallographic data, we could next employ precursors that are of lower cost, greater

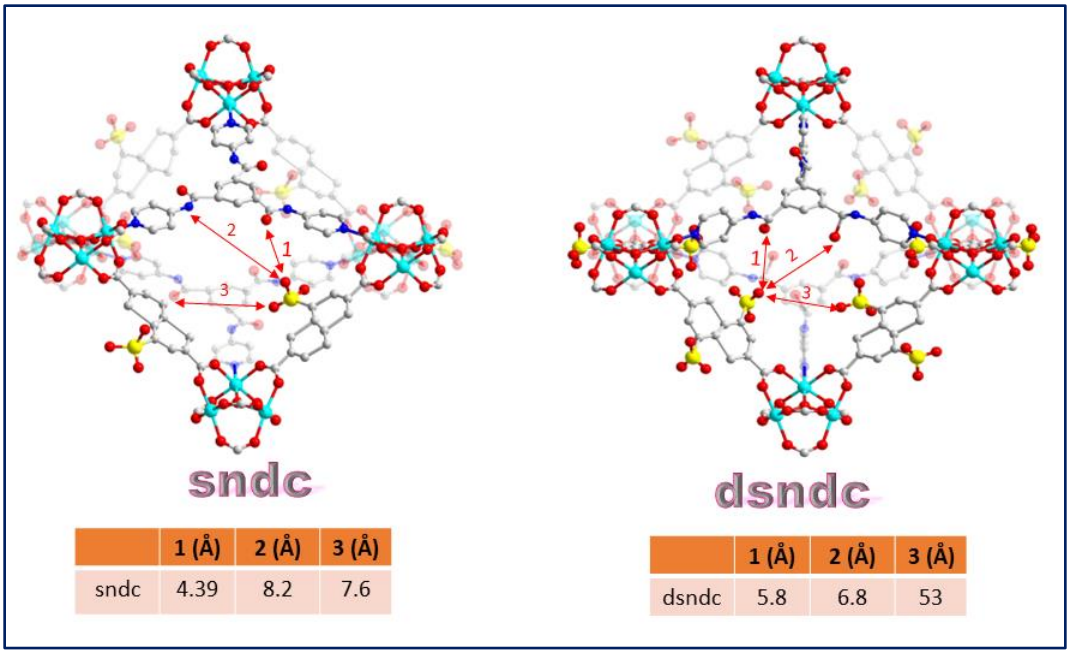

	1 (Å)	2 (Å)	3 (Å)
sndc	4.39	8.2	7.6

	1 (Å)	2 (Å)	3 (Å)
dsndc	5.8	6.8	53

Figure 5.6 crystal structures of CoIn-sndc-tpbtc and CoIn-dsndc-tpbtc.

stability and performances. Our previous study of Fe-based *pacs* materials show high stability, even under every harsh conditions. Thus, $In^{3+}$was substituted to Fe^{3+}. Resulting PXRD of CoFe-sndc-tph and CoFe-dsndc-tph match well with simulated powder patterns from CoIn-sndc-tph phase. Hydrolytic stabilities were next examined. Whereas CoFe-sndc-tph could maintain crystallinity after immersion in water for 24 hrs, CoFe-dsndc-tph is stable at 99% relative humidity for 3 days.

We next monitored CO_2 uptake changes with substitutions of different modules. As shown in Figure 5.7, CoFe phase resulted in higher CO_2 uptake at 273 K than CoIn phase. The higher gravimetric uptake from CoFe-based *pacs* could be a direct result of the lower atomic mass of Fe^{3+}. We also examined changes in CO_2 uptake as a direct result of sulfonate composition. Compared to the linear CO_2 isotherm of CoV-26ndc-tph at 273 K, the CO_2 isotherm has CoFe-sndc-tph exhibits a much higher curvature. With increase of

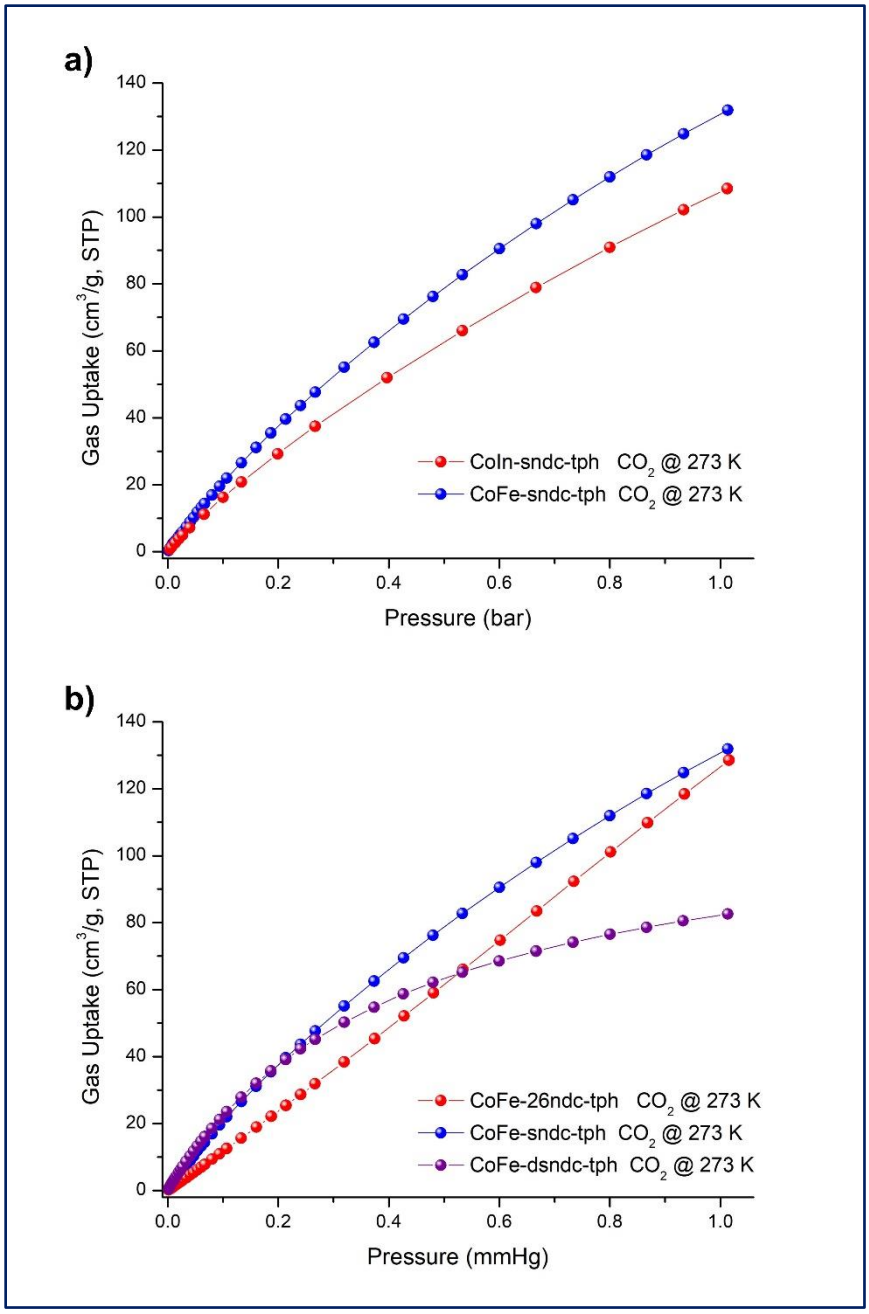

Figure 5.7 Carbon dioxide isotherms at 273 K for (a) sndc-tph-based *pacs* with CoIn and CoFe metals, (b) CoFe-tph-based *pacs* with different concentration of sulfonate groups.

polarity in the CoFe-sndc-tph phase, stronger attraction towards CO_2 molecule is observed, especially in the lower pressure region, where host-guest interaction predominates. Doubling the composition of sulfonate group on the other hand, does not enhance host-guest interaction, meanwhile dramatically decreased CO_2 uptake. This suggests that one $-SO_3$ group per $26ndc^{2-}$ linker is adequate in enhancing CO_2 uptake. Further addition of $-SO_3$ group decreases pore volume, resulting in inefficient packing of CO_2 molecules.

5.3.4 Ionic Conductivity

The high acidity of sulfonic acid makes it one of the best hydrophilic functional groups to examine proton transport. Herein, we applied alternating-current (a.c.) impedance to the pelletized as-synthesized CoFe-dsndc-tph phase. Under ambient

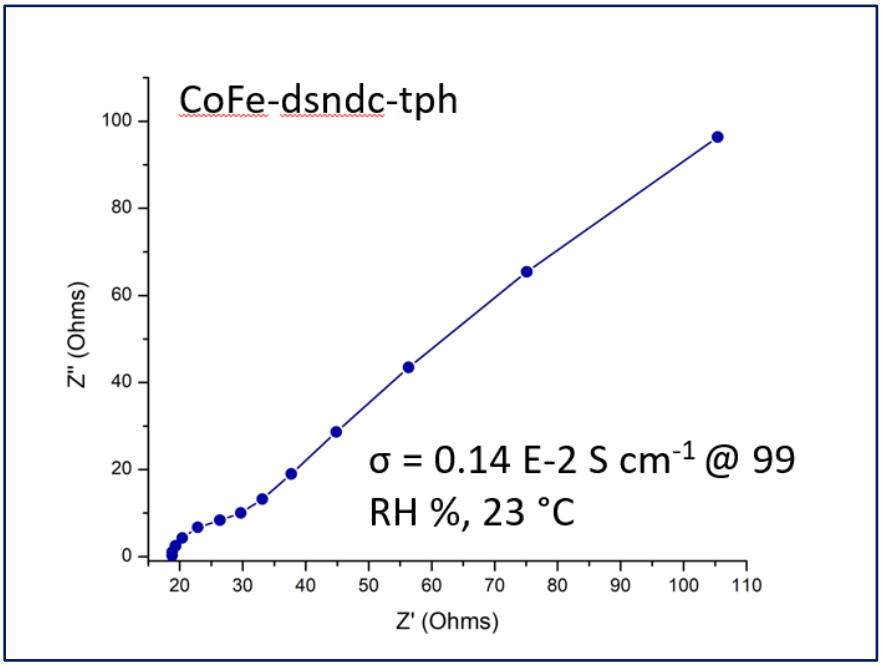

Figure 5.8 Nyquist plot of CoFe-dsndc-tph

temperature and 99% humidity, conductivity of this material achieved 0.14E-2 S cm^{-} which is comparable to commercial Nafion (i.e., 7.8 E-2 S cm^{-} 100% RH, 25 °C). Attempts to enhance conductivity performance through proper activation method and introduction of additional proton transport vehicles and ions are underway.

5.4 Conclusion

In summary, we have successfully merged sulfonic acid group into our highly tunable *pacs* platform through effective crystal engineering techniques. Structural characterization further elucidates important stability information, allowing us to revise and optimize our sulfonated *pacs* structures. Initial hydrolytic stability tests, CO_2 uptake studies and conductivity measurement further reveal great promises, instigating new potential application direction of our *pacs* platform.

5.5 Reference

1. Yang, F.; Xu, G.; Dou, Y.; Wang, B.; Zhang, H.; Wu, H.; Zhou, W.; Li, J.-R.; Chen, B., A Flexible Metal–Organic Framework with a High Density of Sulfonic Acid Sites for Proton Conduction. *Nature Energy* **2017,** *2*, 877-883.

2. Taylor, J. M.; Komatsu, T.; Dekura, S.; Otsubo, K.; Takata, M.; Kitagawa, H., The Role of a Three Dimensionally Ordered Defect Sublattice on the Acidity of a Sulfonated Metal–Organic Framework. *J. Am. Chem. Soc.* **2015,** *137*, 11498-11506.

3. Joarder, B.; Lin, J.-B.; Romero, Z.; Shimizu, G. K. H., Single Crystal Proton Conduction Study of a Metal Organic Framework of Modest Water Stability. *J. Am. Chem. Soc.* **2017,** *139*, 7176-7179.

4. Hurd, J. A.; Vaidhyanathan, R.; Thangadurai, V.; Ratcliffe, C. I.; Moudrakovski, I. L.; Shimizu, G. K. H., Anhydrous Proton Conduction at 150 °C in a Crystalline Metal–Organic Framework. *Nat. Chem.* **2009,** *1*, 705.

5. Dong, X.-Y.; Wang, R.; Li, J.-B.; Zang, S.-Q.; Hou, H.-W.; Mak, T. C. W., A Tetranuclear Cu4([Small Mu]3-Oh)2-Based Metal-Organic Framework (Mof) with Sulfonate-Carboxylate Ligands for Proton Conduction. *Chem. Commun.* **2013,** *49*, 10590-10592.

6. Dong, X.-Y.; Wang, R.; Wang, J.-Z.; Zang, S.-Q.; Mak, T. C. W., Highly Selective Fe3+ Sensing and Proton Conduction in a Water-Stable Sulfonate-Carboxylate Tb-Organic-Framework. *J. Mater. Chem. A* **2015,** *3*, 641-647.

7. Wang, G.-B.; Leus, K.; Hendrickx, K.; Wieme, J.; Depauw, H.; Liu, Y.-Y.; Van Speybroeck, V.; Van Der Voort, P., A Series of Sulfonic Acid Functionalized Mixed-Linker Dut-4 Analogues: Synthesis, Gas Sorption Properties and Catalytic Performance. *Dalton Trans.* **2017,** *46*, 14356-14364.

8. Chang, G.; Huang, M.; Su, Y.; Xing, H.; Su, B.; Zhang, Z.; Yang, Q.; Yang, Y.; Ren, Q.; Bao, Z.; Chen, B., Immobilization of Ag(I) into a Metal-Organic Framework with -So3h Sites for Highly Selective Olefin-Paraffin Separation at Room Temperature. *Chem. Commun.* **2015,** *51*, 2859-2862.

9. Hong, A. N.; Kusumoputro, E.; Wang, Y.; Yang, H.; Chen, Y.; Bu, X.; Feng, P., Simultaneous Control of Pore-Space Partition and Charge Distribution in Multi-Modular Metal–Organic Frameworks. *Angew. Chem. Int. Ed.* **2022,** *61*, e202116064.

10. Fu, X.-P.; Wang, Y.-L.; Zhang, X.-F.; Krishna, R.; He, C.-T.; Liu, Q.-Y.; Chen, B., Collaborative Pore Partition and Pore Surface Fluorination within a Metal–Organic Framework for High-Performance C2h2/Co2 Separation. *Chem. Eng. J.* **2022,** *432*, 134433.

11. Yang, H.; Wang, Y.; Krishna, R.; Jia, X.; Wang, Y.; Hong, A. N.; Dang, C.; Castillo, H. E.; Bu, X.; Feng, P., Pore-Space-Partition-Enabled Exceptional Ethane Uptake and Ethane-Selective Ethane–Ethylene Separation. *J. Am. Chem. Soc.* **2020,** *142*, 2222-2227.

12. Zhai, Q.-G.; Bu, X.; Mao, C.; Zhao, X.; Daemen, L.; Cheng, Y.; Ramirez-Cuesta, A. J.; Feng, P., An Ultra-Tunable Platform for Molecular Engineering of High-Performance Crystalline Porous Materials. *Nat. Commun* **2016,** *7*, 13645.

13. Zhao, X.; Bu, X.; Nguyen, E. T.; Zhai, Q.-G.; Mao, C.; Feng, P., Multivariable Modular Design of Pore Space Partition. *J. Am. Chem. Soc.* **2016,** *138*, 15102-15105.

14. Zhao, X.; Bu, X.; Zhai, Q.-G.; Tran, H.; Feng, P., Pore Space Partition by Symmetry-Matching Regulated Ligand Insertion and Dramatic Tuning on Carbon Dioxide Uptake. *J. Am. Chem. Soc.* **2015,** *137*, 1396-1399.

15. Liu, Q.-Y.; Wang, W.-F.; Wang, Y.-L.; Shan, Z.-M.; Wang, M.-S.; Tang, J., Diversity of Lanthanide(Iii)–Organic Extended Frameworks with a 4,8-Disulfonyl-2,6-Naphthalenedicarboxylic Acid Ligand: Syntheses, Structures, and Magnetic and Luminescent Properties. *Inorg. Chem.* **2012,** *51*, 2381-2392.

Chapter 6: The Roles of Alkali Metals and Ionic Network in Directing the Formation of Conductive Metal-Organic Frameworks

6.1 Introduction

The crystal engineering of metal-organic frameworks (MOFs) has been receiving tremendous attention from many interdisciplinary fields due to the materials' unique architectures,[16-19] intriguing functionalities,[20-24] and facile customizations.[25-28] Anionic frameworks in particular, has an extra capability of transporting ions through channels. Optimization of ionic conductors requires efficient ion-hopping distance, and high concentration of ions. Since these physical properties are strongly tied to intrinsic material design, it is highly important to develop innovative synthetic strategies for the discovery of novel functional MOF materials.

The utilization of structural directing agents (SDA) is an effective means to direct the self-assembly process of metals and organic ligands into fascinating architectures. Specifically, organic structural directing agents (OSDA) such as protonated amines,[29-32] cations of ionic liquids[33-36] and deep eutectic salts[37-39] are often used to direct the synthesis of novel anionic MOFs. In addition, the OSDA can help the transformation of frameworks. For example, the neutral 2D In-oxalate sheets[40] assembled under hydrothermal condition transformed to the 3D **sra** net under influence of diazabicyclo[5.4.0]undec-7-ene,[41] to the **dia** net under ethylenediamine,[42] and to the **lig** net with addition of 1-ethylpiperazine.[43]

Recently, we have found that the addition of ionic liquids such as acetylcholine chloride, 1-ethyl-3-(methylimidazolium) ethyl sulfate, and tris-(2-hydroxyethyl)-methyl-ammonium methylsulfate can further uncover indium-oxalate structures with **rho**, **gis** and **abw** topological nets, respectively.[44]

Compared to the OSDA, inorganic structural directing agents (ISDA) are much less employed in the search for novel anionic MOFs.[45] For the majority of MOFs syntheses, the primary functions of alkali and alkaline earth metals are to act as simple charge balancing and/or mineralizing agents.[46-47] This highly contrasts with the syntheses of zeolites, where both OSDA and ISDA are crucial, individually and in different combinations, to the discovery of novel zeolitic phases. For instance, in the presence of Li^+, K^+, Rb^+, and Cs^+, FAU zeolite transforms into ABW, CHA, MER, and ANA, respectively.[48] Many recent zeolitic phases also rely on simultaneous incorporation of multiple alkalis such as Li^+-Sr^{2+} for MEI[49] and Na^+-K^+ for MSE.[50] Considering that some of these topologies could not be synthesized with only one inorganic salt,[51] we believe that if given suitable conditions, these inorganic cations are just as capable of directing the formation of novel anionic MOFs as their organic counterparts. It is our goal then, to

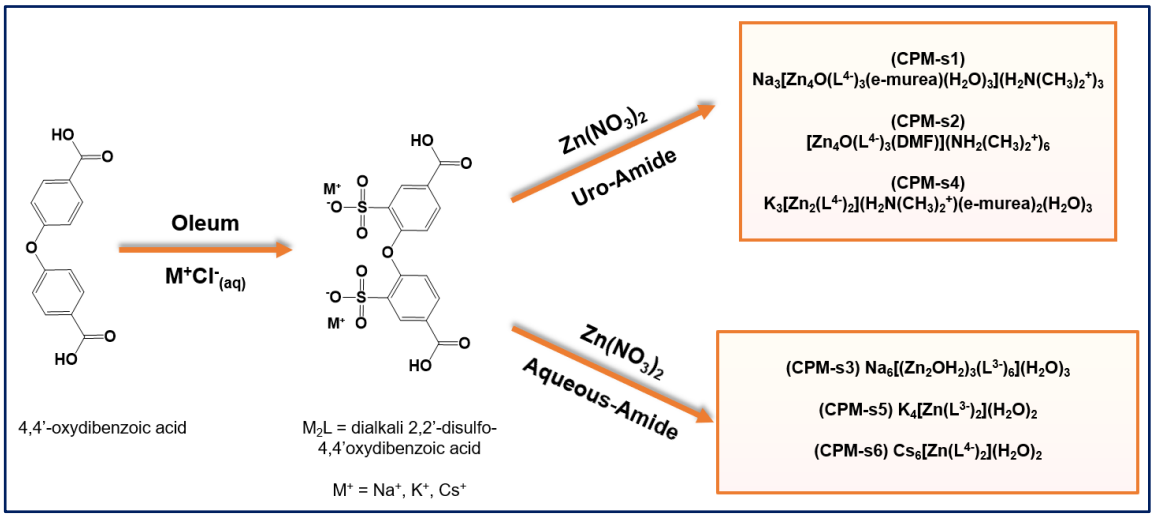

Figure 6.1 Synthetic design for constructing CPM-s1 to CPM-s6.

investigate the cooperative structural directing effects of inorganic cations in different solvent systems.

We first examine MOF-5 type, the iconic MOF whose structural features have been extensively explored and tied to different physical properties.[52-56] In order to transform MOF-5 into novel anionic frameworks, we designed a two-step synthesis procedure with 4,4'-oxydibenzoic acid. We hypothesized that the intrinsic ionic potential of each alkali (Na > K > Cs)[57-58] will affect their interactions with sulfonate ions, leading to different ionic domains. This in turn would influence the molecular arrangements of ligands and impact the formation of the coordination network. Hence, the 4,4'-oxydibenzoic acid is first sulfonated and crystallized in aqueous metal chloride solution to yield M_2L (M^+ = Na^+, K^+, Cs^+). Subsequent dissolution of M_2L in the presence of Zn^{2+} would then allow for the interaction of alkali-sulfonate to influence the spatial arrangement of Zn^{2+} carboxylate coordination, ultimately resulting in novel anionic MOF materials.

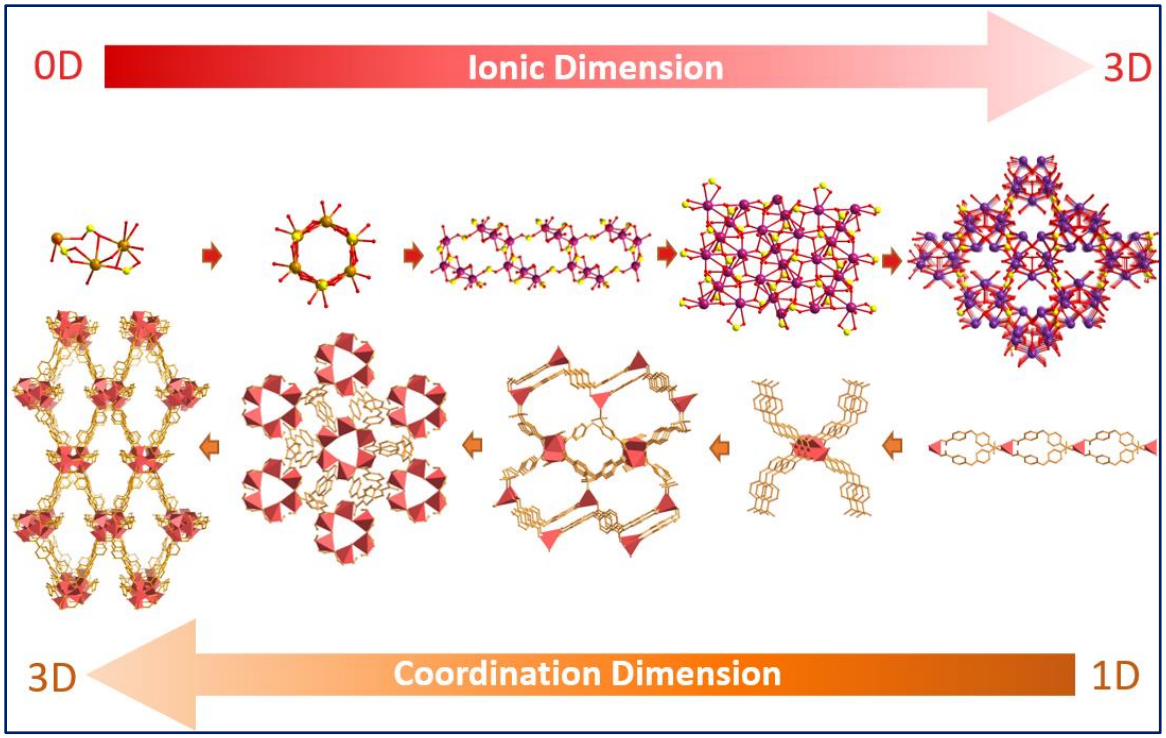

Figure 6.2 Dimension of ionic bonding alkali ions in relation to the overall dimension of coordinating framework. (Top left to right) cluster environments of Na^+, 1D chain and 2D sheet of K^+, 3D network of Cs^+. Na (tan), K (purple), Cs (dark purple), O (red) S (yellow). (Bottom right to left) two 1D chains and three 3D network. Zn coordination polyhedron (dark orange), organic linker (orange).

With the above-mentioned strategy, six novel crystalline phases with varying dimensionalities are synthesized. Some of these structures have topologies or building units closely related to MOF-5. As illustrated in Figure 6.2, the dimensionality of these materials is related to the properties of different inorganic cations. It seems that the increasing of radii (Na < K< Cs) resulted in higher ionic bonding dimension (Na = 0D, K = 1D-2D, Cs = 3D). Different solvent systems also resulted in different types of counter cations. In aqueous-amide solution, only alkali salts existed as counterions, while in the uro-amide solution, the presence of dimethylammonium counter ions ($H_2N(CH_3)_2^+$) are also observed. More interestingly, two orders of magnitude enhancement in conductivity

is achieved when the Na_2L and $Zn(NO_3)_2$ precursors are reacted in an environment with an abundance of water.

6.2 Experimental Section

6.2.1 Chemicals and Material

$Zn(NO_3)_2 \cdot 6H_2O$, NaCl, KCl, CsCl, 4,4′-oxybis(benzoic acid) (H_2oba), oleum, Ethanol (EtOH) and N,N-dimethylformamide (DMF) were purchased from Fischer Scientific Co., while N,N-diethylformamide (DEF) and 1,3-dimethyl-2-imidazolidinone (e-murea) were obtained from TCI-America. All were used as received without further purification.

6.2.2 Construction of M_2dsoba (M = Na, K, Cs).

Sulfonation of H_2oba is modeled after reported literature[5] with additional modifications. Typically, 20-30% fuming sulfuric acid (15 mL) is added to H_2obb (7.5 g) in a 100 mL round-bottom flask equipped with a magnetic stir-bar and a water condenser. The mixture is heated for 2 hours at 110 °C, allowed to cool to ambient temperature, poured over saturated aqueous solution of MCl (M = Na, K, Cs), vacuum filtered, recrystallized with water, and dried at 120 °C for 12 hours. Clear crystalline materials (needle-like (Na), hexagonal-shape (K), rectangular-cube (Cs)) were obtained with expectant yield ~80 %.

6.2.3 Synthesis of sulfonated MOFs

Synthesis of CPM-s1. In a 20 mL glass vial, 2.1 g of DMF and 1.0 g e-murea are added to 74 mg of $Zn(NO_3)_2 \cdot 6H_2O$ and 56 mg Na_2dsoba. The vial is sealed, sonicated for 30

minutes, and placed in a 100 °C oven for 5 days. Large colorless clustering spikes are grown in the presence of an amorphous phase attached to the wall. Pure crystalline material can be obtained by slightly scratching the clusters and pipetting them out without disrupting the powder phase. Yield: 77 % based on Na_2L.

Synthesis of CPM-s2. In a 20 mL glass vial, 60 mg of $Zn(NO_3)_2 \cdot 6H_2O$ and 46 mg Na_2dsoba are dissolved in 2.1 g of DMF and 1.0 g e-murea. The vial is sealed, sonicated for 30 minutes, and placed in a 120 °C oven for 5 days. Pure yellow-tinted crystalline material can be obtained by washing product with DMF followed by quick sonication pulses. Yield: 90 % based on Na_2L.

Synthesis of CPM-s3. In a 23 mL Teflon-lined stainless autoclave, the mixture of 60 mg of $Zn(NO_3)_2 \cdot 6H_2O$, 73 mg Na_2dsoba, 4 g DEF, 4 g EtOH and 2 H_2O is allowed to stir for 1 hour. After sealing and heating the reaction at 120 °C for 7 days, pure samples can be obtained by washing with hot DMF. In cases where only a clear solution is present after cooling to ambient temperature, the solution is transferred to a 20 mL glass vial, sealed, and heated at 120 °C for another 12 h. Yield: 40 % based on Na_2L.

Synthesis of CPM-s4. In a 20 mL glass vial, 63 mg of $Zn(NO_3)_2 \cdot 6H_2O$ and 49 mg K_2dsoba are dissolved in 2.1 g of DMF and 1.0 g e-murea. The vial is sealed, sonicated for 30 minutes and placed in a 120 °C oven for 24 hours. Colorless crystalline cubes can be obtained by washing product with DMF followed by quick sonication pulses. Yield: 30% based on K_2L.

Synthesis of CPM-s5. In a 20 mL glass vial, 30 mg of $Zn(NO_3)_2 \cdot 6H_2O$ and 54 mg K_2dsoba are dissolved in 4.0 g of DEF, 4.0 g EtOH and 2.0 g H_2O. The vial is sealed, sonicated for

30 minutes, and placed in a 120 °C oven for 5 days. Colorless crystalline needles can be obtained by washing product with DMF followed by quick sonication pulses. Yield: 35% based on K_2L.

Synthesis of CPM-s6. In a 20 mL glass vial, 30 mg of $Zn(NO_3)_2 \cdot 6H_2O$ and 105 mg Cs_2dsoba are dissolved in 4.0 g of DEF, 4.0 g MeOH and 2.0 g H_2O. The vial is sealed, sonicated for 30 minutes and placed in a 120 °C oven for 5 days. Colorless crystalline plates can be obtained by washing product with DMF followed by quick sonication pulses. Yield 50% based on Cs_2L.

6.2.4 Property Characterization

Other Characterization: SCXRD, PXRD, and TGA were obtained as mentioned in 2.2.4. Conductivity measurements were obtained as mentioned in 5.2.4.

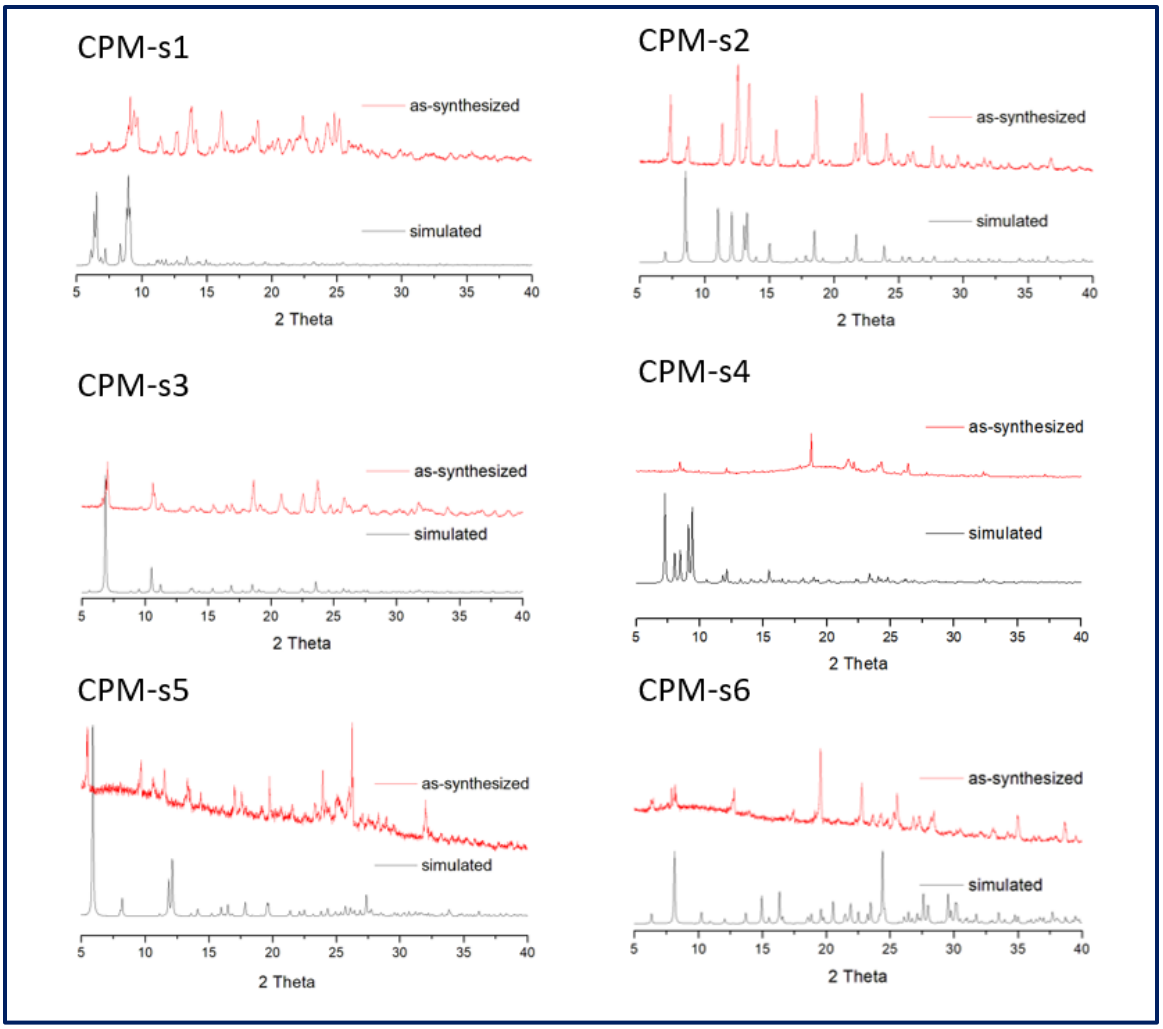

Figure 6.3 PXRD of CPM-s1 to CPM-s6.

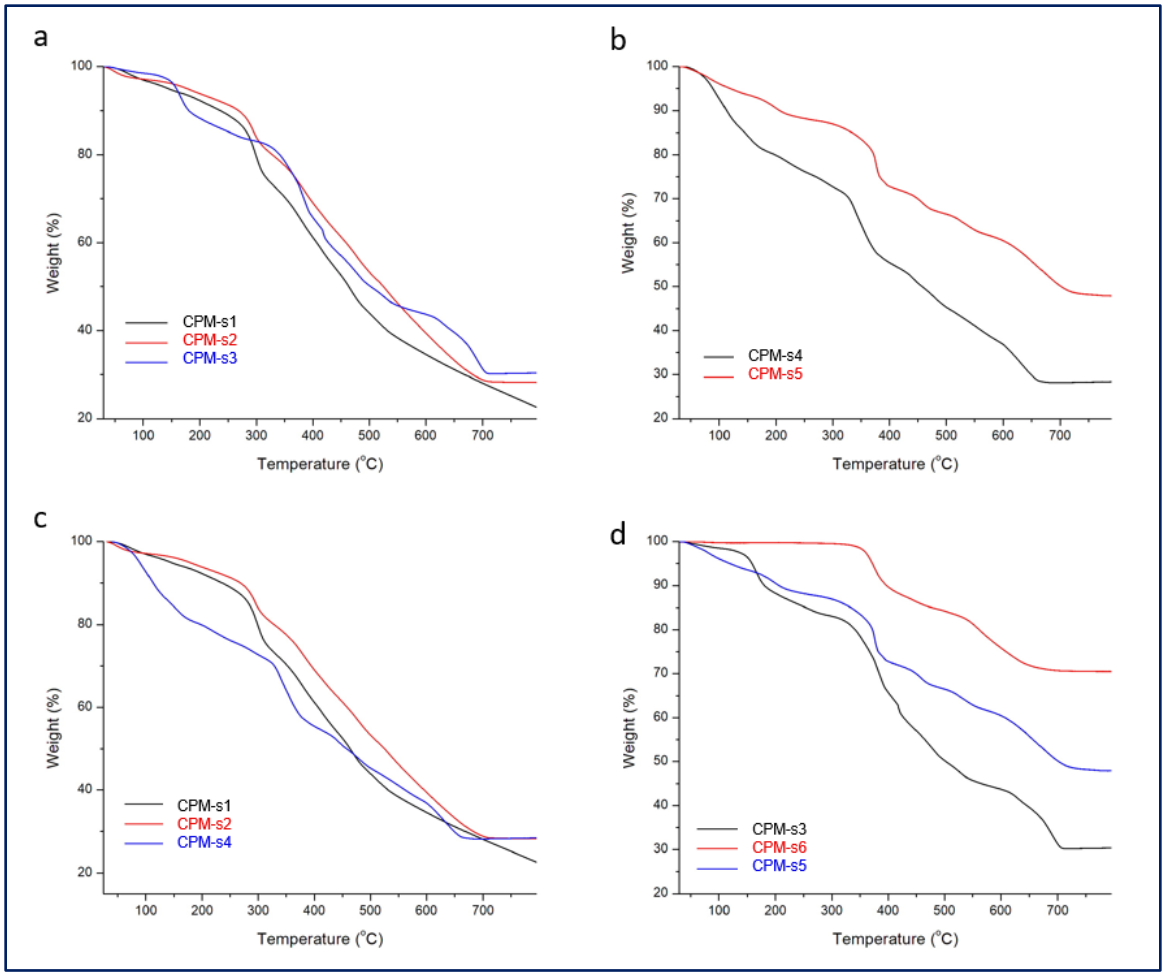

Figure 6.4 Thermal gravimetric analysis curve comparisons of materials in this study: (a) materials made from Na_2dsoba ligand, (b) materials made from K_2dsoba ligand, (c) materials from uro-amide solvent system, (d) materials from the aqueous-amide solvent system.

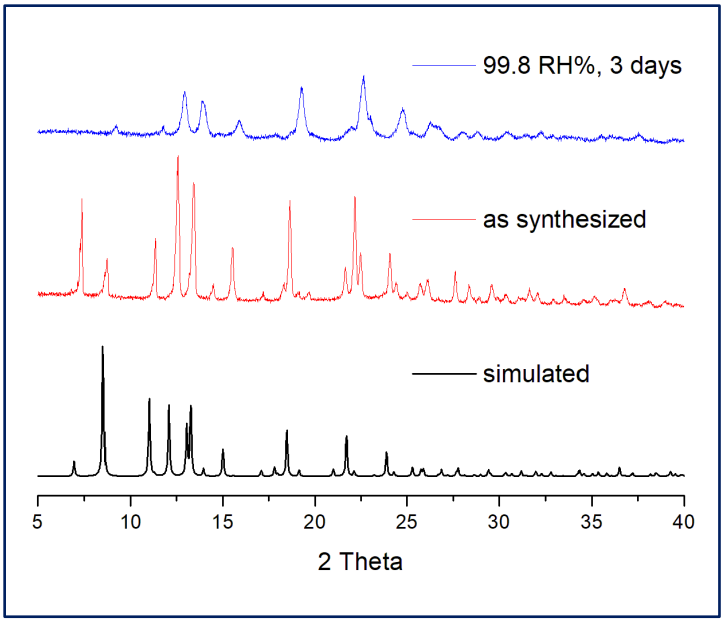

Figure 6.5 PXRD of simulated, as-synthesized and after conduction measurements of CPM-s2.

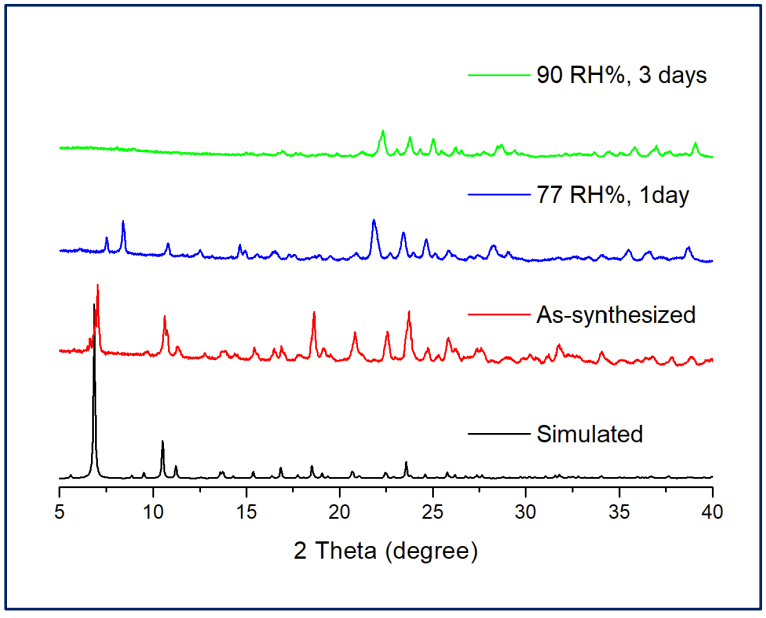

Figure 6.6 PXRD of simulated, as-synthesized and after conduction measurements of CPM-s3.

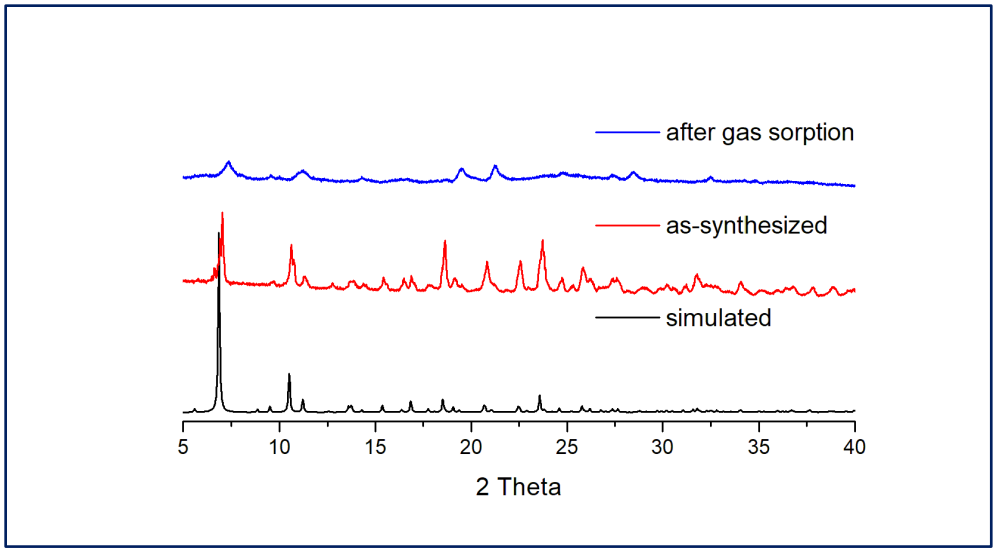

Figure 6.7 PXRD of CPM-s3 after gas sorption.

6.3 Results and Discussion

In reacting $Zn(NO_3)_2 \cdot 6H_2O$ with M_2L ($M = Na^+, K^+, Cs^+$) in two solvent systems with varying temperatures, CPM-s1 to CPM-s6 are obtained (Figure 6.1) and single-crystal structures are summarized in Table 6.1. The cooperative effect between different alkali cations and reaction media yielded a diverse series of SBUs: CPM-s1 and CPM-s2 share the tetrameric $Zn_4O(COO^-)_6$ cluster-type, CPM-s3 exhibits novel hexameric SBU, CPM-s4 comprises of both monomeric and paddlewheel SBUs, CPM-s5 contains infinite chain-type SBU, and CPM-s6 has monomeric SBU. CPM-s1 to CPM-s4 are 3D frameworks while CPM-s5 and CPM-s6 are 1D chains. The powder X-ray diffraction patterns of isolated CPM-s1 to CPM-s3 are consistent with the ones simulated from single-crystal structures, indicating phase purity (Figure 6.3). TGA of the CPM-s1 to CPM-s6 demonstrate all materials have framework stabilities above 300 °C. Gas sorption of CPM-

s3 verify micro-porosity of the framework which allows for better ion transfer and higher conductivity than other crystalline phases.

Table 6.1. Summary of crystal data and structure refinements for CPM-s1 to CPM-s6.*

Name	Formula	*Space Group*	*a* (Å)	*b* (Å)	*c* (Å)	*β*	R(F)
CPM-s1	$Na_3[Zn_4O(L^{4-})_3(\text{e-murea})(H_2O)_3](H_2N(CH_3)_2^+)_3$	$Pna2_1$	28.91	15.422	27.71	90	0.070
CPM-s2	$[Zn_4O(L^{4-})_3(DMF)](H_2N(CH_3)_2^+)_6$	$R\bar{3}c$	25.100	25.100	23.142	90	0.118
CPM-s3	$Na_6[(Zn_2OH_2)_3(L^{3-})_6](H_2O)_3$	$R\bar{3}c$	19.969	19.969	77.038	90	0.047
CPM-s4	$K_3[Zn_2(L^{4-})_2](H_2N(CH_3)_2^+)(\text{e-murea})_2(H_2O)_3$	$P2_1/c$	23.142	12.371	25.092	107.659	0.067
CPM-s5	$K_4[Zn(L^{3-})_2](H_2O)_2$	$C2/c$	44.20	15.892	7.134	98.119	0.057
CPM-s6	$Cs_6[Zn(L^{4-})_2](H_2O)_2$	$P2_12_12$	17.355	9.966	13.918	90	0.043

*L = 2,2'-disulfo-4,4'oxydibenzoic acid, e-murea = 1,3-dimethyl-2-imidazolidinone.

6.3.1 Crystal Structure

In reacting $Zn(NO_3)_2$ with Na_2L in DMF:e-murea (2:1) solution at 100 °C, the crystallization of CPM-s1 is observed (Figure 6.8). The crystalline material has $Pna2_1$ space group with an asymmetric unit containing four Zn^{2+}, one oxo, three Na^+, three $dsoba^{4-}$, three charge balancing dimethylammonium cations, two pendant water, and one e-murea. In each SBU, there are three tetrahedrally coordinated Zn^{2+} and one octahedrally coordinated Zn^{2+} linked to the central oxo group forming the $Zn_4O(COO)_6$ tetramer with two pendant water molecules. Dsoba ligands connect these $Zn_4O(COO)_6$ clusters into a 3D anionic framework with **pcu** topology. The material is further charge-balanced by Na^+ and $H_2N(CH_3)_2^+$.

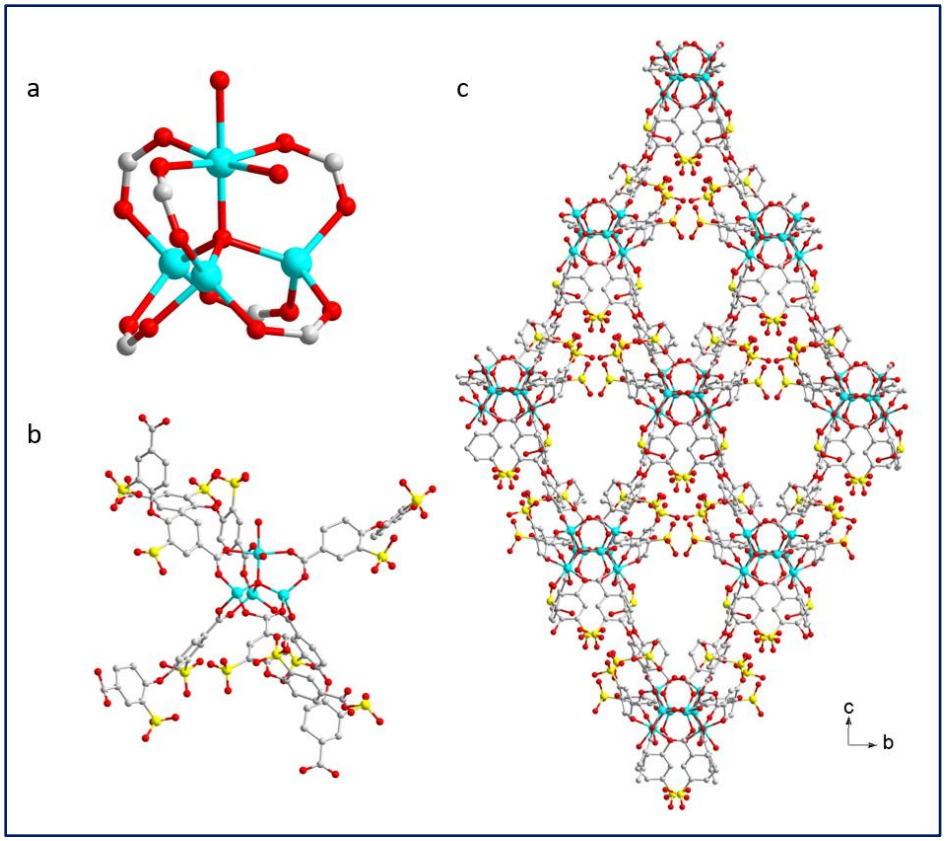

Figure 6.8 Illustration of CPM-s1. (a) Zn_4O SBU, (b) local coordination environment, (c) 3D anionic framework.

Increasing the reaction temperature of CPM-s1 resulted in a phase transformation to the interpenetrated CPM-s2 (Figure 6.8). Although CPM-s2 is also constructed from the coordination between $Zn_4O(COO)_6$ clusters and dsoba ligands into the 3D **pcu** net, the subtle differences in pendant ligands, guest species, pore geometry and degree of catenation all contributed to the different intrinsic and extrinsic physical properties. Compared to CPM-s1, CPM-s2 crystallizes in a more symmetric space group, $R\bar{3}c$, with the asymmetric unit containing two unique Zn^{2+}, one $dsoba^{4-}$ ligand, one oxo ion, one DMF molecule and two $H_2N(CH_3)_2^+$. Since Zn_4O SBU only contains one pendant solvent molecule, the octahedrally coordinated Zn^{2+} with C_1-symmetry in CPM- s1 transformed to

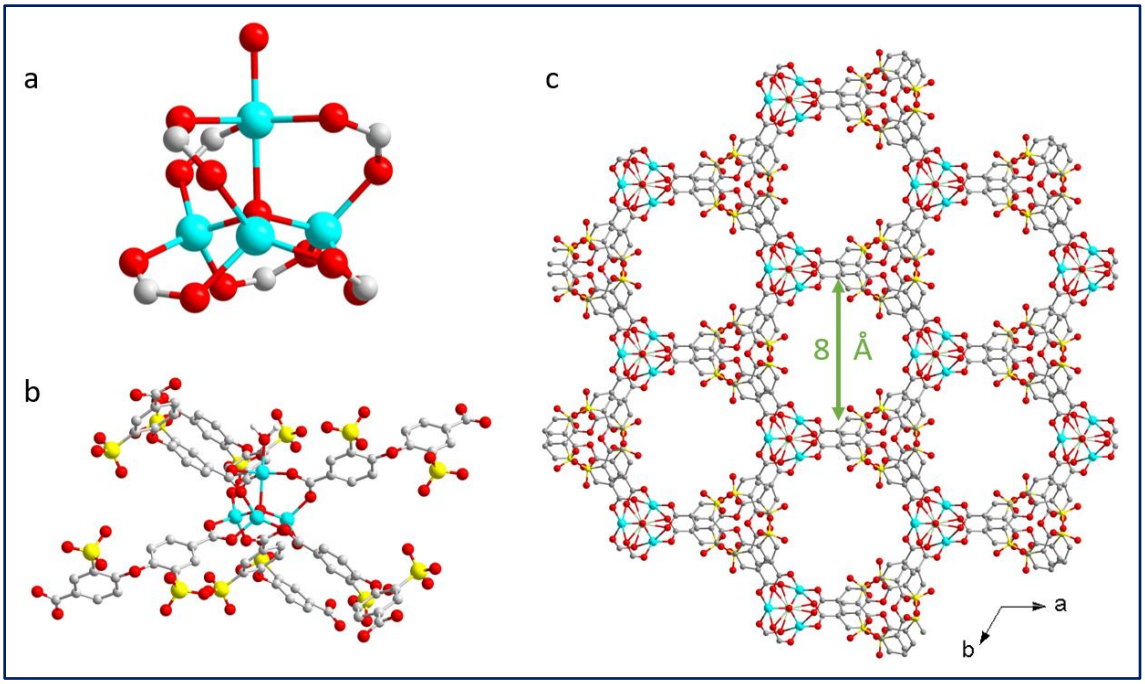

Figure 6.9 Illustration of CPM-s2. (a) Zn_4O SBU, (b) local coordination environment, (c) 3D anionic framework.

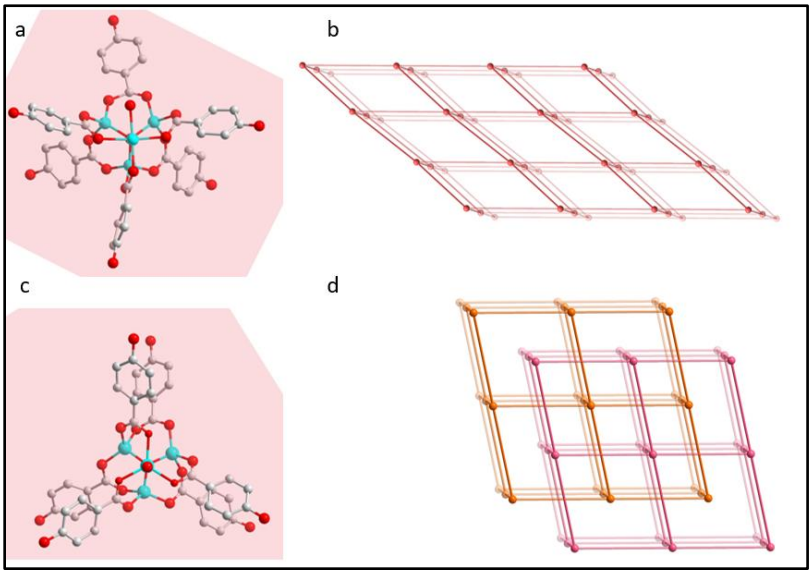

Figure 6.10 Two anionic MOF-5 type structures viewed from the apex of $Zn_4O(COO)_6$ in (a) CPM-s1, and (c) CPM-s2. DMF molecule is drawn as oxygen for clarity. Transformation from CPM-s1 (b) to two-fold interpenetration CPM-s2 (d).

a more symmetrical trigonal bipyramidal coordination mode with C_3-symmetry in CPM-s2. Furthermore, the absence of Na^+ and e-murea in CPM-s2 influenced the configuration of the flexible dsoba ligand to result in interpenetration.

In CPM-s1, the presence of unsymmetrical Na^+ and ($H_2N(CH_3)_2^+$) balancing cations exhibit different interaction strengths with the SO_3 groups of dsoba, causing the ligand to have three different bending angles ($^-$OOC---O---COO$^-$ = 123.74°, 119.78°, 114.88°). In comparison, the SO_3 groups in CPM-s2 only show similar interaction strength with neighboring dimethylammonium cations, resulting in the same bending angle ($^-$OOC---O---COO$^-$ = 123.53°) for all dsoba ligands. Indeed, the increase of reaction temperature resulted in removal coordinating Na^+, H_2O, e-murea molecules, allowing the flexible SBUs and dsoba ligands to have spatial arrangements that ultimately manifested in 2-fold interpenetration for CPM-s2.

In switching from uro-amide solution to aqueous-amide (DEF: EtOH: H_2O, 4:2:2) solution, the crystallization of a novel crystalline phase, CPM-s3, is obtained. CPM-s3 crystallizes in $R\bar{3}c$ space group with an asymmetric unit containing two Zn^{2+}, two Na^+, two dsoba^{3-}, and four H_2O (Figure 6.11). The most striking feature of CPM-s3 is the presence of an unprecedented nonplanar, centrosymmetric hexameric cluster. Each unique Zn^{2+} center coordinates with one carboxylate and is bridged by an aqua molecule to form a dimer. Three pairs of Zn^{2+} dimers are further bridged by six other carboxylates to give a centrosymmetric $[(Zn_2OH_2)_3(COO)_6](COO)_6$ hexamer. More interestingly, the hexameric ring could alleviate all angle strains simply by adopting the more energetically stable

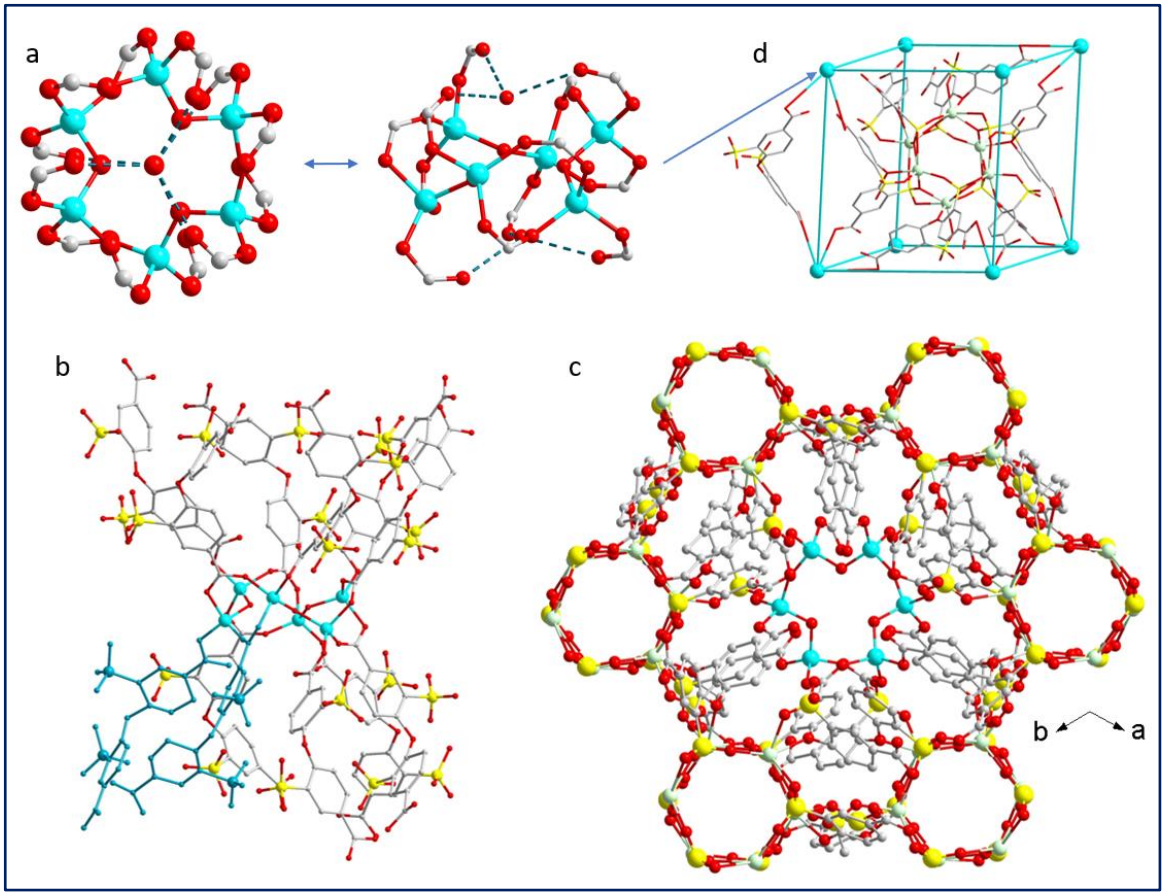

Figure 6.11 Illustration of CPM-s3. (a) Top-down and aerial views of SBU, (b) local coordination environment with two ligands coordinating to same two SBUS highlighted in blue, (c) View of the 3D framework through c-axis, (d) topological net of the framework.

nonplanar puckered conformation. Furthermore, the pendant carboxylate linkers extending from above and below the ring, forming a semi-open cage. These claw-like linkers entrap water molecules within their cage through hydrogen bonding interactions (OH---OH distance = 2.80 Å). Such H-bonding network within the cage further stabilizes the clusters.

Another unusual feature of CPM-s3 is the double-crosslinking mode of the $[(Zn_2OH_2)_3(COO)_6](COO)_6$ SBU. With each pair of $dsoba^{3-}$ extending to the same adjacent hexameric ring, six pairs of $dsoba^{4-}$ extend the SBU into six directions, forming the 3D

pcu-net. The presence of an SBU with higher nuclearity in CPM-s3 enables the accommodation of more surrounding organic linkers, which further reinforces the coordination bond of the framework and leads to enhanced thermal stability.

Through two different solvent conditions, we observe two different Na^+ cluster formations and varied degree of ligand protonation. In uro-amide solution, Na^+ ions form linear trimeric clusters with neighboring SO_3^- while in the aqueous-amide solution, Na^+ ions form the symmetric hexagonal prisms. Additionally, for the uro-amide condition, all sulfonate groups coordinate to either Na^+ or $H_2N(CH_3)_2^+$ ions, but only half of the sulfonate groups in the aqueous amides coordinate with Na^+. Through careful analysis of electron density peaks, no other counter ion could be identified for the remaining sulfonate groups. Therefore, it is concluded that a quarter of $dsoba^{4-}$ is protonated to maintain framework neutrality.

The substitution of Na_2dsoba with K_2dsoba leads to two novel structures, CPM-s4 and CPM-s5, with drastically different structural features compared to each other and the Na^+ counterparts. In CPM-s4, a rare phenomenon of in-situ mixed SBUs formation is observed. It crystallized in the $P2_1/c$ space group with an asymmetric unit consisting of two unique Zn^{2+}, two $dsoba^{4-}$, three K^+, one $H_2N(CH_3)_2^+$, two e-murea and three H_2O molecules (Figure 6.12). Here, Zn1 has a square pyramidal coordination geometry with four carboxyl groups of dsoba and one pendant keto group from e-murea. Through the center of inversion, another symmetry equivalent Zn1 is generated to complete the paddlewheel $Zn_2(COO)_4$ SBU. In comparison, Zn2 exhibits a distorted octahedral coordinating mode with two carboxyl groups and two sulfo groups. Whereas the presence

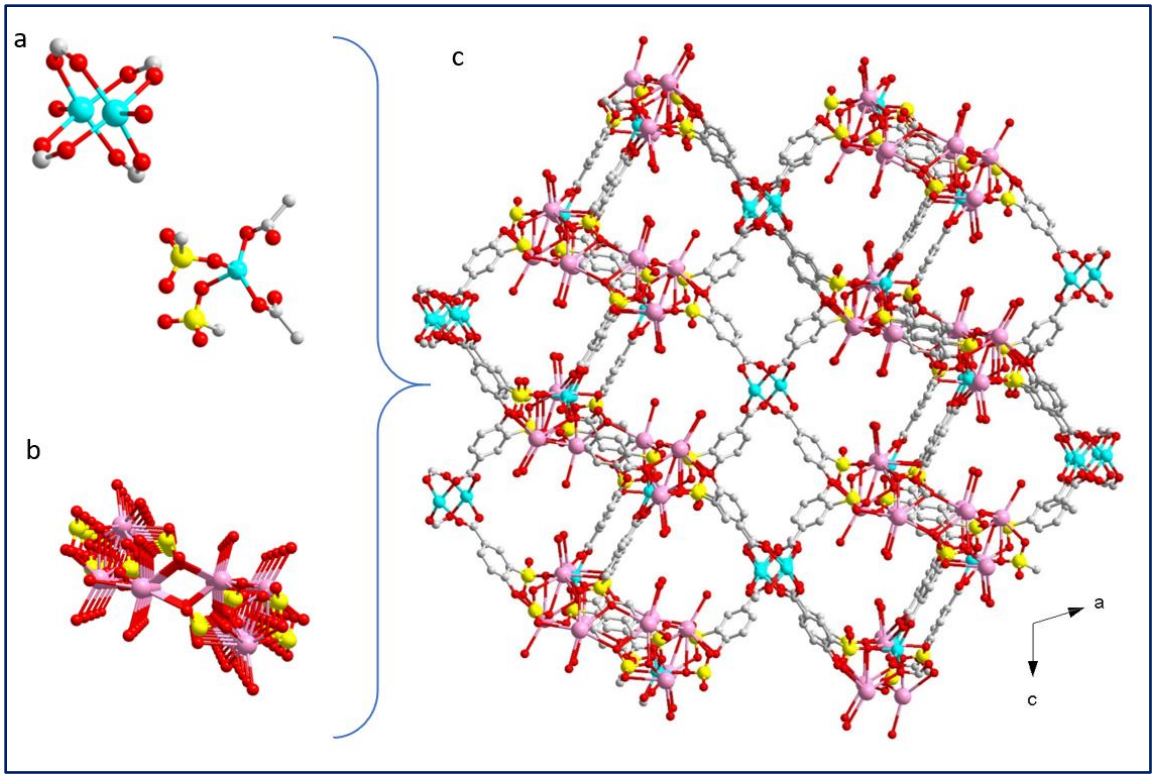

Figure 6.12 Illustration of CPM-s4. (a) monomeric and paddlewheel SBUs of the framework, (b) binding mode of K^+ along the SO_3^- channel, (c) 3D representation of framework.

of metals having a different geometrical configuration in one reaction system is quite common (pendant ligands can reversibly bind to open metal sites, e.g. CPM-s1 and CPM-s2), the presence of metals with different molecular geometries forming distinct SBUs is quite difficult to come across since the system must maintain a perfect equilibrium for both SBUs to coexist.

More interestingly, the presence of mixed SBUs in CPM-s4 resulted in different alternating 2D nets that are linked to form a novel 3D framework. In the first layer, $Zn_2(COO)_4$ are crosslinked by carboxyl groups of dsoba to form the wavy 2D (4,4) **sql**-net. In the alternating layer, Zn links with both sulfo and carboxyl groups to form another

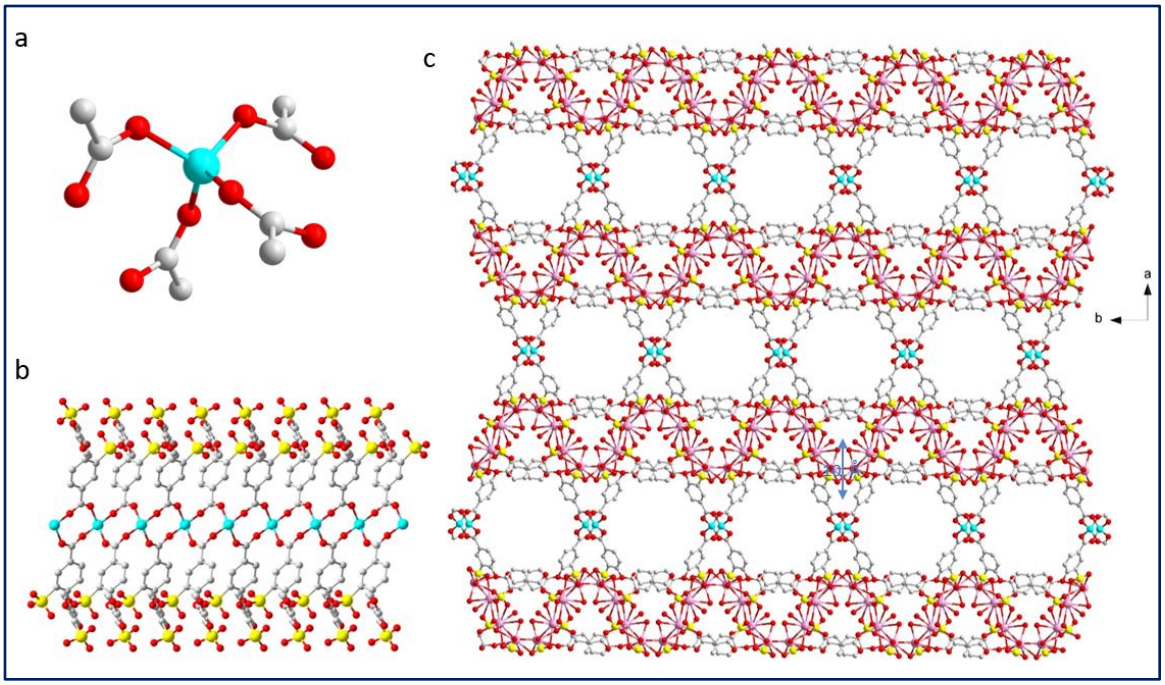

Figure 6.13 Illustration of CPM-s5. (a) metal coordination, (b) 1D metal chain, (c) 3D representation of framework.

wavy 2D (4,8) **fes**-net. The free SO_3 ligands from the wavy **sql**-layer extend from above and below the sheet to link with the Zn^{2+} of the neighboring **fes**-net, hence resulting in a novel 3D framework. It is incredibly fascinating to note that even with the different SBUs leading to different 2D lattices that are seemingly impossible to connect, the flexible dsoba ligands could rearrange themselves in perfect configuration to weave these mismatched SBUs into beautiful 3D architecture.

In switching the precursors of CPM-s4 from an uro-based system to an aqueous-mixed medium, CPM-s5 crystallizes in *C2/c* space group, with an asymmetric unit containing one unique Zn^{2+}, two K^+, one $dsoba^{3-}$ and two H_2O (Figure 6.13). Each Zn^{2+} is bridged by four carboxyl groups to form infinite 1D chains. Although the presence of K^+

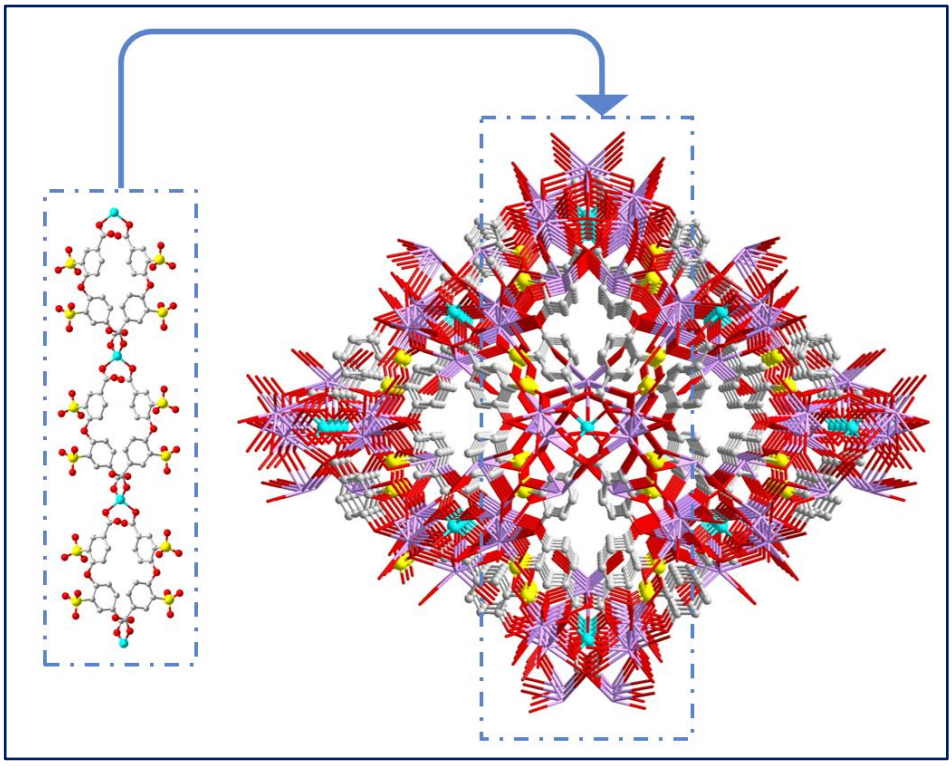

Figure 6.14 Illustration of CPM-s6.

in the system does not affect the tetrahedral coordination of Zn^{2+}, its ionic dimension impacted the overall dimensionality of the framework.

Compared to crystals formed in the presence of Na^{+} ions, the crystals formed in the presence of K^{+} ions show a much larger ionic network. The 0D sodium sulfonate clusters in CPM-s1 and CPM-s3 are replaced with 1D chains and 2D sheets of potassium sulfonate in CPM-s4 and CPM-s5, respectively. Consequently, there was less room available to the coordination bonding between transition metals and dicarboxylates to expand into a 3D framework. This trend is further amplified in CPM-s6, where the ionic-bonding network is 3D while the coordination network is reduced to 1D.

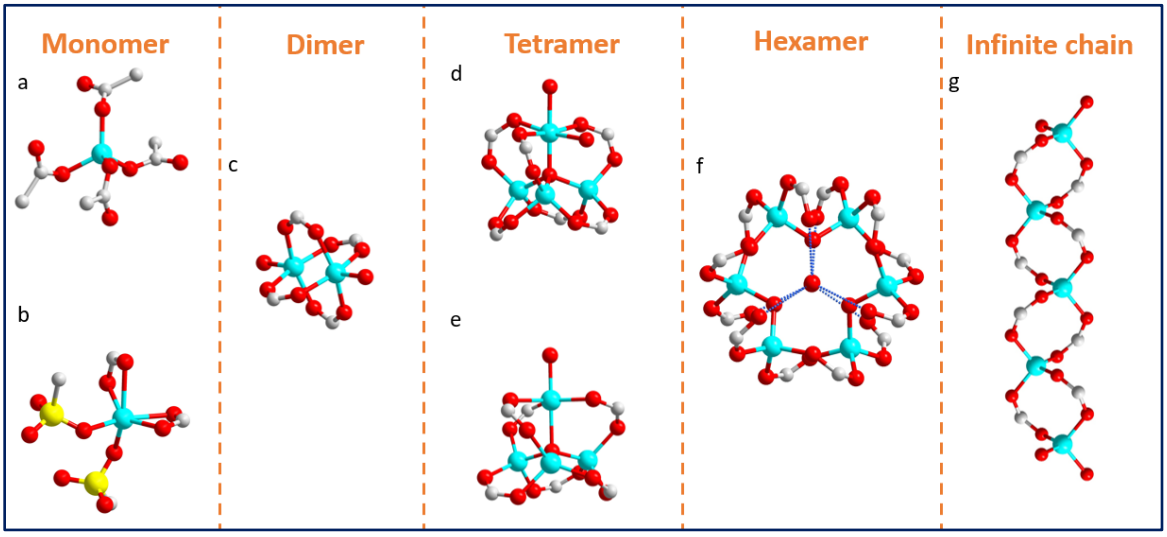

Figure 6.15 Dimension of ionic bonding alkali ions (top) in relation to the overall dimension of the coordinating frameworks (bottom). Zn (cyan), C (grey), O (red), Na (aquamarine), K (pink), Cs (purple).

CPM-s6 crystallizes in *P2₁2₁2* space group, with an asymmetric unit containing half Zn^{2+}, one $dsoba^{4-}$, three Cs^{+}, and one H_2O (Figure 6.14). Here, each pair of dsoba ligands concave up and down to link with Zn^{2+} at both ends to form a closed 4-membered ring. On each side, Zn^{2+} further coordinates with another pair of dsoba ligands to repeat the molecular unit into an infinite $(Zn(COO))_\infty$ chain. These chains are then embedded in the 3D ionic Cs-dsoba network.

Overall, the utilization of pre-synthesized M_2L in controlled media has allowed us to create six novel anionic crystalline materials with unique features. The intrinsic properties of alkali metals are successfully utilized to direct the arrangement of ligands and SBU formations. Under the same uro-amide condition, switching from Na_2L in CPM-s1 and CPM-s2 to K_2L in CPM-s4 transformed the tetrameric SBUs to mixed dimeric-monomeric SBUs (Figure 6.15). With the decrease in the ionic potential of the cation, the

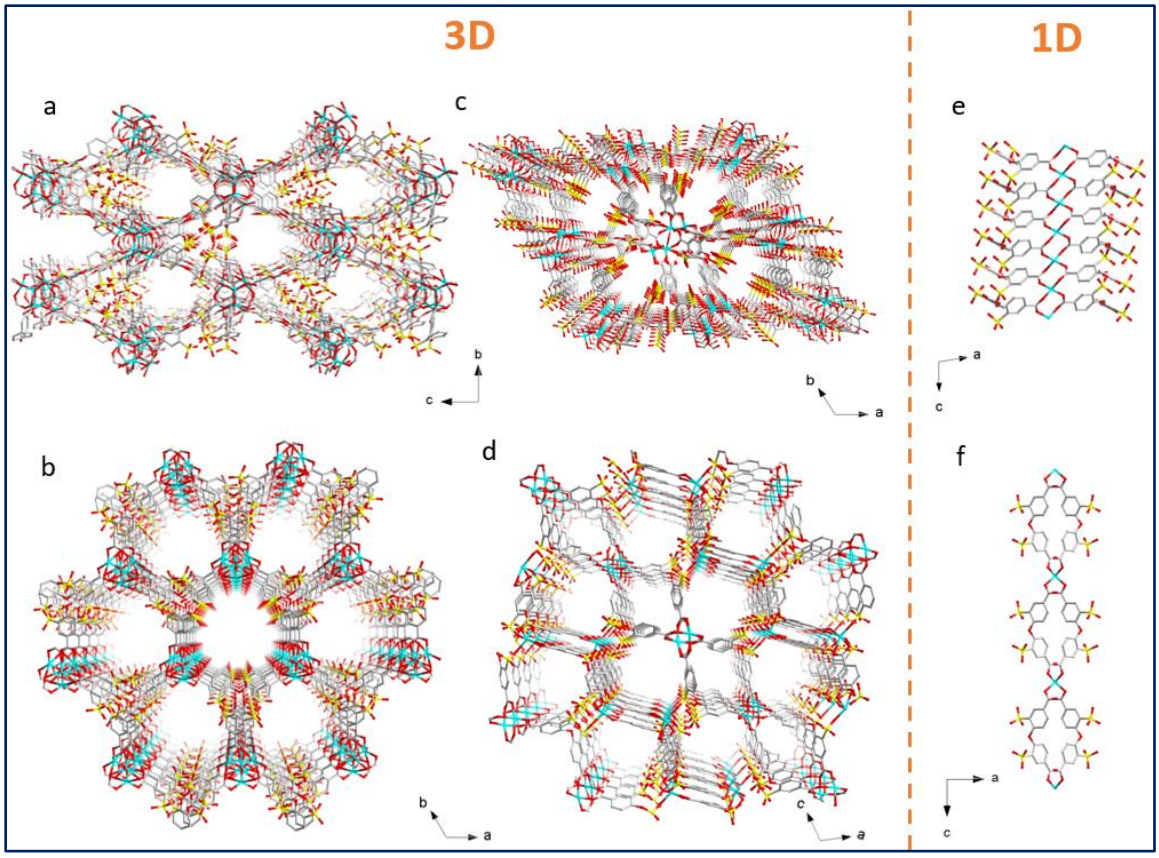

Figure 6.16 Coordination modes of CPM-s1 to CPM-s6. (a-d) 3D framework of CPM-s1 to CPM-s4. (e-f) 1D coordinating chain of CPM-s5 and CPM-s6.

anions are less polarized and showed smaller anion-anion repulsions which resulted in larger ionic domains. This, in turn decreased the nuclearity of SBUs and restricted the coordination network dimension (Figure 6.16). A similar trend is observed for the aqueous-amide solvent system, where incorporation of alkalis with decreasing polarizing power ($Na^+ < K^+ < Cs^+$) in CPM-s3, CPM-s5, and CPM-s6 lead to the transformation of alkali-sulfonate from 0D clusters to 2D sheets and 3D network, respectively. With increasing ionic network dimensionality, the Zn-carboxylate SBU assembly is highly influenced (hexamer with Na^+, infinite chains with K^+, and monomers with Cs^+), resulting

in reduced coordination dimension from 3D (Na^+) to 1D in (K^+ and Cs^+) and hence proving the importance of employing alkali metals as ISDA to drive the condensation of different SBUs and coordination network.

Whereas the alkalis-sulfonate ionic network plays a major role in guiding the formation of specific SBUs and coordination networks, the solvent molecules are important in influencing local coordination of Zn^{2+} and production of counter ions. Under the uro-amide condition, Zn^{2+} exhibits coordination spheres of 4-, 5- and 6-, compared to 4-coordination sphere in aqueous-amide solution.

6.3.2 Thermal Gravimetric Analysis

All structures exhibit two main weight loss stages, where the first corresponds to the removal of guest molecules and the second corresponds to framework decomposition into metal oxides.[59] Compared to the Na-based structures CPM-s1 and CPM-s2 in the uro-amide solution, the Na-based CPM-s3 shows a 40 °C increase in thermal stability in aqueous solution. This higher stability is likely due to the double bridging of dsoba ligands. The twelve dsoba surrounding each metal cluster in CPM-s3 allows for the framework to stay intact throughout a larger temperature range than the six dsoba surrounding each metal cluster in CPM-s1 and CPM-s2. Additionally, TGA confirms the importance of both ionic bonding and coordination bonding in determining the overall thermal stability. Although CPM-s4 primarily exhibits coordination bonding and CPM-s5 exhibits ionic bonding. both structures still exhibit only a framework decomposition temperature difference of only 10 °C. TGA curves of materials in both solvent systems show that alkali metals play a role in increasing the thermal stability of the framework. In both cases, the larger cations show

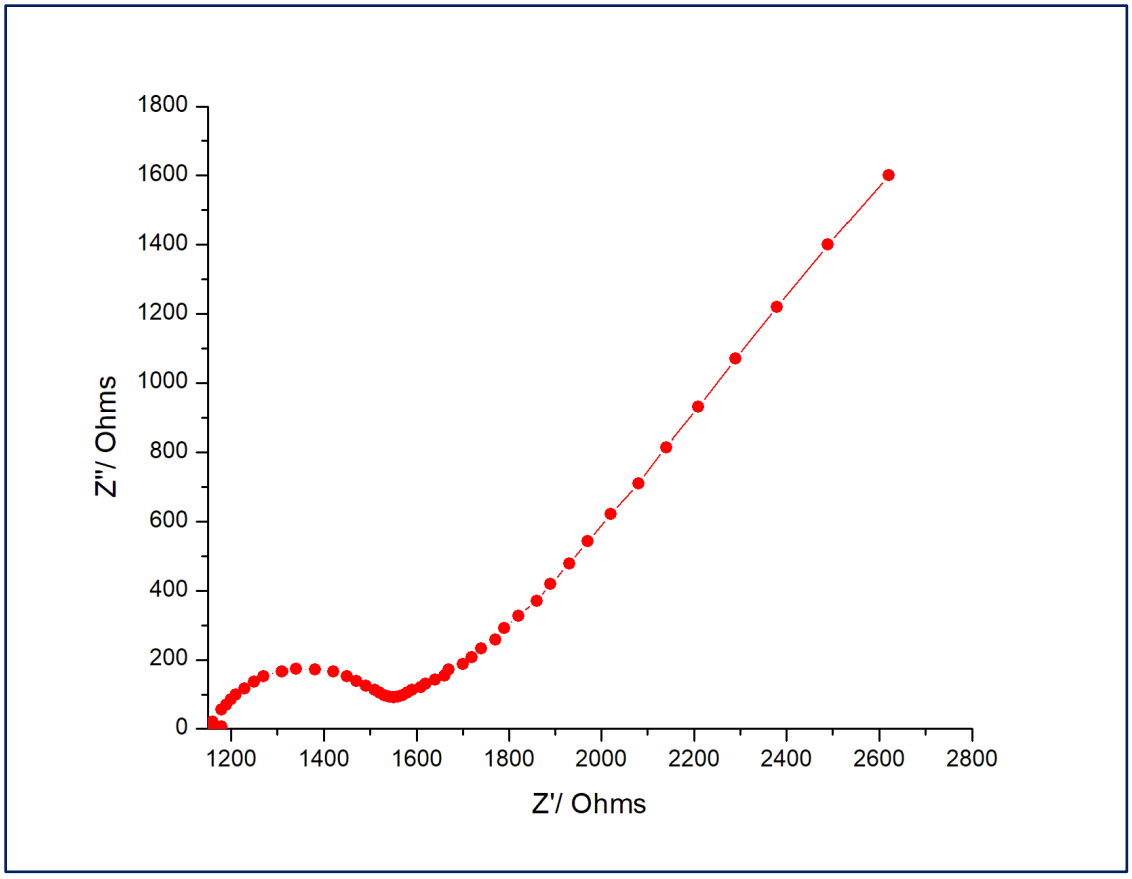

Figure 6.17 Nyquist diagram of the powder sample of CPM-s1 at 22 °C, 99 RH%.

stronger bonding with SO_3 groups, which resulted in a higher framework decomposition temperature.

6.3.3 Ionic Conductivity

Alternating-current (AC) impedance measurements were carried out for pelletized samples. Under ambient temperature and 98% RH, CPM-s3 shows the highest conductivity at 1.25 $x10^{-3}$ S cm^{-1}, a value comparable to the top conducting metal-organic materials (Table S1). Under similar conditions, CPM-s1 and CPM-s2 exhibit much lower performances: 2.7 x 10^{-5} and 2.2 x 10^{-5} S cm^{-1}, respectively. The higher conductivity value of CPM-s3 than of CPM-s1 and CPM-s2 is likely due to an increase in mobility of proton

Table 6.2 Conductivities of MOFs containing alkali-metals under humid conditions.

Compound	Dimension	σ (S cm^{-1})	Temp (°C)	RH (%)	Ref
Zn_3K_2(3,3', 4,4'-BPTC)$_3$(DMF)2][Me_2NH_2]$_4$	3D	8.4x10^{-3}	27	98	[60]
Mg(p-BDC)(pyOH)_Cs	3D	4.97 x10^{-3}	30	90	[61]
CPM-s3	**3D**	1.25 x10^{-3}	**22**	**90**	**This work**
$K_8(PTC)_2(H_2O)1.5]\cdot 4H_2O\}_n$	3D	1.0 x10^{-3}	25	98	[62]
$K_2(H_2adp)[Zn_2(ox)_3]\cdot 2H_2O$	2D	1.2 x10^{-4}	25	98	[63]
$Rb_2(H_2adp)[Zn_2(ox)_3]\cdot 2H_2O$	2D	4.3 x10^{-5}	25	98	[64]
CPM-s1	**3D**	**2.7 x10^{-5}**	**22**	**99**	**This work**
CPM-s2	**3D**	**2.2 x10^{-5}**	**22**	**90**	**This work**
$Li_6(HFTA)_2(H_2O)_3]\cdot 3H_2O$	3D	1.2 x10^{-5}	25	75	[65]
{Na[Cd(MIDC)]}$_n$	3D	1.13 x10^{-5}	25	98	[66]
{[SmK(BPDSDC)(DMF)(H 2O)]•x(solvent)$_n$	3D	1.11x10^{-3}	80	98	[67]
Na_2[Eu(SBBA)$_2$(FA)]•0.375 DMF•0.4H_2O	1D	2.91 x10^{-2}	90	90	[68]

3,3', 4,4'-BPTC = 3,3', 4,4'-biphenyltetracarboxylic acid; DMF = *N*,*N*-dimethylformamide; p-BDC = benzene-1,4-dicarboxylbenzoate; pyOH = 4-pyridinol; PTC 3,4,9,10-perylenetetracarboxylate; H_2adp = adipic acid; ox = oxalate; FTA tetrahydrofuran-2,3,4,5-tetracarboxylate; MIDC = 2-methyl-1H-imidazole-4,5-dicarboxylic acid; BPDSDC = biphenyl-3,3'-disulfonyl-4,4'-dicarboxylic aid; SBBA = 4,4'-sulfobisbenzoic acid, FA = formate

carriers. Crystallization of CPM-s3 in an aqueous environment adds one extra coordinating water molecule per pair of Zn^{2+}, which extends the H-bonding network and facilitates better ion conduction. Conductivity measurements were also investigated at different humidities for better insights into the conducting mechanism. As shown in Figure 6.17, conductivities were highly dependent upon the presence of water in the air. For CPM-s2, a decrease of humidity from 98% to 58% at room temperature. drops conductivity by 2 orders of magnitude, from 3.3 x 10^{-5} to 1.23 x 10^{-7} S $cm^{-1.}$ This strong dependence of conductivity upon humidity signifies the importance of water molecules in transporting

ions through the frameworks. While further investigation is needed for a more detailed mechanism, we hypothesize that the protons are the main sources of mobile ions responsible for the conductivities in these materials.

6.3.4 Gas Adsorption

PLATON calculations show that CPM-s1 to CPM-s6 have potential guest-accessible volumes (solvent and charge-balancing cations) of 46%, 14%, 46%, 23%, 24%, 0%, respectively. While calculations show 46% accessible volume for both CPM-s1 and CPM-s3, we concluded that CPM-s3, without any dimethylammonium counter ion, would have more void space than CPM-s1. As a result, CO_2, C_2H_2, and CH_4 sorption isotherms were collected for the ethanol exchanged CPM-s3. CPM-s3 uptakes a modest amount of gases at 273 K, and it adsorbs CO_2 up to 68.3 $cm^3\ g^{-1}$ at 195 K, 1 atm. The type I isotherm proves that CPM-s3 has permanent microporosity.

6.4 Conclusion

A versatile synthetic method has been proposed and demonstrated to create novel materials with fascinating structural features and dimensionalities. In employing different ISDA agents in the form of ligand counter-balancing ions, six novel Zn(II)-based coordination polymers with different alkali-dsoba salts were successfully synthesized under two different solvothermal systems. In CPM-s1 to CPM-s6, the alkali-sulfonate ionic bonding networks transformed from 0D clusters with Na^+ to 1D chains and 2D sheets with K^+, and 3D network with Cs^+. These vastly differing ionic domains influenced the

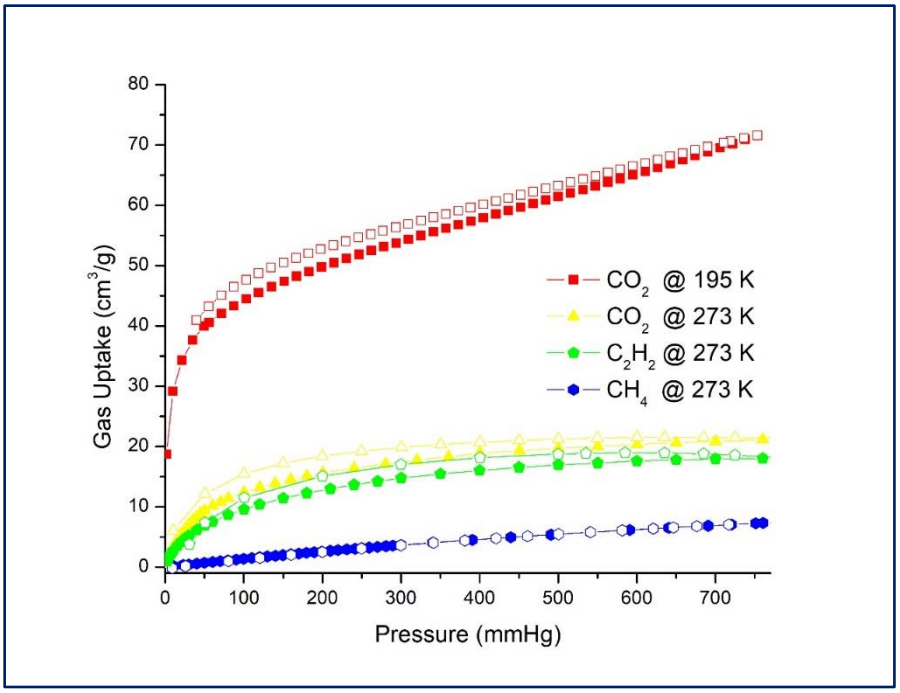

Figure 6.18 Gas sorption data of CPM-s3, after ethanol exchanged, and degassed.

coordination modes and spatial arrangements of the metal-carboxylate linkers, which consequently, directed the dimensionality of the coordination networks from 3D with Na^+ to 1D with Cs^+. CPM-s1 and CPM-s2, made from tetrameric Zn_4O clusters are rare examples of anionic MOF-5-type structures. CPM-s3 features an unprecedented hexameric Zn_6 cluster. Even though a large portion of the charge-balancing cations in these materials would hamper hydrogen bonding networks, some of them still exhibit very high ionic conductivity (e.g. 1.25×10^{-3} S cm^{-1} in CPM-s3), suggesting the potential of these materials as solid-state electrolytes. The simplicity yet effectiveness of such method makes it possible to create a diversity of anionic framework materials with various compositions and topologies for tailored applications.

6.5 Reference

1. Yang, F.; Xu, G.; Dou, Y.; Wang, B.; Zhang, H.; Wu, H.; Zhou, W.; Li, J.-R.; Chen, B., A Flexible Metal–Organic Framework with a High Density of Sulfonic Acid Sites for Proton Conduction. *Nature Energy* **2017,** *2*, 877-883.

2. Taylor, J. M.; Komatsu, T.; Dekura, S.; Otsubo, K.; Takata, M.; Kitagawa, H., The Role of a Three Dimensionally Ordered Defect Sublattice on the Acidity of a Sulfonated Metal–Organic Framework. *J. Am. Chem. Soc.* **2015,** *137*, 11498-11506.

3. Joarder, B.; Lin, J.-B.; Romero, Z.; Shimizu, G. K. H., Single Crystal Proton Conduction Study of a Metal Organic Framework of Modest Water Stability. *J. Am. Chem. Soc.* **2017,** *139*, 7176-7179.

4. Hurd, J. A.; Vaidhyanathan, R.; Thangadurai, V.; Ratcliffe, C. I.; Moudrakovski, I. L.; Shimizu, G. K. H., Anhydrous Proton Conduction at 150 °C in a Crystalline Metal–Organic Framework. *Nat. Chem.* **2009,** *1*, 705.

5. Dong, X.-Y.; Wang, R.; Li, J.-B.; Zang, S.-Q.; Hou, H.-W.; Mak, T. C. W., A Tetranuclear Cu4([Small Mu]3-Oh)2-Based Metal-Organic Framework (Mof) with Sulfonate-Carboxylate Ligands for Proton Conduction. *Chem. Commun.* **2013,** *49*, 10590-10592.

6. Dong, X.-Y.; Wang, R.; Wang, J.-Z.; Zang, S.-Q.; Mak, T. C. W., Highly Selective Fe3+ Sensing and Proton Conduction in a Water-Stable Sulfonate-Carboxylate Tb-Organic-Framework. *J. Mater. Chem. A* **2015,** *3*, 641-647.

7. Wang, G.-B.; Leus, K.; Hendrickx, K.; Wieme, J.; Depauw, H.; Liu, Y.-Y.; Van Speybroeck, V.; Van Der Voort, P., A Series of Sulfonic Acid Functionalized Mixed-Linker Dut-4 Analogues: Synthesis, Gas Sorption Properties and Catalytic Performance. *Dalton Trans.* **2017,** *46*, 14356-14364.

8. Chang, G.; Huang, M.; Su, Y.; Xing, H.; Su, B.; Zhang, Z.; Yang, Q.; Yang, Y.; Ren, Q.; Bao, Z.; Chen, B., Immobilization of Ag(I) into a Metal-Organic Framework with -So3h Sites for Highly Selective Olefin-Paraffin Separation at Room Temperature. *Chem. Commun.* **2015,** *51*, 2859-2862.

9. Hong, A. N.; Kusumoputro, E.; Wang, Y.; Yang, H.; Chen, Y.; Bu, X.; Feng, P., Simultaneous Control of Pore-Space Partition and Charge Distribution in Multi-Modular Metal–Organic Frameworks. *Angew. Chem. Int. Ed.* **2022,** *61*, e202116064.

10. Fu, X.-P.; Wang, Y.-L.; Zhang, X.-F.; Krishna, R.; He, C.-T.; Liu, Q.-Y.; Chen, B., Collaborative Pore Partition and Pore Surface Fluorination within a Metal–Organic Framework for High-Performance C2h2/Co2 Separation. *Chem. Eng. J.* **2022,** *432*, 134433.

11. Yang, H.; Wang, Y.; Krishna, R.; Jia, X.; Wang, Y.; Hong, A. N.; Dang, C.; Castillo, H. E.; Bu, X.; Feng, P., Pore-Space-Partition-Enabled Exceptional Ethane Uptake and Ethane-Selective Ethane–Ethylene Separation. *J. Am. Chem. Soc.* **2020,** *142*, 2222-2227.

12. Zhai, Q.-G.; Bu, X.; Mao, C.; Zhao, X.; Daemen, L.; Cheng, Y.; Ramirez-Cuesta, A. J.; Feng, P., An Ultra-Tunable Platform for Molecular Engineering of High-Performance Crystalline Porous Materials. *Nat. Commun* **2016,** *7*, 13645.

13. Zhao, X.; Bu, X.; Nguyen, E. T.; Zhai, Q.-G.; Mao, C.; Feng, P., Multivariable Modular Design of Pore Space Partition. *J. Am. Chem. Soc.* **2016,** *138*, 15102-15105.

14. Zhao, X.; Bu, X.; Zhai, Q.-G.; Tran, H.; Feng, P., Pore Space Partition by Symmetry-Matching Regulated Ligand Insertion and Dramatic Tuning on Carbon Dioxide Uptake. *J. Am. Chem. Soc.* **2015,** *137*, 1396-1399.

15. Liu, Q.-Y.; Wang, W.-F.; Wang, Y.-L.; Shan, Z.-M.; Wang, M.-S.; Tang, J., Diversity of Lanthanide(Iii)–Organic Extended Frameworks with a 4,8-Disulfonyl-2,6-Naphthalenedicarboxylic Acid Ligand: Syntheses, Structures, and Magnetic and Luminescent Properties. *Inorg. Chem.* **2012,** *51*, 2381-2392.

16. Eddaoudi, M.; Li, H.; Reineke, T.; Fehr, M.; Kelley, D.; Groy, T. L.; Yaghi, O. M., Design and Synthesis of Metal-Carboxylate Frameworks with Permanent Microporosity. *Top. Catal.* **1999,** *9*, 105-111.

17. Eddaoudi, M.; Moler, D. B.; Li, H.; Chen, B.; Reineke, T. M.; O'Keeffe, M.; Yaghi, O. M., Modular Chemistry: Secondary Building Units as a Basis for the Design of Highly Porous and Robust Metal−Organic Carboxylate Frameworks. *Acc. Chem. Res.* **2001,** *34*, 319-330.

18. Guillerm, V.; Kim, D.; Eubank, J. F.; Luebke, R.; Liu, X.; Adil, K.; Lah, M. S.; Eddaoudi, M., A Supermolecular Building Approach for the Design and Construction of Metal–Organic Frameworks. *Chem. Soc. Rev.* **2014,** *43*, 6141-6172.

19. Zhao, D.; Timmons, D. J.; Yuan, D.; Zhou, H.-C., Tuning the Topology and Functionality of Metal−Organic Frameworks by Ligand Design. *Acc. Chem. Res.* **2011,** *44*, 123-133.

20. Yaghi, O. M.; O'Keeffe, M.; Ockwig, N. W.; Chae, H. K.; Eddaoudi, M.; Kim, J., Reticular Synthesis and the Design of New Materials. *Nature* **2003,** *423*, 705-714.

21. Makal, T. A.; Yakovenko, A. A.; Zhou, H.-C., Isomerism in Metal–Organic Frameworks: "Framework Isomers". *J. Phys. Chem. Lett.* **2011,** *2*, 1682-1689.

22. Jiang, H.-L.; Makal, T. A.; Zhou, H.-C., Interpenetration Control in Metal–Organic Frameworks for Functional Applications. *Coord. Chem. Rev.* **2013,** *257*, 2232-2249.

23. Kalmutzki, M. J.; Hanikel, N.; Yaghi, O. M., Secondary Building Units as the Turning Point in the Development of the Reticular Chemistry of Mofs. *Sci. Adv.* **2018,** *4*, eaat9180.

24. Bigdeli, F.; Lollar, C. T.; Morsali, A.; Zhou, H.-C., Switching in Metal–Organic Frameworks. *Angew. Chem. Int. Ed.* **2020,** *59*, 4652-4669.

25. Cohen, S. M., Postsynthetic Methods for the Functionalization of Metal–Organic Frameworks. *Chem. Rev.* **2012,** *112*, 970-1000.

26. Sun, Y.; Zhou, H.-C., Recent Progress in the Synthesis of Metal–Organic Frameworks. *Sci. Technol. Adv. Mater.* **2015,** *16*, 054202.

27. Karagiaridi, O.; Bury, W.; Mondloch, J. E.; Hupp, J. T.; Farha, O. K., Solvent-Assisted Linker Exchange: An Alternative to the De Novo Synthesis of Unattainable Metal–Organic Frameworks. *Angew. Chem. Int. Ed.* **2014,** *53*, 4530-4540.

28. Zhang, Y.; Yang, X.; Zhou, H.-C., Synthesis of Mofs for Heterogeneous Catalysis Via Linker Design. *Polyhedron* **2018,** *154*, 189-201.

29. Huang, Y.; Lin, Z.; Fu, H.; Wang, F.; Shen, M.; Wang, X.; Cao, R., Porous Anionic Indium–Organic Framework with Enhanced Gas and Vapor Adsorption and Separation Ability. *ChemSusChem* **2014,** *7*, 2647-2653.

30. Chen, S.; Zhang, J.; Wu, T.; Feng, P.; Bu, X., Multiroute Synthesis of Porous Anionic Frameworks and Size-Tunable Extraframework Organic Cation-Controlled Gas Sorption Properties. *J. Am. Chem. Soc.* **2009,** *131*, 16027-16029.

31. Yang, S.; Lin, X.; Blake, A. J.; Walker, G. S.; Hubberstey, P.; Champness, N. R.; Schröder, M., Cation-Induced Kinetic Trapping and Enhanced Hydrogen Adsorption in a Modulated Anionic Metal–Organic Framework. *Nat. Chem.* **2009,** *1*, 487-493.

32. Lin, Z.-Z.; Jiang, F.-L.; Chen, L.; Yue, C.-Y.; Yuan, D.-Q.; Lan, A.-J.; Hong, M.-C., A Highly Symmetric Porous Framework with Multi-Intersecting Open Channels. *Cryst. Growth Des.* **2007,** *7*, 1712-1715.

33. Qin, J.-H.; Huang, Y.-D.; Shi, M.-Y.; Wang, H.-R.; Han, M.-L.; Yang, X.-G.; Li, F.-F.; Ma, L.-F., Aqueous-Phase Detection of Antibiotics and Nitroaromatic Explosives by an Alkali-Resistant Zn-Mof Directed by an Ionic Liquid. *RSC Adv.* **2020,** *10*, 1439-1446.

34. Lin, Z.; Slawin, A. M. Z.; Morris, R. E., Chiral Induction in the Ionothermal Synthesis of a 3-D Coordination Polymer. *J. Am. Chem. Soc.* **2007,** *129*, 4880-4881.

35. Zhang, J.; Chen, S.; Bu, X., Multiple Functions of Ionic Liquids in the Synthesis of Three-Dimensional Low-Connectivity Homochiral and Achiral Frameworks. *Angew. Chem. Int. Ed.* **2008,** *47*, 5434-5437.

36. Lin, Z.; Wragg, D. S.; Warren, J. E.; Morris, R. E., Anion Control in the Ionothermal Synthesis of Coordination Polymers. *J. Am. Chem. Soc.* **2007,** *129*, 10334-10335.

37. Zhao, M.-Y.; Zhu, J.-N.; Li, P.; Li, W.; Cai, T.; Cheng, F.-F.; Xiong, W.-W., Structural Variation of Transition Metal–Organic Frameworks Using Deep Eutectic Solvents with Different Hydrogen Bond Donors. *Dalton Trans.* **2019,** *48*, 10199-10209.

38. Zhan, C.-H.; Wang, F.; Kang, Y.; Zhang, J., Lanthanide-Thiophene-2,5-Dicarboxylate Frameworks: Ionothermal Synthesis, Helical Structures, Photoluminescent Properties, and Single-Crystal-to-Single-Crystal Guest Exchange. *Inorg. Chem.* **2012,** *51*, 523-530.

39. Zhang, J.; Wu, T.; Chen, S.; Feng, P.; Bu, X., Versatile Structure-Directing Roles of Deep-Eutectic Solvents and Their Implication in the Generation of Porosity and Open Metal Sites for Gas Storage. *Angew. Chem. Int. Ed.* **2009,** *48*, 3486-3490.

40. Chen, Z.; Zhou, Y.; Weng, L.; Zhang, H.; Zhao, D., Hydrothermal Synthesis of Two Layered Indium Oxalates with 12-Membered Apertures. *J. Solid State Chem.* **2003,** *173*, 435-441.

41. Chen, C.; Luan, L.; Yang, M.; Zeng, H.; Lin, Z., Solvent-Free Synthesis of New Open-Framework Metal Oxalates with Different 4-Connected Topologies. *Inorg. Chem. Commun.* **2016,** *70*, 79-82.

42. Cao, J.-J.; Li, G.-D.; Chen, J.-S., New Indium Selenite-Oxalate and Indium Oxalate with Two- and Three-Dimensional Structures. *J. Solid State Chem.* **2009,** *182*, 102-106.

43. Guo, F.; Chen, C.; Wang, K.; Zhang, Q.; Lin, Z., Supramolecular Templating Approach for the Solvent-Free Synthesis of Open-Framework Metal Oxalates. *Inorg. Chem.* **2016,** *55*, 7817-7819.

44. Yi, F.-Y.; Yang, H.; Zhao, X.; Feng, P.; Bu, X., Zeolite-Type Metal Oxalate Frameworks. *Angew. Chem. Int. Ed.* **2019,** *58*, 2889-2892.

45. Zhu, W.-G.; Zheng, Y.-Q.; Zhu, H.-L.; Wang, J.-J., Structural Diversity Controlled by Alkali/Alkaline Earth Metals for Heterometallic Aei/Aeii-Znii Coordination Polymers Based on 4-Nitrobenzene-1,2-Dicarboxylate. *J. Coord. Chem.* **2016,** *69*, 3115-3129.

46. Lü, J.; Li, F.; Yuan, D.-Q.; Cao, R., Assembly of Two Novel Three-Dimensional Networks Driven by Alkali Metals with an Irreversible Structural Conversion. *Polyhedron* **2007,** *26*, 2979-2986.

47. Zou, R.; Abdel-Fattah, A. I.; Xu, H.; Burrell, A. K.; Larson, T. E.; McCleskey, T. M.; Wei, Q.; Janicke, M. T.; Hickmott, D. D.; Timofeeva, T. V.; Zhao, Y., Porous Metal−Organic Frameworks Containing Alkali-Bridged Two-Fold Interpenetration: Synthesis, Gas Adsorption, and Fluorescence Properties. *Cryst. Growth Des.* **2010,** *10*, 1301-1306.

48. Van Tendeloo, L.; Gobechiya, E.; Breynaert, E.; Martens, J. A.; Kirschhock, C. E. A., Alkaline Cations Directing the Transformation of Fau Zeolites into Five Different Framework Types. *Chem. Commun.* **2013,** *49*, 11737-11739.

49. Wang, G.; Marler, B.; Gies, H.; Fyfe, C. A.; Sidhu, P.; Yilmaz, B.; Müller, U., Synthesis, Characterization and Structure Analysis of Uzm-22, a Mei-Type Zeolite Framework Structure. *Microporous Mesoporous Mater.* **2010,** *132*, 43-53.

50. Jaime G. Moscoso, D.-Y. J. Uzm-35 Aluminosilicate Zeolite, Method of Preparation and Processes Using Uzm-35. US Patent 7,922,997
2011.

51. Shin, J.; Jo, D.; Hong, S. B., Rediscovery of the Importance of Inorganic Synthesis Parameters in the Search for New Zeolites. *Acc. Chem. Res.* **2019,** *52*, 1419-1427.

52. Gamage, N.-D. H.; McDonald, K. A.; Matzger, A. J., Mof-5-Polystyrene: Direct Production from Monomer, Improved Hydrolytic Stability, and Unique Guest Adsorption. *Angew. Chem. Int. Ed.* **2016,** *55*, 12099-12103.

53. Brozek, C. K.; Miller, J. T.; Stoian, S. A.; Dincă, M., No Disproportionation at a Mononuclear Site-Isolated Fe2+ Center in Fe2+-Mof-5. *J. Am. Chem. Soc.* **2015,** *137*, 7495-7501.

54. Brozek, C. K.; Dincă, M., Ti3+-, V2+/3+-, Cr2+/3+-, Mn2+-, and Fe2+-Substituted Mof-5 and Redox Reactivity in Cr- and Fe-Mof-5. *J. Am. Chem. Soc.* **2013,** *135*, 12886-12891.

55. Han, S.; Wei, Y.; Valente, C.; Lagzi, I.; Gassensmith, J. J.; Coskun, A.; Stoddart, J. F.; Grzybowski, B. A., Chromatography in a Single Metal−Organic Framework (Mof) Crystal. *J. Am. Chem. Soc.* **2010,** *132*, 16358-16361.

56. Kaye, S. S.; Dailly, A.; Yaghi, O. M.; Long, J. R., Impact of Preparation and Handling on the Hydrogen Storage Properties of Zn4o(1,4-Benzenedicarboxylate)3 (Mof-5). *J. Am. Chem. Soc.* **2007,** *129*, 14176-14177.

57. Cartledge, G. H., Studies on the Periodic System. I. The Ionic Potential as a Periodic Function1. *J. Am. Chem. Soc.* **1928,** *50*, [2855]-2863.

58. Cartledge, G. H., Studies on the Periodic System. Ii. The Ionic Potential and Related Properties1. *J. Am. Chem. Soc.* **1928,** *50*, 2863-2872.

59. Zhai, Q.-G.; Bai, N.; Li, S. n.; Bu, X.; Feng, P., Design of Pore Size and Functionality in Pillar-Layered Zn-Triazolate-Dicarboxylate Frameworks and Their High Co2/Ch4 and C2 Hydrocarbons/Ch4 Selectivity. *Inorg. Chem.* **2015,** *54*, 9862-9868.

60. Zou, L.; Yao, S.; Zhao, J.; Li, D.-S.; Li, G.; Huo, Q.; Liu, Y., Enhancing Proton Conductivity in a 3d Metal–Organic Framework by the Cooperation of Guest [Me2nh2]+ Cations, Water Molecules, and Host Carboxylates. *Cryst. Growth Des.* **2017,** *17*, 3556-3561.

61. Shalini, S.; Dhavale, V. M.; Eldho, K. M.; Kurungot, S.; Ajithkumar, T. G.; Vaidhyanathan, R., 1000-Fold Enhancement in Proton Conductivity of a Mof Using Post-Synthetically Anchored Proton Transporters. *Sci. Rep.* **2016,** *6*, 32489.

62. Sikdar, N.; Dutta, D.; Haldar, R.; Ray, T.; Hazra, A.; Bhattacharyya, A. J.; Maji, T. K., Coordination-Driven Fluorescent J-Aggregates in a Perylenetetracarboxylate-Based Mof: Permanent Porosity and Proton Conductivity. *J. Phys. Chem. C* **2016,** *120*, 13622-13629.

63. Sadakiyo, M.; Yamada, T.; Kitagawa, H., Proton Conductivity Control by Ion Substitution in a Highly Proton-Conductive Metal–Organic Framework. *J. Am. Chem. Soc.* **2014,** *136*, 13166-13169.

64. Sadakiyo, M.; Yamada, T.; Kitagawa, H., A Study on Proton Conduction in a Layered Metal–Organic Framework, Rb2(Adp)[Zn2(Ox)3]·3h2o (Adp=Adipic Acid, Ox2−=Oxalate). *Inorg. Chem. Commun.* **2016,** *72*, 138-140.

65. Zima, V.; Patil, D. S.; Raja, D. S.; Chang, T.-G.; Lin, C.-H.; Shimakawa, K.; Wagner, T., New Mof Based on Lithium Tetrahydrofuran-2,3,4,5-Tetracarboxylate: Its Structure and Conductivity Behavior. *J. Solid State Chem.* **2014,** *217*, 150-158.

66. Liu, R.; Liu, Y.; Yu, S.; Yang, C.; Li, Z.; Li, G., A Highly Proton-Conductive 3d Ionic Cadmium–Organic Framework for Ammonia and Amines Impedance Sensing. *ACS Appl. Mater. Interfaces* **2019,** *11*, 1713-1722.

67. Zhou, L.-J.; Deng, W.-H.; Wang, Y.-L.; Xu, G.; Yin, S.-G.; Liu, Q.-Y., Lanthanide–Potassium Biphenyl-3,3′-Disulfonyl-4,4′-Dicarboxylate Frameworks: Gas Sorption, Proton Conductivity, and Luminescent Sensing of Metal Ions. *Inorg. Chem.* **2016,** *55*, 6271-6277.

68. Wang, X.; Wang, Y.; Silver, M. A.; Gui, D.; Bai, Z.; Wang, Y.; Liu, W.; Chen, L.; Diwu, J.; Chai, Z.; Wang, S., Superprotonic Conduction through One-Dimensional Ordered Alkali Metal Ion Chains in a Lanthanide-Organic Framework. *Chem. Commun.* **2018,** *54*, 4429-4432.

Chapter 7: Rod-packing Metal-Organic Frameworks for Magnetic Studies

7.1 Introduction

Of great interest to researchers in the field of metal-organic framework (MOF) is the capability to design and construct novel intriguing structures of varied dimensions, pore metrics, and functionalities.[1-3] At the core, MOF design relies heavily upon its secondary building unit (SBU), a module embedded with inherent properties that allow assembled materials to exhibit exceptional performances.[4-5]

Among different secondary building units (SBU) employed in 3D-MOF design, the infinite rod-shaped SBU is of particular interest.[6-10] Compared to 3D MOFs with discrete SBUs, 3D rod-packing MOFs (RPMOF) easily overcome the possibility of interpenetration, a phenomenon that drastically reduces porosity.[11] Rod-shaped SBU exhibits much higher open-metal-site density (e.g., MOF-74-Ni, with inorganic helical chains, has one of the highest metal density at ca. 7.74 mmol cm^{-3}).[12] Without long organic linker connecting different metal nodes, efficiency of transporting electronic information is boosted dramatically.[13] These outstanding features have allowed many 3D RPMOFs to have great potential in a variety of applications.[14-22]

Compared to 3D RPMOFs, the self-assembly of 2D RPMOFs are less known.[23-31] Construction of 2D RPMOF requires a synthetic environment that simultaneously promotes the growth of inorganic unit along one dimension, and caps organic linker along one of the two remaining dimensions, which poses a significant challenge. But given the importance inorganic rod-packing chains, it is of high interest to synthesize and explore properties unique to 2D RPMOF materials.

Herein, we report a metal-mediated design strategy to control dimensions of RPMOFs. Synthetic exploration of manganese salt and a polyfunctional linker, 4,8-disulfo-napthalene-dicarboxylic acid (H_4dsndc) resulted in the assembly of a 3D RPMOF, $[Mn_3(dsndc)(HCOO)_2(H_2O)_3(EtOH)]\bullet H_2O$ (CPM-s7). From structural analysis of CPM-s7, we predicted the possibility of introducing a capping agent to inhibit growth of organic linkers in two directions (Figure 7.1). We took advantage of sulfonic acid hydrolysis, which is generally accelerated at elevated temperature and/or acidity, to *in-situ* generate sulfate capping agent. The presence of sulfate reduces the organic-extension of CPM-s7 by two directions, resulting in a novel 2D RPMOF, $[Co_5(OH)_2(SO_4)_2(HCOO)_2(dsndc)(DMF)_2(H_2O)_2]$ $(NH_2(CH_3)_2)_2(H_2O)_4$ (CPM-s8). More interestingly, the presence of metal-oxide chain allows for long-range magnetic ordering at specified temperature, as predicted by density functional theory calculations and confirmed by magnetization measurements.

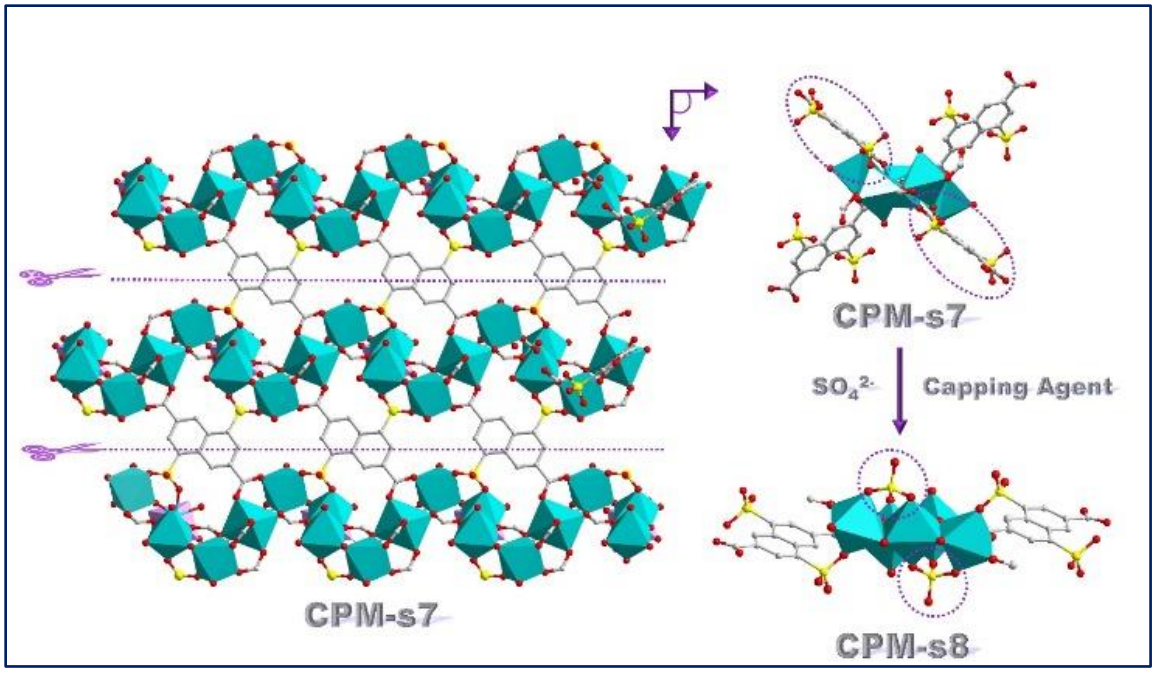

Figure 7.1 Transformation of 3D CPM-s7 to 2D CPM-s8 through in-situ formation of SO_4^{2-} capping agent.

7.2 Experimental Section

7.2.1 Material Synthesis.

All starting materials and solvents were commercially available and used without further purification.

Synthesis of 4,8-disulfo-napthalene-2,6-dicarboxylic acid (H_4dsndc). H_4dsndc was synthesized according to reported literature with slight modification.[32] Naphthalene-2,6-dicarboxylic acid (7 g) was added to 25 mL of oleum (SO_3, 30 w.t. %) in a 100 mL round-bottom flask equipped with reflux condenser. The reaction mixture was stirred vigorously at 150 °C for 6 hours. Solution mixture was dissolved in distilled water, followed by precipitation in HCl (36 w.t.%). Isolated product was washed with ice-water to removed trapped HCl and dried in vacuum over at 120 °C overnight. Yield (85%), ^{1}HNMR (600 MHz, DMSO-d_6 δ, ppm): 8.5 (d), 9.6 (d).

Synthesis of CPM-s7. In a 23 mL glass vial, $MnCl_2 \cdot 4H_2O$ (70 mg, ~0.3 mmol), H_4dsndc (40 mg, 0.1 mmol) were dissolved in 4.0 g N,N-dimethylformamide (DMF), 4.5 g ethanol (EtOH) and 4.0 g deionized water (DI H_2O). After stirring for 1 hours, the vial was placed in a 120 °C oven for 7 days. Clear spindle-shaped crystals are obtained after solution was cooled to ambient temperature. Yield 50% based on H_4dsndc.

Synthesis of CPM-s8. In a 23 mL glass vial, $CoCl_2 \cdot 6H_2O$ (76 mg, 0.3 mmol), H_4dsndc (40 mg, 0.1 mmol) were dissolved in 4.0 g DMF, 4.5 EtOH and 4.0 g DI H_2O. After stirring for 1 hours, the vial was placed in a 120 °C oven for 7 days. Pink spindle-shaped crystals

are obtained after solution was cooled to ambient temperature. Yield 30% based on H_4dsndc.

7.2.2 Property Characterization.

Magnetization Measurement. The magnetization measurements were performed on a physical properties measurement system (PPMS) equipped with a superconducting quantum interference device (SQUID). The zero field and field cooled measurements were performed under magnetic fields of 100 and 1000 Oe. Hysteresis loops were measured between −40000 Oe and 40000 Oe at 5 K. The data were corrected for the sample holder (Teflon tubes). The molar mass used for data analysis was that of the solvent-filled CMP-s8.

DFT Calculation. DFT+U calculations were performed using projector augmented wave pseudo potentials to model core electrons with the Perdew-Burke-Ernzerhof exchange correlation functional.[33] Brillouin zone integration was performed using a 3x3x3 k-point mesh. Starting from structures obtained from XRD, structures were relaxed to minimize energy with a tolerance of 10^{-6} eV. The calculations were performed using a U energy of 3.2eV, but the same qualitative magnetic ordering was found to persist in calculations using U values between 0 and 5 eV.

Other Characterization. SCXRD, PXRD, and TGA were obtained as mentioned in 2.2.4.

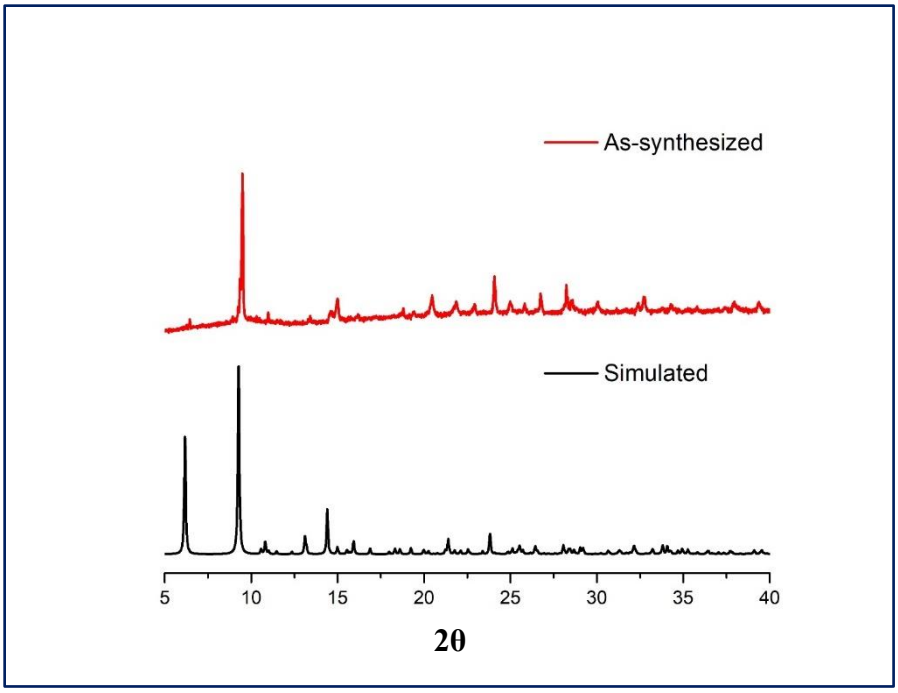

Figure 7.2 Experimental and simulated PXRD patterns of CPM-s8.

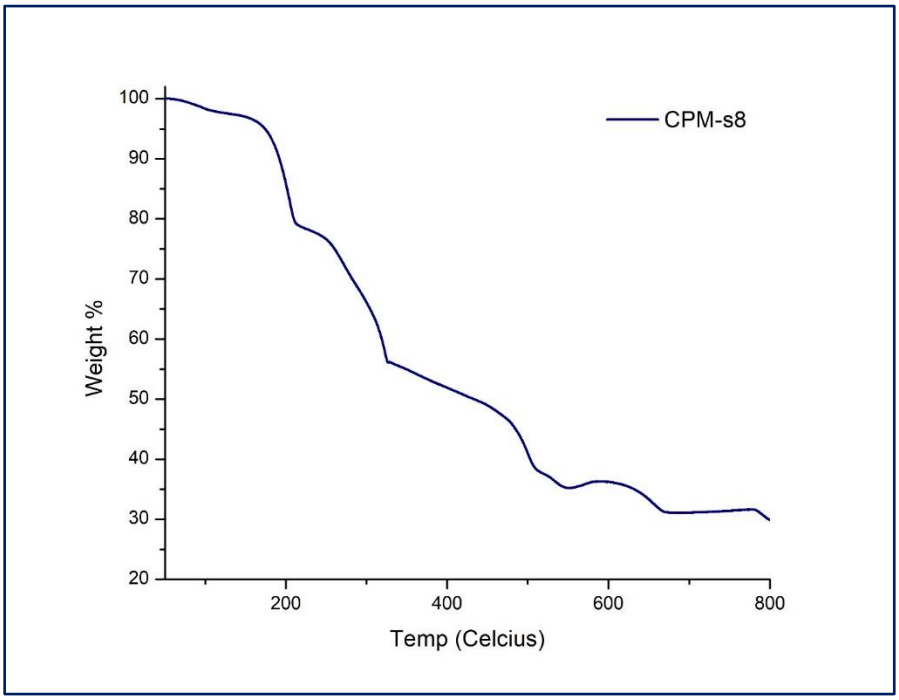

Figure 7.3 TGA graph of CPM-s8.

7.3 Results and Discussion

CPM-s7 crystallizes in P-1 space group, with asymmetric unit consisting of four unique Mn^{2+}, one $dsndc^{4-}$, two $HCOO^-$, one EtOH, and five H_2O molecules, where Mn(1) and Mn(4) reside in symmetry sites, and formate ions originate from hydrolysis of DMF. As shown in Figure 7.4b, Mn(1) and Mn(2) are bridged by six carboxylates into linear trimers. The two carboxylate ends of $dsndc^{4-}$ link these trimers into 2D square layers stacked in ABAB conformation. These layers are further linked into 3D RPMOF framework by connecting two pendant formates of neighboring metal trimer with Mn(3) and sulfonate group of $dsndc^{4-}$ along b-axis to apex of trimer (Figure 7.5). Along ac-plane, pendant formate groups from trimer and sulfonate groups from $dsndc^{4-}$ (parallel to c-axis) further trap Mn(4) ions, and thus removing pore opening along this direction. The 3D RPMOF has 1D rectangular channel with width ~5.7 Å (measured from oxygens of sulfonate groups).CPM-s7 could also be viewed as wavy manganese chains linked by $Mn(HCOO^-)_2$ and $dsndc^{4-}$ into 2D layers (along ac plane). These layers are further pillared by remaining $dsndc^{4-}$ groups into 3D framework. Thus, an introduction of capping agents could block the growth of $dsndc^{4-}$ pillars, leading to construction of 2D RPMOF. Since both amide and sulfonate groups are prone to hydrolysis in elevated temperature, we hypothesized that the synthetic environment of CPM-s7, which favored hydrolysis of DMF and addition of formate into final framework, could also be tuned to favor hydrolysis of sulfonate group and addition of sulfate capping agent into final framework.

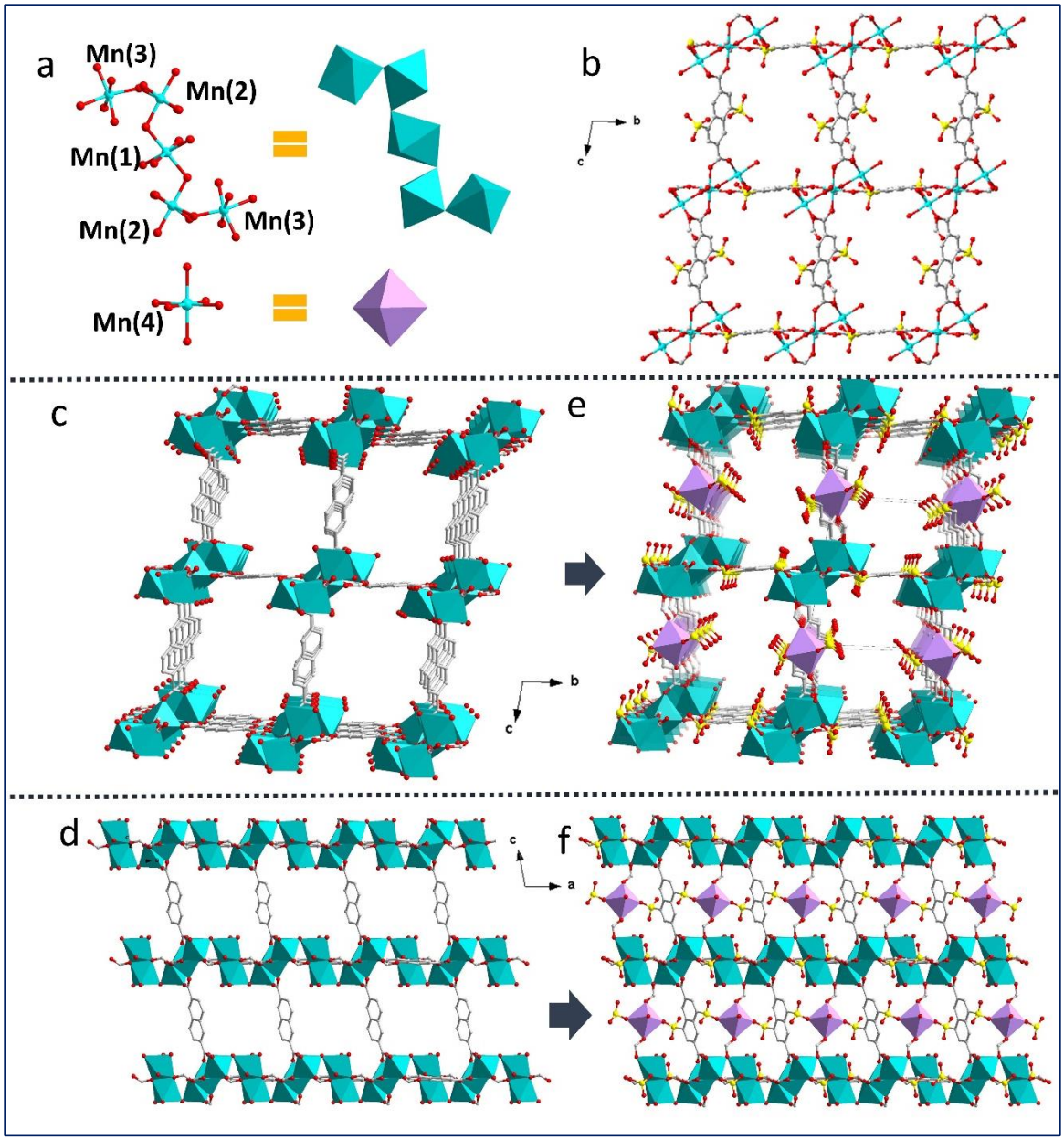

Figure 7.4 Graphic representations of CPM-s7. a) octahedrally coordinated Mn^{2+} chain and monomeric Mn^{2+} building unit, b) Expansion of Mn(1) and Mn(2) into 2D square layer, c-f) layers connected by Mn(3) and Mn(4) and sulfonate groups into 3D framework with 1D channel. In c-d) pendant groups and Mn(4) are removed for clarity. All non-bonding water molecules are also removed from drawings.

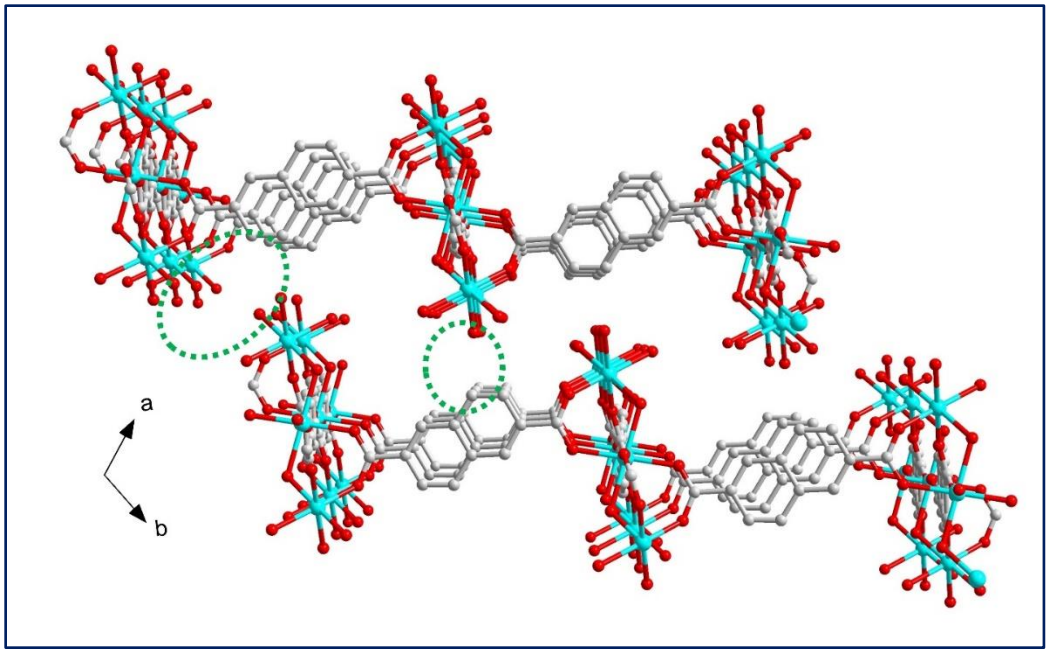

Figure 7.5 View of 2D sheets of CPM-s7 along ab-plane. Green circles represent positions which $Mn(HCOO)_2$ connects two adjacent trimers and sulfonate connects nearby trimer.

Hydrolysis reactions are well known to be accelerated under acidic conditions. With each transition metal-salt offering different Lewis acid strengths, introduction of a different metal could shift equilibrium condition slightly towards formation of sulfate capping agent. To validate our hypothesis, we substituted $MnCl_2 \cdot 4H_2O$ with stronger Lewis acid transition metal salts.

The hydrolysis DMF and H_4dsndc to produce formate and sulfate, combined with evaporation of EtOH and H_2O, resulted in the self-assembly of Co^{2+} and linkers into a novel 2D PRMOF. Similar to CPM-s7, single crystal X-ray diffraction of CPM-s8 also shows crystallization of material in P-1 space group. The composition of CPM-s8, however, differs dramatically from CPM-s7. Asymmetric unit of CPM-s8 contains three

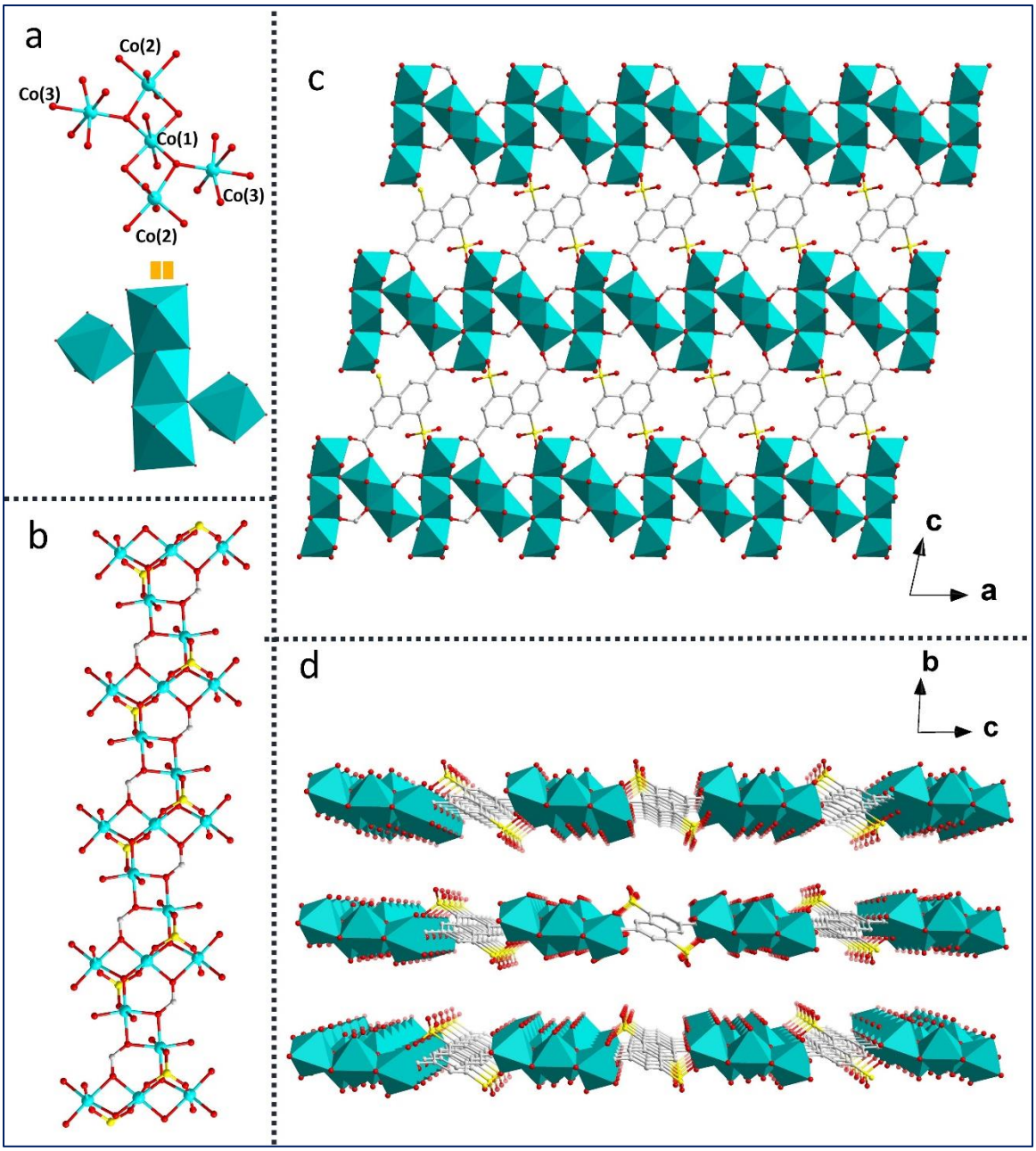

Figure 7.6 Graphic representations of CPM-s8. (a) octahedrally coordinated cobalt pentamer, with Co(1) residing on symmetry equivalent site, (b) 1D cobalt chain with bridging hydroxide, sulfate, and formate linkers, (c) 2D sheet in ac-plane, (d) View of parallelly stacked 2D layers in bc-plane.

unique Co atoms (one of which resides on a symmetry site), half dsndc^{4-}, one OH^-, two $HCOO^-$, one SO_4^{2-}, one $(H_2N(CH_3)_2)^+$, one DMF and three H_2O molecules. All Co^{2+} atoms in this MOF are octahedrally coordinated with slight distortions. The Co—O distance ranges from 2.063(9) to 2.240(8) Å (Figure 7.7). Each pair of (μ_3-OH) bridge two sets of three Co atoms into a cross-shaped pentamer (Figure 7.6). The adjacent Co---Co distance within the pentamer ranges from 3.241(7) to 3.516(6) Å. For each (μ_3-OH) bridged metal trimer, SO_4^{2-} further caps from above or below M_3(μ_3-OH) plane. These pentamers are linked into 1D zigzag chains with $HCOO^-$ ions. These zigzag chains are further linked by both sulfonate and carboxylate functional groups of dsndc^{4-} into 2D layers. The neighbouring layers are parallel to each other, with the shortest interlayer distance of 4.1 Å (O---O distances between two capping sulfates).

The *in-situ* formation of sulfate capping agent resulted in more symmetrical metal oxide chains. In CPM-s7, the manganese oxide chain exhibits 2 corner-sharing MnO_6 octahedra (Mn(1)-O-Mn(2), Mn(2)-O-Mn(3)), and one edge-sharing MnO_6 (Mn(3)-O-Mn(3)). In comparison, cobalt oxide chain of CPM-s7 shows only one corner sharing CoO_6 (Co(1)-O-(Co(3)), and two edge sharing CoO_6 (Co(1)-O-Co(2), and Co(2)-O-Co(2)). The increase of edge-sharing octahedra in CPM-s8 leads to flattening of the metal chain, and could thus allow for better orbital overlap, which is highly beneficial in fabricating magnetic materials. The phase purity of CPM-s8 was determined through powder X-ray diffraction (Figure 7.2). As-synthesized material matches well with simulated patterns from single-crystal data, suggesting high purity of bulk material. Thermal stability of CPM-s8 was further analysed through thermogravimetric analysis (TGA) measurement

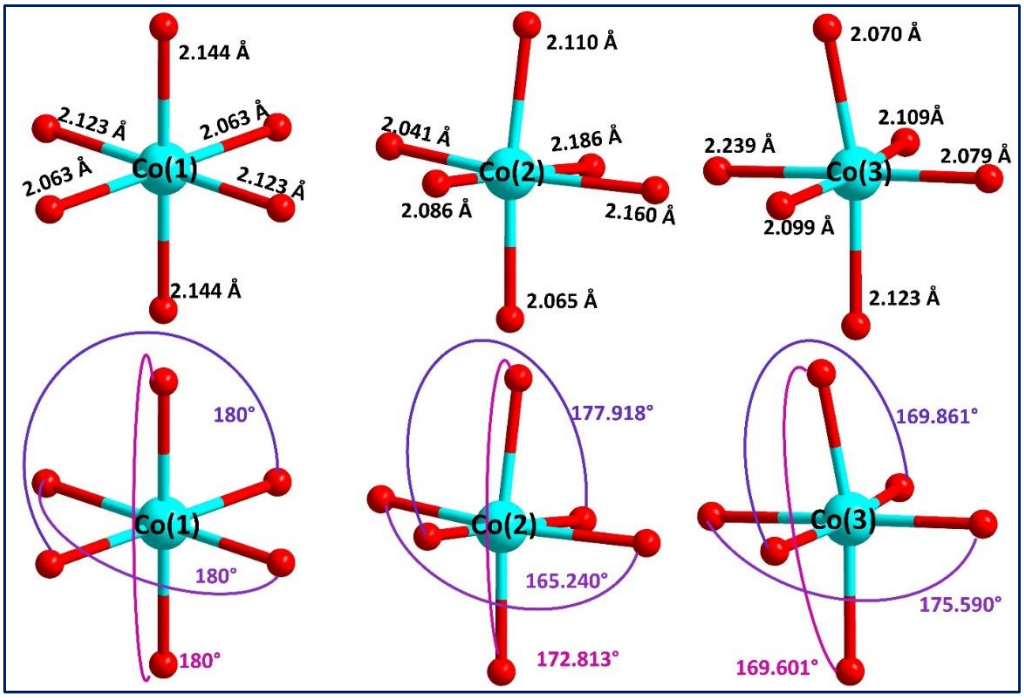

Figure 7.7 Coordination sphere of each unique cobalt in CPM-s8.

under N_2 atmosphere (Figure 7.3). Initial 21% weight loss before 200 °C correspond to solvent molecules in the pore. The second weight loss at 250 °C represent decomposition of organic linker and collapse of framework.

Of particular interest is the potential ordered-alignment of unpaired electrons in zigzag cobalt-oxide chains of CPM-s8. More interestingly, the number of unique crystallographic positions of cobalt is an odd number, thus preventing complete cancelling of antiparallel spins, such as in the case of antiferromagnetic materials. To better understand magnetic property of CPM-s8, we recorded temperature-dependent magnetization data under zero-field-cooling (ZFC) and field-cooling (FC) processes at magnetic field of 100 and 1000 Oe, between 2 and 350 K (Figures 7.8).

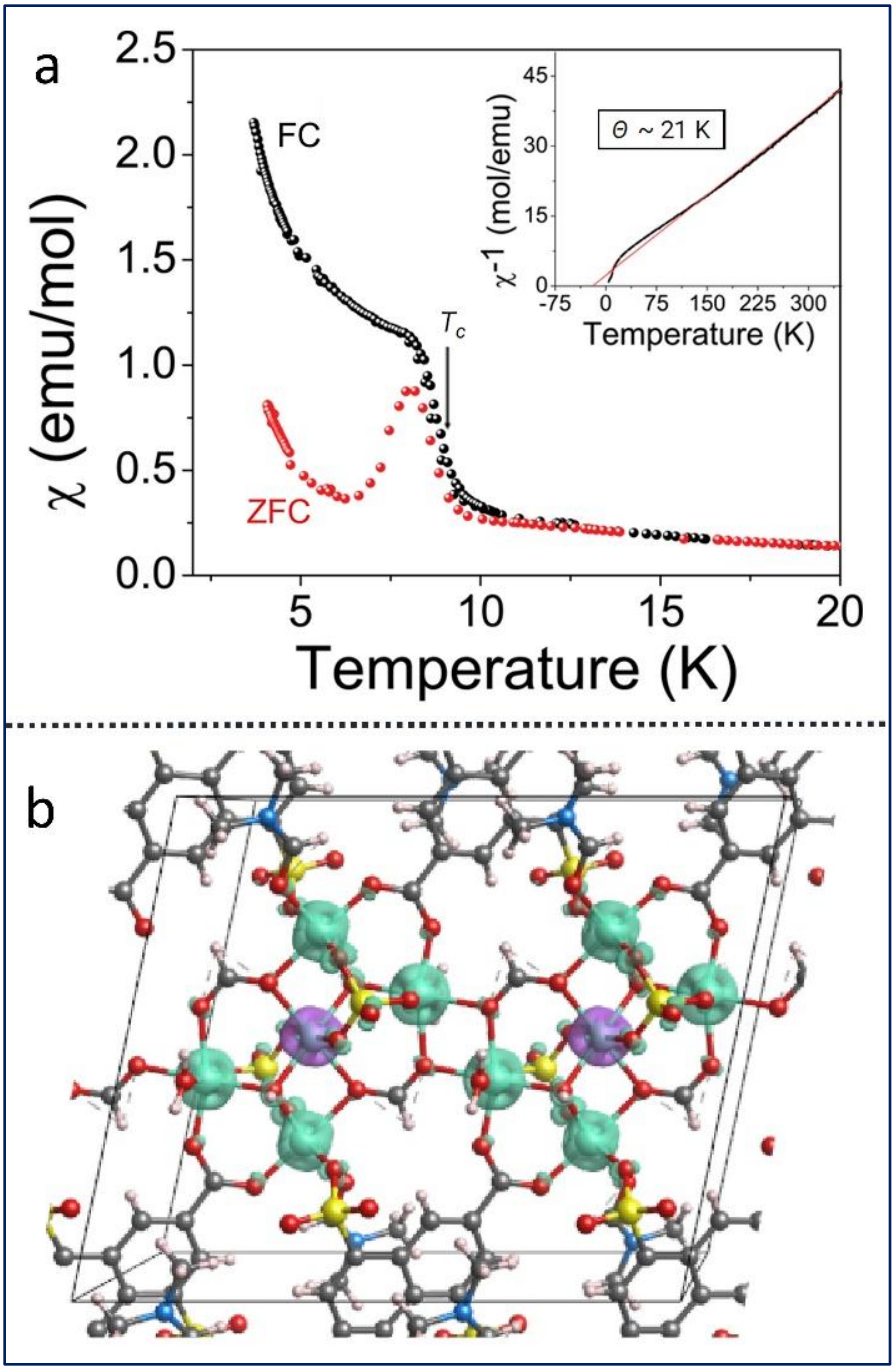

Figure 7.8 (a) Temperature dependent ZFC and FC molar susceptibility curve of CPM-s8 recorded at 100 Oe. Inset shows the FC invese molar susceptibility curve (at 1000 Oe) and the Curie-weisss straight line (red). (b) DFT predicted ground state spin density distribution in a 2x1x1 supercell of CPM-s8

As shown in Figure 7.8 (inset), the FC plot (at 1000 Oe) could be fitted by the Curie–Weiss equation, leading to Curie and Weiss constants of C = 8.75 emu·Oe^{-1}·K per formula unit [5 cobalt(II) ions] and $\theta = -21$ K, respectively (Figure 7.8, inset). The effective magnetic moment per cobalt(II) as estimated from the Curie constant is ~1.67 μ_B, indicative of low-spin cobalt(II) ions (~1.73 μ_B). A negative θ value suggests dominating antiferromagnetic interactions among the cobalt(II) centres. Indeed, the ZFC curve at 100 Oe (Figure 7.8) shows a peak at 8 K, further confirming the presence of antiferromagnetic (AFM) interactions. However, application of a small magnetic field, as the FC curve shows, destroys this peak, thus suggesting that the more likely magnetic ordering is ferrimagnetic with a T_C = 8 K. Density functional theory calculations using the Hubbard onsite potential (DFT+U) have suggested that the ground state spin ordering is ferrimagnetic model with Co(2) and Co(3) in the spin-up configuration while the central Co(1) is spin-down, as shown in the spin density map in Figure 7.8b. This spin arrangement is dominated by AFM interactions (4) versus only 2 FM (ferromagnetic) ones, and a net magnetic moment will result. Furthermore, this pentameric unit is composed of 2 triangles, suggesting that geometric frustration would be possible if the triangles were equilateral. However, the different distances within the triangles eliminate (or strongly reduce) the frustration.

7.4 Conclusion

Based upon structural analysis of newly synthesized 3D rod-packing manganese-based framework, strategic design of capping agent was developed to obtain a 2D rod-packing framework. SQUID measurements and DFT calculations proved ferrimagnetic ordering of the material below 8 K, further illustrating the potential of developing spintronic materials through 2D rod-packing MOFs.

7.5 Reference

1. Jiang, H.; Alezi, D.; Eddaoudi, M., A Reticular Chemistry Guide for the Design of Periodic Solids. *Nature Reviews Materials* **2021,** *6*, 466-487.

2. Freund, R.; Canossa, S.; Cohen, S. M.; Yan, W.; Deng, H.; Guillerm, V.; Eddaoudi, M.; Madden, D. G.; Fairen-Jimenez, D.; Lyu, H.; Macreadie, L. K.; Ji, Z.; Zhang, Y.; Wang, B.; Haase, F.; Wöll, C.; Zaremba, O.; Andreo, J.; Wuttke, S.; Diercks, C. S., 25 Years of Reticular Chemistry. *Angew. Chem. Int. Ed.* **2021,** *60*, 23946-23974.

3. Behera, N.; Duan, J.; Jin, W.; Kitagawa, S., The Chemistry and Applications of Flexible Porous Coordination Polymers. *EnergyChem* **2021,** *3*, 100067.

4. Kalmutzki, M. J.; Hanikel, N.; Yaghi, O. M., Secondary Building Units as the Turning Point in the Development of the Reticular Chemistry of Mofs. *Sci. Adv.* **2018,** *4*, eaat9180.

5. Furukawa, H.; Cordova, K. E.; O'Keeffe, M.; Yaghi, O. M., The Chemistry and Applications of Metal-Organic Frameworks. *Science* **2013,** *341*, 1230444.

6. Rosi, N. L.; Kim, J.; Eddaoudi, M.; Chen, B.; O'Keeffe, M.; Yaghi, O. M., Rod Packings and Metal−Organic Frameworks Constructed from Rod-Shaped Secondary Building Units. *J. Am. Chem. Soc.* **2005,** *127*, 1504-1518.

7. Schoedel, A.; Li, M.; Li, D.; O'Keeffe, M.; Yaghi, O. M., Structures of Metal–Organic Frameworks with Rod Secondary Building Units. *Chem. Rev.* **2016,** *116*, 12466-12535.

8. Zhao, X.; Shimazu, M. S.; Chen, X.; Bu, X.; Feng, P., Homo-Helical Rod Packing as a Path toward the Highest Density of Guest-Binding Metal Sites in Metal–Organic Frameworks. *Angew. Chem. Int. Ed.* **2018,** *57*, 6208-6211.

9. Yang, H.; Peng, F.; Dang, C.; Wang, Y.; Hu, D.; Zhao, X.; Feng, P.; Bu, X., Ligand Charge Separation to Build Highly Stable Quasi-Isomer of Mof-74-Zn. *J. Am. Chem. Soc.* **2019,** *141*, 9808-9812.

10. Peng, F.; Yang, H.; Hernandez, A.; Schier, D. E.; Feng, P.; Bu, X., Bimetallic Rod-Packing Metal–Organic Framework Combining Two Charged Forms of 2-Hydroxyterephthalic Acid. *Chem. Eur. J.* **2020,** *26*, 11146-11149.

11. Wang, L. J.; Deng, H.; Furukawa, H.; Gandara, F.; Cordova, K. E.; Peri, D.; Yaghi, O. M., Synthesis and Characterization of Metal-Organic Framework-74 Containing 2, 4, 6, 8, and 10 Different Metals. *Inorg. Chem.* **2014,** *53*, 5881-3.

12. Li, B.; Wen, H.-M.; Wang, H.; Wu, H.; Yildirim, T.; Zhou, W.; Chen, B., Porous Metal–Organic Frameworks with Lewis Basic Nitrogen Sites for High-Capacity Methane Storage. *Energy Environ. Sci.* **2015,** *8*, 2504-2511.

13. Sun, L.; Hendon, C. H.; Minier, M. A.; Walsh, A.; Dincă, M., Million-Fold Electrical Conductivity Enhancement in Fe2(Debdc) Versus Mn2(Debdc) (E = S, O). *J. Am. Chem. Soc.* **2015,** *137*, 6164-6167.

14. Wang, X.; Li, B.; Wu, Y.-P.; Tsamis, A.; Yu, H.-G.; Liu, S.; Zhao, J.; Li, Y.-S.; Li, D.-S., Investigation on the Component Evolution of a Tetranuclear Nickel-Cluster-Based Metal–Organic Framework in an Electrochemical Oxidation Reaction. *Inorg. Chem.* **2020,** *59*, 4764-4771.

15. Kim, E. J.; Siegelman, R. L.; Jiang, H. Z. H.; Forse, A. C.; Lee, J.-H.; Martell, J. D.; Milner, P. J.; Falkowski, J. M.; Neaton, J. B.; Reimer, J. A.; Weston, S. C.; Long, J. R., Cooperative Carbon Capture and Steam Regeneration with Tetraamine-Appended Metal–Organic Frameworks. *Science* **2020,** *369*, 392.

16. Li, L.; Lin, R.-B.; Krishna, R.; Li, H.; Xiang, S.; Wu, H.; Li, J.; Zhou, W.; Chen, B., Ethane/Ethylene Separation in a Metal-Organic Framework with Iron-Peroxo Sites. *Science* **2018,** *362*, 443-446.

17. Milner, P. J.; Siegelman, R. L.; Forse, A. C.; Gonzalez, M. I.; Runčevski, T.; Martell, J. D.; Reimer, J. A.; Long, J. R., A Diaminopropane-Appended Metal–Organic Framework Enabling Efficient Co2 Capture from Coal Flue Gas Via a Mixed Adsorption Mechanism. *J. Am. Chem. Soc.* **2017,** *139*, 13541-13553.

18. Geier, S. J.; Mason, J. A.; Bloch, E. D.; Queen, W. L.; Hudson, M. R.; Brown, C. M.; Long, J. R., Selective Adsorption of Ethylene over Ethane and Propylene over Propane in the Metal–Organic Frameworks M2(Dobdc) (M = Mg, Mn, Fe, Co, Ni, Zn). *Chem. Sci.* **2013,** *4*, 2054-2061.

19. Bae, Y. S.; Lee, C. Y.; Kim, K. C.; Farha, O. K.; Nickias, P.; Hupp, J. T.; Nguyen, S. T.; Snurr, R. Q., High Propene/Propane Selectivity in Isostructural Metal-Organic Frameworks with High Densities of Open Metal Sites. *Angew. Chem. Int. Ed. Engl.* **2012,** *51*, 1857-60.

20. Bao, Z.; Wang, J.; Zhang, Z.; Xing, H.; Yang, Q.; Yang, Y.; Wu, H.; Krishna, R.; Zhou, W.; Chen, B.; Ren, Q., Molecular Sieving of Ethane from Ethylene through the Molecular Cross-Section Size Differentiation in Gallate-Based Metal-Organic Frameworks. *Angew. Chem. Int. Ed. Engl.* **2018,** *57*, 16020-16025.

21. Jaramillo, D. E.; Jiang, H. Z. H.; Evans, H. A.; Chakraborty, R.; Furukawa, H.; Brown, C. M.; Head-Gordon, M.; Long, J. R., Ambient-Temperature Hydrogen Storage Via Vanadium(Ii)-Dihydrogen Complexation in a Metal-Organic Framework. *J. Am. Chem. Soc.* **2021,** *143*, 6248-6256.

22. Shigematsu, A.; Yamada, T.; Kitagawa, H., Wide Control of Proton Conductivity in Porous Coordination Polymers. *J. Am. Chem. Soc.* **2011,** *133*, 2034-2036.

23. Wang, M.; Gou, X.; Shi, W.; Cheng, P., Single-Chain Magnets Assembled in Cobalt(Ii) Metal-Organic Frameworks. *Chem Commun (Camb)* **2019,** *55*, 11000-11012.

24. Li, X.-B.; Zhang, J.-Y.; Wang, Y.-Q.; Song, Y.; Gao, E.-Q., Tricomponent Azide, Tetrazolate, and Carboxylate Cobridging Magnetic Systems: Ferromagnetic Coupling, Metamagnetism, and Single-Chain Magnetism. *Chem. Eur. J.* **2011,** *17*, 13883-13891.

25. Zheng, Y.-Z.; Tong, M.-L.; Zhang, W.-X.; Chen, X.-M., Assembling Magnetic Nanowires into Networks: A Layered Coii Carboxylate Coordination Polymer Exhibiting Single-Chain-Magnet Behavior. *Angew. Chem. Int. Ed.* **2006,** *45*, 6310-6314.

26. Hu, S.; Yun, L.; Zheng, Y.-Z.; Lan, Y.-H.; Powell, A. K.; Tong, M.-L., Ferrimagnetic [Coii3(M3-Oh)2(Rco2)4] Chains Embedded in a Laminar Hybrid Material Exhibiting Single-Chain Magnet Behaviour. *Dalton Trans.* **2009**, 1897-1900.

27. Hu, B.-W.; Zhao, J.-P.; Yang, Q.; Zhang, X.-F.; Evangelisti, M.; Sañudo, E. C.; Bu, X.-H., Synthesis, Structure and Magnetic Properties of Two New Azido-Coii Coordination Architectures: From Ferromagnetic Coupling to Single-Chain-Magnets. *Dalton Trans.* **2010,** *39*, 11210-11217.

28. Li, Z.-X.; Zeng, Y.-F.; Ma, H.; Bu, X.-H., Homospin Single-Chain Magnet with 1d Ferromagnetic Azido-Cobalt Ising-Type Chain. *Chem. Commun.* **2010,** *46*, 8540-8542.

29. Zhang, S.-Y.; Shi, W.; Lan, Y.; Xu, N.; Zhao, X.-Q.; Powell, A. K.; Zhao, B.; Cheng, P.; Liao, D.-Z.; Yan, S.-P., Observation of Slow Relaxation of the Magnetization and Hysteresis Loop in an Antiferromagnetic Ordered Phase of a 2d Framework Based on Coii Magnetic Chains. *Chem. Commun.* **2011,** *47*, 2859-2861.

30. Wang, Y.-Q.; Cheng, A.-L.; Liu, P.-P.; Gao, E.-Q., Unusual Composition Dependence of Magnetic Relaxation for Coii1−Xniiix Chain-Based Metal–Organic Frameworks. *Chem. Commun.* **2013,** *49*, 6995-6997.

31. Kawamura, A.; Filatov, A. S.; Anderson, J. S.; Jeon, I.-R., Slow Magnetic Relaxation of Co(Ii) Single Chains Embedded within Metal–Organic Superstructures. *Inorg. Chem.* **2019,** *58*, 3764-3773.

32. Liu, Q.-Y.; Wang, W.-F.; Wang, Y.-L.; Shan, Z.-M.; Wang, M.-S.; Tang, J., Diversity of Lanthanide(Iii)–Organic Extended Frameworks with a 4,8-Disulfonyl-2,6-Naphthalenedicarboxylic Acid Ligand: Syntheses, Structures, and Magnetic and Luminescent Properties. *Inorg. Chem.* **2012,** *51*, 2381-2392.

33. Perdew, J. P.; Burke, K.; Ernzerhof, M., Generalized Gradient Approximation Made Simple. *Phys. Rev. Lett.* **1996,** *77*, 3865-3868.

Chapter 8: Conclusion and Outlook

We have achieved a great success in the enrichment of *pacs* platform with novel framework design methodologies to result in the construction of optimized materials with impressive properties in a range of gas storage and separation applications. In Chapter 2, we defined the minimum and maximum c/a ratios of the *pacs*, as well as c/a ratio for which each L1 linker could achieve maximum volume. We constructed structures with c/a limits that were previously thought of, as impossible to achieve. In Chapter 3, we introduced a charge reallocation strategy to develop a second generation of anionic *pacs* materials that is both robust and versatile. Chapter 4 revisited c/a ratio limits in optimizing pore-space of cationic materials. In both chapters, counterbalancing ions have large influences over selective host-guest interactions. In Chapter 5, we succeeded in merging the acidic -SO_3H group into our *pacs* platform and harnessed opportunities associated with this interesting functional group.

We next examined the effects of pore space optimization of *pacs* in important industrial small molecule sorption and separations, namely CO_2 and C_2H_2 uptakes, C_2H_2/CO_2 separation, hydrocarbon separation (C_2H_4/C_2H_6, C_3H_6/C_3H_8, C_6H_6/C_6H_{12}) and CO_2 capture. Different framework enhancements strategies have resulted in exceptional performances that surpassed records of traditional solids such as zeolites and activated carbon. In addition of adsorption performances, *pacs* materials have shown desirable properties such as material stability, regeneration efficiency, and ease of scale-up. While

the extraordinary performances have allowed *pacs* materials to set records in many applications, we hope continuous optimizations could bring these adsorbents to commercialization.

Many unique opportunities offered by the *pacs* platform are still waiting to be explored (e.g., encapsulating interesting molecules through π-π interactions with sandwiching pore-partitioned layers, introducing defects into framework through mixing of different functional sites). Further advances of *pacs* platform will also be helped by combining pore space partition strategy with other MOF design strategies or using PSP-designed materials for still unexplored and much less explored applications.

In general, application-focused studies tend to draw on structural platforms (e.g., MOF-5, HKUST-1, MOF-74) developed at the early stage of the field development given their greater and easily noticeable literature presence, leading to under exploration of newer platforms. In Chapter 6 and 7, we explored new material synthesis directions to construct novel materials. Chapter 6 focused on building novel materials with different proton transport pathways for conductivity measurements. In Chapter 7, we constructed novel 2D material with rod-shaped SBUs that are highly useful in magnetic studies.

Without a doubt, at the basis of the MOF field is still the fundamental synthetic and structural science whose advance has the potential to reshape all other aspects of MOF studies and applications. The vast synthetic space of MOFs encompasses huge numbers of synthetic parameters and variations, giving us plenty of room to investigate new structural features and their related applications.